UNIVERSITY OF TRENTO

Doctoral School in Civil, Environmental and Mechanical Engineering

Curriculum 1. Civil and Environmental Engineering

Andrea Zonato

# Modeling the Urban Boundary Layer in Complex Terrain

2021 - Doctoral thesis

UNIVERSITY OF TRENTO - Italy
Department of Civil, Environmental
and Mechanical Engineering

Doctoral School in Civil, Environmental and Mechanical Engineering
Topic 1. Civil and Environmental Engineering - XXXIII cycle 2017/202

Doctoral Thesis - October 2021

Andrea Zonato

# Modeling the Urban Boundary Layer in Complex Terrain

**Supervisors**
Eng. Lorenzo Giovannini, University of Trento
Prof. Dino Zardi, University of Trento
Dr. Alberto Martilli, Ciemat

DOCTORAL THESIS

# Modeling the Urban Boundary Layer in Complex Terrain

*Author:*

Andrea Zonato

*Supervisors:*

Lorenzo Giovannini
Alberto Martilli
Dino Zardi

Atmospheric Physics Group

Department of Civil, Environmental and Mechanical Engineering

November 25, 2021

UNIVERSITY OF TRENTO

# *Thesis introduction*

Doctor of Philosophy

## Modeling the Urban Boundary Layer in Complex Terrain

Andrea Zonato

Modelling atmospheric processes and land surface-atmosphere interactions occurring in non-homogeneous terrain has been getting increasing attention in the last decades for environmental purposes, enabled by the increase in computer power, that allows to perform numerical simulations at higher spatial resolution. Non-homogeneous terrain, including urban areas and mountainous regions, requires more complex models and parameterizations, to take into account the heterogeneity induced by the surface to the atmospheric dynamics. The modifications due to urban areas and mountainous regions to the atmospheric flow take place in the Planetary Boundary Layer (PBL), which is defined as *"that part of the troposphere that is directly influenced by the presence of the earth's surface, and responds to surface forcings with a timescale of about an hour or less. These forcings include frictional drag, evaporation and transpiration, heat transfer, pollutant emission, and terrain induced flow modification. The boundary layer thickness is quite variable in time and space, ranging from hundreds of meters to a few kilometers* (Stull, 1988). An accurate modelling of the PBL is of fundamental importance, since it is that part of the atmosphere where people live, and a good understanding of the processes and precise forecasts of the atmospheric dynamics within the PBL is beneficial in terms of people life quality, care of the environment and sustainable exploitation of resources, especially in the context of the climate change.

This thesis focuses on the modeling of two different kinds of non-homogeneous PBL: the Urban Boundary Layer (UBL) and the Mountain Boundary Layer (MBL).

### The Urban Boundary Layer

The UBL is defined as *that part of the PBL influenced by the presence of a city* (Oke et al., 2017). UBL behaviour is the result of the fluxes of mass, energy, and momentum exchanged by the air with the urban elements, and it is strongly affected by the city structure (Martilli, 2014). The understanding of the UBL through appropriate models is fundamental for citizen's life, because it impacts air quality, thermal comfort, and the building energy consumption by heating or cooling systems. At the start of the last century, various Urban Canopy Parameterizations (UCPs) have been developed in the context of mesoscale Numerical Weather Prediction

(NWP) models, to describe the interaction between the PBL and urban areas (Kusaka et al., 2001; Martilli et al., 2002; Masson, 2000), leading to a better understanding of the temporal and spatial variability of the UBL, adopting appropriate input datasets. UCPs have been even successfully employed for, e.g., the quantification of energy demand (Pappaccogli et al., 2018), the estimation of the impact of urban expansion (Giovannini et al., 2014) or the quantification of the effect of rooftop mitigation strategies (Li et al., 2014).

**The Mountain Boundary Layer**

The MBL has been recently defined as *the lowest part of the troposphere that is directly influenced by the mountainous terrain, responds to surface and terrain forcings with timescales of about one to a few hours, and is responsible for the exchange of energy, mass, and momentum between the mountainous terrain and the free troposphere* (Lehner et al., 2018). While over flat terrain the exchanges of momentum, energy and moisture are mainly restricted to the vertical turbulent mixing, in mountainous areas a multitude of additional processes can contribute to the exchange at a variety of spatial and temporal scales (Rotach et al., 2015), ranging from the microscale to the global scale. Orography-induced PBL processes are mainly daily-periodic and thermally-driven, including slope winds, blowing along sidewall slopes, and along valley winds (Zardi et al., 2013). PBL turbulence closures have been successfully employed to simulate MBL processes (Giovannini et al., 2014; Tomasi et al., 2019). However, PBL schemes are generally based on measurements over flat terrain, and they are applied by necessity to terrains for which they have not been developed, potentially leading to poor performances (Dimitrova et al., 2016)

The current thesis aims to tackle some open questions regarding the mesoscale modelling of the PBL over urban areas and complex terrain, and its interaction with the underlying surfaces. Specifically, for the Urban Boundary Layer, it focuses on the enhancement of the input datasets to represent urban areas, on the evaluation of the effect of mitigation strategies for thermal comfort and energy consumption, and on the effect of the drag induced by buildings on the mean flow. Regarding the Mountain Boundary Layer, the spotlight is set on the implementation of new turbulence closures, with the aim to improve the reproduction of PBL processes for ideal and real cases.
The following manuscript is organized into five chapters, each of them thought as a scientific paper:

1) a new interpolation technique to improve the capabilities of the WUDAPT method (Stewart et al., 2012), adopted to define the urban morphology at mesoscale resolution, with the aim to improve the reproduction of UBL dynamics for the city of Bologna during a heat-wave period;

2) the development of new parameterizations employed to quantify the effect of rooftop mitigation strategies in improving thermal comfort and diminishing energy consumption under different idealized urban configurations;

3) the development of novel PBL schemes, based on the $K-\varepsilon$ turbulence closure, with the aim to improve the reproduction of PBL dynamics for idealized flat and mountainous cases, for different PBL regimes;

4) the adaptation of the PBL scheme developed in 3) to the Urban Canopy Layer, through the modelling of the drag induced by idealized arrays of buildings under neutral stratification;

5) the application of the PBL schemes developed in 4) and 5) to a real case study. The focus is the city of Trento (Italy) and its surrounding areas, situated in the Alpine Adige Valley.

All the aforementioned works are developed in the context of the mesoscale NWP Weather Research and Forecasting (WRF) model, with the aim to possibly include the schemes developed in the current thesis into the official open-source version of the WRF software. For each paper-like chapter, an introduction contextualizes the topic into the current state-of-the-art. Moreover, the new models and methodologies are presented, followed by the results. Finally, a summary of the results and a brief discussion to evaluate the accomplishments and the potentiality of each study are presented.

# *Acknowledgements*

First of all, I want to thank my main supervisor, Eng. Lorenzo Giovannini, for his constant support and help in developing this Ph.D. work.

Thanks to Prof. Dino Zardi, for welcoming me to the Atmospheric Physics Group at the University of Trento and for the continuous advice regarding my thesis.

A special thank to Dr. Alberto Martilli, who since my Master Thesis keeps guiding me towards the world of atmospheric modeling, with constant advice, help, and always precise suggestions.

Thanks to Dr. Fei Chen, who offered me the possibility to work at NCAR for six months. Thanks even to Dr. Jimy Dudhia, Dr. Pedro A. Jimenez, Dr. Stefano Alessandrini, and Dr. Richard Rotunno who helped me under all the points of view during the research period in Boulder.

Thanks to all my colleagues of the Atmospheric Physics Group, especially Gianluca, Federica, Federica, Andrea, and Marco, for sharing with me continuous knowledge and for contributing to make the team a wonderful team to work with.

Thanks to Lorenzo Castellaccio and Marika Tomasi, who contributes to the design of some figures of this Ph.D. Thesis.

Thanks to my dad, mom, sisters, and nephews, my lovely family, and Stefano and Elisabetta, my Trento family, who supported me during the Ph. D. journey as well as possible.

# Contents

# List of Figures

# List of Tables

*To my curiosity. . .*

# 1 Evaluating the Performanc of a Novel WUDAPT Averaging Technique to Define Urban Morphology within Mesoscale Models

**Abstract**

The definition of accurate input datasets, appropriately representing urban morphology characteristics, has been identified as a crucial point for improving the simulation of urban boundary layer (UBL) dynamics by means of mesoscale numerical weather prediction (NWP) models. However, the scarcity of suitable data to adequately describe urban morphology is in many cases a significant obstacle to overcome. For this purpose, the World Urban Database Portal Tool (WUDAPT) framework was developed in order to obtain a standard classification of urban morphology, even in the absence of ad-hoc data for any city.

In the present work, a modified WUDAPT method to define urban morphology is proposed and compared with two state-of-the-art methods, i.e. the standard WUDAPT method and a urban morphology parameters obtained from LIDAR data. In particular, here morphological features of Local Climate Zones (LCZs), resulting from a 30-m resolution WUDAPT classification, are interpolated to NWP cells, providing averaged features of the urban morphology. In this way, the method produces a unique value of the different urban morphology parameters for each model cell. This technique is tested by means of simulations with the Weather Research and Forecasting (WRF) model at 500 m resolution for the city of Bologna (Italy), located in the Po Plain. Simulation output is compared with measurements from weather stations. Results show that simulations using the modified WUDAPT method reproduce better atmospheric dynamics with respect to those implementing the standard WUDAPT method, and are comparable with simulations using the urban morphology defined with LIDAR data, considered as reference. In particular, the most relevant improvements are found in areas where LCZs are more heterogeneous and where the boundary between rural and urban areas is not clearly defined. It follows that the use of this method improves the classic WUDAPT method for small and scattered cities with respect to large and clustered urban areas, and can be particularly useful for urban areas where detailed LIDAR data are not available.

## 1.1 Introduction

The number and extent of urbanized surfaces are increasing throughout the world. The combination of urbanization with the constant growth of population living in cities makes the understanding of the urban environment a prime topic, concerning in particular the planning of a sustainable development and an efficient exploitation of energy resources. In fact, the increasing urbanization leads to a notable modification of land use, contributing to deteriorate human comfort and quality of life, increase energy demand and modify surrounding ecosystems (Grimm et al., 2008). The main cause of these problems is the increase of air temperature within the urban environment, due to the geometrical and thermal properties of urban structures in combination with the reduction of vegetated areas.

This higher air temperature within the city with respect to its surrounding areas is the well-known Urban Heat Island (UHI) effect. This phenomenon is mainly driven by buildings and paved surfaces, which modify energy, mass and momentum exchanges between the surface and the atmosphere. In particular, street canyon geometry, building material thermal capacity and anthropogenic heat release (from transport and heating/cooling systems) favour the increase of air temperature (Oke, 1987).

In the last years our understanding of the spatial, temporal and intensity variability of the UHI has greatly advanced thanks to Numerical Weather Prediction (NWP) models, along with the increasing availability of high computational power resources, in addition to experimental campaigns (Giovannini et al., 2011). To take into account the effects of urban areas within NWP models, different parameterizations have been developed in the last decades, with different levels of complexity, depending on the scopes. For example, the *Building Effect Parameterization* (BEP) and the *Building Energy Model* (BEM) (Martilli et al., 2002; Salamanca et al., 2010; Salamanca et al., 2011) have been designed to take into account urban scale processes within mesoscale models and are currently implemented in the Weather Research and Forecasting (WRF) model (Chen et al., 2011) . In order to correctly perform numerical simulations with the above mentioned parameterizations, an adequate representation of urban canopy parameters (UCPs) is required to provide proper information to the numerical scheme (di Sabatino et al., 2010). In fact, a correct definition of urban morphology has been identified as crucial to enhance model performance (Masson, 2006; Stewart et al., 2014). UCP data can be assembled from numerous sources, such as land use maps, building databases and satellite/LIDAR data. Several works in the literature show that a good representation of UCPs allows to correctly simulate the temperature variability in the urban area (Giovannini et al., 2014; Li et al., 2018; Salamanca et al., 2012b), climatological modifications induced by urban areas expansion (Tewari et al., 2017), the building energy budget (Gutiérrez et al., 2015; Pappaccogli et al., 2018), and the effect of mitigation strategies applied to cities (Salamanca et al., 2016; Yang et al., 2015).

However, for many cities, adequate urban morphology information is not available, or not suited for NWP modelling, due to a lack in resolution or to the absence of some variables. On the other hand, even if in situ data are available for a given city, they are often difficult to obtain or complicated to incorporate in meteorological models. To fill this gap, in the recent years the World Urban Database Access Portal Tool (WUDAPT) initiative is engaged in creating a

global database for cities, to be used for urban climate studies (Ching et al., 2018). It permits to classify a city and its sourrounding areas into 17 Local Climate Zones (LCZs), ten of which are urban. Each of the ten Urban Climate Zones (UCZs) is associated with parameters describing the urban morphology and the material properties with standard values. Recently, Brousse et al. (2016) incorporated WUDAPT classification into WRF, demonstrating that for the city of Madrid, adopted as case study, this method improves model performance with respect to the use of CORINE land cover (*https://land.copernicus.eu/pan-european/corine-land-cover/clc2012*). However, in that work, each grid cell of the mesoscale model (333 m $\times$ 333 m) was represented by one urban LCZ only, adopting the most frequent one within the grid cell. Given that the LCZ map produced by WUDAPT had a resolution of 100 m, the drawback of this technique is the degradation of the information contained in the high resolution original WUDAPT map to the coarse resolution of the mesoscale model.

To overcome this problem, and to take the maximum advantage of the high resolution of the LCZ maps produced by WUDAPT, a new method to obtain customized UCPs from the WUDAPT classification is presented here. Each morphological parameter (building plan area density, total building area density, building height distribution, and urban fraction) derived from the WUDAPT LCZ classification (at a resolution of 30 m) is interpolated in order to obtain customized UCPs for each NWP grid cell, overtaking the categorical definition of the LCZs. This new method is tested by means of simulations with the Weather Research and Forecasting (WRF) model, using BEP+BEM as urban parameterization schemes, and adopting the city of Bologna (Italy) as a case study.

The paper is organized as follows. The climatic and morphological features of the case study, along with the weather stations adopted in the present work, are described in Section 1.2. In Section 1.3, the method proposed here for defining UCPs is presented and the urban morphology obtained is compared with results from the classical WUDAPT method and with the urban morphology defined with LIDAR data. In Section 1.4 numerical results are validated against measurements, in order to evaluate the benefits of the proposed method. Finally, results are summarized and discussed in Section 1.5.

## 1.2 Case study

### 1.2.1 Study Area

Bologna (44°29′38″ N, 11°20′34″ E) is a city of 387.500 inhabitants located in the center of the so called "Città metropolitana di Bologna" (metropolitan area), where almost one million people live. It is the administrative center of the Emilia-Romagna region and the seventh most populated city in Italy. Bologna is situated at the feet of Apennines in the Po Plain between the rivers Reno and Savena; its center is at 54 m above sea level (ASL). The historical center, with a quasi-circular shape, is one of the widest and most ancient in Europe. In the centuries the urbanization developed radially from the city center, rather in the north than to the south, where it was somehow impeded by the presence of the hills. Bologna has a humid temperate climate with hot summers. In particular, during summertime, under sub-tropical anticyclonic conditions, temperatures can easily exceed 38 °C. Precipitation occurs especially during spring

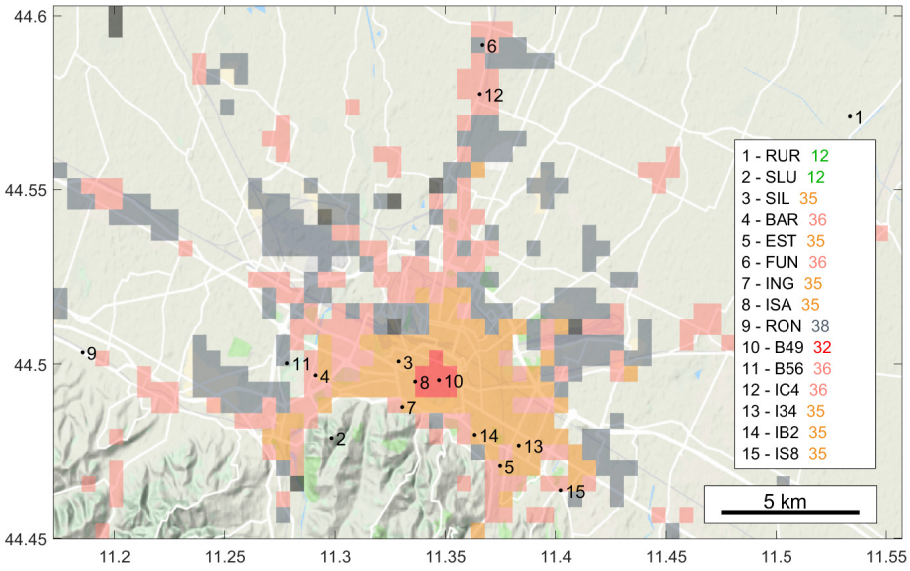


**Figure 1.1:** Map of the weather stations in the domain of interest. LCZ using CAT method have been overlaid.The last number in the legend refers to the MODIS landuse class.

and autumn, but thunderstorms are frequent during summer. Thermal inversion (TI) conditions frequently develop during nighttime in the Po Plain, due to radiative cooling and also to drainage flows close to mountain slopes. During summer, stagnation of warm and moist air is favored by the low ventilation associated with blocking by the Alps and Apennines, leading to hot and sultry conditions, especially during heat waves. The high humidity during summertime is also the source of frequent and strong storms, including some hailstorms.

### 1.2.2 Study period

In the present work simulations focus on a clear-sky period, 17-20 July 2015, when diurnal circulations and UHI were well developed due to weak synoptic forcing. In fact, the month of July 2015 was characterized by a subtropical air mass with stable conditions over the study area. This led to a monthly mean temperature above the climatological (1961-1990) average by 4 °C, with anomalies up to 7 °C during some days. Moreover, TI occurred on each day of that period, as detected both by radiosoundings at San Pietro Capofiume, North of Bologna (http://weather.uwyo.edu/cgi-bin/sounding?region=europe &TYPE=TEXT%3 ALIST&YEAR=2015&MONTH=07&FROM=1700&TO=2000&STNM=16144) and by surface weather stations (see Fig. 1.13, upper-left panel). Since Bologna is situated close to the slopes of the Appenines, at slightly higher altitude with respect to the Po Plain, nighttime temperature differences between the city and rural areas in the Po Plain are the consequence of both the UHI and the TI (Giovannini et al., 2011).

### 1.2.3 Weather Stations

In this study, observational data from three separate sources are used, namely the Regional Agency for Environmental Protection (3 stations, AR in Fig. 1.1), the private association

Emilia-Romagna Meteo (6 stations, EM in Fig. 1.1) and the Wunderground's Personal Weather Station Network ( PWSN, https: //www.wunderground.com/ ) (6 stations, WG in Fig. 1.1). Two of the above stations are located in rural areas, while the other 13 are located in different UCZs. While the first two sources provide official and verified data, the PWSN are often not verified and WMO installation guidelines (WMO, 2019) are not always followed. For this reason, data were quality-controlled and several PWSN data were filtered out, since during the simulation period these stations provided unreliable measurements. The method adopted here to filter erroneous data is the same used in Hammerberg et al. (2018), to discard data from stations located indoor or close to building surfaces. In particular, weather stations showing an average daily minimum temperature, in the period 1 July-31 August 2015, 4°C higher than measured at all the official weather stations, are removed. For the same reason, stations displaying daily maxima more than 3°C above the average of the official ones on at least 10% of the days in the same period are also neglected. This comparison is performed between urban stations, since UHI affects the diurnal temperature range. To compare weather station data with simulations output, the closest cell to the station position is chosen. Measurements from surface weather stations are compared to simulated 2-m temperatures, while the proper level of the vertical grid is chosen for stations located at higher levels (typically above roof level).

## 1.3 Urban Morphology

Here three different techniques are adopted to derive the morphological parameters needed as input for the urban parameterizations BEP and BEM. Two of them are based on the LCZ map derived using the WUDAPT methodology, while the third one adopts LIDAR data.

The LCZ map of Bologna (Fig. 1.2) is created using the WUDAPT method at Level 0 (see www.wudapt.org), with a resolution of 30 m. It consists of a supervised classification of Landsat images using a Random Forest Classification algorithm (Breiman, 2001). The method requires first to draw polygons of uniform land cover in Google Earth (training areas, TAs). Then the algorithm combines spectral bands with the TAs defined before to obtain the LCZ classification to be used as input for WRF. In this case, for a robust classification, Landsat images from different days (18/03/213, 16/07/2013 and 10/06/2014) are used. Through the visual comparison with real morphology, TAs are then modified to obtain a satisfactory definition of LCZs. It has been decided to create the WUDAPT landmask with a resolution of 30 m (instead of the commonly used 100 m), in order to better distinguish between urban and rural areas, and to better distinguish different LCZs within a single mesoscale cell. The pixels categorized as urban, covering the 13.3% of the total surface, are divided as follows: 1.0% as LCZ 2 (compact mid-rise), 16.1% as LCZ 5 (open mid-rise), 50.0% as LCZ 6 (open low-rise), 31.1% as LCZ 8 (large low-rise) and 13.3% as LCZ E (bare rock or paved), in this work considered as an effective urban class (LCZ 11) defining sufficiently large roads, highways, and parking lots.

### 1.3.1 WUDAPT categorical

This methodology to derive urban parameters for mesoscale models (called CAT hereafter), developed by Brousse et al. (2016), assigns to each WRF cell the dominant WUDAPT category

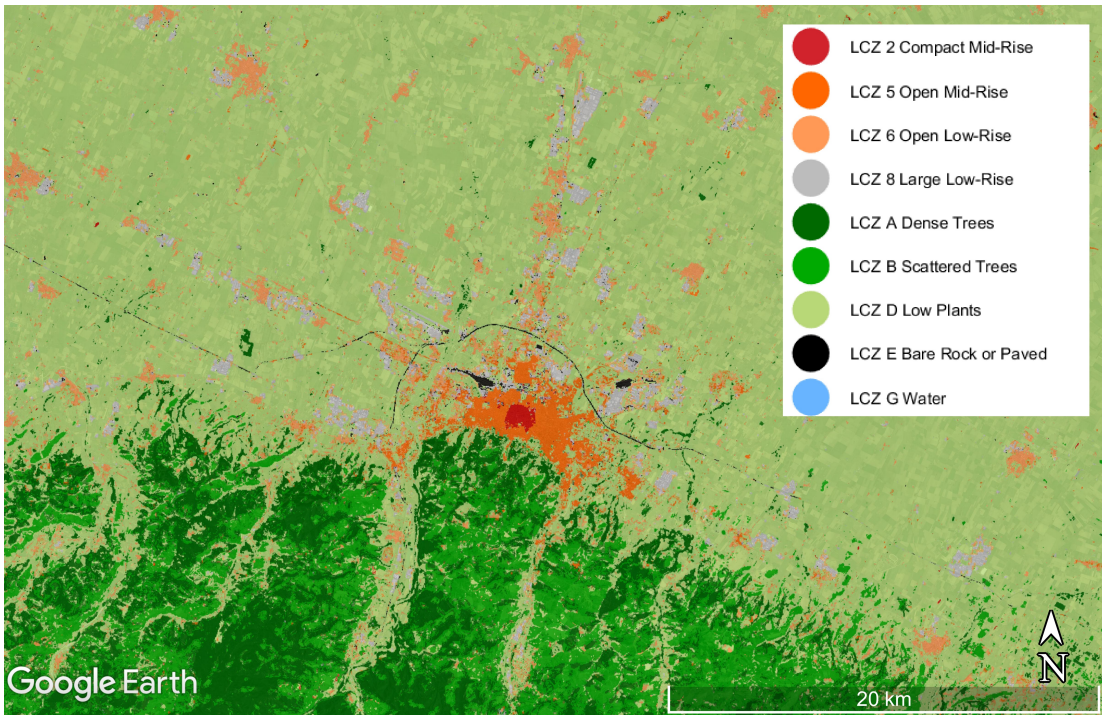


**Figure 1.2:** Map of LCZs over Bologna at 30-m resolution.

(see Fig. 1.3), as explained in Martilli et al. (2016). From these geometrical parameters, the plan area fraction ($\lambda_p$), the area weighted mean building height ($h_m$) and the building surface to plan area ratio ($\lambda_b$), are derived as input for WRF (following Glotfelty et al. (2013)) and calculated as follows:

$$\lambda_p = \frac{b}{s+b}, \qquad h_m = \frac{\sum_i p_i}{100} h_i, \qquad \lambda_b = \frac{2h_m}{b+w} + \lambda_p. \tag{1.1}$$

Here $b$ is the building width, $s$ is the street width and $p_i$ is the percentage of buildings in an interval of heights with average $h_i$. The cells with less than 50% of urban landuse are considered as rural. This method introduces a rough approximation in the representation of the urban morphology in the mesoscale meteorological model; indeed, when the cell is composed of a mix of urban and rural surfaces, through this interpolation method the contribution of the less represented categories is completely neglected. Similarly, also the heterogeneity of the morphology of the urban area is greatly reduced adopting this approach. To solve this problem a new method is developed and tested, as explained in the next section.

Each UCZ is characterized by typical geometrical parameters and physical properties of the surface materials. Geometrical parameters are shown in Tab. 1.1. Since the aim of this work is to develop a general method for better describing urban morphology in mesoscale models, rather than building ad hoc UCP datasets for Bologna, geometrical parameters are set to values typical for each LCZ, based on those suggested in Stewart et al. (2012). On the other side, building material properties (Tab. 1.2) are those characterizing solid brick for LCZ 2, LCZ 5 and LCZ 6 and concrete for LCZ 8 (industrial and commercial areas), according to typical

**Table 1.1:** Geometrical Parameters for UCZs.

| | LCZ 2 | LCZ 5 | LCZ 6 | LCZ 8 | LCZ 11 |
|---|---|---|---|---|---|
| Urban Fraction | 0.99 | 0.7 | 0.65 | 0.85 | 1 |
| Road Width [m] | 5 | 33.3 | 12.4 | 32.5 | 100 |
| Buildings Width [m] | 10 | 10 | 10.5 | 28.8 | 5 |
| Buil. % with h $<$ 5 m | - | - | 65 | 35 | 100 |
| Buil. % with 5 $<$ h $<$ 10 m | 25 | 10 | 35 | 65 | - |
| Buil. % with 10 $<$ h $<$ 15 m | 45 | 25 | - | - | - |
| Buil. % with 15 $<$ h $<$ 20 m | 20 | 40 | - | - | - |
| Buil. % with 20 $<$ h $<$ 25 m | 20 | 25 | - | - | - |

**Table 1.2:** Thermal and physical parameters for UCZs.

| LCZ | Heat Capacity (MJ m$^{-3}$ $K^{-1}$ ) | | | Thermal Conductivity (Wm$^{-1}$ $K^{-1}$) | | |
|---|---|---|---|---|---|---|
| | Roof | Walls | Road | Roof | Walls | Road |
| 2,5,6 | 1.77 | 1.37 | 1.94 | 0.84 | 0.83 | 0.75 |
| 8 | 2.11 | 2.11 | 1.94 | 1.51 | 1.51 | 0.75 |
| 11 | 1.94 | 1.94 | 1.94 | 0.75 | 0.75 | 0.75 |
| All LCZs | Roof | Walls | Road | - | - | - |
| Albedo | 0.20 | 0.20 | 0.10 | Target Temp. for ACs | | 25 °C |
| Emissivity | 0.90 | 0.90 | 0.95 | Perc. of windows | | 20% |

materials of these LCZs. For all classes, the physical properties of the asphalt have been set for the ground. Physical properties of building materials and of asphalt are left constant in all simulations, in order to highlight only differences induced by the different urban morphology.

### 1.3.2 WUDAPT interpolated

As explained in the previous section, the classical WUDAPT procedure for describing the urban landuse is limited in representing heterogeneous areas by the use of categorical values instead of specific values for each cell. To better describe the urban morphology, a new method to interpolate the WUDAPT classification to the meteorological model grid is proposed, fully exploiting the 30-m resolution of the WUDAPT landmask and passing from categorical to continuous urban morphology values. Hereafter, this method is called INTERP. First of all, the values of the morphological parameters shown in Tab. 1.1 are assigned to each WUDAPT cell at 30-m resolution.Then, the WUDAPT landuse has been interpolated at the WRF resolution, averaging each geometrical value, in order to have a unique mean value for each WRF cell. From geometrical parameters, the plan area fraction ($\lambda_p$), the area weighted mean building height ($h_m$) and the building surface to plan area ratio ($\lambda_b$), are derived, as CAT, using Eq. 1.3.1. A similar consideration can be done for the urban fraction. Each LCZ is characterized by a value of urban fraction, i.e. the ratio of the area covered by artificial surfaces (buildings and roads) to the total area of the cell. Then, for each WRF cell, the urban fraction is calculated as the weighted average of the values resulting from the WUDAPT classification.

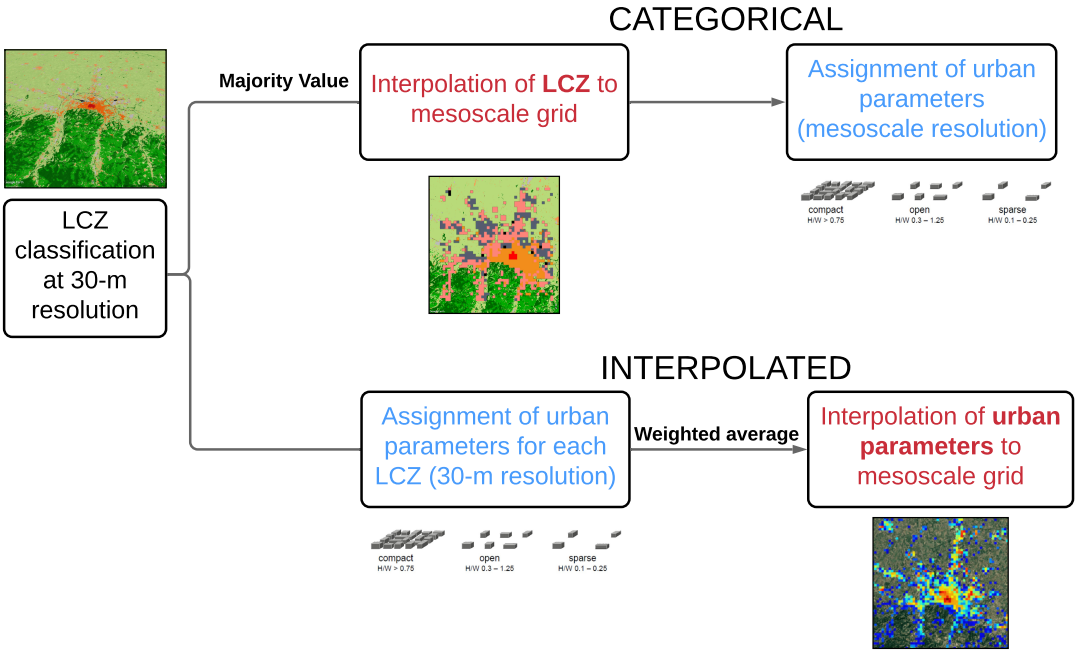


**Figure 1.3:** Flow chart of the two methods adopted to derive UCPs from the WUDAPT classification.

### 1.3.3 LIDAR

Morphological parameters were also derived from LIDAR measurements provided by the Municipality of Bologna (http://dati.comune.bologna.it/node/2521) in a georeferenced file containing information about position, height, shape, surface and volume of each building within the municipal territory. Such data have been spatially averaged in order to evaluate the parameters $\lambda_p$, $\lambda_b$, $h_m$ and $p_i$ as defined in Section 1.3.2. Unfortunately, from the dataset no information can be obtained about the urban fraction, since they do not provide any information about the spatial extent of vegetated areas. For this reason, the urban fraction obtained by interpolating the WUDAPT landmask is adopted also for this urban morphology dataset. However, the 30-m resolution adopted in this work for the WUDAPT classification allows to detect even small parks or clustered trees within the urban environment, so the urban fraction used here may be considered as a good approximation of the real one. Since LIDAR data cover only the area inside the municipality of Bologna, for the remaining urban cells the CAT classification is used.

### 1.3.4 Comparison of different methods

In the following section, the CAT and the INTERP methods are compared with the LIDAR-derived urban morphology, which is considered the reference classification. In Fig. 1.4, the maps of UCPs are shown for the three methods, while in Tab. 1.3 the error of CAT and INTERP with respect to LIDAR are reported. Urban fraction is the only variable that cannot be compared, since it is used for both LIDAR and INTERP.

It is clear that CAT fails in representing areas at the boundary between the urban and the rural environment, as it is not able to take into account subgrid variability in the landuse. This is

**Table 1.3:** Mean-root-square errors (RMSE) and mean bias (MB) for plan area fraction ($\lambda_p$), building surface to plan area fraction ($\lambda_b$) and mean height of buildings ($h_m$) each LCZ for CAT (CAT) and INTERP (I) compared with LIDAR urban morphology.

| | $\lambda_p$ | | | | $\lambda_b$ | | | | $h_m$ | | | |
|---|---|---|---|---|---|---|---|---|---|---|---|---|
| | RMSE | | MB | | RMSE | | MB | | RMSE | | MB | |
| | C | I | C | I | C | I | C | I | C | I | C | I |
| LCZ 2 | 0.14 | 0.18 | -0.11 | 0.13 | 0.77 | 1.70 | -0.19 | 1.60 | 2.7 | 3.6 | -1.5 | -2.4 |
| LCZ 5 | 0.15 | 0.19 | -0.07 | -0.13 | 0.78 | 0.59 | -0.52 | 0.12 | 8.4 | 6.4 | -6.8 | -2.8 |
| LCZ 6 | 0.38 | 0.32 | -0.37 | -0.29 | 0.87 | 0.27 | -0.85 | 0.04 | 4.0 | 4.2 | 1.7 | -0.1 |
| LCZ 8 | 0.35 | 0.38 | -0.33 | -0.36 | 0.34 | 0.62 | 0.24 | -0.58 | 4.2 | 4.1 | -0.3 | -0.1 |
| LCZ 11 | 0.08 | 0.17 | 0.05 | -0.13 | 0.10 | 0.81 | 0.07 | -0.70 | 6.9 | 3.8 | 6.7 | -2.0 |

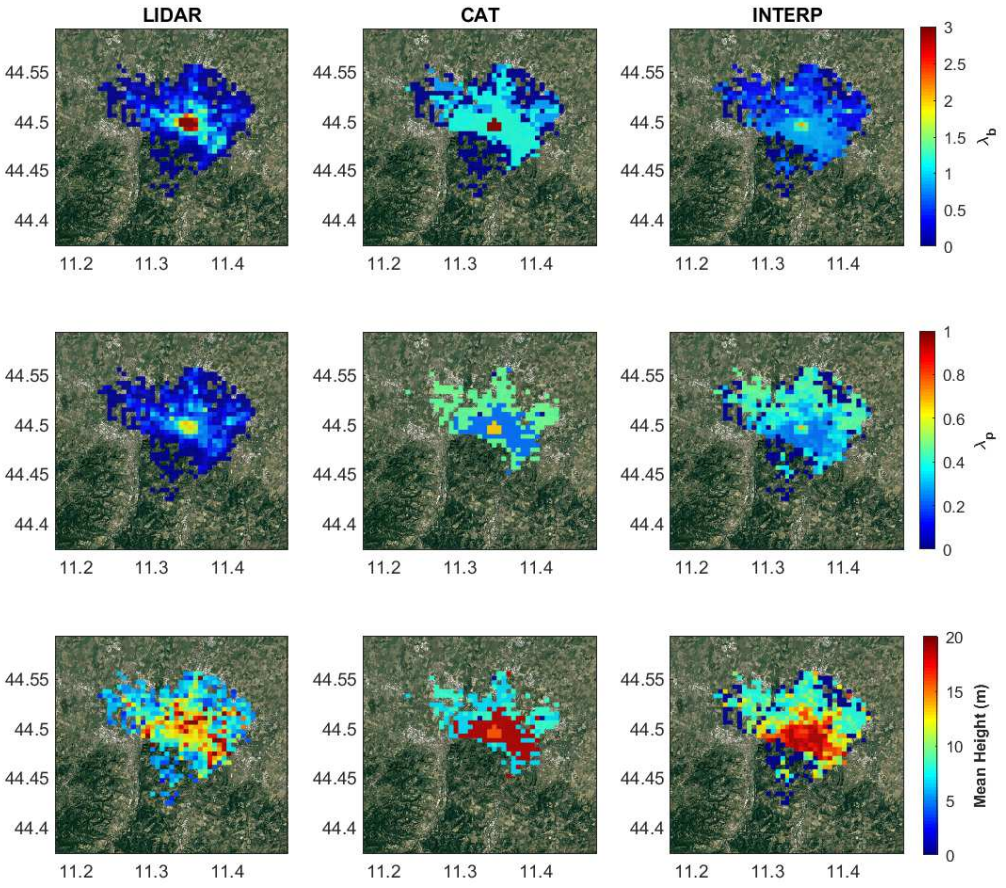


**Figure 1.4:** Urban morphology parameters used as input for the different simulations. Building surface to plan area fraction $\lambda_b$ (first row), plan area fraction $\lambda_p$ (second row), mean height $h_m$ (third row). The three methods adopted are LIDAR (left), CAT (center) and INTERP (right).

evident in particular for LCZ 8, representing industrial and commercial areas ($\lambda_u$=0.85), which are mostly located at the boundaries of the city in scattered clusters (Fig. 1.2). The dominant value used by CAT chooses either to assign the cell as urban or rural, while INTERP can consider both paved and unpaved surfaces within a single cell. The same consideration can be done for rural areas close to the city, where mixed situations can coexist within a single model cell. On the other hand, INTERP fails in describing LCZ2 for all UCPs. Errors are due to the fact that only a few number of LCZ 2 cells are present (1%), surrounded by LCZ 5 cells; the INTERP method tends to decrease the high values of $\lambda_p$ and $\lambda_b$ of LCZ 2, averaging with the surrounding LCZ 5. However, since the number of LCZ 2 cells is much lower than LCZ 5 cells, this error will not greatly affect simulations results. Concerning the other LCZs, on average INTERP better represents the urban morphology with respect to CAT, showing lower errors apart for LCZ 11, that is represented by a few cells only (its percentage diminish substantially when LCZs are interpolated using the most present value method), so its statistics is not robust. The best results are found for LCZ 5, LCZ 6 and LCZ 8 for $\lambda_p$ and $\lambda_b$, while $h_m$ does not show improvements, since buildings height variability within the same class is considered even in the CAT method through the height distribution, and differences between adjacent LCZs are not significant. It can be seen that CAT on average underestimates all UCPs, since it neglects urbanized surfaces within cells with less than 50% of urban fraction. Obviously, if the parameters assigned to each WUDAPT cells had been derived from real data (for example, averaging LIDAR data for each LCZ), errors would have been lower with respect to those presented here. However, the aim of this work is to evaluate the capability of the new method in the absence of in situ data, so urban parameters for each LCZ were not conducted from LIDAR data.

### 1.3.5 WRF Simulations

Simulations are performed with WRF version 3.9.1 (Skamarock et al., 2008). Start time is set at 1800 UTC 16 July 2015 and end time at 0600 UTC 20 July 2015. The first 12 hours are considered as spin-up period for the initialization, so they are not taken into account for the analysis. The horizontal domain consists in four two-way nested domains with $100 \times 100$, $103 \times 103$, $103 \times 103$ and $112 \times 112$ grid cells centered over Bologna, with resolution of 13.5, 4.5, 1.5 and 0.5 km respectively (Fig. 1.5). As to the vertical resolution, 51 terrain-following levels, with 10 of them in the first 110 m above ground level, are adopted. 6-hourly NCEP Final Operational Global Analysis data with a resolution of 0.25 °$\times$0.25°are used as initial and boundary conditions (NCEP, 2000). Urban parameterization schemes adopted are BEP (Martilli et al., 2002) and BEM (Salamanca et al., 2010). For BEM, a target indoor temperature of 298 K is set, with a comfort range of 0.5 K. BEP+BEM work coupled with the Bougeault et al. (1989) 1.5-order scheme for vertical turbulence and the NoahMP (Niu et al., 2011) land surface model (Salamanca et al., 2018). WSM 6-class scheme (Hong et al., 2006a) is used for microphysics, and the Grell 3D Ensemble Scheme (Grell et al., 2002) for cumulus in the coarser domain. Dudhia (1989) is used for short-wave radiation and the Rapid Radiative Transfer Model (RRTM, Mlawer et al. 1997) for long-wave radiation. Smagorinsky (1963) first-order closure is used for horizontal diffusion. Since sub-kilometer simulations are performed, the default WRF datasets for landuse and topography (30″ of resolution), are not suitable. Therefore, MODIS

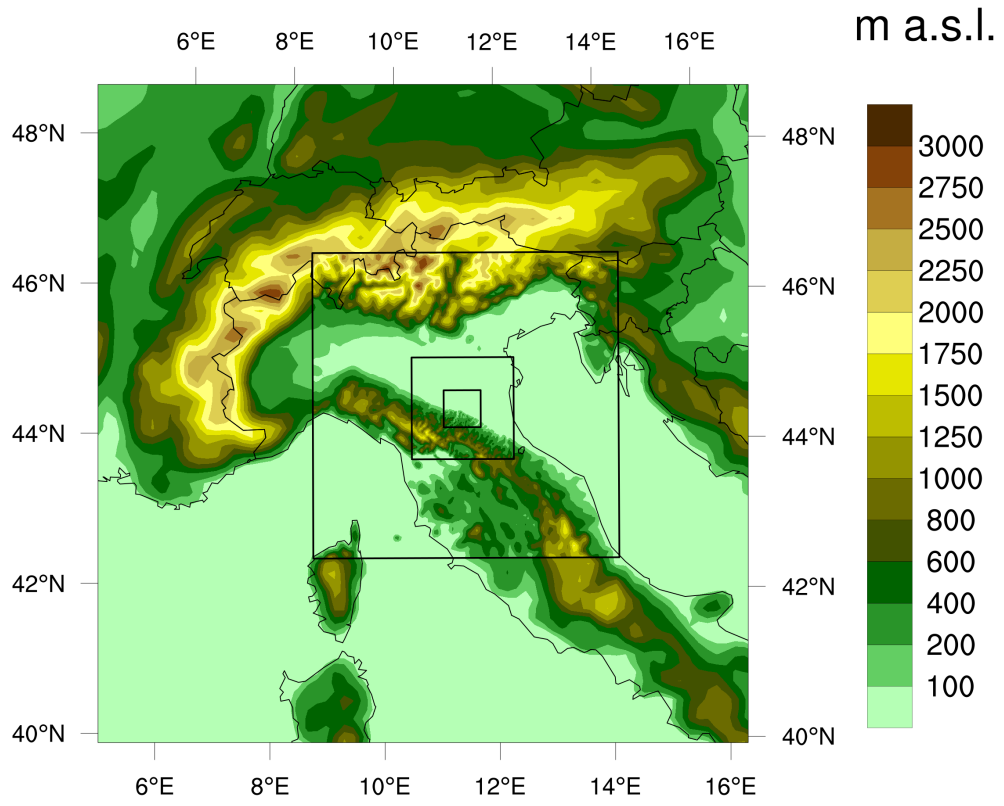


**Figure 1.5:** The four nested domains used for the numerical simulations. The color scale represents height above sea level (a.s.l.).

landuse is replaced by the CORINE Land Cover (CLC) dataset (Giovannini et al., 2014), updated to 2012, with a resolution of 100 m. The 44 CLC classes are interpolated to each domain resolution choosing the dominant value method, and reclassified into 20 (+11 WUDAPT-like urban classes) MODIS categories. The default topography is replaced by a topography dataset obtained by Viewfinder Panoramas website (http://www.viewfinderpanoramas.org), with a resolution of $3''$. Other input datasets are left as default.

A total of four simulations are run: one for each urban morphology definition method (LIDAR, CAT, INTERP), and one simulation performed substituting urban land use with croplands (MODIS class 12), in order to quantify the effect of artificial surfaces on air temperature (hereafter called NOURBAN). The NOURBAN simulation is presented here for a better interpretation of the model results, and in particular to better understand the interaction between UHI and TI, as highlighted in the next Section.

## 1.4 Results

**Table 1.4:** Mean-root-square error (RMSE), mean bias and hit rate for temperature for LIDAR (L), CAT (C) and INTERP (I), compared with measurements at the weather stations.

| | RMSE (K) | | | Mean Bias (K) | | | Hit Rate (-) | | |
|---|---|---|---|---|---|---|---|---|---|
| | L | C | I | L | C | I | L | C | I |
| RUR | 1.44 | 1.55 | 1.57 | 0.78 | 0.80 | 0.82 | 0.82 | 0.81 | 0.85 |
| SLU | 1.16 | 1.17 | 1.11 | -0.09 | -0.03 | -0.07 | 0.93 | 0.92 | 0.95 |
| SIL | 0.99 | 0.94 | 1.09 | 0.04 | 0.09 | 0.27 | 0.96 | 0.96 | 0.93 |
| BAR | 1.15 | 1.14 | 1.26 | 0.25 | 0.21 | 0.47 | 0.89 | 0.90 | 0.84 |
| EST | 1.26 | 1.25 | 1.28 | -0.41 | -0.19 | -0.14 | 0.92 | 0.90 | 0.90 |
| FUN | 1.02 | 1.24 | 1.00 | 0.12 | 0.03 | 0.20 | 0.96 | 0.90 | 0.96 |
| ING | 1.18 | 1.64 | 1.17 | -0.42 | -0.90 | -0.36 | 0.95 | 0.81 | 0.95 |
| ISA | 1.64 | 1.56 | 1.76 | -0.39 | -0.46 | -0.24 | 0.85 | 0.84 | 0.81 |
| RON | 1.64 | 1.58 | 1.67 | -0.40 | -0.52 | -0.24 | 0.75 | 0.79 | 0.70 |
| B49 | 1.44 | 1.43 | 1.53 | -0.19 | -0.58 | -0.38 | 0.86 | 0.85 | 0.86 |
| B56 | 1.73 | 1.65 | 1.71 | -0.34 | -0.29 | -0.17 | 0.66 | 0.73 | 0.68 |
| IC4 | 2.07 | 2.60 | 1.73 | -1.46 | -1.63 | -0.95 | 0.6 | 0.51 | 0.71 |
| I34 | 1.27 | 1.19 | 1.31 | -0.30 | -0.15 | 0.07 | 0.88 | 0.92 | 0.89 |
| IB2 | 1.29 | 1.83 | 1.11 | -0.17 | -0.77 | 0.00 | 0.89 | 0.75 | 0.97 |
| IS8 | 1.80 | 2.12 | 1.52 | -1.00 | -1.06 | -0.76 | 0.74 | 0.56 | 0.88 |
| Ave | 1.46 | 1.56 | 1.43 | -0.18 | -0.30 | -0.06 | 0.83 | 0.80 | 0.84 |

In this Section, the results of the four simulations are compared against measurements. First, a general overview of the model performance is provided, then the differences between the four simulations are outlined.

To quantify the model performance and to compare the different simulations, the mean bias (MB), the root-mean-square error (RMSE) and the hit-rate (HR) at 2°C between each simulation and observations have been calculated for each weather station (omitting the NOURBAN simulation, that gave obviously the worst results). Moreover, the mean-centered pattern errors are discussed by means of the Taylor diagrams (Taylor, 2001). These diagrams summarize the performance of the model against observations on the basis of the correlation coefficients (CC),

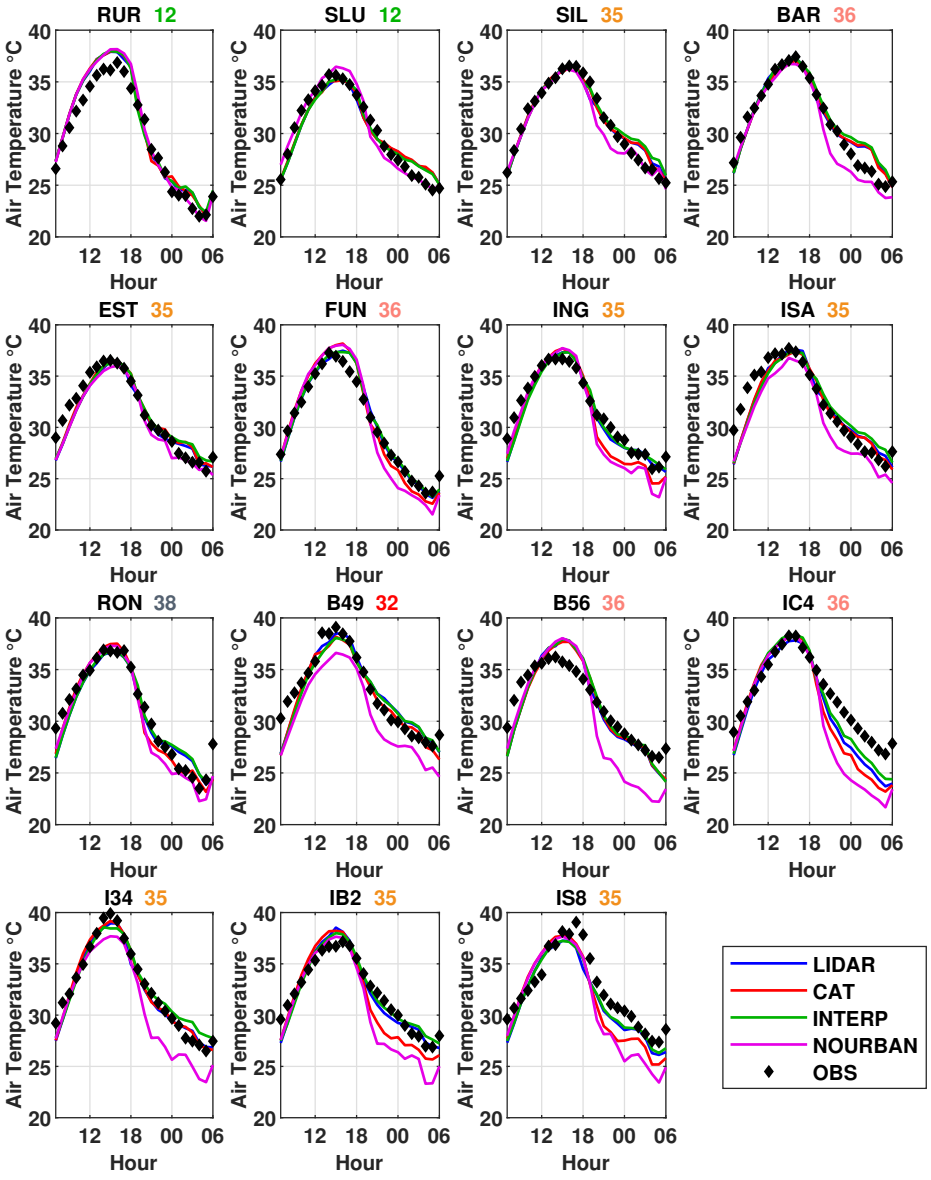


**Figure 1.6:** Temperature time series for the period of simulation for LIDAR, CAT, INTERP and NOURBAN and observed at different weather stations, averaged over a single diurnal cycle.

the normalized centered root-mean-square differences (RMSD), and the normalized standard deviations (NSD), which are second-order statistics calculated subtracting the average value from the time series. These statistical indexes are defined as follows:

$$FB = \frac{1}{n}\sum_{i=1}^{n}(y_i - f_i) \tag{1.2}$$

$$RMSE = \sqrt{\frac{1}{n}\sum_{i=1}^{n}(y_i - f_i)^2} \tag{1.3}$$

$$HR = \sum_{i=1}^{n}\frac{k_i}{n} \qquad k_i = \begin{cases} 1 & if\ |y_i - f_i| \leq 2 \\ 0 & if\ |y_i - f_i| > 2 \end{cases} \tag{1.4}$$

$$\sigma_y^2 = \frac{1}{n}\sum_{i=1}^{n}(y_i - \bar{y})^2 \tag{1.5}$$

$$CC = \frac{\sum_{i=1}^{n}\left[(y_i - \bar{y})\left(f_i - \bar{f}\right)\right]}{n\sigma_y\sigma_f} \tag{1.6}$$

$$NSD = \frac{1}{n\sigma_y}\sum_{i=1}^{n}\left(f_i - \bar{f}\right)^2 \tag{1.7}$$

$$RMSD = \frac{\sum_{i=1}^{n}\left[(y_i - \bar{y})\left(f_i - \bar{f}\right)\right]^2}{n\sigma_y^2} \tag{1.8}$$

where $n$ is the total hours of the simulation, $f_i$ the modeled temperature and $y_i$ the observation.

In general, all simulations considered here show a good agreement with observational data, with RMSE $< 2$ °C for almost all stations, with an average value of $\sim 1.5$°C. In particular, the best results are found for stations located in the Bologna urban area. Here the urban morphology is well defined and the difference with rural areas is sharp, so the model can correctly represent air temperature dynamics. The station displaying the worst results is IC4. In this area, in the northern part of the city, the urban morphology is not well-defined, neither is the boundary between urban and rural areas. For this reason, mesoscale simulations at 500-m resolution are not able to properly simulate air temperature. In general, a net trend for the MB (either negative or positive) cannot be appreciated in the different simulations. However, rural and city center stations show a slight overestimation of temperature during daytime, whereas temperatures measured by stations located at the boundary between urban and rural areas are in general underestimated by all simulations, especially for IC4. The HR displays on average values of $\sim 0.8$ for all simulations, showing a good agreement between simulations and observations.

Figure 1.6 allows to evaluate the performance of the model in simulating the diurnal cycle of temperature at the different stations considered. Regarding maximum and minimum temperatures, simulated values are in overall agreement with measurements. However at B56 station, the maximum temperature is overestimated and the minimum temperature is underestimated. This error might be linked to the fact that this station is close to the Reno river, which is not represented in the input land use. As expected, all urban simulations show better results than NOURBAN, except for SLU rural station, where the urban simulations overestimate temperature during nighttime. SLU is located on the hills close to the city, so a local error in the

definition of the urban morphology affects its temperature trend.

Taylor diagrams show again a good agreement between all simulations and measurements; CC is never lower than 0.9, and RMSD is almost never higher than 0.5.

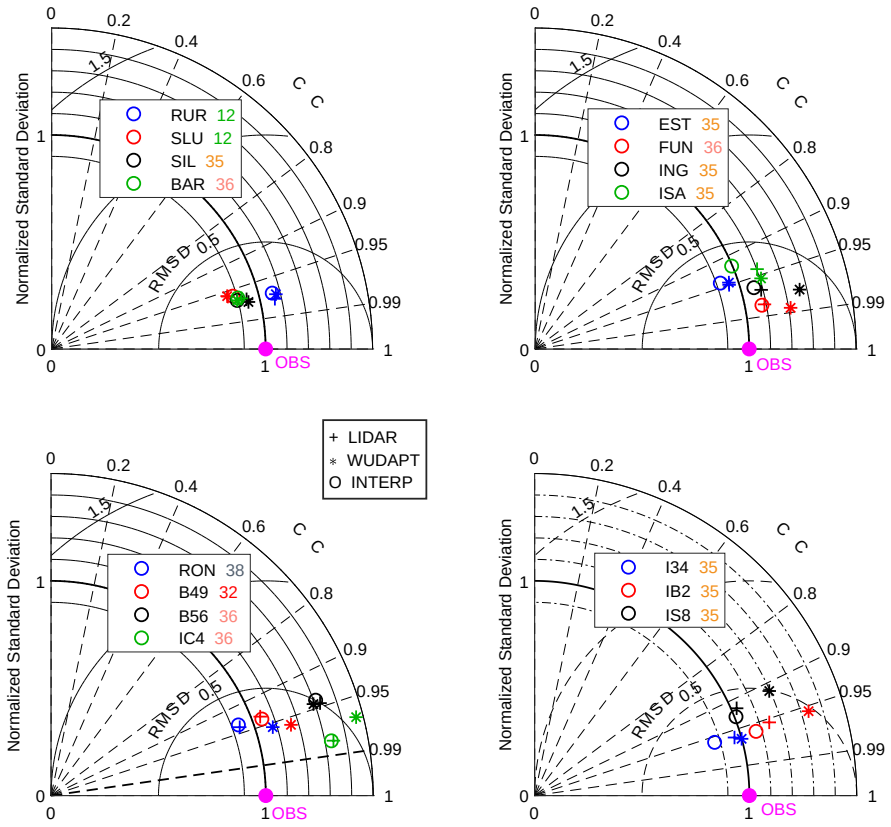


**Figure 1.7:** Taylor diagrams describing the statistical patterns of the modeled temperature time series computed by simulations LIDAR (+) , CAT (∗) , and INTERP (○) compared to observations. Numbers near acronyms represent the corresponding LCZ.

### 1.4.1 Evaluation of the UHI and interaction with the TI

Results presented in the previous Section highlighted that the model is able to reproduce coherently the diurnal temperature cycles at all stations. Here urban-rural temperature differences are analyzed in more details. Fig. 1.8 shows the average diurnal cycle of the temperature differences between each station and a rural station located 17 km NE of the city center, taken as the rural reference. Results show that a nocturnal (0000-0600 UTC) UHI of $\sim 4$°C is detected by measurements, slightly higher in the city center defined by LCZ 2 (B49 station, $\sim 6$°C). Model simulations reproduce well the nocturnal UHI at most stations and its variability in the different areas. Figure 1.8 shows that a weak UHI occurs even during daytime, progressively diminishing from the nocturnal maximum, and attaining a minimum at 1800 UTC. Similarly to the night, diurnal UHI gets stronger for stations closer to the city center. However, model simulations are not able to capture this behavior, since temperature in RUR is overestimated during daytime, systematically affecting urban-rural temperature differences.

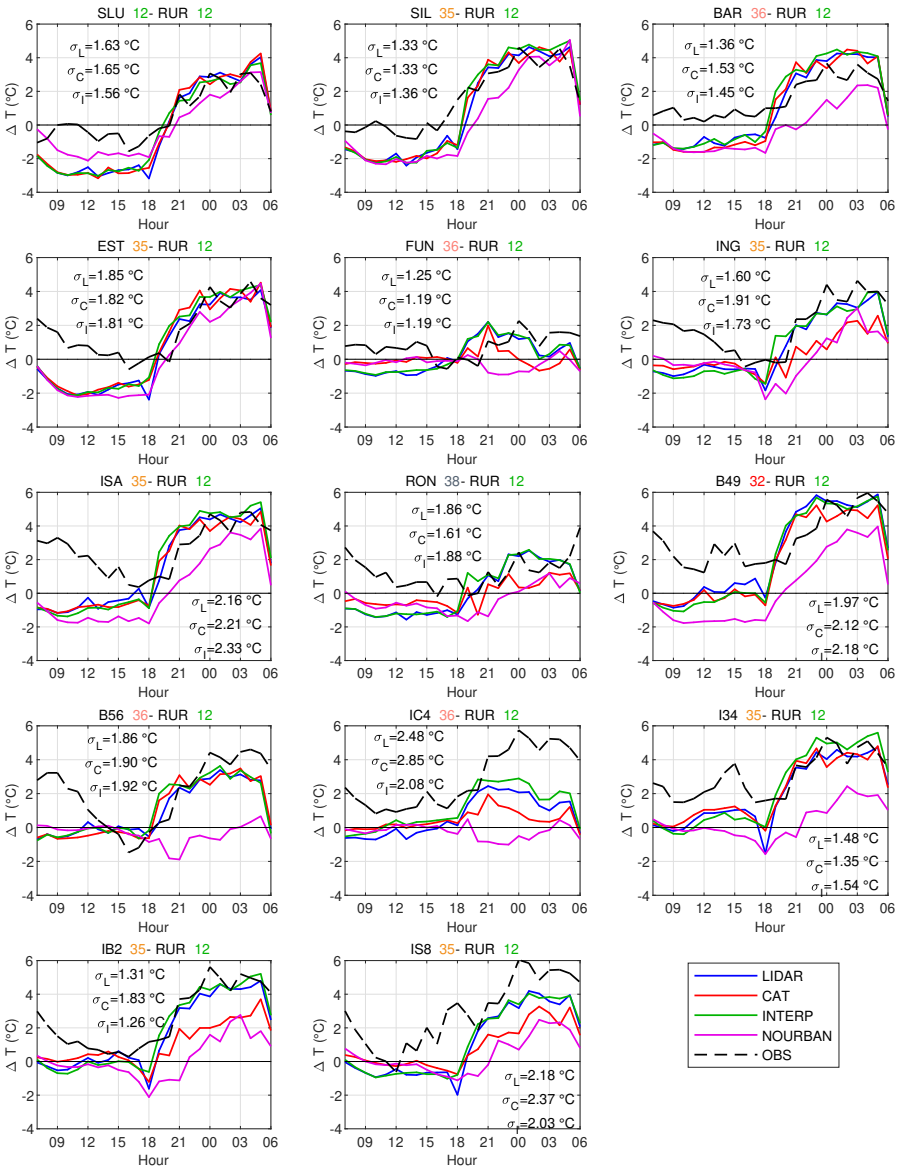


**Figure 1.8:** Temperature difference between RUR and all other weather stations from observation (dashed), LIDAR (blue), CAT (red) and INTERP (yellow) simulations, averaged over a single diurnal cycle. RMSE ($\sigma_i$) is calculated comparing each simulation with observational data.

It is interesting to notice in Fig. 1.8 that significant temperature differences with RUR are simulated at most stations also by NOURBAN, even if the urban land use is not represented. In particular, positive temperature differences are found during nighttime (similarly to the effects of the UHI), while negative temperature differences occur during the day. This is due to the fact that Bologna is situated at a higher altitude (between 50 and 100 m, Fig. 1.9) with respect to the Po Plain, where the RUR station is located. The result is a slightly higher temperature during daytime, and lower temperatures (up to 4°C) during nighttime in the lower Po Plain with respect to the foothills areas, due to the presence of the surface-layer TI. Surface-layer TI is a frequent phenomenon in the Po Plain, even in summer, during heat waves and under weak synoptic forcing. TI has been captured by the radiosounding (performed daily at 0000 UTC at San Pietro Capofiume in the lower Po Plain at 10 m ASL), and is well simulated by WRF, especially for the lowest levels of the surface layer (Fig. 1.10). For example, the other rural station (SLU), which is located at 286 m ASL, is $\sim$ 3°C warmer than RUR (20 m ASL), close to San Pietro Capofiume, during nighttime (2100-0600 UTC). Therefore, both altitude and urban land cover affect temperature differences between the urban area of Bologna and the open Po Plain, and in particular during nighttime the observed temperature contrasts are the sum of UHI and TI effects, as shown in Fig. 1.11. Here we can observe the effect of the UHI, which prevails on the TI in the urban area (SIL station) in the first layers of the boundary layer in the LIDAR simulation, with a TI that takes place around 60 m AGL. Similar considerations can be made observing Fig. 1.12, which shows 2-m air temperature averaged for daytime (top) and nighttime (bottom) for LIDAR (left) and NOURBAN (right). It can be seen that the results of the two simulations are similar during daytime, when the UHI is weaker, with only slightly higher temperatures in the city center for LIDAR. On the other hand, during nighttime the effect of the urban land cover is stronger. Moreover, in NOURBAN higher temperatures with respect to the lower Po Plain are found in the foothills of the Apennines, marking the area not affected by the surface TI.

### 1.4.2 Sensitivity to UCP method

Referring to Fig. 1.6, Tab. 1.4 and Fig. 1.7, in this Section the performance of the three urban morphology definition methods are compared, on the basis of their ability to reproduce air temperature at different stations. In general, INTERP simulation shows the best agreement with measurements: on average the HR is 4% higher and the mean RMSE is $\sim$ 0.1°C lower with respect to CAT, and similar to LIDAR. The most significant improvements are reported for ING ($\sim$ 0.5°C), IS8 ($\sim$ 0.6°C), IB2 ($\sim$ 0.7°C), and IC4 ($\sim$ 0.9°C), while at the other stations results are similar for all simulations. All these stations have in common their position: they are located in urban areas at the boundaries of the city, or in a mix of rural and urban fraction. They even display a systematic underestimation of temperature (negative MB) for CAT with respect to the other two urban simulations: this means that the CAT method, which selects the most frequent categorical value within each cell, lacks in considering part of urban surfaces contributing to increase temperature with respect to rural areas. The better results of INTERP with respect to CAT are evident also from Fig. 1.8. In particular, CAT simulations tend to underestimate the strength of the UHI (and then air temperature) at urban stations. This

behavior is evident at ING and IB2 stations, where LIDAR and INTERP correctly simulate the nocturnal UHI, while CAT is closer to NOURBAN.

Even the Taylor diagrams show better results for INTERP than for CAT: while CC is on average similar between INTERP and CAT, improvements are detected for NSD for most urban stations at the boundaries of the city. This means that INTERP is able to better capture the diurnal temperature variability compared to CAT. In particular, CAT shows in general NSD values systematically greater than 1, meaning that the average temperature range is overestimated, due to the underestimation of nighttime temperatures. On the other hand, values of NSD for LIDAR and INTERP are closer to observations.

In order to better appreciate differences between the three urban landmask definition methods implemented, average 2-m air temperature contrasts between these simulations for nighttime (2000-0300 UTC) and daytime (0800-1500 UTC) hours are calculated. Results are presented in Fig. 1.13 for the urban cells where the LIDAR classification is available. Both CAT and INTERP (the latter with better agreement) underestimate temperature in the city center (represented by LCZ 2) with respect to LIDAR during nighttime. This means that urban parameters for this class have not been correctly defined (especially the building surface to plan area ratio $\lambda_b$, see Tab. 1.3). On the other hand, LCZ 5 temperature is slightly underestimated for CAT and overestimated for INTERP with respect to LIDAR at night. During nighttime CAT fails to reproduce temperature at the city boundaries, due to its lack in representing urban land use in these areas, as already underlined in Section 1.3. Here temperature differences up to 2 °C are found, since a rural-type cell is simulated by CAT. The same occurs for areas inside the city where a mixed urban/rural land use is present. During daytime, differences with respect to LIDAR are lower than 0.5°C, with higher differences for CAT, showing an overestimation at the city boundaries. On the other hand, temperatures in LCZ 5 are in general underestimated by CAT with respect to LIDAR, while differences are lower for INTERP and it is not possible to detect coherent trends among the same class.

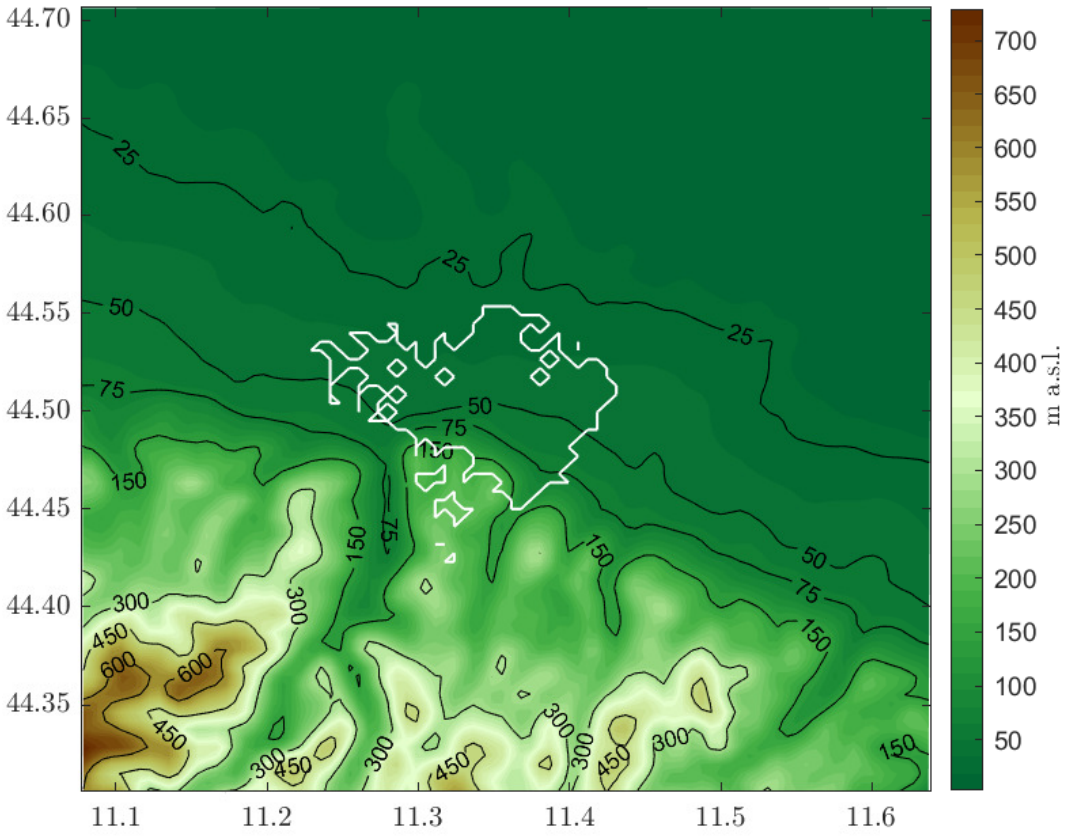


**Figure 1.9:** Terrain height in the innermost domain of simulation. City boundaries are overlayed.

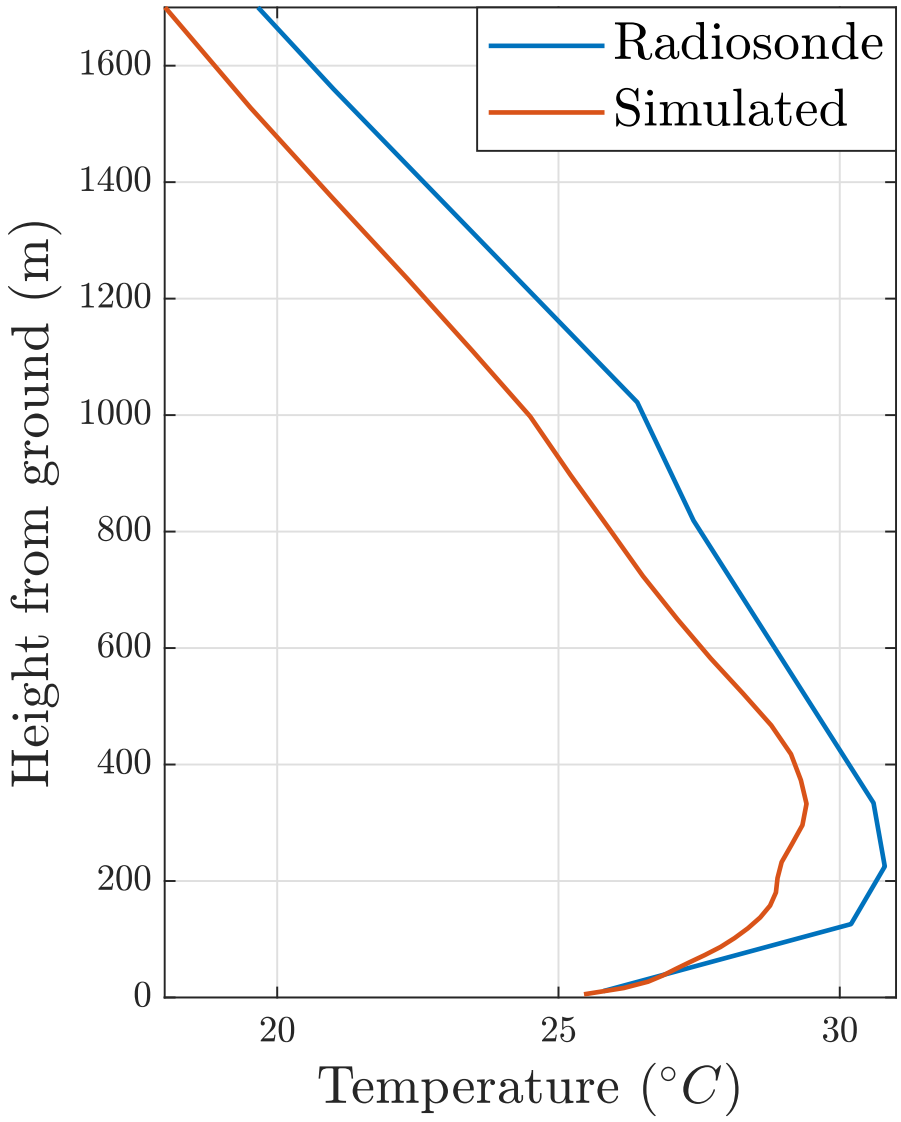


**Figure 1.10:** Measured (blue) and simulated (red) vertical profiles of temperature at San Pietro Capofiume at 0000 UTC 19/07/2015.

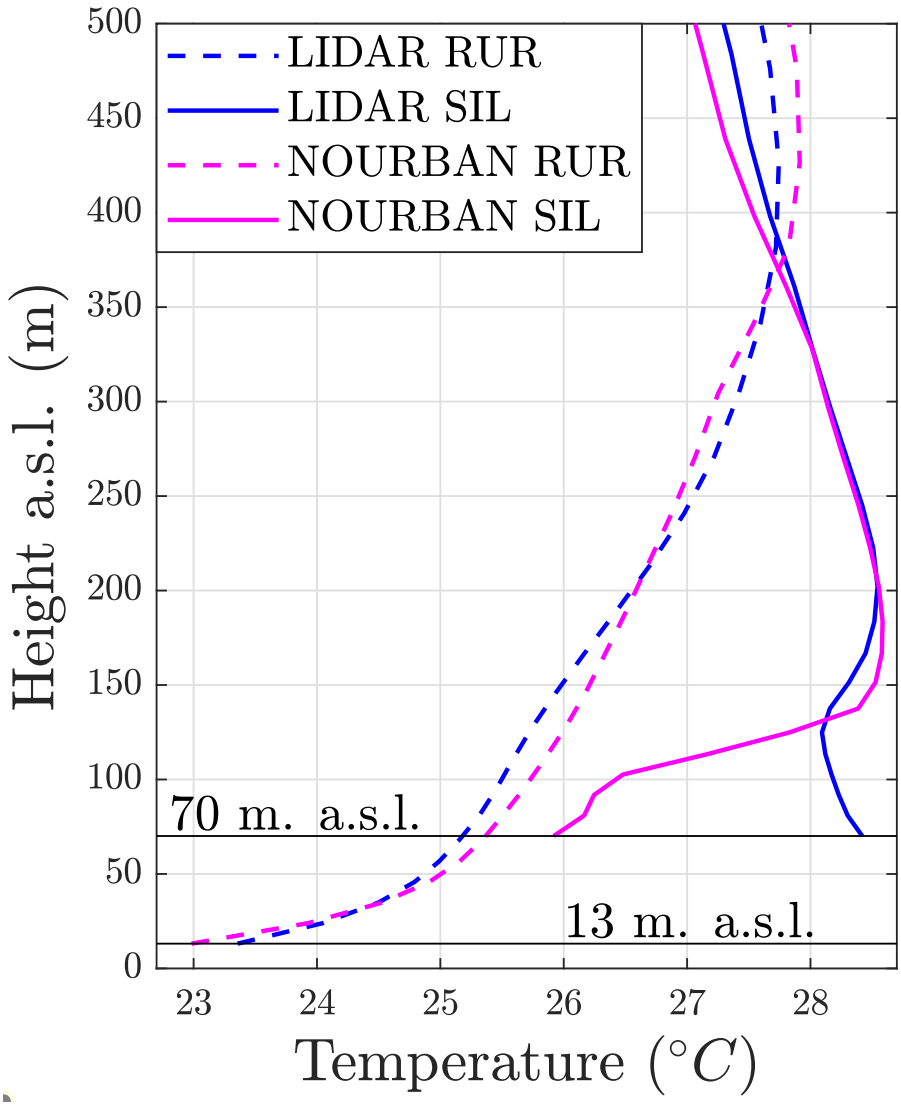


**Figure 1.11:** Simulated vertical profiles of temperature at RUR (dashed lines) and SIL (solid lines) weather stations for LIDAR (blue) and NOURBAN (magenta) simulations at 0000 UTC, averaged over the three days of simulation.

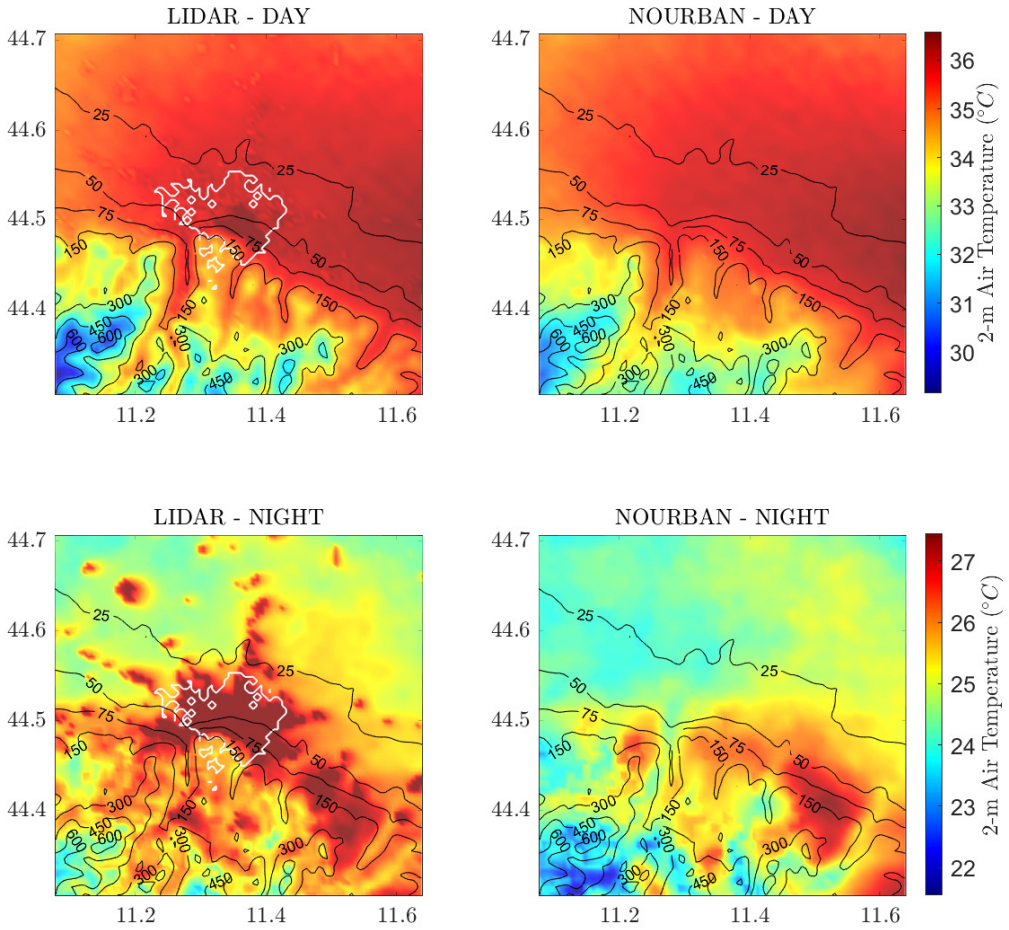


**Figure 1.12:** Maps of 2-m air temperature for LIDAR (left) and NOURBAN (right), averaged for daytime (0800-1500 UTC) (top) and nighttime (2000-300 UTC) (bottom). White line marks the urban area of Bologna. Height contours are in m ASL.

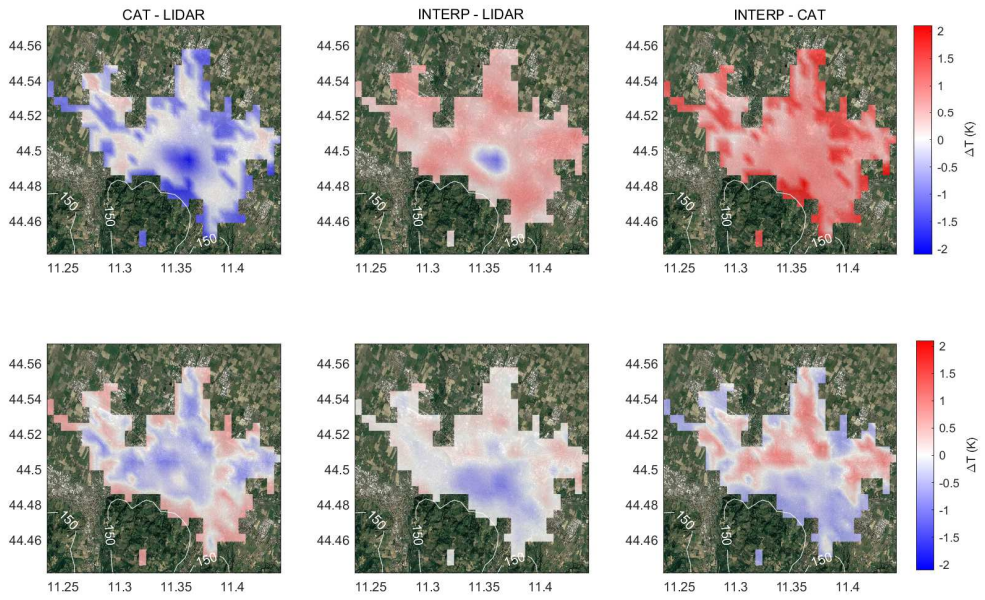


**Figure 1.13:** Maps of 2-m air temperature differences between CAT and LIDAR (left), INTERP and LIDAR (center) and INTERP and CAT (right) averaged for nighttime (2000-0300 UTC) (top) and daytime (0800-1500 UTC) (bottom). Only LIDAR urban grid cells are considered.

## 1.5 Summary and conclusions

Simulations with the WRF model, coupled with the BEP-BEM urban parameterization schemes, were performed to test the capability of a new method (INTERP) to derive urban canopy parameters for mesoscale models from the WUDAPT classification. The performance of this new method was compared against two state-of-the-art methods, i.e. the original WUDAPT method (CAT, Brousse et al., 2016), and urban canopy parameters derived from LIDAR data (LIDAR), during a heat wave in summer 2015 for the city of Bologna (Italy). The original WUDAPT method, which uses categorical values, adopts the prototypical urban parameters of the eleven UCZ classes (choosing the most present value for each mesoscale model grid cell). The method proposed here (INTERP) calculates ad hoc urban parameters for each mesoscale model cell from a 30-m resolution WUDAPT classification, according to the subgrid area covered by each UCZ. This means that while the original WUDAPT method is not able to take into account the subgrid land use variability, the new method allows to consider different UCZs within the same WRF grid cell, giving more realistic urban canopy parameters. Considering LIDAR as the reference classification, the new method generally provides better urban parameters with respect to CAT. Improvements are particularly evident at the city boundaries, where the original WUDAPT method cannot cope with the transition between urban and rural land use.

Subsequently, simulation results were compared with measurements from weather stations, in order to evaluate the model capability to reproduce air temperature time series. All simulations display a good agreement with observed temperatures, with root mean squared errors $\sim$ 1.5 °C. The model is also able to simulate well the UHI, which becomes appreciable around 2000 UTC, and lasts until 0600 UTC, with an intensity of $\sim$ 4 °C, being stronger closer to

the city center. The UHI occurs even during daytime, and then gradually decreases, reaching a minimum around 1800 UTC. It is partly detected by the simulations, although the model overestimates the daytime rural temperature.

The comparison of the results of the three simulations highlights that INTERP presents similar performance to LIDAR and clearly outperforms CAT, especially at stations close to the boundaries of the city, where improvements up to $\sim$ 0.9 °C are found. In these transitional areas CAT fails to assign the correct values of the urban morphology, while INTERP is able to cope with scattered and complex land use. In particular, since CAT assigns an urban land use only when at least 50% of the WRF cell is covered by urban LCZs, according to the WUDAPT 30-m resolution map, temperatures are generally underestimated, due to the fact that the urban land cover is less extended than the real one.

The above results highlight that the proposed method for defining urban canopy parameters, taking full advantage of the WUDAPT 30-m resolution maps, improves the capability of reproducing air temperature distribution and heterogeneity within the city, and in particular in areas at the boundary between the city and surrounding vegetated surfaces.

# 2 Exploring the effects of rooftop mitigation strategies on urban temperatures and energy consumption

**Abstract**

This paper describes and evaluates physical parameterizations accounting for the effect of rooftop mitigation strategies (RMSs) on the urban environment, in the context of the mesoscale model Weather Research and Forecasting (WRF). Through the new implementation, the sensitivity of near-surface air temperature and building energy consumption to different RMSs is evaluated by means of numerical simulations in idealized urban areas, for typical summer and winter conditions. Rooftop mitigation strategies considered include cool roofs, green roofs, and rooftop photovoltaic panels. The reference case simulations are performed assuming buildings made by bricks, with roof composed of clay tiles. Results indicate that near-surface air temperature is reduced by cool and green roofs during summer: cool roofs are the most efficient in decreasing air temperature, followed by irrigated green roofs. Photovoltaic panels, instead, induce a temperature increase during daytime and a small decrease during nighttime. Cool roofs reveal to be the most efficient strategy in reducing the energy consumption by air conditioning systems. During wintertime, green roofs maintain a higher near-surface air temperature than clay-tile roofs and largely decrease energy consumption. Even PVPs increase air temperature, as in the summer case. On the other hand, cool roofs reduce near-surface air temperature during daytime, inducing an increase in energy consumption. The results presented here show that the parameterization schemes implemented in the WRF model can be a valuable tool to evaluate the effects of mitigation strategies in the urban environment.

## 2.1 Introduction

It is well known that rooftop technologies, such as cool roofs (CRs), green roofs (GRs), or rooftop photovoltaic panels (RPVPs) can significantly modify fluxes of energy and momentum in the urban canopy layer (Santamouris, 2014). Their deployment is nowadays largely adopted worldwide, with the aim of improving thermal comfort for citizens and diminishing the energy

demand for heating/cooling of buildings (Lai et al., 2019). Therefore, a better understanding of the physical mechanisms driving the modifications induced by rooftop mitigation strategies (RMSs) is desirable, for quantifying their effects on the urban environment, for a wide range of urban structures, and under different climatic conditions. A better comprehension of these processes is receiving increasing attention from planners and policymakers, especially under growing urbanization and climate change (Chapman et al., 2017). In particular, the increasing number and duration of heatwaves interact nonlinearly with the well-known urban heat island phenomenon (Li et al., 2013), resulting in extremely high heat stress for citizens and in increased use of energy resources. On the other hand, cold winters present the same features of heatwaves in terms of thermal discomfort and energy demand (Yang et al., 2014), despite cities remain warmer than the surrounding environment. The above-mentioned RMSs have been widely proposed in the literature in recent years, and their effect has been investigated in different specific case studies. While all RMSs reduce the sensible heat release by roofs (and consequently the heat stored into the building materials), acting on the roof surface energy budget, the mechanisms for GRs, CRs and RPVPs are different. GRs redirect available energy to latent heat at the expense of sensible heat, increasing the evapotranspiration through the vegetation on the rooftop. On the other hand, CRs increase the reflection of the incoming solar radiation by increasing the roof albedo and preventing heat storage within roof materials. Finally, PVPs act as screens for the underlying roof, converting part of the incoming solar radiation into electricity. Several studies quantify the impact of RMSs at the building scale, through field campaigns or numerical simulations (see e.g, Kolokotroni et al. (2013) for CRs, de Munck et al. (2013) for GRs and Dominguez et al. (2011) for PVPs). However, results cannot be simply upscaled to evaluate mitigation effects at the city scale, because the impact of RMSs depends on urban geometry, thermal properties of the building materials, and climatic conditions, so a different approach is needed. To this purpose, some recent studies employed mesoscale meteorological models to investigate the city-wide impact of RMSs, adopting urban parameterizations with various levels of complexity. For example, Li et al. (2014) evaluated the city-scale mitigation effect of CRs and GRs over the Baltimore-Washington metropolitan area, using the Weather Research and Forecasting (WRF) model coupled with the Princeton Urban Canopy Model, detecting improvements in terms of air temperature during a heatwave period of the same order of magnitude for the two roof technologies. Yang et al. (2014) incorporated the effect of green roofs in the single-layer urban canopy model Noah/SLUCM (Kusaka et al., 2001) and tested it for several megacities, while de Munck et al. (2018) used the Town Energy Balance model (TEB, Masson (2000)), to evaluate the impact of various urban greening scenarios on thermal comfort and energy and water consumption for the city of Paris. For the same city, Masson et al. (2014) demonstrated that PVP arrays can reduce the near-surface air temperature, especially during nighttime. Finally, Salamanca et al. (2016) tested a novel PVP parameterization, coupled with the multilayer urban canopy scheme BEP+BEM (Martilli et al. (2002) and Salamanca et al. (2010)) for the cities of Phoenix and Tucson, detecting a decrease of both near-surface temperature and energy demand for air conditioning systems (ACSs).

In general, all the above-mentioned studies proposed novel physically-based RMS parameterization schemes, which modify the roof surface energy budget, demonstrating a citywide

decrease in air temperature during summer climatic conditions. However, these studies generally lack in generalization, since every RMS parameterization scheme is applied for specific cities under unique climatic conditions. Hence, it is not possible to identify the dependence of the impact of RMSs on urban geometry or atmospheric forcing. Moreover, despite RMSs are worldwide employed to improve thermal conditions in the urban environment during summertime, it is important to evaluate the city-scale effect induced by RMSs also during winter, with the aim of detecting possible reductions in temperatures that may increase thermal discomfort and energy demand for heating systems.

Accordingly, the present study offers a systematic evaluation of the impact of the three above-mentioned RMSs (CRs, GRs, and RPVPs) on both near-surface air temperature and building energy consumption (EC), for a wide range of idealized urban configurations and for two different climatic conditions. To this purpose, GR and RPVP parameterizations have been incorporated in the BEP+BEM urban canopy scheme, in the context of the WRF mesoscale meteorological model (v4.1.2, Skamarock et al. (2019)). The modelling system adopted in the present study (WRF coupled with BEP+BEM) has been evaluated through the comparison against measurements in several cities, proving to be a suitable tool to reproduce meteorological conditions and EC in urban areas (e.g. Giovannini et al. (2014), Salamanca et al. (2018)).

The paper is organized as follows: Section 2.2 describes the schemes adopted to calculate the surface energy budget of RPVPs and GRs, while Section 2.3 presents the set-up of the idealized simulations and the methods adopted to conduct the sensitivity analysis. Simulations results are discussed in Section 2.4, focusing on the comparison between simulations in idealized urban areas composed of buildings with clay tile roofs and with the implementation of the RMSs for different urban configurations and climatic conditions. Finally, results are summarized and discussed in Section 2.5.

## 2.2 The Rooftop Mitigation Strategies schemes

### 2.2.1 Rooftop Photovoltaic Panels parameterization

The parameterization developed in this work in view of taking into account the effects of RPVPs within BEP-BEM assumes the photovoltaic arrays to be parallel and detached from roofs and composed of a single layer. The time derivative of PVP temperature ($T_{PV}$ hereafter) reads: (Fig. 2.1):

$$C_{\text{module}} \frac{\partial T_{PV}}{\partial t} = (1-\alpha_{PV})\, SW^{\downarrow}_{\text{sky}} + \varepsilon^{U}_{PV} LW^{\downarrow}_{\text{sky}} - LW^{\uparrow}_{PV} + LW^{\updownarrow}_{roof-PV} \quad (2.1)$$

$$-E_{PV} - H^{\uparrow} - H^{\downarrow} \quad (2.2)$$

$$+(1-\text{VF})\left[(1-\alpha_{PV})\, SW_{\text{DIFF}} + LW^{\downarrow}_{\text{sky}}\right] \quad (2.3)$$

with (all terms in W m$^{-2}$):

- $C_{\text{module}} = 5.72$ MJK$^{-1}$m$^{-2}$ is the equivalent heat capacity per unit area, assuming that the PVP is composed of three layers, as in Jones et al. (2002): a monocrystalline silicon

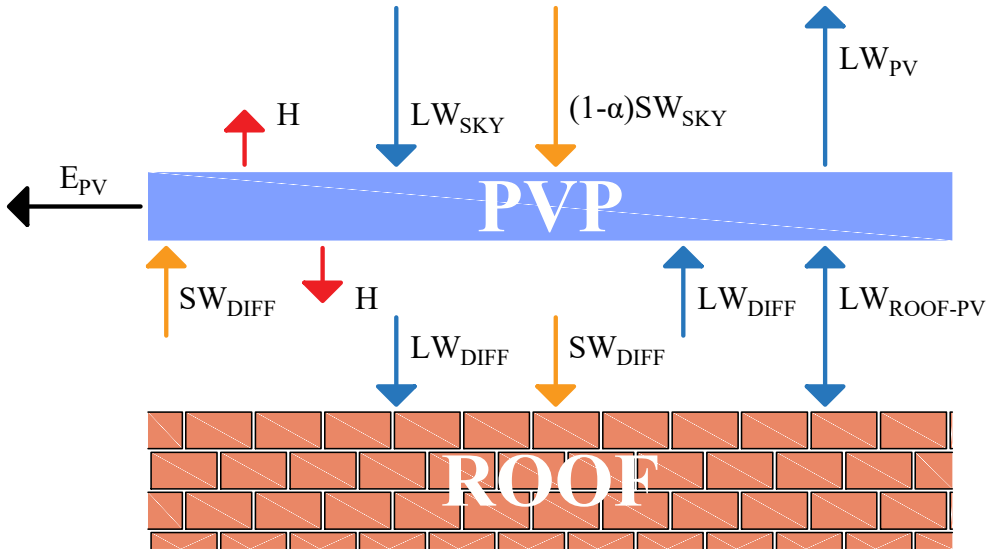


**Figure 2.1:** Photovoltaic panel design, with a schematic representation of the energy exchanges with the underlying roof and the environment.

PV cell, a polyester trilaminate and a glass face, with a total depth of 6.55 mm. For the values of heat capacity, depth, and density for each layer, refer to Jones et al. (2002);

- $(1-\alpha_{PV})SW^{\downarrow}_{\text{sky}}$: net shortwave radiation gained by the upward surface of the PVP, assuming an albedo $\alpha_{PV} = 0.11$;
- $\varepsilon^{U}_{PV} LW^{\downarrow}_{sky}$: incoming longwave radiation at the upper surface of the PVP, where $\varepsilon^{U}_{PV} = 0.79$ is the emissivity of the glass face;
- $LW^{\uparrow}_{PV} = \varepsilon^{U}_{PV}\sigma T^{4}_{PV}$: upward longwave radiation emitted by the PVP;
- $LW^{\updownarrow}_{\text{roof}-PV} = \text{VF}\,\frac{1}{\frac{1-\varepsilon^{D}_{PV}}{\varepsilon^{D}_{PV}} + \frac{1-\varepsilon_{\text{roof}}}{\varepsilon_{\text{roof}}}}\sigma\left(T^{4}_{PV} - T^{4}_{\text{roof}}\right)$: longwave radiation exchanged between the monocrystalline silicon downward face of the PVP ($\varepsilon^{D}_{PV} = 0.95$) and the upward face of the roof. The radiation fluxes coming from the PVP and from the roof are considered together in order to take into account the multiple reflections between the two surfaces. VF is the view factor between the downward face of the PVP and the roof. Assuming a 10 m $\times$ 10 m PVP (covering completely the roof, with a clearance of 0.3 m from the underlying surface, VF = 0.06);
- $E_{PV} = \eta_{PV} SW^{\downarrow}_{\text{sky}} min\left[1, 1 - 0.005\left(T_{PV} - 298.15\right)\right]$: energy production by the PVP. It takes into account that the efficiency of PVPs decreases at temperatures higher than 25°C; $\eta_{PV}$ is the conversion efficiency of the PVP, i.e. the fraction of shortwave radiation converted into electricity. Efficiency varies from 7% for quantum dot cells to 44% for multijunction cells used in research applications (NREL, 2020). In this work, since the most common arrays used for rooftop are mono- and poli-crystalline silicon PVPs, we use an efficiency $\eta_{PV} = 0.19$;
- $H^{\uparrow} + H^{\downarrow} = \left(h^{\uparrow} + h^{\downarrow}\right)\left(T_{PV} - T_{\text{air}}\right)$: the sensible heat fluxes at the upward and downward faces of the PVP. The formulation for $h = \sqrt{h_c^2 + a\,|V|^b}$ depends on empirical fits and is

adopted from the EnergyPlus model (US Department of Energy, 2010), which has been validated against measurements (Scherba et al., 2011). $h_c$ depends on the material of the surface (glass, in this case), on whether the surface faces upward or downward, and on the sign of the difference between surface and air temperature. The absolute value of wind speed is taken at the first level of WRF above the roofs and it is supposed to be the same for the upward and downward face;

- $(1-\mathrm{VF})\left[(1-\alpha_{PV})SW_{\mathrm{DIFF}}+LW^{\downarrow}_{\mathrm{sky}}\right]$: diffuse shortwave and longwave isotropic radiations reaching the downward PV surface. $LW^{\downarrow}_{sky}$ is the incoming longwave radiation, while $SW_{\mathrm{DIFF}}$ is the diffuse shortwave radiation. The same amount of diffuse shortwave and longwave radiation reaches also the roof below the PVP.

Differently from Masson et al. (2014) and Salamanca et al. (2016), which parameterized $T_{PV}$ through its dependence on short-wave solar radiation, here we directly solve numerically Eq. (2.1), in a way similar to Jones et al. (2002), to get a PVP temperature that depends on all the involved contributions. Once $T_{PV}$ is calculated, the value of the outgoing heat flux is updated and passed to the multi-layer urban scheme.

### 2.2.2 The Green Roofs parameterization

The land surface scheme for GRs has been developed based on De Munck et al. (2013) and Gutierrez (2015). It calculates energy and water budgets, taking into account incoming net radiation, water input from precipitation and irrigation, evapotranspiration from vegetation, heat exchange with the atmosphere, and diffusion of energy and moisture throughout the soil. The model is one-dimensional, i.e. horizontal transport and subsurface flows are neglected.

A GR consists of ten layers with a total depth of $\sim 0.3$ m (Fig. 2.2). Five levels (0.08 m of total thickness) represent the organic matter substrate where vegetation grows. Vegetation roots reach the bottom of the substrate, and vegetation is assumed to intercept all the incoming radiation from the atmosphere. One layer represents the drainage layer (0.05 m), where surplus water is removed. Finally, four levels describe the insulation layer, composed of a waterproofing membrane (0.003 m), an insulating sheet (0.06 m), a further waterproofing membrane (0.003 m), and finally a layer for insulating the structural roof (0.1 m).

#### Hydrology for Green Roofs

The latent heat flux $LE$ is modeled considering only evaporation from soil moisture and transpiration through leaves of the water absorbed by roots in the layers composing the substrate:

$$LE = \frac{\rho_a L\,(q_{surf,S}-q_a)}{R_a+R_S} \tag{2.4}$$

where $\rho_a$ is the air density, $L$ the latent heat of vaporization, $(q_{surf,S}-q_a)$ the difference between the saturated soil specific humidity and the actual air humidity around the plants (De Munck et al., 2013), $R_a$ the aerodynamic resistance (Louis, 1979) and $R_S$ the stomatal resistance. The latter depends on the atmospheric state, water availability, and vegetation features,

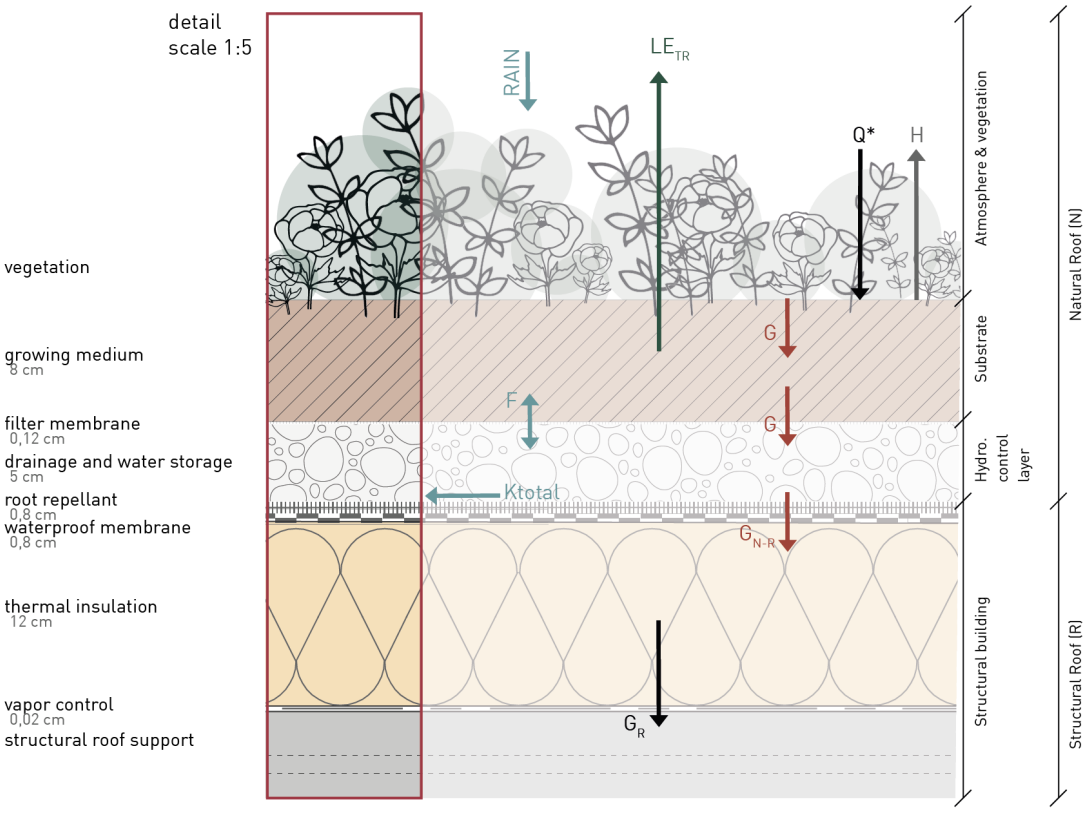


**Figure 2.2:** Green roof design. Arrows refer to the sensible/latent heat exchange between the different layers and the atmosphere.

and it is written as:

$$R_S = \frac{R_{S_{min}}}{LAI\, F_1 F_2 F_3 F_4} \tag{2.5}$$

where $R_{S_{min}}$ is the minimum stomatal resistance of the vegetation, while LAI is the leaf area index. $F_1$ describes the effect of photosynthetic radiation, $F_2$ the hydrological features, $F_3$ and $F_4$ the effect on evapotranspiration of temperature and humidity respectively (see Jacquemin et al. (1990) for more details). The Richards' equation (Short et al., 1995) is used to represent the one-dimensional transport of soil moisture ($\Theta$) throughout the soil:

$$\frac{\partial \Theta}{\partial t} = \frac{\partial}{\partial z}\left(D\frac{\partial \Theta}{\partial z} + K\right) + F_\Theta \tag{2.6}$$

where D and K are respectively soil water diffusivity and hydraulic conductivity calculated as:

$$K = K_S \left(\frac{\Theta}{\Theta_S}\right)^{2b+3} \tag{2.7}$$

$$D = \frac{-bK_S\Psi_s}{\Theta}\left(\frac{\Theta}{\Theta_S}\right)^{b+3} \tag{2.8}$$

$\Psi = \Psi_s \left(\frac{\Theta_S}{\Theta}\right)^b$ is the moisture potential, $b = 3.9$ is an empirical coefficient of water retention of organic matter, while all the terms with the subscript "S" refer to the soil in saturation conditions. $F_\Theta$ considers all source and sink terms. For the uppermost layer $F_\Theta = Ir + P - E$,

where $Ir$ is the irrigation, $P$ the precipitation rate and $E$ the evapotranspiration. For the drainage layer, just under the substrate, $F_\Theta = -K$ represents the surplus rain drained, if in excess.

#### Thermodynamics for Green Roofs

The heat transfer between GRs layers is calculated using the Fourier diffusion equation for soil temperature (T):

$$\frac{\partial T}{\partial t} = \frac{\partial}{\partial z}\left(\lambda \frac{\partial T}{\partial z}\right) + F_T \tag{2.9}$$

where $F_T$ represents source and sink terms. For the uppermost layer $F_T$ is calculated from the surface energy balance:

$$\frac{F_T}{\Delta z \lambda} = H - LE + (1-\alpha_{GR})SW^{\downarrow}_{sky} + LW^{\downarrow}_{sky} - LW^{\uparrow}_{GR} \tag{2.10}$$

where $\alpha_{GR}$ is the albedo of the GR, $\lambda$ the thermal diffusivity of the substrate layers and $LW^{\uparrow}_{GR} = \varepsilon_{GR}\sigma T^4_{GR}$ is the longwave radiation emission of the GR, with $\varepsilon_{GR} = 0.93$ the emissivity of the GR and $T_{GR}$ its surface temperature. For the layer close to the conventional roof, $F_T$ is the heat conduction flux calculated using the temperature gradient between the bottom layer of the natural roof and the uppermost layer of the structural roof, using a weighted average of their thermal diffusivities. The thermal diffusivity for natural roof layers depends on soil moisture:

$$\lambda = \begin{cases} \frac{e^{-(log_{10}|\Psi|+2.7)}}{C_S} 4.186 \times 10^7 \text{ if } log_{10}|\Psi| \leq 5.1 \\ \frac{4.1\times10^{-5}}{C_S} 4.186 \times 10^7 \text{ if } log_{10}|\Psi| > 5.1 \end{cases} \tag{2.11}$$

where $C_S = (1-\Theta)C_d + \Theta C_w$ is the volumetric specific heat for wet soil, calculated as the weighted average of the volumetric specific heat for dry soil ($C_d$) and water ($C_w$).

## 2.3 Methodology

### 2.3.1 Set-up of the idealized simulations

The set-up of the idealized simulations is similar to the one proposed in Pappaccogli et al. (2020). The effect of different RMSs on air temperature and EC has been evaluated through two-dimensional idealized simulations for various urban geometries and under different meteorological conditions. The idealized simulations, also thanks to their low computational cost, allows investigating a great number of cases, adopting different urban geometries under controlled atmospheric conditions. A total of 168 simulations has been performed for an ideal city situated at a latitude of 45°N. Two different seasons are simulated: a typical summer period (21-23 June, SUM hereafter) and a typical winter period (21-23 December, WIN hereafter), to quantify the effects of rooftop modifications with completely different solar radiation forcing. Simulations consist of a common numerical domain (Fig. 2.3), composed of $200 \times 3$ grid cells with a horizontal spatial resolution of 1 km and 51 vertical grid cells with a finer resolution close to the ground, with 9 cells in the first 110 m. Simulations run with a time step of 10 s, starting at 0000 LST for 72 h. The first 24 h are considered as spin-up period, allowing to reach a quasi-steady diurnal cycle, while the last 48 h are taken into account for the sensitivity

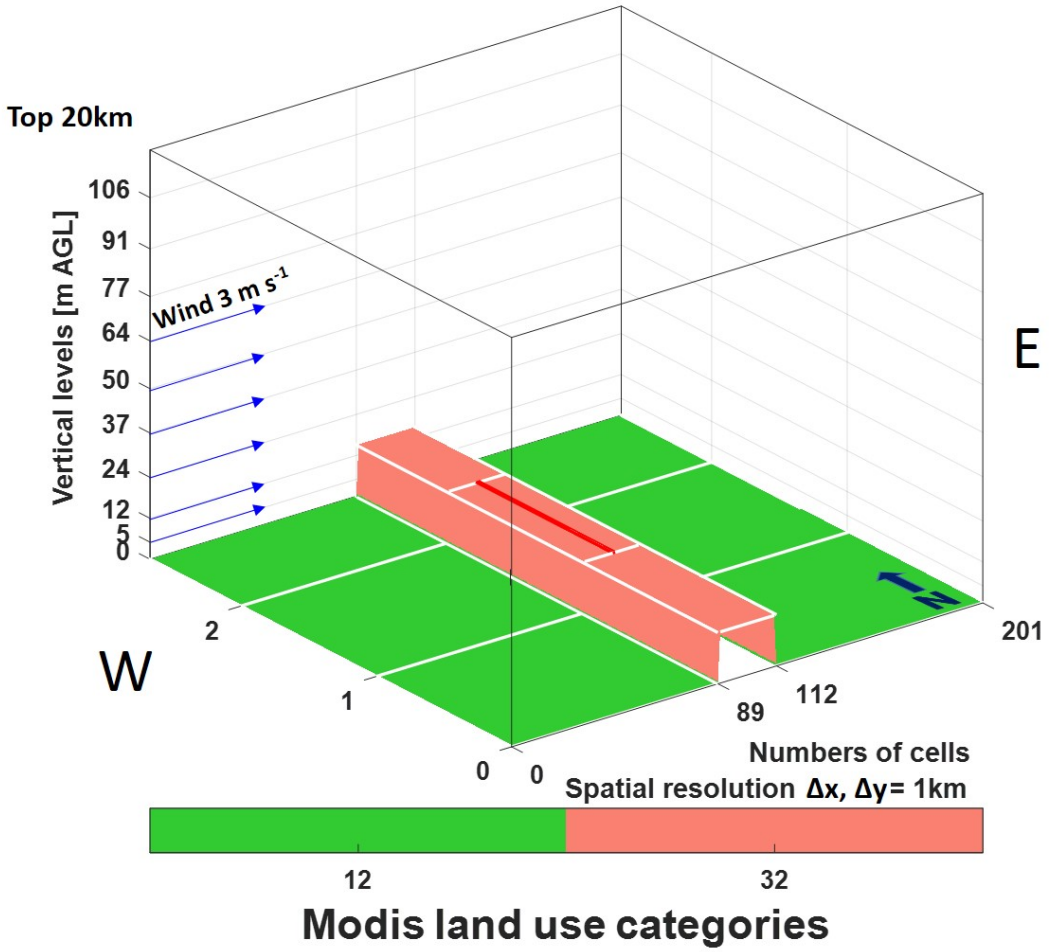


**Figure 2.3:** Schematic representation of the domain used for the idealized simulations. The red line represents the cell chosen to analyze the numerical results, from Pappaccogli et al. (2020).

analysis. Initial conditions are specified adopting a potential temperature profile with a positive gradient of 3.5 K km$^{-1}$ and a westerly wind with an intensity of 3 m s$^{-1}$ constant with increasing height. Surface temperature is set to 27°C in SUM and to 4°C in WIN everywhere in the domain. The relative humidity is set to 20% and 50% at the surface for SUM and WIN respectively, linearly decreasing to 0% at $\sim$ 5000 m above ground level.

Regarding physics parameterizations, the Bougeault et al. (1989) scheme is used as Planetary Boundary Layer (PBL) parameterization, while Noah-MP (Niu et al., 2011) is adopted for land-surface processes. Dudhia (1989) is used for shortwave radiation and the Rapid Radiative Transfer Model (RRTM, (Mlawer et al., 1997)) for longwave radiation. Horizontal turbulent exchange coefficients are kept constant and equal to 300 m$^2$ s$^{-1}$. Finally, microphysics and cumulus schemes are turned off, to avoid the formation of clouds. Periodic lateral boundary conditions are set for all the input variables, in both N-S and W-E directions.

A 23-km wide city is situated in the center of a completely flat domain, while the surrounding rural areas are classified as "cropland", according to the MODIFIED IGBP MODIS NOAH

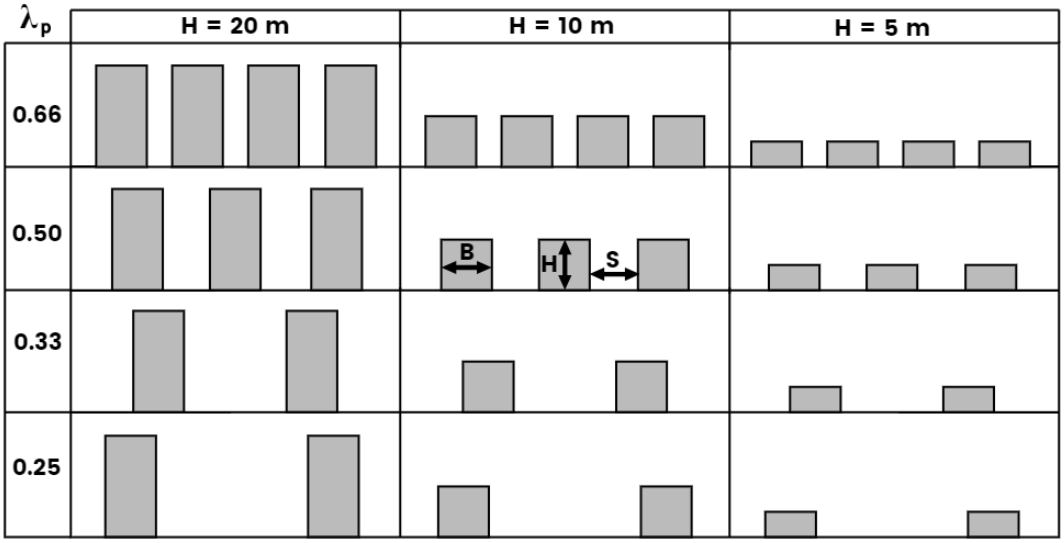


**Figure 2.4:** Schematic representation of the 12 different urban configurations for the idealized simulations. $B$ is the building width, $S$ the street width, $H$ the building height, and $\lambda_p$ the building area to total area ratio.

classification in WRF. The width of the city is the same for all the simulations, as well as buildings and urban ground thermal properties. Since this work aims at quantifying the impact of different mitigation strategies on air temperature and EC, several geometrical building features are tested, to consider a large spectrum of possible urban configurations. In Fig. 2.4, the schematic representation of all the scenarios simulated in this work is shown. For all the simulations, the building width $B$ is set to 10 m, and artificial surfaces are supposed to occupy the entire cell, hence the urban fraction is set to 1. The urban geometry in the simulations varies depending on building height, which is set to 5, 10, and 20 m, and building surface to total surface fraction, defined as $\lambda_p = B/(B+S)$, where $S$ is the street width. $\lambda_p$ varies with the street width, that is set, ranging from scattered to packed configurations, equal to 30, 20, 10 and 5 m, resulting in $\lambda_p$ = 0.25, 0.33, 0.50 and 0.66 respectively. This range of $\lambda_p$ has been identified by Grimmond et al. (1999) as representative of most of the cities worldwide. Hence, the 12 possible building geometric configurations represent a wide range of Local Climate Zones, from residential areas with low and scattered buildings, to city centers with high and compact buildings. For all the simulations, thermal and physical properties of buildings are kept constant (Tab. 2.1). In particular, building walls are assumed to be composed of solid brick, with windows covering 20% of the surface, while roofs are covered with clay tiles. No insulating layers are assumed within roofs and walls. For ground, we adopt thermal parameters of asphalt (values are taken from Oke et al. (2017)). SUM and WIN differ with respect to the indoor target temperature. It is set to 20°C for WIN and to 25°C for SUM, according to the directive UNI/TS 11300–1 (Pappaccogli et al., 2018; UNI/TS 11300–1, 2014). Internal temperature fluctuations of $\pm$ 2°C are permitted, and it is prescribed that the heating/cooling system is on during the whole time of the simulations. For WIN a coefficient of performance (COP) of 0.9 is adopted, which represents the average energy efficiency of most heating systems (i.e. gas and fuel-fired boilers, electrical resistance heaters, heat pumps, etc., (Martilli, 2014)), while for SUM it is set to 3.5, representing the typical coefficient of performance of air conditioning systems (ACSs).

**Table 2.1:** Thermal and physical parameters for the idealized simulations.

| | Roof | Walls | Road |
|---|---|---|---|
| Heat capacity (MJ $m^{-3}$ $K^{-1}$ ) | 1.77 | 1.37 | 1.94 |
| Thermal conductivity (W $m^{-1}$ $K^{-1}$) | 0.84 | 0.83 | 0.75 |
| Albedo | 0.30 | 0.35 | 0.15 |
| Emissivity | 0.90 | 0.90 | 0.95 |
| Target temp. for ACs (°C) | $25 \pm 2$ (SUM), $20 \pm 2$ (WIN) | | |
| Percentage of glass windows | 20% | | |
| Persons per area (person $m^{-2}$) | 0.02 | | |

In order to estimate the energy consumed per person (and to calculate the heat generated by inhabitants), 0.02 person $m^{-2}$ are assumed within buildings, a typical value for European cities (Eurostat, 2018).

### 2.3.2 Sensitivity analysis

In this work, we quantify the effect on near-surface air temperature and EC of the implementation of several RMSs with respect to clay tiles roofs (NORMS), taken as the reference simulation for each urban configuration, for a total of 12 different urban geometries (combination of three building heights and four $\lambda_p$). In particular, a total of six RMSs are tested, as here summarized:

- Cool Roof (CR): for this scenario, the clay tiles roof albedo (Table 2.1) is replaced with $\alpha = 0.80$;
- Green Roof with grass (GRASS): the roof is supposed to be completely covered with a green roof, as shown in Fig. 2.2. The GR is covered by grass, assuming $LAI = 2$, $\alpha_{gr} = 0.154$, $R_{S_{min}} = 40$ and initial green roof soil moisture $SM = 0.2$ $m^3$ $m^{-3}$;
- Green Roof with sedum (SEDUM): same as GRASS, but in this case the GR is covered with sedum, assuming $LAI = 3$, $\alpha_{gr} = 0.3$, and $R_{S_{min}} = 150$. Sedum is the most frequent vegetation type used for GRs in dry and moderate climates, due to their ability to withstand long periods of heat and water stress by partially closing their stomata during the day (De Munck et al., 2013);
- Green Roof with grass and irrigation (GRASS+IRRI): same as GRASS, but assuming to irrigate the GR vegetation in the period 0100-0300 LST. A total of 25 L $m^{-2}$ of water per week (as in de Munck et al. (2018)) is set at the surface of the uppermost GR layer;
- Photovoltaic panels (PVP): photovoltaic panels with albedo $\alpha = 0.11$ and efficiency $\eta_{PV} = 0.19$ (typical of monocrystalline silicon cells) are assumed to be superimposed over all the roofs, 0.3 m over them.
- Green Roof with grass and photovoltaic panels (GRASS+PVP): same as GRASS, but with the GR covered with PVPs. PVPs are assumed to be 0.3 m above the green roof.

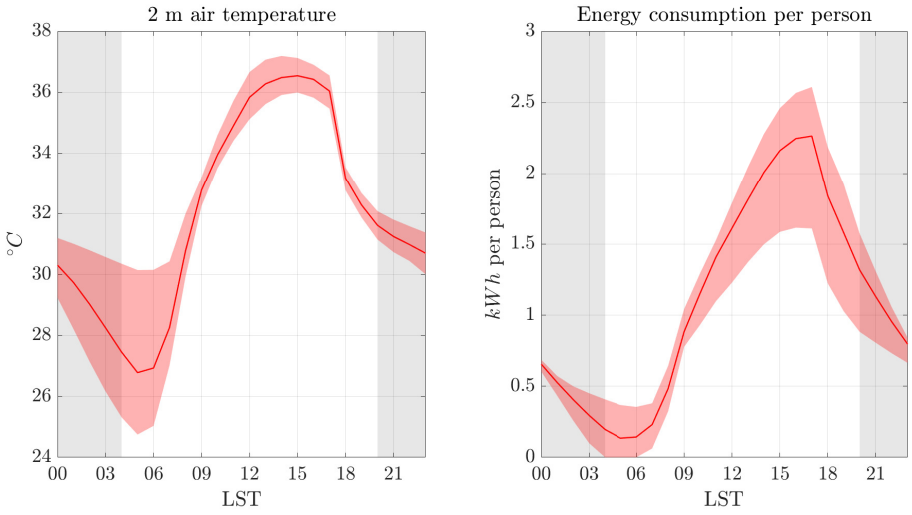


**Figure 2.5:** Summertime average air temperature at 2 m AGL (left) and energy consumption per person (right) averaged over a single diurnal cycle for the NORMS simulations (red line). The red shaded regions represent the variability obtained in the simulations with different urban configurations. Shaded background indicates nighttime hours.

## 2.4 Results

In this section, the differences in 2-m air temperature and EC between the simulations implementing the RMSs and NORMS are evaluated. Results are analyzed considering both the full diurnal cycles, to understand when RMSs are more effective, and the average differences over all the simulation period, to evaluate which is the best mitigation strategy and with which urban configuration. Finally, the analysis focuses on temperature and energy budget time series at the roof level, to understand the physics governing each RMS. Results are presented separately for SUM and WIN, to better understand the effects of the RMSs in the two seasons. Since the diurnal cycles of the variables considered here are very similar on the two days analyzed, we decided to average both days into a single diurnal cycle, to cancel out random fluctuations and obtain more robust results.

### 2.4.1 Summertime

Figure 2.5 shows the diurnal cycle of 2-m air temperature (left) and EC by air conditioning per person (right) for the central cell representing the idealized city in the NORMS simulations. The solid line represents the mean value of the different simulations, while the variability is shown by the shaded regions. On average, a maximum temperature of $\sim$ 36°C is reached at 1500 LST, while the minimum temperature is $\sim$ 27°C at 0500 LST. These temperature values are representative of typical climatic conditions during a strong heatwave in an urban area at mid-latitudes. Temperature variability between different urban configurations is low during daytime, while it becomes larger during nighttime, because of the strong influence of the urban geometry on UHI intensity during nighttime (Martilli (2014), Zonato et al. (2020)). EC is very low during nighttime when indoor temperature decreases below the target value and ACSs are not needed (for some cases), while it reaches its maximum around 1600 LST ($\sim$ 2.3 kWh per person), shifted by one hour with respect to the 2-m air temperature peak, due to the thermal

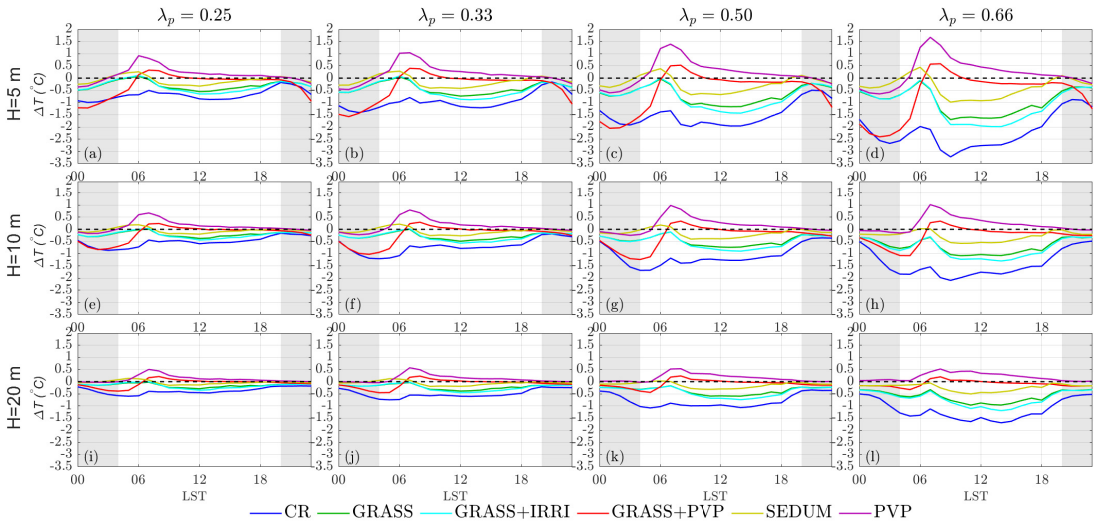


**Figure 2.6:** Summertime 2-m air temperature differences between NORMS and each RMS, averaged for the central urban cell, and for a single diurnal cycle. Building height is kept constant along the rows, while $\lambda_p$ along the columns. Shaded background indicates nighttime hours.

inertia of the buildings. The variability of EC between different urban configurations is higher during daytime with respect to temperature variability, since EC for each cell does not depend only on external temperature but has a strong dependence also on urban morphology, and in particular on the number of floors in each cell. In fact, buildings with more than one floor exhibit a lower EC per person, since overlaying floors insulate lower floors and reduce heat dispersion in the vertical direction.

### Impact on 2-m air temperature

Figure 2.6 shows the time series of 2-m air temperature differences between the NORMS scenario and all the RMSs for all the possible urban configurations. A feature common to CR and GR is a general decrease in temperature for all configurations, with higher differences for lower buildings (the roof surface is closer to the ground, so the effect of the RMSs is more intense) and higher $\lambda_p$ (the cooling effect increases as a larger ground surface is covered by buildings). For all RMSs, the diurnal cycles in Fig. 2.6 are mainly driven by radiation: the largest mitigation effect takes place in the central hours of the morning (0800-1000 LST) for CRs, when radiation starts to increase and in the central hours of the day (1200-1400 LST) for GRs, when less available radiation is converted into sensible heat. A secondary negative peak is present in the central hours of the night for the GR cases, due to the reduced storage of heat within buildings. However, this effect rapidly vanishes around sunrise (0500-0600 LST), when small positive differences (i.e. higher temperatures) are present. This is due to the larger temperature gradients between roof surfaces and air, and, as a consequence, higher sensible heat fluxes, as will be shown in Section 2.4.1.

CR presents a nocturnal peak of reduction of air temperature at 0300 LST. This nocturnal counter intuitive peak is due to the combination of several factors: 1) the reduction of the heat

stored in the roofs, and a small release during nighttime, 2) the city-wide reduction of temperature during daytime, which affects also the nighttime period and 3) the decrease of energy consumption by ACSs (as shown in Fig. 2.8), that consequently reduces the heat emitted by buildings.

PVP and GRASS+PVP cases behave differently with respect to the others RMSs: both show an increase in temperature during daytime, with a sharp peak of $\sim$ 1.5°C at 0800 LST. This is due to the fact that the PVP is thin (6.55 mm), so it presents a smaller thermal inertia than the roof surface. For this reason, air temperature for the PVP cases remains higher during the day, with higher values for packed and low buildings. Moreover, for the configurations with H = 5 m, during the night temperature is lower than in NORMS, since the shading effect of the PVP avoids the heat to be stored and then released during nighttime, with differences up to $\sim$ 0.5°C. This effect is negligible for higher buildings, which present a smaller influence on near-surface air temperature. GRASS+PVP shows a behavior similar to PVP, even if the presence of the GR mitigates the effect of the PVP for all the diurnal cycles, with a diurnal peak up to $\sim$ 0.5°C and a minimum value during nighttime comparable with the CR case. The highest impact during daytime is detected in the H = 5 m, $\lambda_p$ = 0.66 configuration (panel (d)), with a maximum reduction of $\sim$ 3.3°C at 0800 LST for CR. It is followed by GRASS+IRRI and GRASS, which reduce the temperature during the peak of solar radiation of $\sim$ 2°C and $\sim$ 1.7°C respectively. The difference between these two cases, i.e. with and without irrigation, increases as the simulation time advances: indeed, while for GRASS the soil moisture continues to diminish, for GRASS+IRRI the soil moisture is periodically increased by irrigation (not shown). SEDUM and PVP display an average temperature reduction of $\sim$ 0.8°C, with a peak at 1300 LST for the latter. Despite SEDUM and GRASS share the same roof design, the different type of vegetation deployed on the roof changes the impact on the surface energy balance. Grass is more efficient with respect to sedum in converting solar radiation to latent heat flux, resulting in a lower outgoing sensible heat flux.

In order to quantify the average effect of the different RMSs varying the urban configuration, 2-m air temperature differences are averaged for all the period of simulation and compared for each building height (Fig. 2.7). As said before, CR is the most effective RMS, with an average reduction of $\sim$ 2.2°C. The negative temperature differences induced by GRs and CRs display a quasi-linear increase with increasing $\lambda_p$, with increasing negative slope as the efficiency of the RMS increases. For example, for 5-m high buildings the difference between CR and SEDUM is of $\sim$ 0.4°C for $\lambda_p$ = 0.25 and of $\sim$ 1.7°C for $\lambda_p$ = 0.66. With increasing building height the effect of the RMSs diminishes, and so does also the difference between the slopes. PVP is the only RMS that shows average increases of air temperature, with slightly increasing differences as $\lambda_p$ increases. However the average effect of PVP is low, and no particular trends have been detected varying the building height.

While the effects of the RMSs are linear with respect to $\lambda_p$, temperature reduction is not linear with decreasing building height: if $\lambda_p$ is kept constant, the difference in temperature reduction between H = 5 m and H = 10 m is higher compared to that observed between H = 10 m and H = 20. Again, apart from PVP, SEDUM is the least efficient strategy in mitigating 2-m air temperature, since this type of vegetation converts less radiation into latent heat flux with respect to all the simulations with grass. Focusing on GRASS and GRASS+IRRI, it is possible to notice that

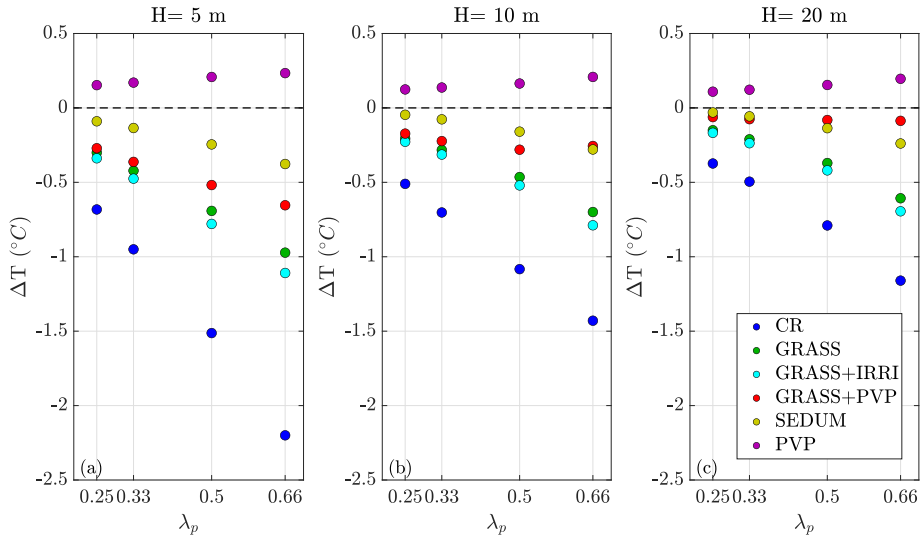


**Figure 2.7:** Summertime 2-m air temperature differences for each RMS averaged over all the period of simulations, depending on $\lambda_p$. The left panel shows 5-m building configurations, central panel 10-m buildings, and right panel 20-m buildings.

GRASS+IRRI is slightly more efficient in reducing 2-m air temperature: assuming to irrigate the GR during nighttime, the latent heat flux during daytime will be higher with respect to the case without irrigation, resulting in a reduced sensible heat flux release. Finally, GRASS+PV shows a net temperature decrease for H = 5 m, even higher than in SEDUM. Increasing the building height, the effects induced by GRASS+PVP disappear, being almost null for H = 20 m.

### Impact on energy consumption

Figure 2.8 shows the time series of the differences in EC per person between NORMS and all the RMSs for all the possible urban configurations. Also in this case it can be seen that the effect of the RMSs increases with increasing $\lambda_p$ and with decreasing building height. The impact of RMSs is more significant in the floor close to the roof, therefore a higher reduction of EC is found for low buildings, composed of a single floor, than for higher buildings, where the effect on lower floors is lower. The different RMSs do not affect EC in the same way they affect air temperature: the largest reduction occurs at 1500 LST for CR, coincident with the EC peak, and at 1700 LST for simulations with GRs and for PVP. The shift in time of the maximum difference is probably linked to the higher thermal inertia of the insulating waterproof layers composing the GRs, and to the screening effect of the PVPs. All the simulations implementing GRs and CR show a similar maximum reduction in EC, by $\sim$ 0.8 kWh per person for H = 5 m, larger than for PVP ($\sim$ 0.2 kWh per person). However, CR displays a higher EC reduction in the night and in the morning. It is remarkable that, despite different types of vegetation and soil moisture, GR cases show the same reduction in EC. This means that the impact of the insulating waterproof layer, which prevents heat from penetrating into the roof, is more important than the effect of the different surface energy balance, even if a PVP layer is superimposed. If the energy produced by PVPs is neglected in the net computation of EC, the PVP case is the least efficient in diminishing EC: while the screening effect is beneficial during daytime,

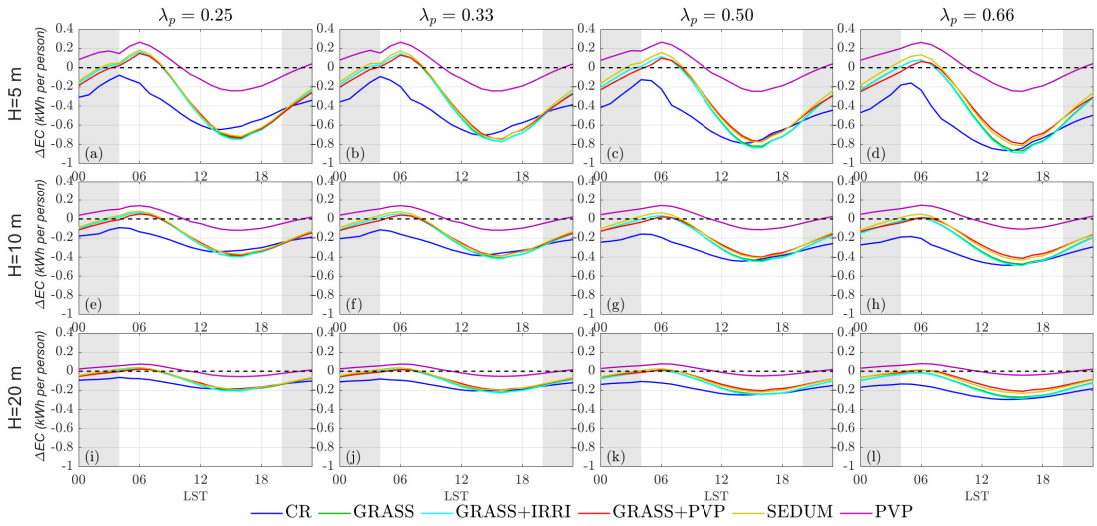


**Figure 2.8:** Differences in energy consumption per person between NORMS and each RMS averaged for the central urban cell and for a single diurnal cycle during summertime. Building height is kept constant along the rows, while $\lambda_p$ along the columns. Shaded background indicates nighttime hours.

**Table 2.2:** Energy-saving per person (kWh/person) during summertime in the PVP cases in absolute values and in percentage (in brackets) with respect to the ACSs consumption.

| $H$ \ $\lambda_p$ | 0.25 | 0.33 | 0.50 | 0.66 |
|---|---|---|---|---|
| 5 m () | −2.78 (−211%) | −2.77 (−212%) | −2.77 (−213%) | −2.76 (−218%) |
| 10 m () | −0.23 (−107%) | −1.38 (−109%) | −1.38 (−113%) | −1.37 (−119%) |
| 20 m () | −0.69 (−53%) | −0.68 (−55%) | −0.68 (−60%) | −0.67 (−67%) |

with a consequent decrease coincident with the peak of EC, during nighttime it prevents the heat to be released by the roof surface through longwave radiation, resulting in an increase of EC. The maximum increase in EC takes place at the same hour as the maximum increase of temperature, around sunrise (Fig. 2.7), due to the cumulative effect of the reduced radiative cooling occurring during nighttime.

In Fig. 2.9, the cumulative difference in EC per person is shown for each RMS, expressed as a percentage with respect to NORMS, for all the period of simulation and for each urban configuration. The decrease in EC becomes linearly larger with growing $\lambda_p$ for all the RMSs: this linearity is mainly due to the linear decrease of 2-m air temperature, which contributes to diminishing the EC by ACSs. As shown in Fig. 2.8, all the simulations implementing GRs perform similarly in reducing EC, with a cumulative decrease comparable to the CR case. While CR and simulations with GRs can diminish EC up to 30-45% for 5-m buildings, PVP does not reduce EC, due to the compensation of the decrease during daytime and the increase during nighttime. In fact, while CRs prevent 80% of radiation to reach the roof, PVPs reflect only 11% of radiation and convert an additional 19% into electricity. Therefore, radiation entering the surface energy budget is almost four times higher in PVP with respect to CR. Moreover, no additional insulating layers as in the simulations with GRs are implemented in PVP, resulting in a higher heat flux through the roof layers. However, if we assume to instantly

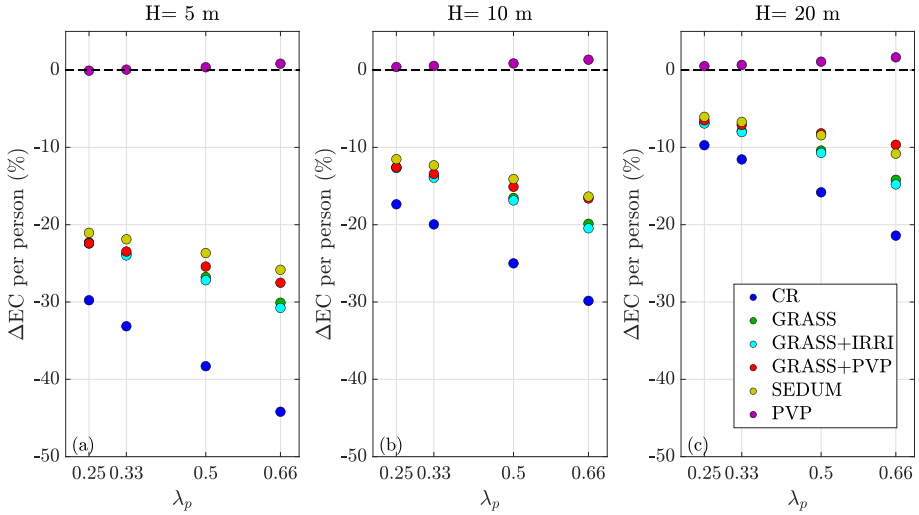


**Figure 2.9:** Variation (percentage) in energy consumption per person with respect to the NORMS case, for each RMS for all the period of simulation during summertime, depending on $\lambda_p$. The left panel shows results for 5-m buildings, the central panel for 10-m buildings and the right panel for 20-m buildings.

use electricity produced by PVPs for the ACSs energy supply, we have a surplus of energy with respect to consumption (if the ACSs energy saving in Table 2.2 is less than -100%, the production overcomes the demand). In the worst-case scenario (H = 20 m, $\lambda_p$ = 0.25), the production of electricity allows a decrease of EC due to ACSs of $\sim$ 53% (-0.69 kWh per person on average), while, for H = 5 m and $\lambda_p$ = 0.66, the consumption due to ACSs is less than half of the total energy produced by PVPs (2.78 kWh per person on average), under the assumption that the roof surface is totally covered by PVPs.

### Temperatures and energy budget at the roof level

Figures 2.10 and 2.11 show the diurnal cycles of air and roof temperatures and of surface fluxes, respectively, for a roof situated in the center of the city, for all the simulations in the configuration with H = 10 m and $\lambda_p$ = 0.50. This configuration has been chosen as an example to highlight the effects of the RMSs on the surface energy budget and on air and roof temperatures. Considering NORMS, the surface temperature reaches its maximum value ($\sim$ 50°C) around noon, with a corresponding maximum in the outgoing sensible heat flux of $\sim$ 300 W $m^{-2}$. On the other hand, the peak of the internal roof layer temperature is reached at 1700 LST ($\sim$ 36°C), due to the thermal inertia of building materials. During nighttime surface roof temperature is always lower than the temperature of the internal layer, reaching a minimum value of $\sim$ 22°C at 0400 LST.

CRs have a significant impact on surface temperature, with maximum values reaching $\sim$ 34°C, i.e. 16°C less than NORMS, influencing also near-surface air temperature. Also the temperature of the internal roof layer is diminished by 4°C, causing the decrease of EC. In this case, the sensible heat flux is almost null during all the daily cycle. Regarding the scenarios implementing GRs, it is clear that the emission of latent heat flux from vegetation and natural soil is the principal factor in diminishing air temperature. Looking at GRASS, the maximum temperature

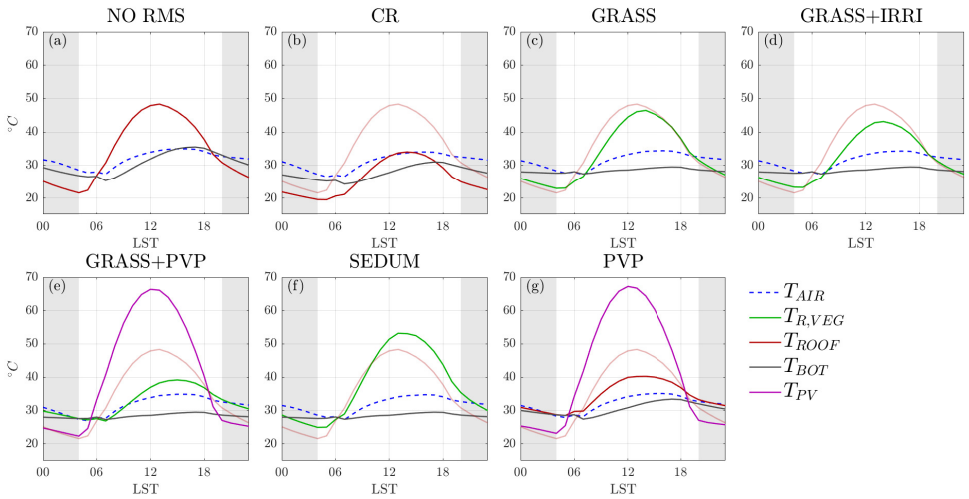


**Figure 2.10:** Summertime temperature diurnal cycles of first air layer above the roof (dashed blue), vegetated roof surface (green), upper roof layer (red), lower roof layer (gray), and PVP (purple), for the central cell representing the city, for the configuration with H = 10 and $\lambda_p$ = 0.50. The temperature of the upper roof layer of NORMS is represented in pink also in the other panels for comparison. Shaded background indicates nighttime hours.

of vegetation is slightly lower with respect to the clay tiles roof temperature by $\sim$ 3°C, especially in the first part of the day. Moreover, the latent heat flux always overcomes the sensible heat flux. The peak of latent heat flux occurs at noon, two hours before the peak of sensible heat flux: this means that the impact of vegetation is more marked in the earlier hours of the day, resulting in a higher difference with respect to clay tiles roofs at noon, when also 2-m air temperature differences are larger, as shown in Fig. 2.6. Also the temperature of the internal roof layer is lower ($\sim$ 5°C) with respect to NORMS: in this case, the waterproof insulating layers of the green roof prevent the heat to diffuse through building materials, and hence inside building rooms. This is evident also observing the indoor sensible heat flux, which is almost null for all the cases with GRs. Differences in magnitude between sensible and latent heat flux are even larger in GRASS+IRRI, since irrigation contributes to increase the soil moisture of the GR, and hence to increase the latent heat flux. On the other hand, since sedum is less efficient in converting solar radiation into latent heat flux with respect to grass, the roof temperature in SEDUM is similar before noon, and higher in the afternoon with respect to NORMS, probably because of the reduced diffusion of heat towards the internal layers of the roof, due to the waterproof insulating layers, that makes the substrate temperature higher. However, the temperature of the internal roof layer in SEDUM is comparable to the one in GRASS, strengthening the hypothesis that processes taking place within the building are not significantly affected by the vegetation type, but rather by the thermal properties of building materials.

Focusing on the PVP case, the panel temperature reaches very high maximum values ($\sim$ 67°C), corresponding to the peak of solar radiation. Despite a considerably higher temperature with respect to the environment, the outgoing heat flux from the PVP is lower with respect to the one from the clay tiles roof surface, because the material constituting the PVP is less efficient in releasing heat. However, the sum of the sensible heat flux from the PVP and the roof is higher than the sensible heat flux in NORMS. This explains why the temperature, especially in the

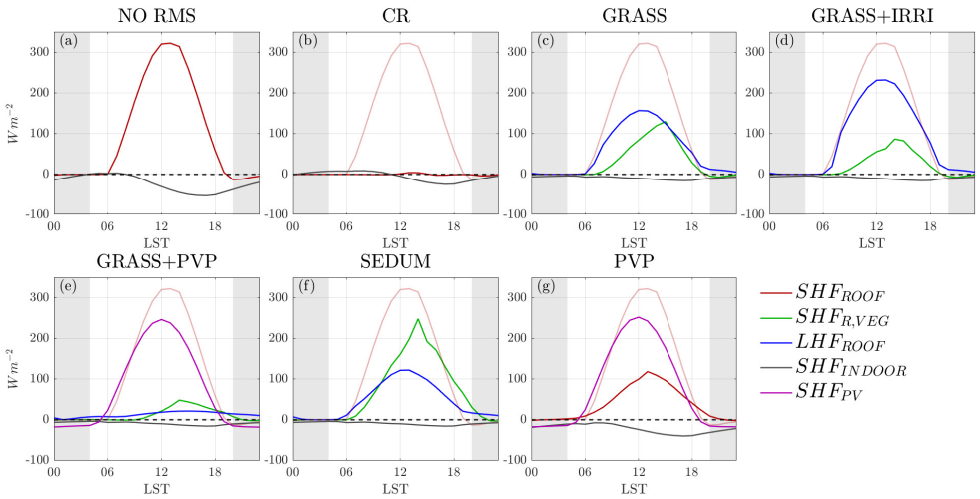


**Figure 2.11:** Summertime diurnal cycles of sensible heat flux for clay tiles roof (red), vegetated roof (green), indoor (grey), PVP (purple) and of latent heat flux for vegetation (blue), for the central cell representing the city, for the configuration with H = 10 and $\lambda_p$ = 0.50. The sensible heat flux of NORMS is represented in pink also in the other panels for comparison. Shaded background indicates nighttime hours

first hours of the day, is higher with respect to NORMS. Moreover, the shading effect exerted by the PVP on the roof, despite the longwave radiation exchange between the two surfaces, decreases the surface temperature of the roof by $\sim$ 8°C, resulting in a lower EC due to ACSs during daytime. This has been observed even in the experimental study by Dominguez et al. (2011). On the other hand, during nighttime, PVP temperature is lower than both air and roof temperature, resulting in a negative heat flux (i.e. heat goes from the environment to the PVP), contributing to decreasing air temperature during nighttime. However, the screening effect of the PVP makes the roof warmer than the exposed roof of $\sim$ 7°C, explaining the increase in EC shown by PVP during nighttime. Similar results, from an experimental campaign, are presented in Broadbent et al. (2019), where the temperature of the PVP is $\sim$ 30°C higher during daytime and $\sim$ 10°C lower during nighttime with respect to the one of the underlying surface. No substantial differences with respect to PVP are shown by GRASS+PVP, in terms of temperature and fluxes of the PV module; this means that the heat exchange processes of the PVP are not significantly influenced by the characteristics of the underlying surface. On the other hand, shading affects the heat exchange between vegetation and the atmosphere: vegetation temperature in GRASS+PVP is slightly lower during daytime than in GRASS, because of the lower radiation that reaches the vegetation. Moreover, the sensible heat flux from vegetation is lower than the flux from a normal roof shaded by the PV, explaining why the diurnal temperature in GRASS+PVP is lower than the simple PVP case.

### 2.4.2 Wintertime

Figure 2.12 shows the diurnal cycle of 2-m air temperature (left) and EC per person due to space heating (right) during wintertime for the central cell representing the idealized city in the NORMS simulations. On average, the maximum temperature reached by the simulations is $\sim$ 6°C at 1300 LST, while the minimum value is $\sim$ 3°C at 0800 LST, depicting, as expected,

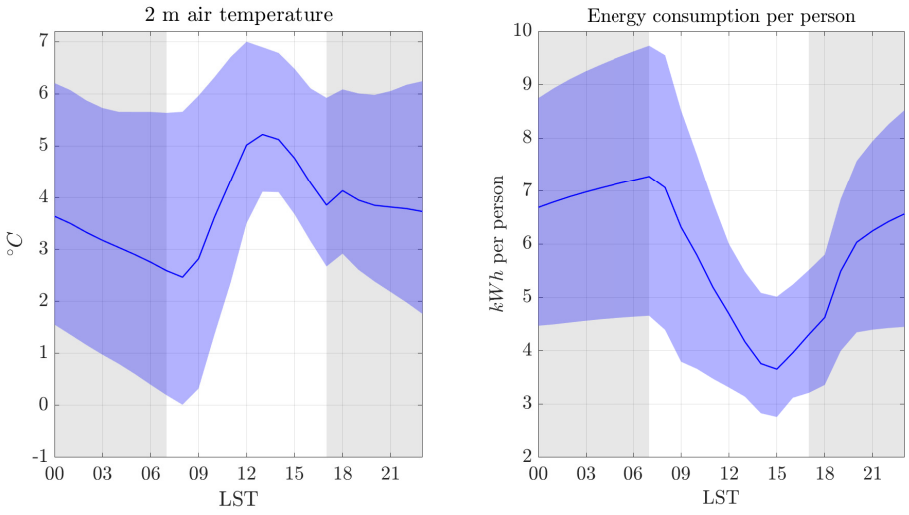


**Figure 2.12:** Wintertime average air temperature at 2 m AGL (left) and energy consumption per person (right) averaged over a single diurnal cycle for the NORMS simulations (blue line). The blue shaded regions represent the variability obtained in the simulations with different urban configurations. Shaded background indicates nighttime hours

a lower diurnal variability than the summer scenario. Temperature variability between different urban configurations is again larger during nighttime, due to the dependence of the UHI effect on urban geometry, with a range of $\sim$ 5°C between the different urban configurations. The trend of the heating EC with time is opposite with respect to the summer case: EC is minimum during the central hours of the day, when solar radiation warms building materials, while it increases during nighttime, keeping a quasi-constant value from 0000 to 0600 LST. Also in this case EC variability between different urban configurations is higher with respect to temperature variability. Values are $\sim$ 3 times higher with respect to the summer case; in fact, while the coefficient of performance (COP) for cooling systems is 3.5, for heating systems is 0.9, resulting in higher consumptions during wintertime and moreover temperature differences between the indoor air and the outside are larger.

### Impact on 2-m air temperature

Figure 2.13 shows the time series of 2-m air temperature differences between NORMS and all the RMSs for all the possible urban configurations. It is worth noting that, opposite to the summer season, during wintertime a higher temperature is beneficial both for thermal comfort and for reducing EC due to heating. Figure 2.13 shows that, differently from the summer season (Fig. 2.6), only CR decreases 2-m air temperature in winter. In general, the temperature in the simulations implementing GRs and PVPs is higher than in NORMS, especially during nighttime. The peak of temperature decrease for CR coincides with the peak of solar radiation, while the peak of increase for PVP takes place at 0900 LST, at the same time as in the summer simulations. For all the RMSs and all the urban configurations, the differences with respect to NORMS are smaller than in the summer case: being winter solar radiation considerably weaker than during summertime, also the modifications of the surface energy budget induced by the RMSs are less significant in winter than in summer. Also in this case the highest differences

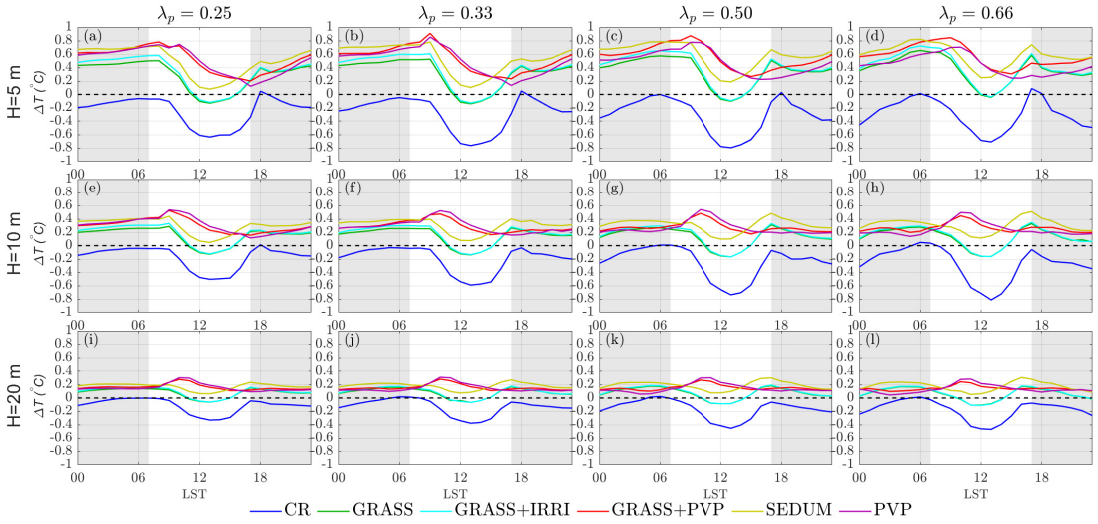


**Figure 2.13:** Wintertime 2-m air temperature differences between NORMS and each RMS, averaged for the central urban cell, and for a single diurnal cycle. Building height is kept constant along the rows, while $\lambda_p$ along the columns. Shaded background indicates nighttime hours.

with respect to NORMS occur in urban configurations with higher $\lambda_p$ and lower buildings. In general, simulations with PVPs exhibit the highest temperature peaks, with an increase in 2-m air temperature up to $\sim$ 0.9°C. This is again due to the instant release of heat by the panels, since they are much thinner than the roof and they respond quicker to solar radiation. On the other hand, during nighttime simulations with PVPs maintain a higher temperature than NORMS. PVPs act 1) avoiding radiation to be stored in the roof layers and 2) screening the roof, inhibiting the release of longwave radiation. Apparently, effect 2) is dominant in the winter case, since roof layers are now heated by the internal rooms. For this reason, PVPs prevent the heat produced by the heating systems to be released (Fig. 2.17 shows that the nighttime temperature of the roof is $\sim$ 5°C higher than the exposed roof), resulting in an increased air temperature during nighttime. The diurnal cycle of 2-m air temperature differences for CR is similar to the summer case, with the highest negative difference at noon ($\sim$ -0.6°C for most cases). On the other hand, during nighttime CR maintains a temperature $\sim$ 0.4°C lower than NORMS, and differences become null at sunrise. Simulations implementing GRs present the highest dissimilarities compared to the summer case: while during the central hours of the day (when thermal comfort is higher than at nighttime) 2-m air temperature differences with NORMS are often negative ($\sim$ -0.2°C for all the configurations with $\lambda_p = 0.66$), in the evening and during nighttime all simulations with GRs show a higher temperature than NORMS, up to $\sim$ 0.8°C for SEDUM. The increase in temperature, which is beneficial for both thermal comfort and EC, is mainly due to the combination of the higher thermal capacity of the GR with respect to the clay tiles roof (heat stored during daytime, and released in higher amounts during nighttime) and to the low latent heat flux during daytime (the low winter radiation never makes the latent heat flux to overcome the sensible heat flux, as shown in Fig. 2.18). This is due to the fact that the stomatal resistance is inversely proportional to the solar radiation, and consequently the conversion of solar radiation into latent heat is less favoured during wintertime. The effect of the reduced latent heat is clear if we refer to SEDUM: sedum vegetation is

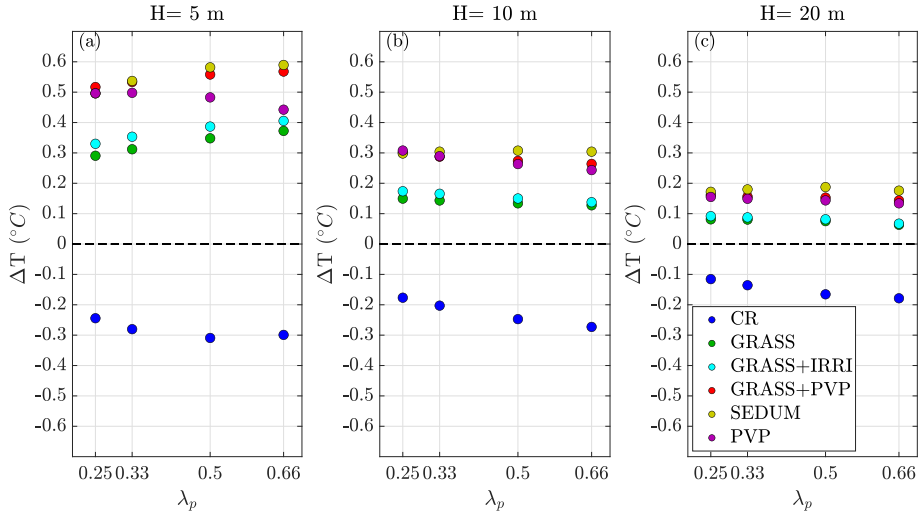


**Figure 2.14:** Wintertime 2 m air temperature differences for each RMS averaged over all the period of simulations, depending on $\lambda_p$. The left panel shows 5-m building configurations, the central panel 10-m buildings, and the right panel 20-m buildings.

less efficient in converting solar radiation into latent heat flux, therefore this RMS is the one that shows the highest temperature differences with respect to NORMS. Finally, GRASS+PVP behaves similarly to PVP, with slight nighttime increases, due to the screening effect of the PVPs.

On average (Fig. 2.14), 2-m temperature differences induced by the RMSs slightly increase with increasing $\lambda_p$ for the H = 5 m cases (with the exception of PVP, which remains almost constant). The other building heights, apart from CR, whose average negative temperature differences becomes slightly larger with $\lambda_p$, show instead a constant increase in temperature at the different values of $\lambda_p$ explored. SEDUM and GRASS+PVP are the RMSs showing the largest increases in temperature, and thus the largest benefits in terms of thermal comfort, up to $\sim$ 0.6°C for the configuration with $\lambda_p$ = 0.66 and H = 5 m. PVPs increases are comparable to the ones of SEDUM, but discrepancies are notable with increasing $\lambda_p$. It can also be observed that the positive differences (cases with GRs and PVPs) decrease faster increasing the building height than the negative differences induced by CRs.

### Impact on energy consumption

Figure 2.15 shows the time series of the differences in EC per person due to space heating between NORMS and all the RMSs for all the urban configurations. Since EC is low during daytime, the effect of the RMSs takes place mainly during nighttime hours. During the night, at constant H (i.e. for each row of Fig. 2.15) the differences in EC induced by the variation of $\lambda_p$ are very low, due to fact that temperature differences are not influenced by this parameter (cf. Fig. 2.14). The influence of GRs on EC does not depend on the type of vegetation and on soil moisture, since all the simulations with GRs show the same trend. In particular, while during daytime the differences with NORMS are small, from 0000 to 1100 LST all simulations with GRs depict a constant decrease in EC, up to 3 kWh per person for the H = 5 m cases, where the effect is stronger since buildings are composed of a single floor. Concerning

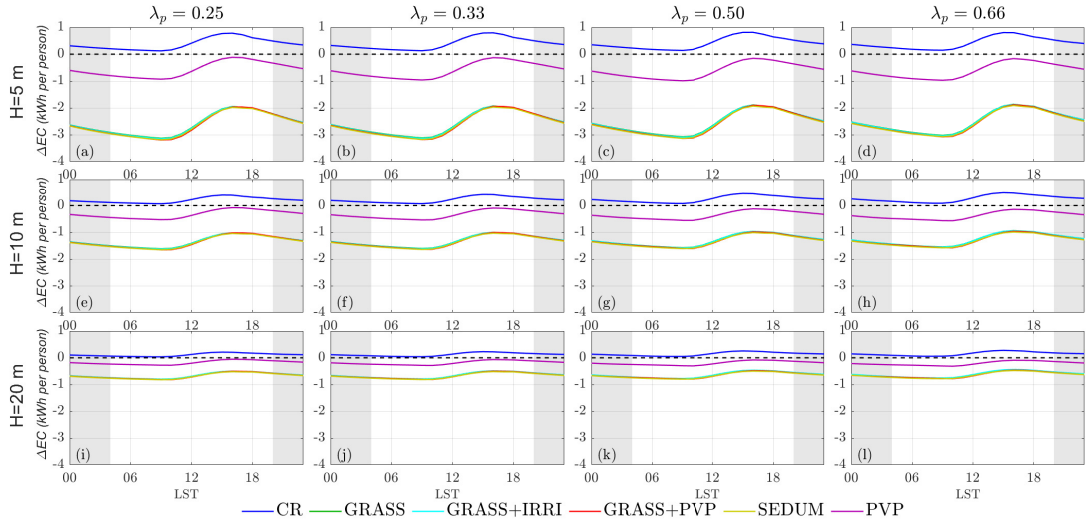


**Figure 2.15:** Differences in energy consumption per person between NORMS and each RMS averaged for the central urban cell and for a single diurnal cycle during wintertime. Building height is kept constant along the rows, while $\lambda_p$ along the columns. Shaded background indicates nighttime hours (Notice that the range of the axes is different varying the building height).

**Table 2.3:** Energy-saving per person (kWh/person) during wintertime in the PVP cases in absolute values and in percentage (in brackets) with respect to the heating consumption.

| $H$ \ $\lambda_p$ | 0.25 | 0.33 | 0.50 | 0.66 |
|---|---|---|---|---|
| 5 m () | −0.67 (−13%) | −0.68 (−14%) | −0.69 (−14%) | −0.70 (−15%) |
| 10 m () | −0.36 (−9%) | −0.37 (−9%) | −0.38 (−10%) | −0.39 (−11%) |
| 20 m () | −0.19 (−6%) | −0.19 (−6%) | −0.20 (−7%) | −0.20 (−8%) |

CR, there is always an increase in EC by heating, especially for low buildings. Differences are almost null or slightly positive during nighttime, when the modified roof albedo does not affect the energy budget of the roof surface, while they display a maximum around 1600 LST, due to the reduction of the roof surface temperature. PVPs present small differences with respect to NORMS in the afternoon and in the evening, while during night hours and in the morning the decrease in EC is more significant: while during daytime PVPs reduce roof surface temperature, during nighttime they trap the infrared radiation emitted by the roof, keeping it warmer than in NORMS and consequently decreasing the energy demand (see Fig. 2.17).

Figure 2.16 shows the cumulative differences in the percentage of EC by heating per person between all RMSs and NORMS for all the simulations. As shown above, for the same building height, differences are almost insensitive to $\lambda_p$. Therefore, contrary to the summer case, street width does not influence the effects of RMSs on EC. Regarding PVP, differences are always negative as explained in the previous subsection ($\sim$ 8% for the H = 5 m cases), because of the screening effect on longwave radiation during the night. On the other hand, CR always increases EC by $\sim$ 5% for all the urban configurations. Again, all the simulations with GRs show a relevant saving of EC by heating. In particular, the combined effect of insulation by waterproof layers and higher thermal capacity consents a reduction of the heating EC up to $\sim$ 33% for the H = 5 m cases, and of $\sim$ 22% and $\sim$ 15% for the H = 10 m and H = 20 m

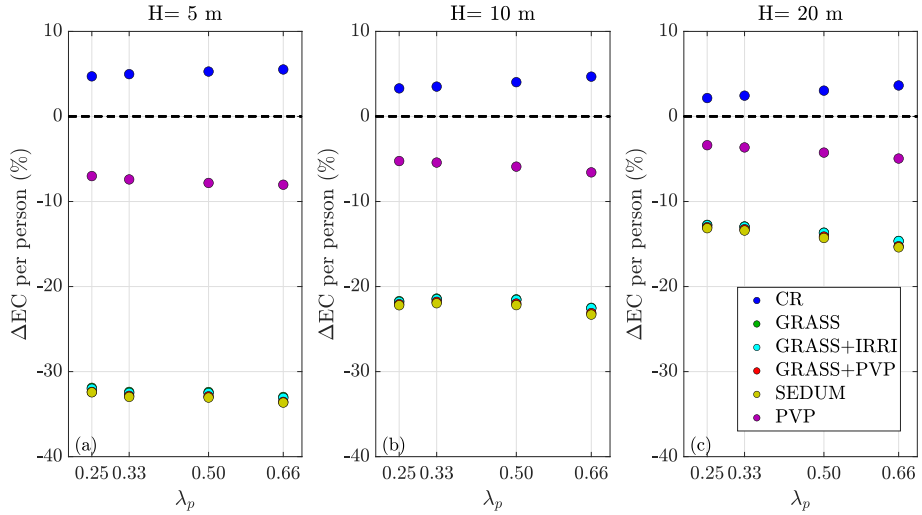


**Figure 2.16:** Variation (percentage) in energy consumption per person with respect to the NORMS case, for each RMS for all the period of simulation during wintertime, depending on $\lambda_p$. The left panel shows results for 5-m buildings, the central panel for 10-m buildings and the right panel for 20-m buildings.

cases respectively. As in the summer case, there are no relevant differences induced by the GR vegetation type and the soil moisture availability, indicating that the insulating layers are the dominating effect in reducing EC by heating.

In Table 2.3 the energy-saving per person in the PVP simulations, in percentage with respect to the heating consumption and on average over the period of integration, is shown, assuming to instantly use the energy produced by the photovoltaic modules for heating: in contrast to the summer case, during wintertime electricity production never overcomes energy demand, due to the fact that the energy produced by PVPs is lower than during summertime, due to the lower incoming solar radiation. The maximum reduction is 0.67 kWh per person, compared to 2.78 kWh per person in the summer period, i.e. roughly four times lower. In particular, the maximum percentage saving of $\sim 15\%$ is reached for the H = 5 m cases, while for 20-m tall buildings, heating EC can be reduced by up to 13%.

### Temperatures and energy budget at the roof level

Figures 2.17 and 2.18 show the time series of air and roof temperature and of heat fluxes respectively, for the configuration with $\lambda_p = 0.50$ and H = 10 m for the winter season, for all the simulations. Considering NORMS, as in the summer season, roof temperature is higher than air temperature during daytime and lower during nighttime, reaching a maximum temperature of $\sim 10$°C at 1300 LST and a minimum value of $\sim 0$°C after sunset. Contrarily to the summer case, the temperature of the internal roof layer is always higher than both air and roof surface temperature, since a target temperature of 20°C is required for the building rooms. The temperature of the internal roof layer oscillates between $\sim 10$°C during nighttime and $\sim 15$°C during daytime, always lower than the target temperature. Since the temperature of the internal roof layer is always higher than the external surface temperature, the indoor heat flux is always outgoing (i.e. from the internal room to the environment), with minimum values during daytime,

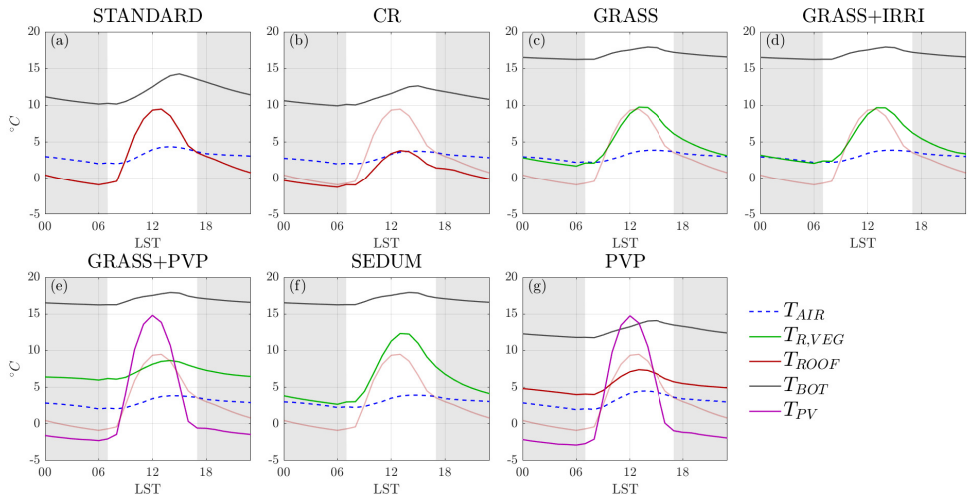


**Figure 2.17:** Wintertime diurnal cycle of temperature of near-surface air (dashed blue), vegetated roof (green), upper roof layer (red), lower roof layer (gray) and PVP (purple), for the central cell representing the city, for the H = 10 m, $\lambda_p = 0.50$ configuration. The temperature of the upper roof layer of NORMS is represented in pink also in the other panels for comparison. Shaded background indicates nighttime hours.

when solar radiation heats the roof. CR behaves as in the summer case: roof temperature is reduced, comparable with the NORMS roof during nighttime and with air temperature during dayttime. Internal roof temperature is lower than NORMS, especially during daytime. During daytime PVP acts similarly to CR: the PVP prevents the radiation to reach the roof surface, thus the roof is cooler than in NORMS, despite the PVP temperature reaches $\sim$ 15°C. On the other hand, during nighttime, the roof, shielded by the PVP, is warmer ($\sim$ 5°C) than in NORMS. PVP temperature during nighttime is much lower than the air temperature, with differences of $\sim$ 6°C, with a resulting negative PVP sensible heat flux ($\sim$ -30 W m$^{-2}$). The heat flux from the roof covered by the PVP remains significantly positive even during nighttime, explaining the higher air temperature in PVP simulations during night hours. Simulations with GRs instead show an increase of roof surface temperature with respect to NORMS, especially after 1300 LST and during nighttime. In this time period GRs are warmer than NORMS by $\sim$ 5°C due to the combination of 1) the reduced upward latent heat flux (almost null even during daytime), due to a lower incoming shortwave radiation in the winter season with respect to summertime and 2) the higher volumetric thermal capacity of the GR layers with respect to the clay tiles roof, resulting in a reduction of the upward sensible heat flux during daytime, and an increase during nighttime. In fact, while the peak of the upward sensible heat flux in NORMS is $\sim$ 100 W m$^{-2}$, the peak in the simulations with GRs is $\sim$ 50 W m$^{-2}$ and shifted in time, due to the higher thermal inertia. Moreover, just after sunset, the upward sensible heat flux assumes slightly positive values, increasing outdoor temperature, as seen in Sec. 2.4.2. The effect of insulating waterproof layers is again clear looking at the temperature of the internal roof layer, which is constantly warmer than in NORMS by $\sim$ 7°C, and from the indoor sensible heat flux, that oscillates around zero. Regarding SEDUM, the lower efficiency in converting radiation into latent heat flux with respect to grass is beneficial during wintertime, since roof surface temperature is higher than in GRASS, and contributes to increasing air temperature. Finally,

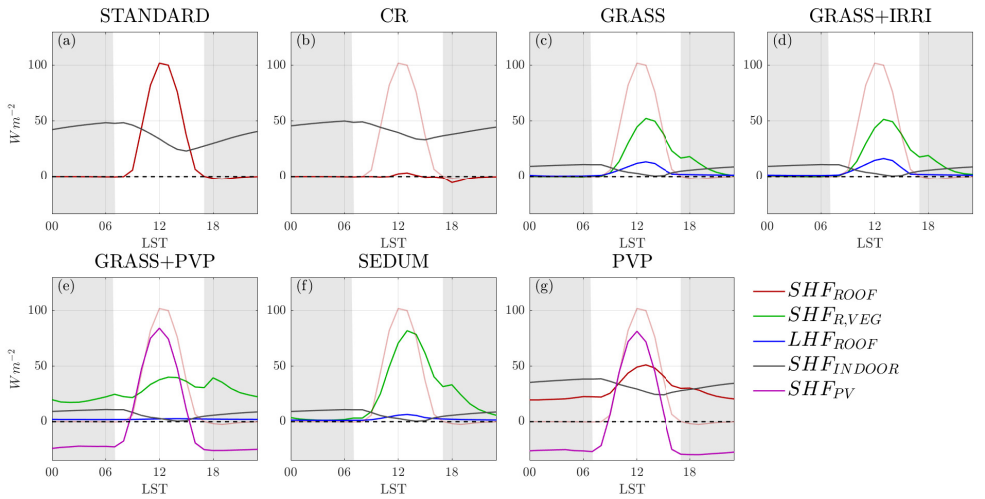


**Figure 2.18:** Wintertime diurnal cycle of sensible heat flux for clay tiles roof (red), vegetated roof (green), indoor (grey), PVP (purple) and of latent heat flux for vegetation (blue), for the central cell representing the city, for the H = 10 m,$\lambda_p = 0.50$ configuration. The sensible heat flux of NORMS is represented in pink also in the other panels for comparison. Shaded background indicates nighttime hours.

GRASS+PVP behaves similar to PVP, with an almost null latent heat flux during all the day, and nocturnal sensible heat flux higher than in the PVP case, resulting in higher temperatures than in PVP during nighttime.

## 2.5 Discussion and conclusions

This study presented the results of two-dimensional idealized simulations with the mesoscale WRF model in the urban environment, implementing innovative parameterizations of RMSs, coupled with the BEP-BEM urban parameterization schemes. In particular, simulations were performed under two different climatic conditions (i.e. summertime and wintertime), for twelve different urban configurations, with the aim of quantifying the effect of different RMSs, i.e. cool roofs, green roofs, and rooftop photovoltaic panels, on 2-m air temperature and on EC, for several urban geometries. Below we summarize the key results, highlighting the main differences between simulations implementing rooftop mitigation strategies and a simulation with clay tiles roofs, taken as the reference:

- *Dependence of air temperature on urban configuration.*
  The mitigation effect on air temperature varies almost linearly with the building surface to total surface fraction ($\lambda_p$) during summertime, while in wintertime it linearly increases only for 5-m high buildings. The mitigation effect is higher for low buildings, with a non-linear decrease of the impact with building height. Therefore, the urban configuration with the lowest buildings and the highest $\lambda_p$ (H = 5 m and $\lambda_p$ = 0.66) shows the highest effect of the RMSs.

- *Dependence of energy consumption on urban configuration.*
  During summertime, similarly to temperature, the saving of EC per person by ACSs induced by RMSs increases linearly with $\lambda_p$, and decreases with building height, since RMSs act mostly on the floor just below the roof. During wintertime, instead, no dependence of EC by heating with varying $\lambda_p$ was detected. As in the summer case, the energy saving percentage decreases as the building height increases.

- *Temperature mitigation during summertime*
  All mitigation strategies with CRs and GRs induce a decrease in air temperature with respect to the clay tiles roof, with a greater effect during daytime. For these RMSs, the highest temperature reductions occur starting from the central daytime hours, with a secondary peak before sunrise. In general, CR is the most efficient in reducing summer temperatures, with a maximum decrease of $\sim$ 3.3°C and a daily average decrease of $\sim$ 2.2°C for the urban configuration with $H$ = 5m and $\lambda_p$ = 0.66. The second most efficient RMS is GRASS+IRRI, thanks to the latent heat flux increased by irrigation. SEDUM is the RMS employing GRs with the smallest impact on air temperature: sedum vegetation is less efficient in converting solar radiation into latent heat flux, hence the mitigation effect is, in general, less than half with respect to GRASS. Air temperature in PVPs increase during daytime because the heat flux from PVPs is instantly released and summed to the heat flux from the roof surface. On the other side, during nighttime PVP maintains a lower temperature until sunrise, due to the reduction of the heat stored within the building materials during daytime. On average, PVPs slightly decrease thermal comfort. This result is in contrast with the works of Masson et al. (2014) and Salamanca et al. (2016), but it is consistent with different observational data that demonstrate that PVPs generally increase temperature during daytime (Broadbent et al., 2019). Results of GRASS+PVP are mainly driven by the PVP energy balance, with higher reductions with respect to PVP, both during daytime and nighttime, due to the GRs presence.

- *Energy consumption during summertime*
  In general, CRs and GRs decrease EC by ACSs, with the maximum saving during the late afternoon. All simulations implementing GRs, even the one with overlaying PVPs, show the same behavior, since for EC the dominant feature is the insulating effect of the waterproof layers constituting the GR (and not the vegetation type), and they are the most efficient during daytime. The effect of CRs is comparable to that of GRs during daytime, while during nighttime hours the reduction in EC is larger than in the GR cases, because the increased albedo decreases the heat storage within the roof. On average, CR can save up to 45% of EC by ACs (for the urban configuration with H = 5 m and $\lambda_p$ = 0.66), while the average effect of PVPs is null. If we assume to employ all the electricity produced by PVPs for the ACSs supply, we obtain a net gain for all the urban configurations, with an energy production up to $\sim$ 210% of the ACSs EC for 5-m buildings.

- *Temperature mitigation during wintertime*
  Contrary to summertime, during wintertime RMSs are beneficial if they induce an increase in air temperature. During wintertime, CRs act similarly to the summer period, i.e. diminishing temperature during all the day, with higher reductions during daytime,

corresponding to the peak of solar radiation. However, since during wintertime solar radiation forcing is weaker, the reduction is limited to up to $\sim 0.3$°C, around ten times less than in summertime. On the other hand, all simulations with GRs perform differently with respect to summertime. Since the latent heat flux is greatly reduced, because of the dependence of stomatal resistance on solar radiation, more energy is stored in building materials. As a consequence, more heat is released during nighttime: since sedum vegetation is the less efficient in triggering evapotranspiration, SEDUM is the most efficient in warming up during wintertime, with an average increase of $\sim 0.5$°C for the configuration with H = 5 m and $\lambda_p = 0.66$. Even PVPs increase 2-m air temperature during the winter season: during daytime the effect is the same as in the summer case, while during nighttime they prevent the roof cooling by longwave radiation release, with a consequent higher temperature up to $\sim 0.8$°C.

- *Energy consumption during wintertime*
  The temperature decrease induced by CRs during wintertime causes an increase in EC by heating of $\sim 5\%$ for all the urban configurations. On the other hand, PVP slightly decreases the energy demand (around $\sim 6\%$), because of the combined effect of the temperature increase and the screening of the PVP for longwave radiation during nighttime. The electricity produced by PVPs is not sufficient to cover all the EC by heating, due to the lower energy production from the weak incoming solar radiation. All the simulations with GRs, because of the combined effect of increased external temperatures and of the insulating layer (that prevents the diffusion of indoor heat through the roof), reduce EC up to 35% for the urban configurations with H = 5 m.

The aim of this study was to quantify the effect of various rooftop mitigation technologies under different climatic conditions, in order to set a benchmark for urban climate studies. A wide range of urban configurations with uniform building heights, under two typical climate scenarios was investigated, so as to provide a comprehensive set of results, that can be representative of most mid-latitude cities. Results, limited to simplified urban geometrical configurations, pointed out that advanced parameterization schemes are needed to simulate the complex feedback between buildings and the atmosphere, in order to obtain reliable results, that can be used by urban planners and decision-makers to make informed choices to improve the sustainability of urban areas.

# 3 A new $K-\varepsilon$ turbulence parameterization for hetereogeneous terrains

**Abstract**

A new one-dimensional 1.5-order Planetary Boundary Layer (PBL) scheme, based on the $K-\varepsilon$ turbulence closure applied to the Reynolds averaged Navies Stokes (RANS) equations, is developed and implemented within the Weather Research and Forecasting (WRF) model, to improve the representation of PBL processes. The new scheme includes an analytic solution of the strongly coupled equations of the turbulent kinetic energy and dissipation rate. The here presented analytic solution can reduce numerical errors arising from the discretization of the equations and lengthen the time-step required for the numerical integration, usually obligatorily low for stability reasons. The new PBL schemes proposed include a model for the calculation of the Prandtl number, a correction to the equation of the dissipation rate, and a prognostic equation for the temperature variance. Five different idealized cases are investigated: four of them assume convective conditions, and they differ in initial thermal stratification and terrain complexity, while one simulates the very stable boundary layer case known as GABLS. For each case study, an ensemble of different Large Eddy Simulations (LES), varying on the initial temperature perturbations, has been taken as reference for the comparison with the novel PBL schemes and other state-of-the-art 1-,1.5- and 2.5-order turbulence closures. Results show that the new PBL $K-\varepsilon$ scheme bring improvements in all the cases tested in this study. Specifically, the largest enhancements are brought by the turbulence closure including a prognostic equation for the temperature variance. Moreover, the largest benefits with respect to conventional PBL schemes are obtained for the idealized cases simulating a typical thermal circulation within a two-dimensional valley. This suggests that the use of prognostic equations for the dissipation rate and temperature variance, which take into account their transport and history, is particularly important with increasing complexity of PBL dynamics.

## 3.1 Introduction

One of the prime sources of uncertainty in mesoscale Numerical Weather Prediction (NWP) models is the representation of thermodynamic and kinematic structures (Cohen et al., 2015;

Nielsen-Gammon et al., 2010). These structures, whose development takes place within the planetary boundary layer (PBL), are driven by the vertical mixing induced by the earth surface, and they are associated with turbulent eddies. Spatiotemporal scales of such eddies cannot be explicitly resolved at grid scales and time steps typical of NWP models at the mesoscale (Stull, 1988). For this reason, PBL parameterization schemes based on the Reynold average Navier Stokes (RANS) equations are employed at the typical resolution of mesoscale models, ranging from hundreds of meters to some kilometers, to parameterize the vertical turbulent flux of momentum, heat, and moisture.

PBL schemes can be divided into two main categories (Zhang et al., 2020): the eddy-diffusivity mass-flux (EDMF) approach and the traditional eddy-diffusivity (K-theory) parameterizations. The EDMF approach consists of the combination of the K-theory closure, which parameterizes the turbulent transport by small eddies, with the mass flux component accounting for nonlocal organized eddy fluxes (Angevine et al., 2010; Han et al., 2016). On the other hand, K-theory turbulence closures can be classified depending on the order resolved of the RANS equations. 1-order turbulence closures estimate the eddy viscosity/diffusivity ($\nu_M$, $\nu_H$) based on the vertical stratification and wind shear. One example is the well-known Yonsei State University scheme (YSU, Hong et al., 2006b). 1.5-order closures comprise a prognostic equation for the turbulent kinetic energy (TKE) and a turbulent mixing length scale ($\ell_K$) for calculating vertical mixing coefficients (K-$\ell$ approach). The equation for the TKE accounts for the contribution of buoyancy, shear, vertical transport, and dissipation rate ($\varepsilon$). The latter term is assumed to be proportional to a dissipation mixing length ($\ell_\varepsilon$), set equal to $\ell_K$ in the most simple 1.5-order turbulence closures. However, Bougeault et al. (1989) (BouLac hereafter) utilized two different length scales, depending on the atmospheric stability. Higher-order closures involve diagnostic or prognostic equations of higher-order moments of the RANS equations, with the same assumptions of 1.5-order closures in terms of TKE and mixing length scales. One of the most widely used is the $K-\ell$ 2.5-order Mellor-Yamada-Nakanishi-Niino scheme (MYNN2.5, Nakanishi et al., 2004). An alternative approach to determine the TKE and the vertical mixing coefficients in 1.5-order (or higher) closures is to employ an additional prognostic equation for the dissipation rate, in order to avoid to define the diagnostic length scales. This kind of closure, called $K-\varepsilon$ hereafter, has been widely used to reproduce vertical PBL profiles at various regimes (Detering et al., 1985; Duynkerke, 1988; Langland et al., 1996; Launder et al., 1974). Beljaars et al. (1987) compared $K-\ell$-based and $K-\varepsilon$-based schemes and found that the $K-\varepsilon$ better preserves the "memory effects" of the PBL, because of the prognostic equation of $\varepsilon$ and its vertical transport, not considered in $K-\ell$ schemes.

Wang (2001, 2002) implemented a $K-\varepsilon$ scheme in a regional climate model, successfully simulating the Asian summer monsoon. More recently, Zhang et al. (2020) incorporated the $K-\varepsilon$ version of Wang (2001, 2002) in the Weather Research and Forecasting (WRF) model (Skamarock et al., 2019). The new scheme has been evaluated over the stratocumulus that dominates the Southeast Pacific and over the Southern Great Plains, finding that the $K-\varepsilon$ performs similarly to other state-of-the-art PBL schemes. However, several studies (Launder et al., 1983; Lazeroms et al., 2015; Sukoriansky et al., 2005; van der Laan et al., 2017; Zeng et al., 2020a; Zeng et al., 2020b) highlighted the necessity to modify the standard $K-\varepsilon$ turbulence closure, since it is not consistent with the Monin-Obukhov similarity theory (MOST), and does

not perform well in both convective and stable regimes. Recent insights have even assessed the necessity for additional prognostic equations, in particular for the potential temperature variance (Mauritsen et al., 2007; Zilitinkevich et al., 2013; Zilitinkevich et al., 2007).
This work aims to employ the $K-\varepsilon$ turbulence closure, with appropriate modifications, to face the problems highlighted in the aforementioned works, to improve the capability of PBL schemes to reproduce simple idealized cases in the context of the WRF mesoscale model. Specifically, the standard $K-\varepsilon$ closure has been modified, through the estimation of the vertical profile of the Prandtl number as in Hong et al. (2006b) (to consider the difference between the eddy diffusivity and eddy viscosity), the addition of a correction term in the prognostic equation for the dissipation rate as in Zhang et al. (2020) (to make the new closure consistent with the MOST), and the coupling with a prognostic equation for the turbulent potential energy (TPE, proportional to the temperature variance) as in Lazeroms et al. (2015) and Želi et al. (2019) (to consider its effect in the turbulent heat flux). The latter, for convective cases, has also been compared with a closure employing a non-local counter-gradient term, computed as in Ching et al. (2014). The novel PBL scheme has been tested by means of idealized simulations. Idealized simulations include several flat terrains with different thermal stratification in convective regimes, complex terrain with various wind forcing, and a stable case. The aim is to assess if the employment of additional prognostic equations, leading to "memory effects" and turbulent transport of the dissipation rate and temperature variance is beneficial for the reproduction of PBL processes. The newly-developed PBL scheme has been validated against ensemble large eddy simulations (LES), taken as reference for each case study, and compared with state-of-the-art PBL schemes, at different orders, already implemented in the WRF model.
This paper is organized as follows: the theory of the newly-introduced PBL scheme, along with the novel computational solution is presented in Section 3.2. The set-up of the five idealized case study and the methodology for the calculation of the turbulent fluxes are described in Section 3.3. In Section 3.4 model outputs are compared with LES simulations for each case study, and the performance of various PBL schemes is quantified through statistical parameters. Finally, in Section 3.5, results are summarized and discussed.

## 3.2 The model

The turbulence parameterization scheme presented here is developed in the framework of the Reynolds-averaged Navier-Stokes (RANS) equations, in which each variable of the mean flow is decomposed into its mean (upper case letters) and fluctuating part (lower case letters), representing an ensemble average. It is customary for the planetary boundary layer (PBL) to assume horizontal homogeneity, in absence of horizontal gradients, to neglect advection (i.e. the material derivative coincides with the local time derivative) and to consider only the vertical derivative of the turbulent fluxes. Then the mean flow equations are:
Zonal wind speed:

$$\frac{\partial U}{\partial t} = -\frac{\partial \overline{uw}}{\partial z} + f(V - V_g) \tag{3.1a}$$

Meridional wind speed:

$$\frac{\partial V}{\partial t} = -\frac{\partial \overline{vw}}{\partial z} - f(U - U_g) \tag{3.1b}$$

Potential temperature:

$$\frac{\partial \Theta}{\partial t} = -\frac{\partial \overline{w\theta}}{\partial z} \tag{3.1c}$$

where $f = 2\Omega \sin\phi$ is the Coriolis parameter and $\vec{U_g} = (U_g, V_g)$ is the geostrophic wind. The quantities $\overline{wc}$, where $c = (u, v, \theta)$ represent the vertical turbulent fluxes. The aim of this work is to find a closure for these turbulent fluxes, in terms of mean velocity, mean potential temperature (and mean water vapor mixing ratio, but here we consider only dry atmosphere cases), that does not depend on a diagnostic length scale, but instead on the local properties of the atmospheric state, e.g. adopting a prognostic equation for the dissipation rate, skipping the step of defining a diagnostic length scale which depends on the atmospheric conditions.

### 3.2.1 The standard $K-\varepsilon$ turbulence closure

Similarly to most turbulence models, in the turbulent closure presented here the turbulent fluxes are parameterized, in analogy with molecular diffusion, as a function of an eddy viscosity/diffusivity and of the mean gradients:

$$\overline{uw} = -\nu_M \frac{\partial U}{\partial z} \tag{3.2a}$$

$$\overline{vw} = -\nu_M \frac{\partial V}{\partial z} \tag{3.2b}$$

$$\overline{w\theta} = -\nu_H \frac{\partial \Theta}{\partial z} \tag{3.2c}$$

where $\nu_M$ is the eddy viscosity and $\nu_H$ the eddy diffusivity. In order to close Eq. 3.1, the eddy coefficients need to be parameterized. Moreover, in subsection 3.2.3 we will discuss an additional term for the turbulent heat flux, that takes into account the vertical transport by large eddies. A simple scaling analysis suggests:

$$\nu_M, \nu_H \sim \ell_K \cdot K^{1/2} \tag{3.3}$$

where $\ell_K$ is a mixing length scale, and $K = \left(\overline{u^2} + \overline{v^2} + \overline{w^2}\right)/2$ is the turbulent kinetic energy (K) per unit of mass. The prognostic equation for $K$ allows to take into account the history and the transport effects of the turbulent velocity scale and, considering again horizontal homogeneity and neglecting the pressure fluctuations, is given by:

$$\frac{\partial K}{\partial t} = -\frac{\partial \overline{wk}}{\partial z} - \overline{uw}\frac{\partial U}{\partial z} - \overline{vw}\frac{\partial V}{\partial z} + \frac{g}{\Theta_0}\overline{w\theta} - \varepsilon \tag{3.4}$$

The terms on the right hand side represent, respectively, the turbulent transport, the shear production in both horizontal wind directions, the buoyancy production/destruction and the dissipation rate. To close Eq. 3.4, the dissipation rate $\varepsilon$ is usually set dependent on $K$ and a length scale, in a way similar to Eq. 3.3:

$$\varepsilon \sim \frac{K^{3/2}}{\ell_\varepsilon} \tag{3.5}$$

Combining Eq. 3.5 and Eq. 3.3, one obtains:

$$\nu_M = c_\mu \frac{K^2}{\varepsilon} \tag{3.6a}$$

$$\nu_H = \frac{c_\mu}{Pr} \frac{K^2}{\varepsilon} \tag{3.6b}$$

where $c_\mu$ is a constant and usually set equal to 0.09 (Launder et al., 1983), and $Pr$ is the turbulent Prandtl number. The dissipation rate $\varepsilon$ is calculated through its prognostic equation:

$$\frac{\partial \varepsilon}{\partial t} = -\frac{1}{\sigma_\varepsilon} \frac{\partial \overline{\varepsilon w}}{\partial z} - \left[ c_1 \left( \overline{uw} \frac{\partial U}{\partial z} + \overline{vw} \frac{\partial V}{\partial z} \right) - c_3 \frac{g}{\Theta_0} \overline{w\theta} \right] \frac{\varepsilon}{K} - c_2 \frac{\varepsilon^2}{K} \tag{3.7}$$

where $c_1$, $c_2$, $c_3$ and $\sigma_\varepsilon$ are set equal to 1.44, 1.92, 1.44 and 1.3, respectively (Launder et al., 1974). The terms on the right hand side represent, respectively, the turbulent transport, the shear production and the buoyancy production/destruction and the viscous dissipation. The Prandtl number is computed as in Hong et al. (2006b), depending on the height above the ground $z$, the PBL height $h$ and the state of the surface layer:

$$Pr = 1 + (Pr_0 - 1) \exp \left[ \frac{-3\,(z - 0.1h)^2}{h^2} \right] \tag{3.8}$$

where $Pr_0 = \phi_h / \phi_m + 0.68 v_k$, calculated using the similarity functions $\phi_i$ evaluated at the top of the surface layer, assumed 10% of the boundary layer height and $v_k = 0.4$ is the von Kármán constant. The PBL height is calculated, similarly to Nakanishi (2001), as the level at which the potential temperature first exceeds the minimum potential temperature within the boundary layer by 1.5 K. The similarity functions are defined as:

$$\phi_m = \begin{cases} 1 + 4.7 \frac{z}{L} & \text{if } \frac{z}{L} \geq 0 \\ \left(1 - 16 \frac{z}{L}\right)^{-1/4} & \text{if } \frac{z}{L} < 0 \end{cases} \tag{3.9a}$$

$$\phi_h = \begin{cases} 1 + 4.7 \frac{z}{L} & \text{if } \frac{z}{L} \geq 0 \\ \left(1 - 16 \frac{z}{L}\right)^{-1/2} & \text{if } \frac{z}{L} < 0 \end{cases} \tag{3.9b}$$

where $L$ is the Obukhov length (Monin et al., 1954).

### 3.2.2 The correction term for the $\varepsilon$ equation

The standard $K - \varepsilon$ model does not work well for flows with large mean shear, spreading of jets, or rotating turbulence (Shih et al., 1995). In fact, several terms in the exact dissipation rate equation are unknown. For this reason, the dissipation equation (Eq. 3.7) was created with a similar structure as the TKE equation, by assuming that the source and sink terms of the dissipation rate are proportional to the source and sink terms of TKE times the large eddy turnover timescale $K/\varepsilon$. To improve the standard model for the stable atmosphere, Zeng et al. (2020b) introduced an additional source term $A_\varepsilon$ in the buoyancy term of the dissipation

equation, to represent the dependence of energy drain on the eddy scale:

$$A_\varepsilon = c_4 \min\left(1, \sqrt{\frac{Ri}{c_5}}\right) N\varepsilon, \tag{3.10}$$

where $Ri$ is the gradient Richardson number $Ri = \frac{g}{\Theta_0}\frac{\partial\Theta/\partial z}{(\partial U/\partial z)^2+(\partial V/\partial z)^2}$, $N$ is the Brunt-Väisälä frequency $N = \left(\frac{g}{\Theta_0}\frac{\partial\Theta}{\partial z}\right)^{1/2}$, while $c_4$ and $c_5$ are chosen to be consistent with the Monin-Obukhov similarity theory (MOST), and set equal to 0.44 and 0.8, respectively. This additional term acts only in case of stable atmosphere (i.e. when the Richardson number is greater than zero, then in the CBL it is non-zero only in the capping inversion layer).

### 3.2.3 The Counter-Gradient Heat Flux

Deardorff (1966) highlighted the need of considering a non-local term into the vertical heat flux parameterization, in order to take into account large eddies and surface-driven motions in unstable conditions. It allows a vertical transport of heat upward without a superadiabatic lapse rate. The counter-gradient enters in the vertical heat flux. It now reads:

$$\overline{w\theta} = -\nu_H\left(\frac{\partial\Theta}{\partial z} - \gamma\right) \tag{3.11}$$

and $\gamma$ is parameterized following Troen et al. (1986):

$$\gamma = C\frac{\overline{w\theta}_s}{w_\star h} \tag{3.12}$$

where $C = 10$, $\overline{w\theta}_s$ is the surface heat flux, and $w_\star = \left(g/\Theta_0\overline{w\theta}_s h\right)^{1/3}$ is the convective velocity scale. The above mentioned counter-gradient is largely adopted in state-of-the-art PBL parameterizations, demonstrating its ability in reducing instabilities and in better describing the vertical temperature profile (Ching et al., 2014).

### 3.2.4 The temperature variance equation

The counter-gradient term does not act in stably stratified regimes, when turbulence production has actually been observed (Mauritsen et al., 2007) and parameterized (Zilitinkevich et al., 2013; Zilitinkevich et al., 2007). So, its efficiency is limited only to unstable regimes only; therefore for stable regimes an additional term should be considered. Standard models usually assume a critical Richardson number ($\sim 0.25$) above which turbulence is completely damped. In order to consider even turbulence in stably stratified regimes, similarly to Lazeroms et al. (2016) and Želi et al. (2019), besides the prognostic equations for $K$ ( Eq. 3.4) and $\varepsilon$ (Eq. 3.7), we added a prognostic equation for the half of the temperature variance ($K_\theta = \frac{1}{2}\overline{\theta^2}$), that reads:

$$\frac{\partial K_\theta}{\partial t} = -\frac{\partial\overline{wK_\theta}}{\partial z} - \overline{w\theta}\frac{\partial\Theta}{\partial z} - \varepsilon_\theta \tag{3.13}$$

where the terms on the right hand side represent the turbulent transport, the production/destruction by buoyancy and the dissipation, respectively. The dissipation term is parameterized as:

$$\varepsilon_\theta = \frac{K_\theta}{\tau R} = \frac{K_\theta}{KR}\varepsilon \tag{3.14}$$

where $\tau = \frac{K}{\varepsilon}$ is the turbulence time scale and

$$R = \frac{2}{3\left(1+\frac{\overline{w\theta}^2}{KK_\theta}\right)} \tag{3.15}$$

as described in Craft et al. (1996).

$K_\theta$ is proportional to the turbulent potential energy (TPE), that is defined as:

$$TPE = \frac{1}{2}\frac{g}{\Theta_0}\frac{\overline{\theta^2}}{\frac{\partial\Theta}{\partial z}} \tag{3.16}$$

The main idea of adopting a prognostic equation for $K_\theta$ (or TPE) is the conversion between TKE and TPE depending on the vertical stratification. $K_\theta$ acts both in stable and in unstable boundary layers, as a counter-gradient in analogy to the $\gamma$ term introduced above. In particular, it enters in the computation of the vertical heat flux, which now is calculated as (Lazeroms et al., 2016):

$$\overline{w\theta} = -\nu_H\frac{\partial\Theta}{\partial z} + \Phi_{cg} \tag{3.17}$$

where:

$$\Phi_{cg} = c_\mu\frac{g}{\Theta_0}\frac{KK_\theta}{\varepsilon} \tag{3.18}$$

Its effect is larger in areas with large temperature fluctuations (i.e. large $K_\theta$), thus in the surface layer and in the inversion layer, where temperature gradients are stronger than in the other regions. $\Phi_{cg}$ replaces the counter-gradient term of Eq. 3.12. While $\gamma$ is null for stable regimes, $\Phi_{cg} > 0$.

### 3.2.5 The numerical solver

Equations for wind speed, potential temperature, and water vapor mixing ratio are solved implicitly, using the tridiagonal matrix algorithm, adding source and sink terms at the surface (as explained later). For the coupled equations of $K$ and $\varepsilon$, a more complex method is needed, since the strong nonlinearities may interact with discretization errors in such a way to destabilize computation (Lew et al., 2001).

Substituting the flux-gradient relation into the respective fluxes (Eq. 3.2), and neglecting the first temporal step the of diffusion term (first term on the right hand side of Eq. 3.4 and 3.7) and the counter-gradient term (Eq. 3.12 or 3.18), which will be added later, since it is always stable using the tridiagonal matrix, we obtain:

$$\frac{\partial K}{\partial t} = c_\mu(S^2 - \frac{N^2}{Pr})\frac{K^2}{\varepsilon} - \varepsilon \tag{3.19a}$$

$$\frac{\partial \varepsilon}{\partial t} = c_\mu \left( c_1 S^2 - c_3 \frac{N^2}{Pr} \right) K - c_2 \frac{\varepsilon^2}{K} \tag{3.19b}$$

where $S^2 = \left(\frac{\partial U}{\partial z}\right)^2 + \left(\frac{\partial V}{\partial z}\right)^2$ is the wind shear and $N^2$ the squared the Brunt-Väisälä frequency.

Introducing the new variables $X = \frac{K}{\varepsilon}$ and $Y = \varepsilon^\alpha K^\beta$, and differentiating opportunely, we obtain a set of two decoupled equations:

$$\frac{\partial X}{\partial t} = -CX^2 + (c_2 - 1) \tag{3.20a}$$

$$\frac{\partial \ln Y}{\partial t} = (\alpha A + \beta B) X - (\alpha + \beta c_2) \frac{1}{X} \tag{3.20b}$$

with

$$A = c_\mu (S^2 - \frac{N^2}{Pr}), \tag{3.21}$$

$$B = c_\mu (c_1 S^2 - c_3 \frac{N^2}{Pr}) \tag{3.22}$$

and

$$C = B - A = c_\mu \left[ (c_1 - 1) S^2 - (c_3 - 1) \frac{N^2}{Pr} \right] \tag{3.23}$$

. $C$ can be either positive or negative, depending on the sign and the magnitude of buoyancy. This set of equations has an analytical solution. $X$ has three possible solutions, depending on the sign of C. For C = 0 the solution is simple:

$$X^{n+1} = X^n + (c_2 - 1)\,\Delta t$$

For $C > 0$:

$$X^{n+1} = \frac{\tanh\left( \operatorname{atanh}\left( \frac{\sqrt{C} X^n}{\sqrt{c_2 - 1}} \right) + \sqrt{C}\,\Delta t \sqrt{c_2 - 1} \right) \sqrt{c_2 - 1}}{\sqrt{C}}$$

For $C < 0$:

$$X^{n+1} = -\frac{\sqrt{1 - c_2} \left( \tan\left( \sqrt{-C}\,\Delta t \sqrt{1 - c_2} \right) \sqrt{1 - c_2} - \sqrt{-C}\,\Delta t \right)}{\sqrt{-C} \left( \sqrt{1 - c_2} + \sqrt{-C} X^n \tan\left( \sqrt{-C}\,\Delta t \sqrt{1 - c_2} \right) \right)}$$

while for $Y$ the solution is obtained, assuming $\alpha = 1$ and $\beta = -1/c_2$, by eliminating the second term in Eq. 3.20b which can contribute to numerical instabilities:

$$\varphi^{n+1} = \varphi^n \exp\left[ \Delta t\, X^{n+1} \left( A - \frac{B}{c_2} \right) \right]$$

After solving these coupled equations, $K$ and $\varepsilon$ are calculated inverting $X$ and $Y$, and then diffusion terms (first term of the r.h.s. of Eq. 3.4 and Eq. 3.7) are added to both variables.
The analytical solution has the advantage of being stable for every time-step $\Delta t$ and is not affected by numerical approximations errors.

The equation for $K_\theta$ (Eq. 3.13) is solved separately from the $K-\varepsilon$ system of equations. Expliciting all the terms, the equation for temperature variance reads :

$$\frac{\partial K_\theta}{\partial t} = +\frac{\partial}{\partial z}\left(\nu_M \frac{\partial K_\theta}{\partial z}\right) + \nu_H \left(\frac{\partial \Theta}{\partial z}\right)^2 - c_\mu \frac{g}{\Theta_0}\frac{K K_\theta}{\varepsilon}\frac{\partial \Theta}{\partial z} - \frac{K_\theta \varepsilon}{R K} \tag{3.24}$$

This equation can be solved by applying the Thomas' tridiagonal algorithm (Lee, 2011) for the diffusion part, and treating explicitly the second term on the right-hand side, while the other two are treated implicitly since they depend on $K_\theta$.
Similar to the Troen et al. (1986) counter gradient, $\Phi_{cg}$ enters both in the computation of the vertical heat flux term and in the prognostic equations for potential temperature and for the vertical heat flux. The equation for potential temperature becomes:

$$\frac{\partial \Theta}{\partial t} = \frac{\partial}{\partial z}\left(\nu_M \frac{\partial \Theta}{\partial z}\right) - \frac{\partial \Phi_{cg}}{\partial z} \tag{3.25}$$

### 3.2.6 Boundary and Initial conditions

Regarding initial conditions for the simulations, we set the values $K_0 = 10^{-4}$ m$^2$s$^{-2}$, $\varepsilon_0 = 10^{-7}$ m$^2$s$^{-3}$ and $K_{\theta 0} = 10^{-7}$ °C for all the column of air. As boundary conditions, we set $k_{TOP} = \varepsilon_{TOP} = K_{\theta TOP} = 0$ at the top of the domain of simulation. On the other hand, at the surface, we use a mix of Neumann and Dirichlet boundary conditions. For $U$, $V$ and $\Theta$ we assume Neumann boundary conditions:

$$\frac{\partial U_1}{\partial t} = -\frac{u_\star^2}{\Delta z_1 |U_{TOT}|} U_1 \tag{3.26a}$$

$$\frac{\partial V_1}{\partial t} = -\frac{u_\star^2}{\Delta z_1 |U_{TOT}|} V_1 \tag{3.26b}$$

$$\frac{\partial \Theta_1}{\partial t} = \frac{\overline{w\theta}_s}{\Delta z_1} \tag{3.26c}$$

where the subscript "1" refers to the variable calculated at the center of the first grid cell close to the surface, $u_\star$ is the friction velocity and $\Delta z_1$ is the height of the first level. For $K$ and $\varepsilon$, we assume Dirichlet boundary condition, adopting MOST (Hartogensis et al., 2005; van der Laan et al., 2017):

$$k_1 = \frac{u_\star^2}{\sqrt{c_\mu}} \sqrt{\frac{\phi_\varepsilon}{\phi_m}} \tag{3.27a}$$

$$\varepsilon_1 = \frac{u_\star^3}{\nu_k \frac{\Delta z_1}{2}} \phi_\varepsilon \tag{3.27b}$$

where:

$$\phi_\varepsilon = \begin{cases} \left(1 + 2.5\left(\frac{z}{L}\right)^{0.6}\right)^{3/2} & \text{if } \frac{z}{L} \geq 0 \\ 1 - \frac{z}{L} & \text{if } \frac{z}{L} < 0 \end{cases} \tag{3.28}$$

For $K_\theta$, we assume again Neumann boundary conditions, employing in Eq. 3.13 the boundary conditions in Eq. 3.26c, 3.27a and 3.27b.

| | PBL type | $dT_S/dt$ $(K/h)$ | $d\Theta_0/dz$ $(K/km)$ | Terrain | $U_g$ $(m/s)$ | $V_g$ $(m/s)$ | Domain Size $(m \times km \times km)$ |
|---|---|---|---|---|---|---|---|
| CBL_F_3 | Convective | 3.5 | 3.3 | Flat | 0 | 10 | $10 \times 10 \times 3$ |
| CBL_F_10 | Convective | 3.5 | 10 | Flat | 0 | 10 | $10 \times 10 \times 3$ |
| CBL_V_NOW | Convective | 3.5 | 3.3 | Valley | 0 | 0 | $40 \times 10 \times 5$ |
| CBL_V_W | Convective | 3.5 | 3.3 | Valley | 0 | 10 | $40 \times 10 \times 5$ |
| GABLS | Stable | -0.25 | 10 | Flat | 8 | 0 | $0.4 \times 0.4 \times 0.4$ |

**Table 3.1:** Schematic overview of the different case studies

## 3.3 Setup and case studies

In this study the Advanced Research version of the Weather Research and Forecasting model (WRF) version 4.1 is used for the numerical simulations (Skamarock et al., 2019). WRF has been successfully applied in several studies for idealized cases for both RANS simulations and large-eddy simulations (LES), in flat terrain (Moeng et al., 2007; Zhang et al., 2018) and complex terrain (Schmidli et al., 2011; Wagner et al., 2014). The third-order Runge-Kutta is used for time integration for all simulations in this study. In LES mode, we use the 1.5-order 3DTKE model for the sub-grid turbulence parameterization (Deardorff, 1980). We take a three-dimensional average of 20 different LES, differing in the random potential temperature perturbations of 0.1 K amplitude and zero mean, applied at the first four vertical layers, necessary to trigger turbulence at the initial time-step (Beare et al., 2006). LES is considered as our reference for each case analyzed, and is compared with RANS simulations performed with the novel $K-\varepsilon$ schemes presented here, which have been implemented in the WRF model, and with other conventional 1D PBL schemes already implemented in the standard version of the WRF model. These PBL schemes are the BouLac (Bougeault et al., 1989), the Mellor-Yamada-Nakanishi-Niino level 2.5 (MYNN2.5, Nakanishi et al., 2004) and the Yonsei University (YSU, Hong et al., 2006b) schemes. All simulations are performed with a time step of 0.2 s, for a 4-h period. Lateral boundary conditions in both W-E and S-N directions are periodic, allowing to replicate an infinite domain. The results from the different RANS simulations are compared with the LES considering the hourly average values computed on all the time-steps between the third and the fourth hour of simulation. Similarly, simulation outputs are averaged horizontally, in order to compare model results on a single column value for the flat cases (average in both horizontal directions) and on a cross-valley section for the valley cases (average along the south-north direction). All simulations are performed for a dry atmosphere, with zero humidity both in the air and in the soil. In this study, five different cases (summarized in Tab. 3.1) are considered, varying in thermal stratification, surface temperature forcing, orography, and geostrophic wind. In Section 3.4 we will present the comparison, for the five case studies, between each reference LES, the aforementioned conventional PBL schemes, and two different flavor of the $K-\varepsilon$ closure: the first experiment ($K-\varepsilon-\gamma$ hereafter) assuming a constant counter-gradient term, calculated as in Eq. 3.12, and the second experiment ($K-\varepsilon-\theta^2$ hereafter), in which the equation for the temperature variance is calculated from Eq. 3.13 and the

counter-gradient term is computed using Eq. 3.18. Moreover, in the stable case (called GABLS hereafter), we run the $K-\varepsilon-\theta^2$ closure removing the additional term in the buoyancy production into the dissipation equation (Eq. 3.10), in order to evaluate its contribution in improving the reproduction of the PBL in stable regimes ($K-\varepsilon-\theta^2-NOA_\varepsilon$ hereafter).

### 3.3.1 CBL on flat terrain

We assume a homogeneous terrain and a PBL in convective conditions, similar to Zhang et al. (2018). The simulation is performed over a 10 km $\times$ 10 km domain with a horizontal grid size of 50 m and 1 km for LES and RANS simulations, respectively. The model top is at 3 km with 150 equally spaced vertical layers (i.e. the depth of each layer is 20 m). The CBL is driven by a surface heating rate of 3.5 K h$^{-1}$, with an initial surface skin temperature of 300 K, and geostrophic wind in the N-S direction of 10 m s$^{-1}$, constant along the vertical, with Coriolis forcing turned off. We tested two cases, differing in the intensity of the unperturbed thermal stratification. The initial potential temperature sounding is:

$$\theta = \begin{cases} 300 & \text{if } z \leq 100 \text{ m} \\ 300 + (z - 100m) \cdot \Gamma & \text{if } z > 100 \text{ m} \end{cases} \tag{3.29}$$

With $\Gamma$ = 3.3 K km$^{-1}$ for the weakly stable case (CBL_F_3 hereafter), and $\Gamma$ = 10 K km$^{-1}$ for the very stable case (CBL_F_10 hereafter).

### 3.3.2 CBL in an idealized valley

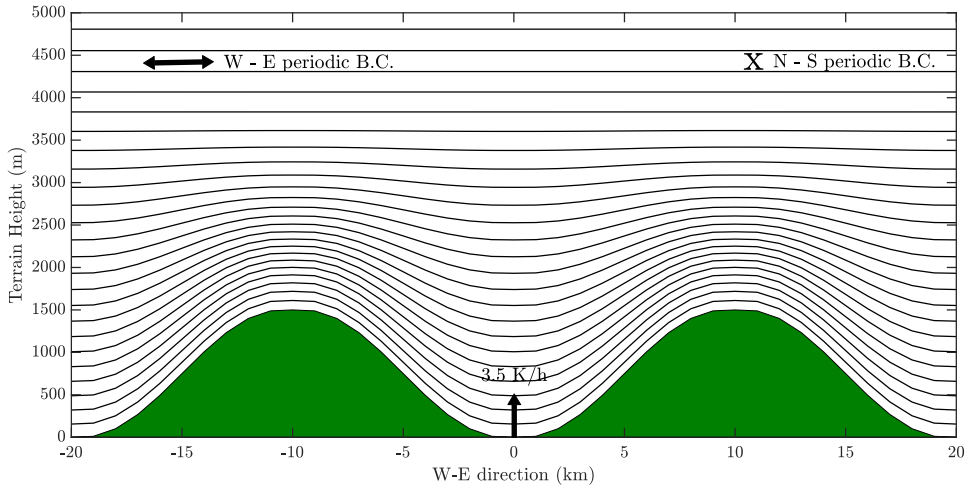


**Figure 3.1:** Design of the domain, forcing, and boundary conditions for the valley cases. Vertical layers are plotted by multiples of ten.

Here we consider a W-E symmetric valley, infinite in the S-N direction, with sidewall crests at 1500 m. The analytical expression for the topography, identical to the one used in Schmidli

et al. (2011), is given by:

$$h(x) = 1500 \times \begin{cases} \frac{1}{2} - \frac{1}{2}\cos\left(\pi \frac{|x|-X_1}{S_x}\right) & X_1 < |x| < X_2 \\ 1 & X_2 < |x| < X_3 \\ \frac{1}{2} + \frac{1}{2}\cos\left(\pi \frac{|x|-X_3}{S_x}\right) & X_3 < |x| < X_4 \end{cases} \tag{3.30}$$

with sloping sidewall width $S_x = 9$ km, $X_1 = 0.5$ km, $X_2 = 9.5$ km, $X_3 = 10.5$ km and $X_4 = 19.5$ km. Simulations are performed over a 40 km $\times$10 km domain, to suite a coherent reproduction of the cross-valley circulation for RANS, with a horizontal grid size of 50 m and 1 km for LES and RANS simulations, respectively, as in the flat case. The model top is at 5 km with 250 hybrid sigma–pressure vertical layers. Hybrid levels are chosen in order to reduce upper-level disturbances which, in terrain-following coordinates, can be produced by the advection of strong horizontal flow perturbed by the terrain influence (Park et al., 2019). The CBL is driven by a surface heating rate of 3.5 K h$^{-1}$ and the initial surface skin temperature is 300 K at the valley floor, increasing as the lapse rate ($\Gamma$ = 3.3 K km$^{-1}$) with increasing height. The initial vertical temperature profile is the same as the CBL_F_3 case. We test two different cases for the valley configuration: one with null initial geostrophic wind (CBL_V_NOW hereafter), and one with a constant geostrophic wind of 10 m s$^{-1}$ in the N-S direction (CBL_V_W hereafter). This wind is imposed in the initial conditions with the aim of reproducing an along valley wind, usually present in Foehn wind conditions or with the development of thermally-driven circulations, and deeply studied through observations (Giovannini et al., 2017) and numerical simulations (Rampanelli et al., 2004). The design of the idealized simulations in the valley case is reported in Fig. 3.1. In this case, LES results are averaged on a W-E section of the valley, using the RANS grid as query grid.

### 3.3.3 SBL in flat terrain

This case is based on the simulations of an Arctic SBL (GEWEX Atmospheric Boundary Layer Study, (GABLS)) presented in Kosović et al. (2000), and subsequently used for the intercomparison of LES (Beare et al., 2006) and RANS (Cuxart et al., 2006) simulations, aiming to quantify the reliability of different PBL schemes through the comparison with observational data. The initial potential temperature profile consists of a mixed layer up to 100 m with a potential temperature of 265 K, with an overlying inversion of 10 K km$^{-1}$. A surface cooling rate of 0.25 K h$^{-1}$ is applied for 9 hours, so a quasi-equilibrium state is reached. The geostrophic wind is set to 8 m s$^{-1}$ in the W-E direction, with a Coriolis parameter of $1.39 \cdot 10^{-4}$s$^{-1}$. For this case study, we take as reference the LES presented in Beare et al. (2006) at 3.125 m vertical and horizontal resolution (namely CORA, CSU, IMUK, LLNL, NCAR, NERSC, UIB in Beare et al. (2006)). They are produced by different NWP models and adopt various sub-grid turbulence closures. The simulation domain is a box of 400 m $\times$ 400 m $\times$ 400 m, and simulations outputs are averaged spatially over the horizontal domain and temporally between the eighth and ninth hours of the simulation. RANS instead are run on a 10 km $\times$ 10 km horizontal domain; the top is set at 1 km above ground level, with a depth of 5 m for each vertical level.

### 3.3.4 Calculation of turbulent fluxes

Calculation of turbulent fluxes is performed differently for LES and RANS simulations. Turbulent fluxes for RANS simulations are computed in the same way for all turbulence parameterization schemes, through the tendency of each variable. If $C$ is a variable of the mean flow ($C = U, V, \Theta$) from Eqs. 3.1 it follows that, for each vertical layer:

$$\overline{wc}|_{n+1} - \overline{wc}|_n = -\int_n^{n+1} \frac{\partial C}{\partial t}\, dz \tag{3.31}$$

where we impose a null flux at the top of the domain, and surface fluxes as in Eqs. 3.26 for $n = 1$. On the other hand, vertical turbulent fluxes in LES consist on the sum of the resolved (RES) part and of the subgrid-scale (SGS) part:

$$\overline{wc} = \overline{wc}_{RES} + \overline{wc}_{SGS} \tag{3.32}$$

The RES part is calculated directly from the model output, for each time step, and then averaged temporally over one hour:

$$\overline{wc}_{RES} = \overline{(w - W)(c - C)} \tag{3.33}$$

while the SGS is calculated as:

$$\overline{wc}_{SGS} = -K_{CV} \frac{\partial C}{\partial z} \tag{3.34}$$

where $K_{CV}$ is the vertical diffusivity coefficient for the mean variable $C$. RANS turbulent fluxes are then averaged temporally over an hour , and spatially over the entire domain for the flat cases, and over a W-E section for the valley cases.

## 3.4 Results

This section presents the results of the comparison between the idealized RANS simulations with the different PBL schemes and the LES, for the different case studies shown in Tab. 3.1. In the following subsections (3.4.1, 3.4.2 and 3.4.3), we present the comparison between the different case studies, separating between CBL in flat terrain (CBL_F_3,CBL_F_10), CBL in an idealized valley (CBL_V_NOW,CBL_V_W) and SBL in flat terrain (GABLS).

### 3.4.1 CBL in flat terrain

Figure 3.2 shows the vertical profiles of wind speed (left) and potential temperature (right) for the CBL_F_3 case, considering the temporal average between the third and the fourth hour of time integration. The profile is typical of a CBL, with a surface boundary layer with a thickness of $\sim$ 150 m and a PBL height of $\sim$ 1500 m. The wind speed follows this pattern, approaching $\sim$10 m s$^{-1}$ over the PBL, remaining almost constant in the mixed layer and rapidly decreasing to $\sim$ 5 m s$^{-1}$ in the first vertical level. All RANS simulations reasonably agree with the LES in terms of potential temperature. In particular, $K - \varepsilon - \theta^2$ ouperforms the other schemes within the surface layer, while BouLac is the best in reproducing the capping inversion over the mixed layer. On the other hand, YSU overestimates the PBL height, while MYNN2.5 shows

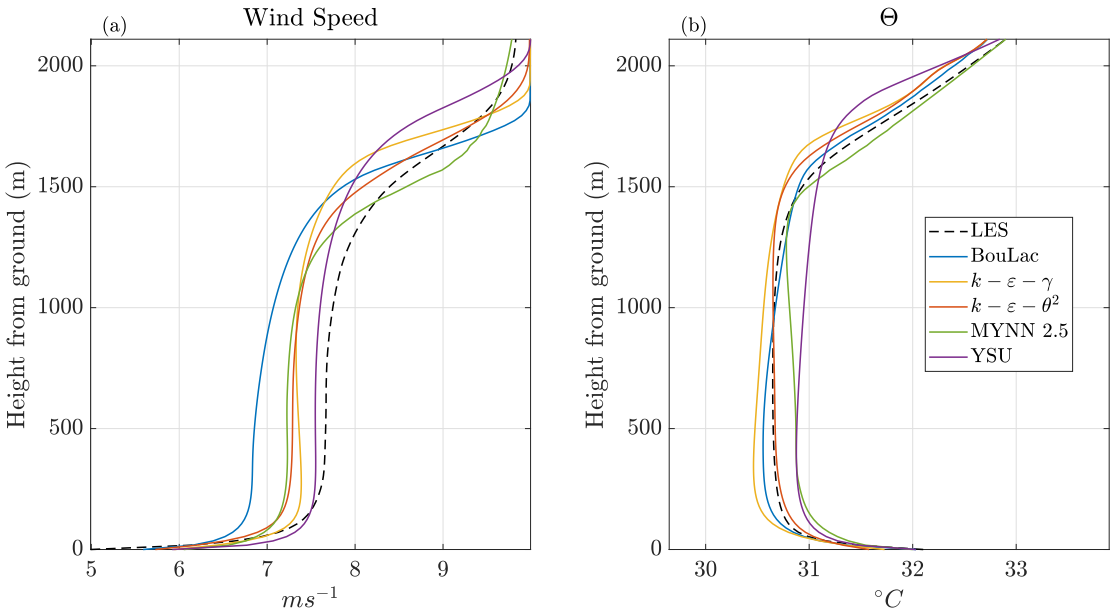


**Figure 3.2:** Vertical profiles of wind speed (left) and potential temperature (right) for the CBL_F_3 case. Dashed black line refers to the ensemble of LES simulations, while coloured lines refer to the different RANS simulations.

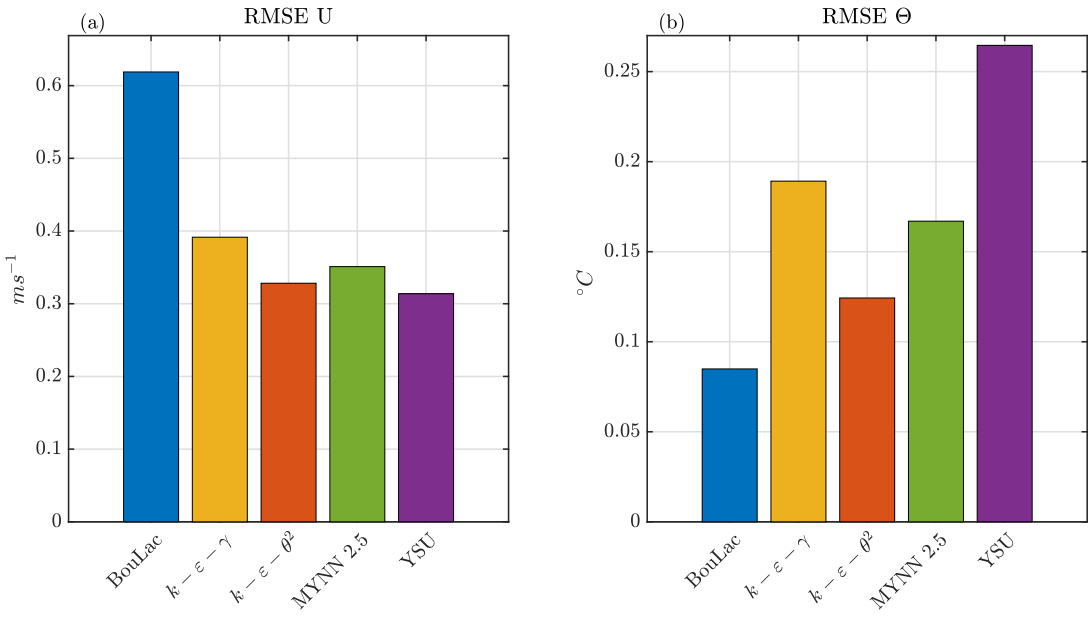


**Figure 3.3:** Root Mean Square Error (RMSE) for each RANS simulation with respect to the reference LES, calculated for an air column up to 2050 m above ground level for the CBL_F_3 case, for wind speed (left) and potential temperature (right).

a quasi-unstable boundary layer instead of a mixed layer. $K-\varepsilon-\gamma$ reasonably reproduces the mixed layer, but it overestimates the absolute value of the potential temperature gradient in the surface layer, and it slightly overestimates the PBL height. Regarding the wind speed profile, YSU is the best in reproducing the vertical profile within the surface and the mixed layer, but as for the potential temperature, the overestimation of the PBL height leads to an underestimation of wind speed at the capping layer. Despite a good performance in terms of

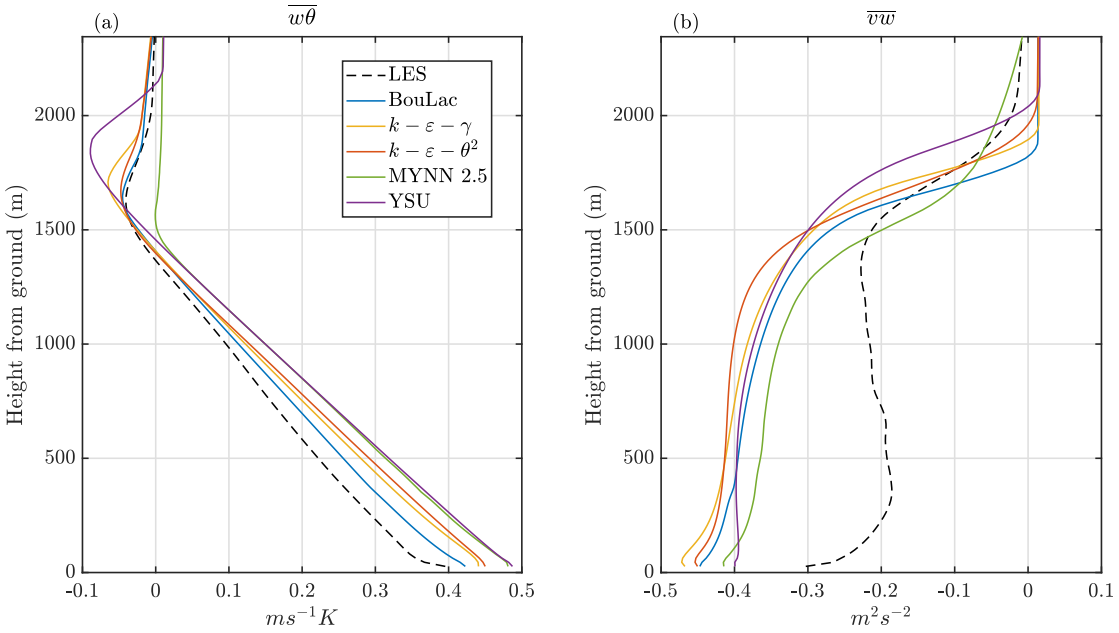


**Figure 3.4:** Vertical profiles of vertical heat flux (left) and vertical momentum flux (right) for the CBL_F_3 case. Dashed black line refers to the ensemble of LES simulations, while coloured lines refer to the different RANS simulations.

potential temperature, BouLac fails in reproducing the wind profile in the mixed layer, while MYNN2.5 underestimates the wind speed of the capping layer. $K-\varepsilon-\theta^2$, instead, performs similarly to MYNN2.5 in the mixed layer, but it is the best simulation in reproducing the wind shear in the capping layer. $K-\varepsilon-\gamma$ performs similarly to $K-\varepsilon-\theta^2$, but again overestimating the PBL height and then underestimating the wind speed in the capping layer.
In order to quantify the ability of the RANS simulations in reproducing the CBL, in Fig. 3.3 we show the Root Mean Square Error (RMSE), calculated along the air column, between each RANS simulation and the reference LES. All RANS simulations, apart from BouLac, where the error is twice as large as in the others, show an error of $\sim 0.35$ m s$^{-1}$ for the wind speed. On the other side, BouLac is the best in reproducing the potential temperature profile (RMSE $\sim 0.1$ °C), followed by $K-\varepsilon-\theta^2$ and MYNN2.5. The highest errors are shown by $K-\varepsilon-\gamma$ and YSU since they overestimate the height of the inversion layer.
Figure 3.4 reports the vertical profiles of vertical heat flux (left) and vertical momentum flux (right). $\overline{w\theta}$ is well reproduced by all the simulations, up to the inversion layer. Here, BouLac and $K-\varepsilon-\theta^2$ better reproduce the negative peak in the inversion layer with respect to the others. On the other side, all RANS simulations overestimate the intensity of $\overline{vw}$ in the surface and mixed layer while, above the top of the PBL, the two $K-\varepsilon$ turbulence closures are the best in reproducing the decrease of the vertical momentum flux, showing a better agreement in terms of slope and height.

Figure 3.5 shows the vertical profiles of wind speed (left) and potential temperature (right) for the CBL_F_10 case. This case differs from the previous one only in the vertical temperature gradient, which is now set to 10 K km$^{-1}$. Due to this stronger stratification, the PBL height reaches $\sim 800$ m, with a less unstable surface layer with respect to the previous case. While there are no relevant differences in the surface layer, in the mixed layer, and in the entrainment

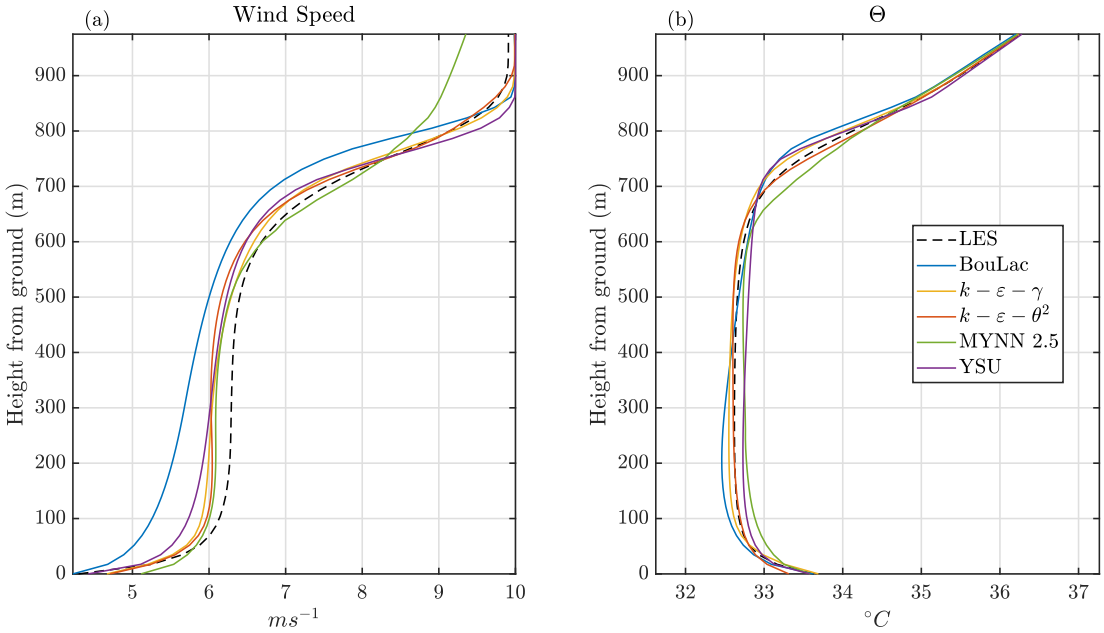


**Figure 3.5:** Vertical profiles of wind speed (left) and potential temperature (right) for the CBL_F_10 case. Dashed black line refers to the ensemble of LES simulations, while coloured lines refer to the different RANS simulations.

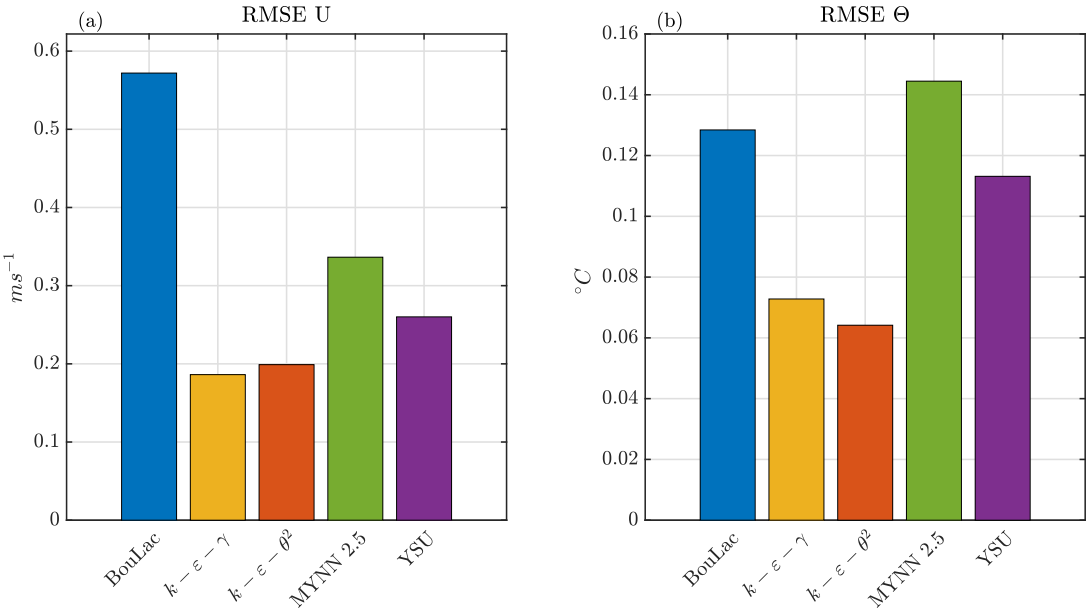


**Figure 3.6:** Root Mean Square Error (RMSE) for each RANS simulation with respect to the reference LES, calculated for an air column up to 1000 m for the CBL_F_10 case, for wind speed (left) and potential temperature (right).

zone, $K-\varepsilon-\theta^2$ provides the best simulation of the temperature profile, followed by $K-\varepsilon-\gamma$. On the other hand, YSU and BouLac overestimate and MYNN2.5 underestimates the inversion layer height. Improvements by the $K-\varepsilon$ schemes are found even reproducing the wind speed, where better results occur again at the capping layer level. Again, BouLac shows a too low wind speed in the mixed layer, while MYNN2.5 over the capping layer. RMSEs (Fig. 3.6) show indeed the lowest values for the two $K-\varepsilon$ flavors, even half with respect to the other

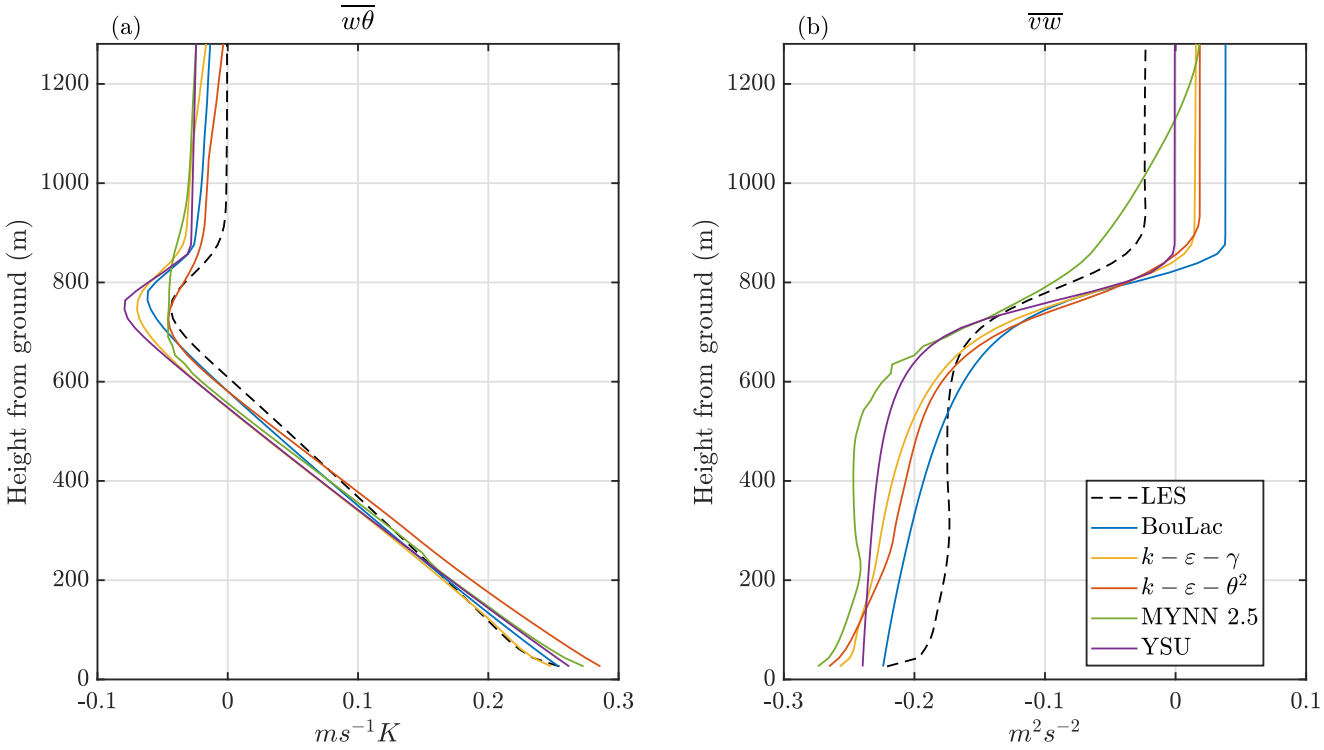


**Figure 3.7:** Vertical profiles of vertical heat flux (left) and vertical momentum flux (right) for the CBL_F_10 case. Dashed black line refers to the ensemble of LES simulations, while coloured lines refer to the different RANS simulations.

RANS simulations for the potential temperature. They are followed by YSU, while MYNN and BouLac are the worst since they cannot capture precisely the capping layer height. Even for the turbulent fluxes (Fig. 3.7), better results are found for $K-\varepsilon-\theta^2$: while in the surface and mixed layers it is not possible to identify particular differences between the different RANS simulations, at the inversion layer the new turbulence scheme can better reproduce the negative peak of the vertical heat flux (left) and the slope of the vertical momentum flux (right).

### 3.4.2 CBL in an idealized valley

In this subsection, the results from the simulations for the idealized valley are presented. Figure 3.8 shows the cross-valley section of zonal wind (left), potential temperature (center), and meridional wind (right) averaged along the N-S direction and from the third to the fourth hour of simulation for the CBL_V_W case study for the reference ensemble of LES (CBL_V_NOW shows similar patterns for $U$ and $\Theta$). A cross valley circulation is well distinguishable from the zonal wind speed map, with two cross-valley circulation cells on top of each other, similar to those identified in Wagner et al. (2014). Upslope winds are weaker on the part of the slopes close to the valley floor, and they reach a maximum value of $\sim 4$ ms$^{-1}$ close to the ridge. A return flow towards the center of the valley is evident between 1500 and 2500 m: warmer air is advected from the ridge top to the center of the valley, despite the presence of an underlying smaller thermal convective cell, in analogy with what is found in Serafin et al. (2010). Because of this return flow, the temperature profile shows a double mixed layer, one just over the surface layer, and the second at the level of the return-flow layer. The presence of upslope

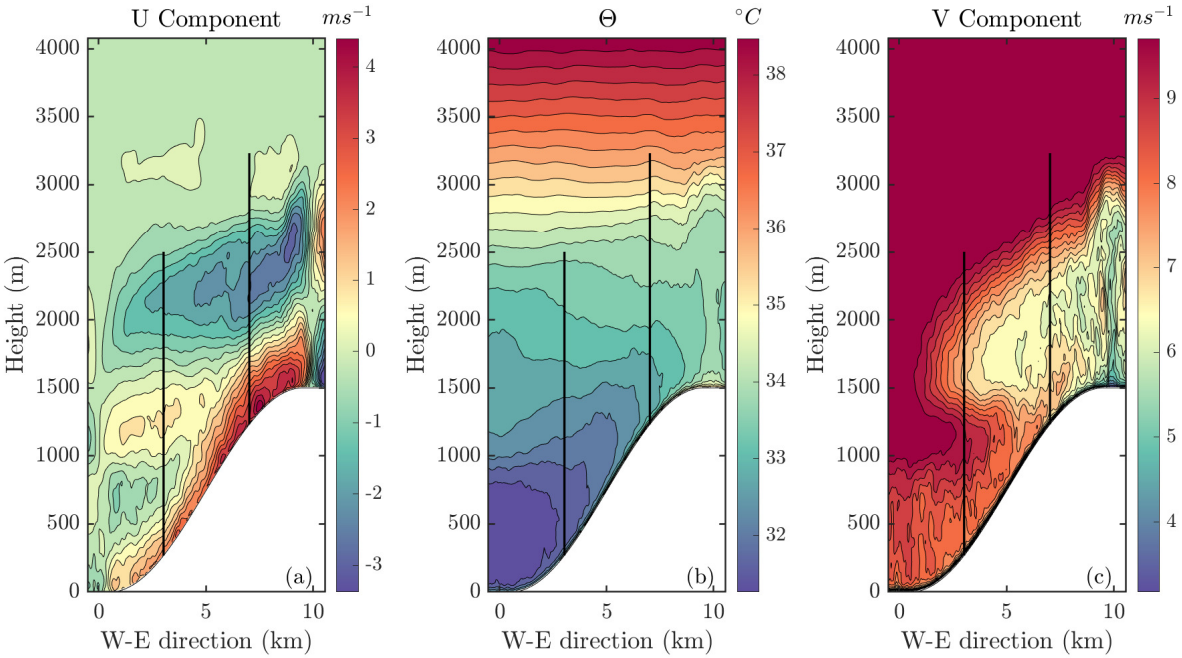


**Figure 3.8:** Zonal section of zonal wind speed (left), potential temperature (center) and meridional wind speed (right), for the ensemble LES of the CBL_V_W case study. Vertical black lines refer to the position of vertical profiles shown in Figs. 3.9 and 3.12 for the lower point, and in Figs. 3.10 and 3.13 for the upper point along the slope.

circulations along the ridges increases the wind shear, decreasing the meridional wind speed through increased turbulence production. Indeed, the vertical profile of meridional wind speed (right panel of Fig. 3.8) is not constant along the valley slope, but it is influenced by the branch of the upslope circulation pointing towards the center of the valley. As a consequence, above the ridge level, the meridional wind speed is lower.

Figure 3.9 shows the vertical profiles of zonal wind speed (left) and potential temperature (right) for a point along the eastern slope situated at 267 m above the valley floor. The zonal wind speed presents four different peaks, with the lowest and the highest more intense than the other two in absolute value, representing the two convective cells described before (negative values represent air moving from the ridge to the valley center). All RANS simulations are able to capture the double circulation along the vertical, but with some errors. In particular, YSU overestimates the height of the three upper peaks, BouLac and MYNN2.5 overestimates the third peak, while the two $K-\varepsilon$ underestimate the second and the fourth peak, but they are the best in reproducing the third peak.

Regarding the potential temperature profile, the two $K-\varepsilon$ flavors better describe the surface layer and the lower mixed layer and inversion, while the others cannot capture correctly the height of the lower inversion (BouLac and MYNN2.5) or its gradient is too low (YSU). All RANS simulations can capture the higher mixed layer above the ridge level, with a better performance of the two $K-\varepsilon$, both in terms of depth and absolute value.

Figure 3.10 shows the vertical profiles of zonal wind speed (left) and potential temperature (right) for a point along the eastern slope situated at 1232 m above the valley floor, i.e. where only the upper cell is present. For this reason, zonal wind vertical profiles display just the peak

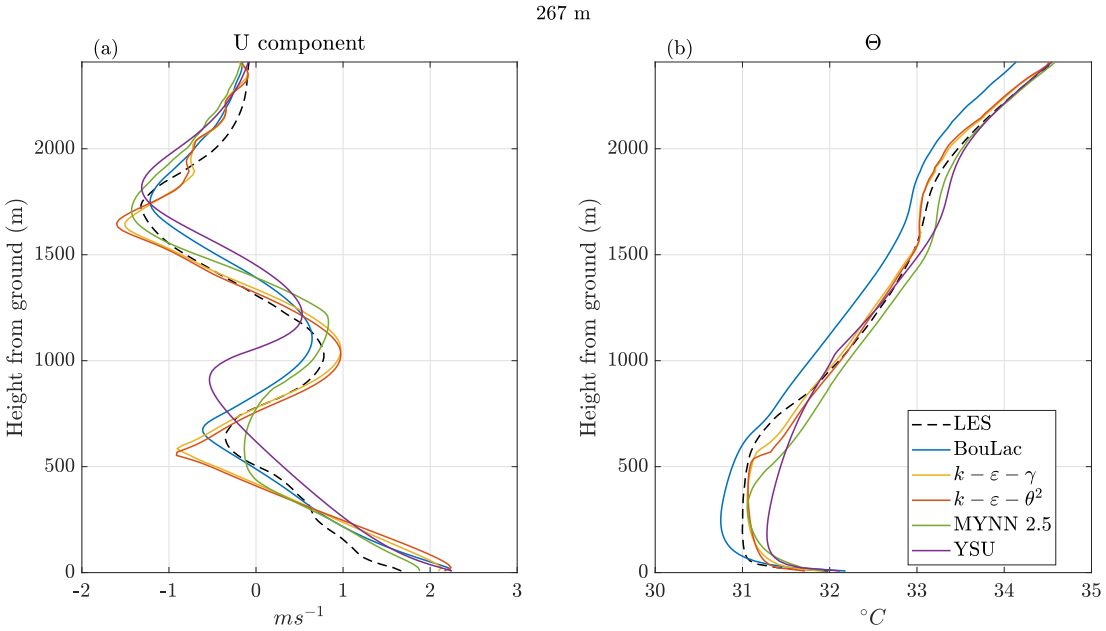


**Figure 3.9:** Vertical profiles of zonal wind speed (left) and potential temperature (right) for the CBL_V_NOW case for a point situated at 267 above the valley floor on the eastern slope. Dashed black line refers to the ensemble of LES simulations, while coloured lines refer to the different RANS simulations.

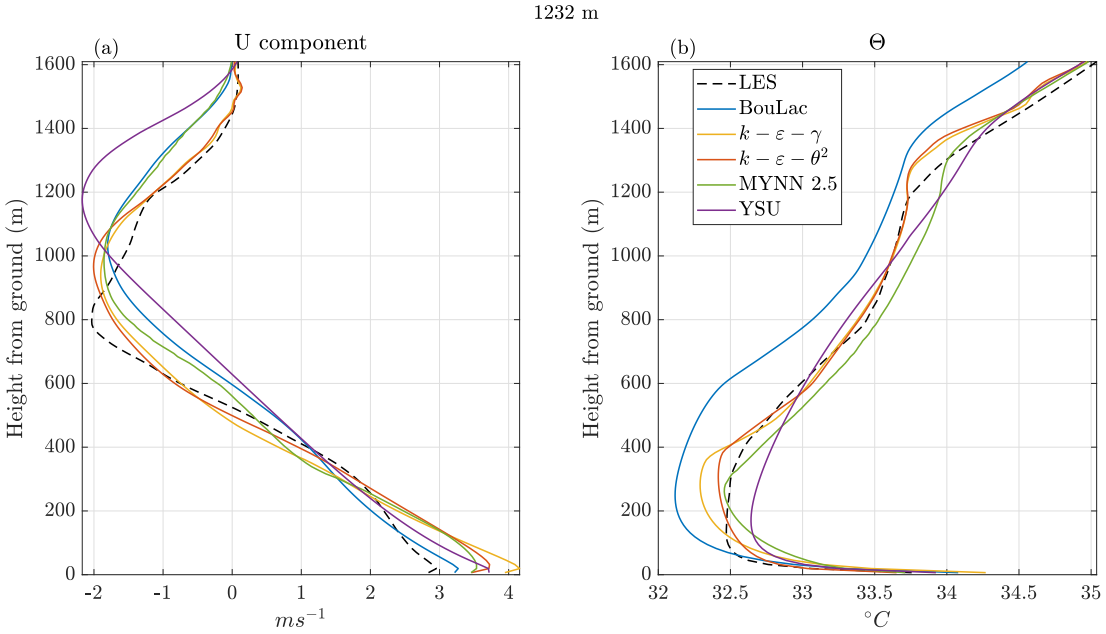


**Figure 3.10:** Vertical profiles of zonal wind speed (left) and potential temperature (right) for the CBL_V_NOW case for a point situated at 1232 m above the valley floor on the eastern slope. Dashed black line refers to the ensemble of LES simulations, while coloured lines refer to the different RANS simulations.

close to the surface and the peak of the return wind above the ridge level (around 800 m above ground level). All RANS simulations capture the cell circulation, but they all overestimate the height of the second peak (in particular YSU). However, the two $K-\varepsilon$ experiments are the ones that get closer in representing the peak, and can better capture the decrease of wind speed with height (especially from 1200 to 1600 m above ground level). The two $K-\varepsilon$ display

better results considering especially the vertical profile of potential temperature (right panel of Fig. 3.10). In particular, $K-\varepsilon-\theta^2$ shows a better agreement for all the air column with respect to the other RANS simulations. BouLac always underestimates the potential temperature, MYNN2.5 often displays an overestimation, while YSU underestimates the depth of both the mixed layers.

In order to quantify the ability of each RANS simulation to reproduce the thermal circulation

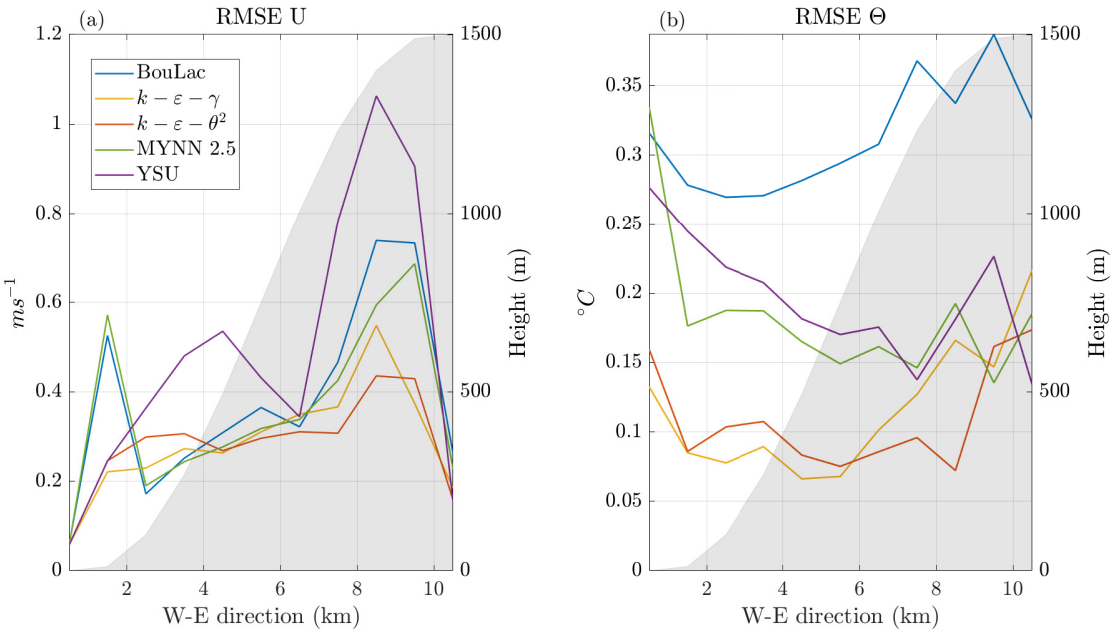


**Figure 3.11:** RMSEs of zonal wind speed (left) and potential temperature (right) with respect to LES, calculated as the average of the first 170 vertical levels for each point from the valley floor to the eastern ridge, for the CBL_V_NOW case for each RANS simulation. The gray area represents the height a.s.l. along the W-E direction.

of the CBL_V_NOW case study, in Fig. 3.11 we show the RMSE, calculated along the first 170 vertical levels, of zonal wind speed (left) and potential temperature (right) along the eastern slope of the valley. In general, the highest errors for zonal wind are located in the parts of the slope close to the valley floor and close to the ridge, while they are really low where the wind tends to zero, i.e. in the valley floor and above the ridge. The lowest errors occurs for $K-\varepsilon-\theta^2$, always between 0.2 and 0.4 m s$^{-1}$ in the central part of the slope. YSU is the worst in representing the wind profile in the highest part of the valley (errors up to 1 m s$^{-1}$), while BouLac and MYNN2.5 present the highest errors in the lower part of the valley (up to 0.6 m s$^{-1}$).

Regarding the RMSE for potential temperature, again $K-\varepsilon$ simulations show the best agreement with respect to the LES, especially in the lower part of the valley, followed by MYNN2.5 and YSU. BouLac is constantly the worst in terms of potential temperature, due to its constant underestimation over all the vertical column. While $K-\varepsilon$ simulations maintain a constant value of the RMSE along the slope, YSU and MYNN2.5 errors increase approaching the valley floor. For all RANS simulations, the highest RMSEs are found at the valley floor and at the ridge.

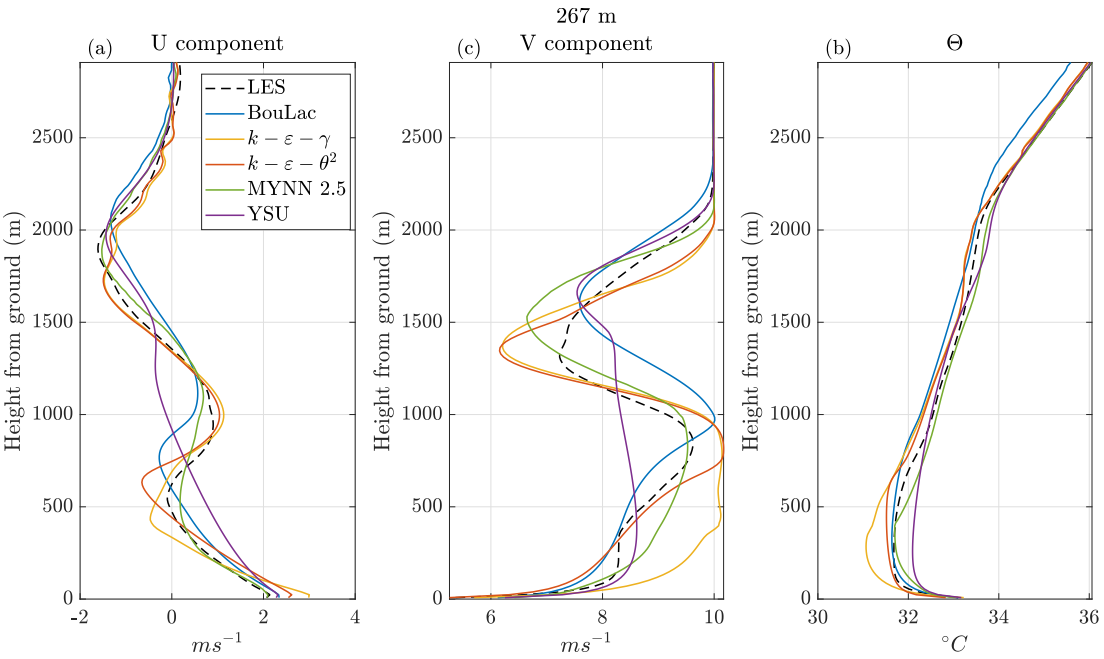


**Figure 3.12:** Vertical profiles of zonal wind speed (left), potential temperature (center), and meridional wind speed (right) for the CBL_V_W case for a point situated at 267 m above the valley floor on the eastern slope. Dashed black line refers to the ensemble of LES simulations, while coloured lines refer to the different RANS simulations. Background gray area represents the idealized slope height a.s.l.

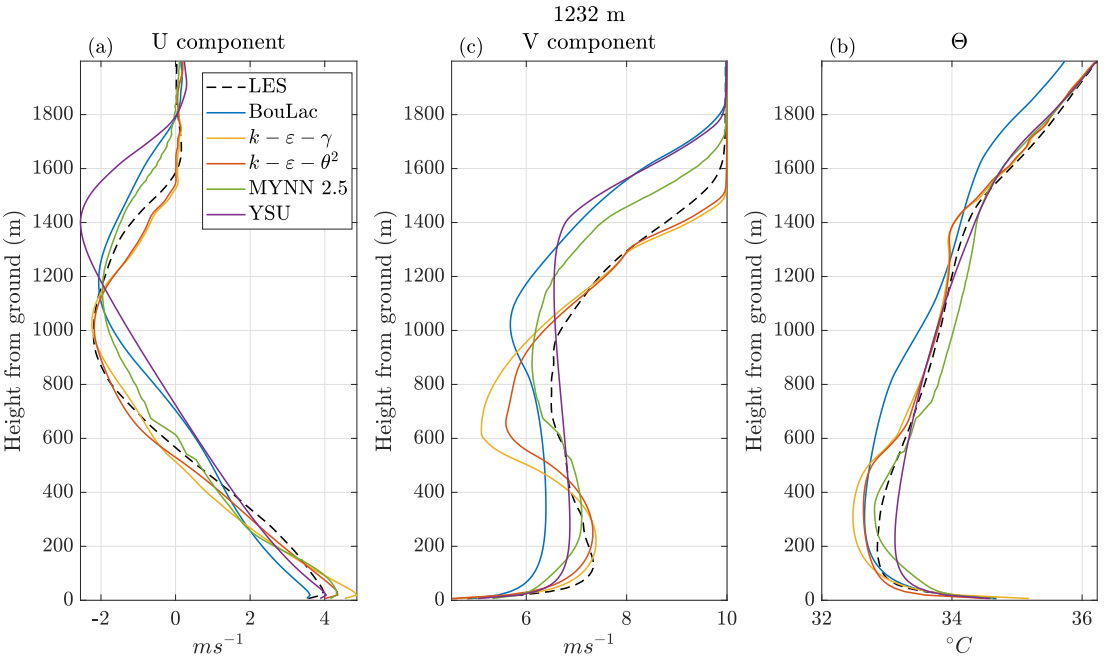


**Figure 3.13:** Vertical profiles of zonal wind speed (left), potential temperature (center), and meridional wind speed (right) for the CBL_V_W case for a point situated at 1232 m above the valley floor on the eastern slope. Dashed black line refers to the ensemble of LES simulations, while coloured lines refer to the different RANS simulations.

Figures 3.12 and 3.13 shows the vertical profile of zonal wind speed (left), potential temperature (center), and meridional wind speed (right) for the CBL_V_W case, for two points situated on the eastern slope at 267 and 1232 m above the valley floor, respectively. CBL_V_W

differs from CBL_V_NOW for a geostrophic meridional wind of 10 m $s^{-1}$ imposed in the initial conditions, with the aim of simulating an up/down-valley wind and its interaction with the cross-valley thermal circulation.

Regarding the cross valley winds and the potential temperature profiles, no substantial differences can be noticed with respect to the CBL_V_NOW case. The $K-\varepsilon$ simulations are the most appropriate RANS for simulating both wind speed and potential temperature, especially in terms of potential temperature for the lower point (267 m above the valley floor) and of wind speed for the upper point (1232 m above the valley floor). The presence of the meridional wind causes stronger differences between the results of the two $K-\varepsilon$ with respect to the CBL_V_NOW case. In fact, $K-\varepsilon-\theta^2$ is more precise than $K-\varepsilon-\gamma$, since it better reproduces the up-slope wind intensity and the potential temperature in the surface layer at both heights. Most likely, the prognostic calculation of the counter-gradient flux in $K-\varepsilon-\theta^2$ becomes more efficient, with respect to a diagnostic value (assumed by $K-\varepsilon-\gamma$), with the increasing complexity of PBL dynamics. Indeed, the largest improvements take place for the potential temperature at the lowest PBL levels where, in unstable conditions, the temperature variance is larger with respect to the upper levels, as shown initially by Willis et al. (1974). The vertical profile of the meridional wind is more complex than in the flat case (left panel in Fig. 3.2), especially for the point at 267 m above the valley floor. This is the effect of the cross valley circulation: the thermal cross-valley circulation increases the wind shear and consequently increases the turbulence production, resulting in a decrease of wind speed in correspondence to the maximum wind shear. All RANS simulations, except for YSU, can capture the effect of the cross-valley thermal circulation on the along-valley meridional wind, and also the different intensity between the lower and upper points. The inefficiency of YSU in representing the vertical profiles of the along-valley wind is probably linked to the non-locality of this turbulence parameterization (developed for flat uniform terrains) since local parameterizations become more efficient with increasing complexity (Chrobok et al., 1992). $K-\varepsilon-\theta^2$ is the most efficient in capturing the height of the local minima and maxima of the along valley wind for the lower point, despite the overestimation (underestimation) of the maximum (minimum) at 900 m (1300 m) for the lower point. The same occurs for the higher point, where the minimum of meridional wind speed in the upper levels is overestimated. On the other hand, $K-\varepsilon-\theta^2$ better performs with respect to the other RANS simulations (which overestimate the height of the inversion layer) in reproducing the meridional wind speed from 1000 to 1600 m, i.e. at the height of the inversion layer, for the upper point. Even in the case of along-valley wind, $K-\varepsilon-\theta^2$ performs better with respect to $K-\varepsilon-\gamma$, especially in terms of the intensity of the various peaks.

Figure 3.14 displays the RMSE, calculated along the first 170 vertical levels, of the zonal wind speed (left), potential temperature (center), and meridional wind speed (right) for each point on the eastern slope of the valley. As in the CBL_V_NOW case, the two $K-\varepsilon$ simulations perform better in the reproduction of the cross valley wind, especially for the points close to the ridge and to the valley floor. In this case, the difference between $K-\varepsilon-\theta^2$ and $K-\varepsilon-\gamma$ is higher, with the first that maintains good results close to the valley floor, where the performance of the other RANS simulations decrease significantly.

$K-\varepsilon-\theta^2$ displays good results also for the potential temperature profile (central panel). As for

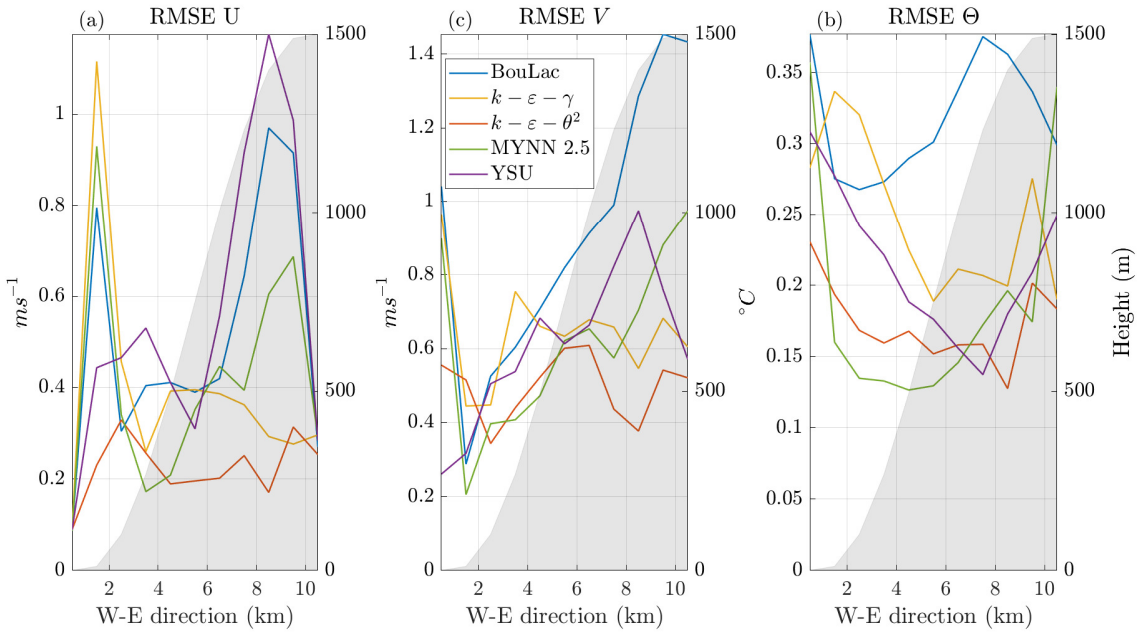


**Figure 3.14:** RMSEs of zonal wind speed (left), potential temperature (center), and meridional wind speed (right) with respect to LES, calculated for the first 170 vertical levels for each point from the valley floor to the right ridge, for the CBL_V_W for each RANS simulation. The gray area represents the height a.s.l. along the W-E direction.

the CBL_V_NOW case, BouLac presents the worst results, since it always underestimates the potential temperature in the air column. In this case, MYNN performs similarly to $K-\varepsilon-\theta^2$, while $K-\varepsilon-\gamma$ fails to satisfactorily reproduce potential temperature in the points close to the valley floor.

Regarding the along-valley wind, $K-\varepsilon-\theta^2$ reveals to be the best for the points close to the ridge, where also $K-\varepsilon-\gamma$ shows lower RMSEs with respect to the other simulations. Approaching the valley floor, all RANS simulations present similar errors, while in correspondence of the valley, where the influence of the sidewalls is lower, YSU performs better than the others.

### 3.4.3 SBL in flat terrain

Figure 3.15 displays the vertical profiles of zonal wind speed (left), potential temperature (center), and meridional wind speed (right) for the GABLS case study, averaged between the eighth and the ninth hours of simulation. LES, as stated in Beare et al. (2006), shows a boundary layer height between 150 and 200 m, and predict a low-level jet (in the S-N direction) forced by the Coriolis term, as well as a peak in the zonal wind speed corresponding to the PBL height. The best RANS simulation in reproducing both wind speed and potential temperature is again $K-\varepsilon-\theta^2$, which can correctly capture the height of the boundary layer, while $K-\varepsilon-\gamma$ (where $\gamma$ is zero in stable conditions) slightly overestimates the PBL height. Also YSU overestimates the PBL height, and, in addition, it underestimates the potential temperature gradient in the inversion layer, resulting in smoother peaks for both $U$ and $V$ at the top of the PBL. MYNN2.5 performs similarly to $K-\varepsilon-\theta^2$, but it underestimates the magnitude of the low-level jet. On

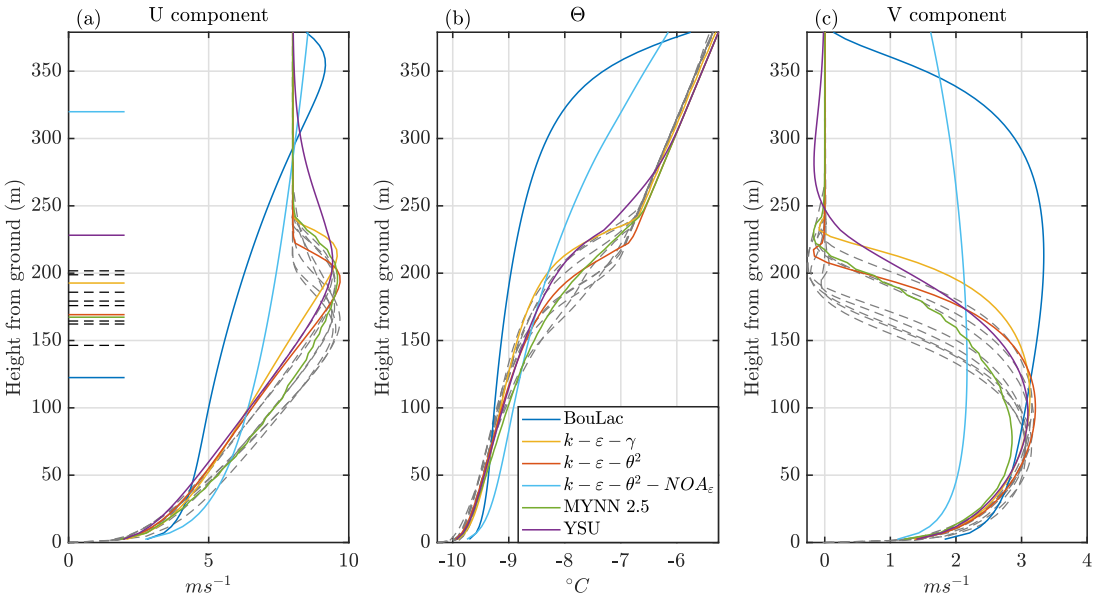


**Figure 3.15:** Vertical profiles of zonal wind speed (left), potential temperature (center), and meridional wind speed (right) for the GABLS case. Panel (a) displays, through the horizontal lines on the left, the diagnostic boundary layer height for RANS and LES. The series of dashed gray lines refers to the different LES, while colour lines refer to the RANS simulations.

the other hand, BouLac fails in reproducing all the vertical profiles, since it does not capture the correct shape of the potential temperature and, as a consequence, wrongly estimates the PBL height ($\sim$120 m) and overestimates the inversion layer height ($\sim$360 m, while it should be $\sim$ 200 m). The lack of BouLac in correctly representing the vertical profiles in this specific stable regime is probably due to the wrong calculation of the correct length scale, which strongly depends on the atmospheric stability (see Bougeault et al., 1989 for further details). Similarly, $K-\varepsilon-\theta^2-NOA_\varepsilon$, which does not include the additional term in the dissipation rate equation (Eq. 3.10), largely overestimates the PBL height ($\sim$ 320 m), and overestimates also the height of the inversion layer, with even larger errors than in BouLac. This overestimation underlines the importance of the additional term $A_\varepsilon$ for the dissipation rate equation, which depends linearly on $N$ and on $\varepsilon$ itself, increases the dissipation rate where N is higher (i.e. between 100 and 250 m), hence reducing the PBL height and showing a better agreement with the LES. Indeed, as shown in Fig. 3.16 (left panel), the TKE of $K-\varepsilon-\theta^2-NOA_\varepsilon$ is highly overestimated, while the TKE of $K-\varepsilon-\theta^2$ and $K-\varepsilon-\gamma$ lay always in the range of the different LES. The reduction of the TKE is due to the increase of the dissipation rate in the higher levels (central panel). Since the eddy viscosity and diffusivity are inversely proportional to the dissipation rate, an increase in $\varepsilon$ corresponds to a decrease of $\nu_M$ and $\nu_H$, and hence in a decrease of TKE, heat and momentum flux. The $A_\varepsilon$ term confirms its capacity to better represent the turbulent variables, even for temperature variance (right panel of Fig. 3.16). $\overline{\theta^2}$ evaluated by the LES assumes a quasi-constant value, with a peak around the PBL height, with different magnitudes for the different simulations. While the temperature variance reproduced by $K-\varepsilon-\theta^2$ agrees in terms of shape and magnitude with the various LES, the temperature variance computed by $K-\varepsilon-\theta^2-NOA_\varepsilon$ is largely overestimated, since its computation is

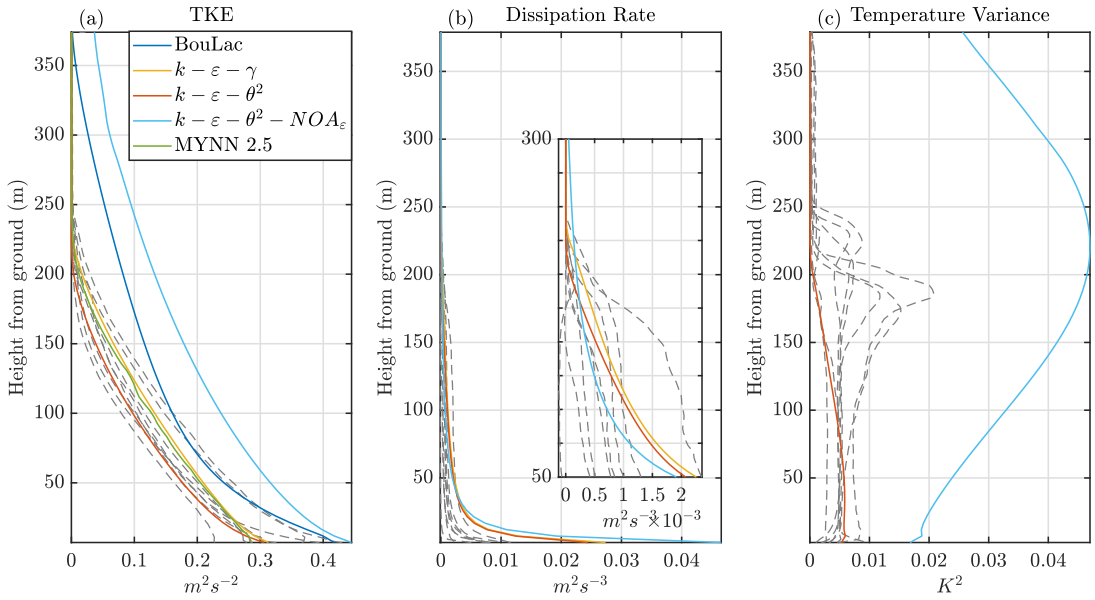


**Figure 3.16:** Vertical profiles of TKE (left), dissipation rate (center) and temperature variance (right) for the GABLS case. The series of dashed gray lines refers to the different LES, while colour lines refer to the RANS simulations.

linearly dependent on TKE and inversely proportional to $\varepsilon$ (see Eq. 3.13).

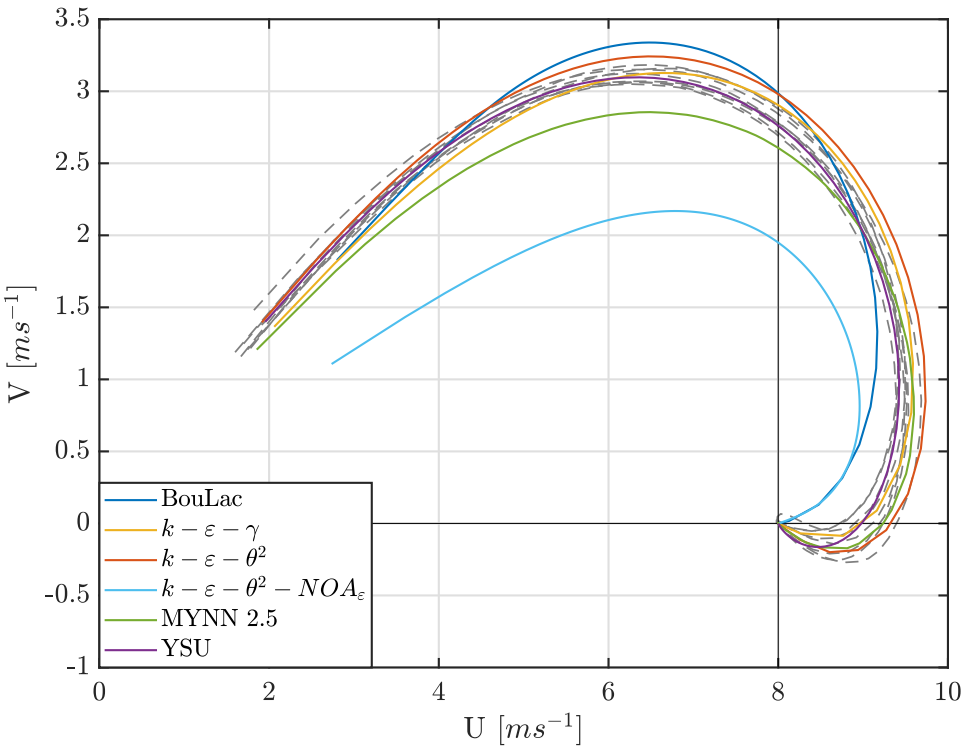


**Figure 3.17:** Hodograph of the mean velocity vector for the GABLS case. Dashed black lines refers to the different LES, while colour lines refer to the RANS simulations.

Figure 3.17 displays the odographs of the wind. All the simulations, apart from $K-\varepsilon-$

$\theta^2 - NOA_\varepsilon$ (which fails throughout the whole vertical air column), well capture the intensity and the direction of the wind speed in the surface layer. At the peak of the low-level jet (where $V \sim 3$ m s$^{-1}$ and $U \sim 6.5$ m s$^{-1}$ ), MYNN 2.5 underestimates, while BouLac and $K-\varepsilon-\theta^2$ slightly overestimate the low-level jet intensity. Above the low-level jet peak, all the RANS simulations behave well returning to geostrophic conditions, while the two failing in capturing the PBL height (BouLac and $K-\varepsilon-\theta^2-NOA_\varepsilon$), reach the geostrophic conditions at higher levels.

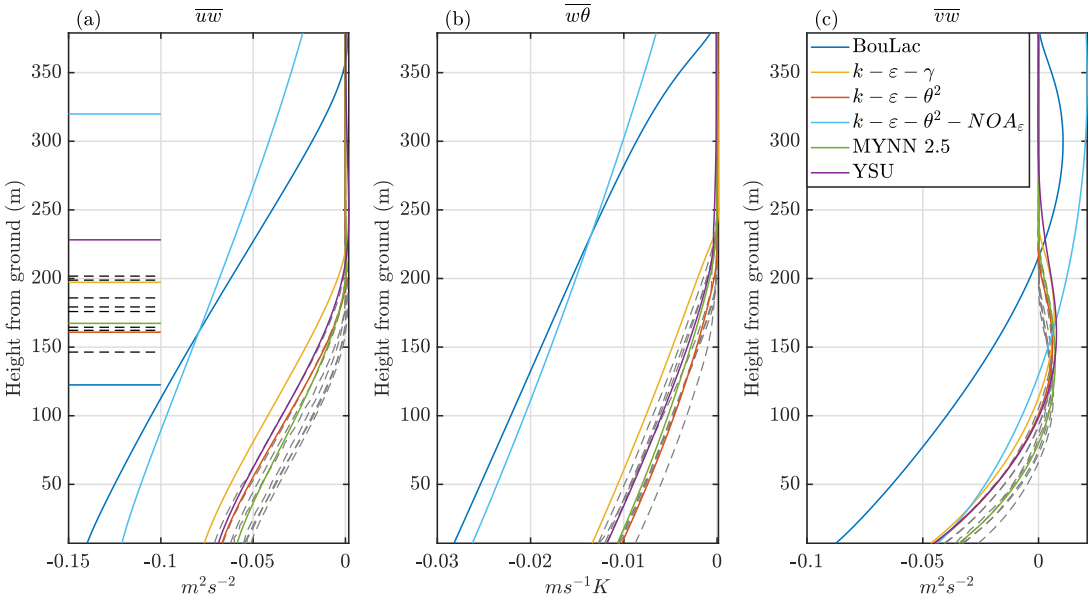


**Figure 3.18:** Vertical profiles of vertical zonal momentum flux (left), vertical heat flux (center), and vertical meridional momentum flux (right) for the GABLS case. Panel (a) displays, through the horizontal lines on the left, the diagnostic boundary layer height for RANS and LES. The series of dashed gray lines refers to the different LES, while colour lines refer to the RANS simulations.

Figure 3.18 shows the vertical profiles of zonal momentum flux (left), heat flux (center) and meridional momentum flux (right). While BouLac and $K-\varepsilon-\theta^2-NOA_\varepsilon$ largely overestimate the absolute value of all the fluxes, due to an overestimation of the turbulent production (panel (a) of Fig. 3.16), the other RANS simulations reasonably reproduce the vertical profile of the fluxes. In particular, the surface heat flux $\overline{w\theta}|_0$ is well-reproduced by the set of RANS simulations that correctly capture the PBL height. $K-\varepsilon-\gamma$ slightly overestimates (in absolute values) all the vertical fluxes and in particular the turbulent heat flux, underlying the importance of adopting a prognostic equation for temperature variance in both unstable and stable regimes, as pointed out by Zilitinkevich et al. (2007).

## 3.5 Summary and Conclusions

As the demand for more accurate numerical weather prediction models increases, especially for complex and heterogeneous terrains, the development of more precise and local turbulence closures is required. To this end, a novel one-dimensional parameterization scheme have been developed, based on the coupled equations for TKE and $\varepsilon$ at 1.5 order, for the WRF model,

with the aim to implement a RANS turbulence closure independent from any length scale. The standard $K-\varepsilon$ turbulence scheme has been improved by calculationg the turbulent Prandtl number (similarly to Hong et al. (2006b)) the prognostic equation for temperature variance (Lazeroms et al., 2016), and including an additional term to better reproduce the dissipation rate in stable regimes (Zeng et al., 2020b).

Since NWP models are adopted in all areas around the world, particular attention is put on the numerical method adopted to solve this set of equations, to obtain the most stable numerical integration that can work at time-steps suitable for forecasting applications. With this goal in mind, an analytical solution for TKE and $\varepsilon$ equations is derived. In this way, the numerical solution is stable and can work for large time steps.

The new turbulence closure is tested in various idealized case studies, varying on atmospheric stability and terrain complexity. Tests include the convective boundary layer in flat terrain, the convective thermal circulation induced by a valley, and the well-known GABLS campaign for the very stable boundary layer. For each test case, our $K-\varepsilon$ parameterizations (in two different forms, differing in the parameterization adopted for the counter gradient term) have been tested against an ensemble of LES, differing in the initial temperature perturbation, and against state-of-the-art RANS turbulence schemes at the first order (YSU), or depending on various diagnostic length scales (BouLac and MYNN2.5).

Results show that in general the novel $K-\varepsilon$ scheme outperforms the other parameterizations, for both wind speed and potential temperature, in all the cases considered in this work. In particular, the largest improvements take place in connection with inversion layers, where the gradients of the mean variables are stronger. The model performance increases with the increasing complexity of the atmospheric conditions, since enhancements are substantial for the valley cases.

The comparison between the various $K-\varepsilon$ closures, differing in the calculation of the counter-gradient term for the turbulent heat flux, underlines the importance of adopting a prognostic equation for the temperature variance $\overline{\theta^2}$. Improvements due to the prognostic equation of temperature variance are evident both in the valley and GABLS cases. Furthermore, the GABLS case confirms that the standard $K-\varepsilon$ without the additional production term in the prognostic equation for dissipation rate is unsuitable for stable boundary layers, and therefore the term in Eq. 3.10 is needed for a coherent reproduction of the flows. As pointed out by Zhang et al. (2020), the diagnostic calculation of the dissipation rate $\varepsilon$ is important for many fields, especially for aviation applications (Muñoz-Esparza et al., 2018).

Finally, this work proves that the new scheme discussed here can improve the reproduction of the atmospheric motion in several conditions, going beyond the definition of a diagnostic turbulent length scale commonly adopted in state-of-the-art PBL closures. Future developments will include the validation of the current model in real conditions, through the comparison with observational data, and its coupling with multi-layer urban canopy model schemes, in the context of the WRF model, in order to improve the representation of the complex boundary layer developing over urban areas.

# 4 On a New One-Dimensional $K-\varepsilon$ Turbulence Closure for Building-Induced Turbulence

**Abstract**

To take into account the modifications induced by buildings on flow and turbulent structure, various Urban Canopy Parameterizations (UCPs) have been developed in the last two decades. UCPs are integrated in mesoscale meteorological models to consider the impact of buildings on the flow, without explicitly resolving the urban structures. However, even though several UCPs were successfully able to reproduce wind flow in the urban environment, they lack in correctly defining the mixing length scale for dissipation rate and eddy viscosity. The main objective of this work is to address this shortcoming by developing a new one-dimensional turbulence closure that takes building-induced turbulence into account independent of turbulence length scales. This model directly solves not only the equation for turbulent kinetic energy but also the equation for its dissipation rate ($k$-$\varepsilon$ model). Similar closure schemes have been successfully adopted for vegetated canopies, but its applicability to urban canopies is still unknown. The performance of the new $k$-$\varepsilon$ model, with additional sources and sinks for wind speed, turbulent kinetic energy, and dissipation rate is tested by means of single-column Reynolds-Averaged Navier-Stokes (RANS) simulations in idealized urban areas, using different building packing densities. Results are in good agreement with spatially averaged building-resolving CFD simulations. In particular, vertical profiles of mean and turbulent variables show better results with respect to simulations using turbulence closures adopting a parameterization of the mixing length scale. The best improvements take place for wind speed, with errors half than state-of-the-art UCPs for high packing densities, and for dissipation rate. Therefore, besides the enhancement in the reproduction of the mean flow for urban areas, the here-presented turbulence closure does not need additional tuning of coefficients depending on the packing density, resulting in a more general and efficient scheme.

## 4.1 Introduction

Accurate mesoscale meteorological modelling in urban areasis critical for assessing urban climate and informing air quality and urban planning studies. However, the main difficulties in simulating Planetary Boundary Layer (PBL) processes within the urban canopy layer (UCL)is due to the heterogeneity of the urban land-use. Scales of the processes ranging from the microscale ($\sim$ 1 m) to the mesoscale ($\sim$ 100 km) (Britter et al., 2003). Therefore mesoscale

models, usually set to $\sim$ 1 km of horizontal resolution for computational reasons, cannot explicitly resolve turbulent structures and atmospheric flow around buildings, highlighting the necessity to develop proper Urban Canopy Parameterizations (UCPs) to consider the effect of urban obstacles and surfaces. Roth (2000) highlighted the two main effects induced by urban structures on the PBL structure, and they are 1) the mechanical drag from buildings, due to differences in pressure between roughness elements and 2) the heating by urban surfaces, which modifies the vertical temperature stratification. In the past decades, UCPs have been developed to model the interaction between urban structures and the airflow within mesoscale models, at different levels of complexity. The simplest way to model urban obstacles within numerical models is to increase the roughness length and modify soil thermal properties in the context of the Monin-Obukhov similarity theory (MOST). Other UCPs are single layer, i.e. the UCL is represented in the first vertical level of the atmospheric model, and provide averaged values based on the urban morphology features (Giovannini et al., 2013; Kanda et al., 2005; Kusaka et al., 2001; Masson, 2000). Increasing the complexity, multi-layer schemes have been developed based on the interaction of urban canopies with several levels of the atmospheric model , treating the urban areas as a porous medium where the sink of momentum depends on the drag induced by buildings (Coceal et al., 2006; Di Sabatino et al., 2008; Martilli et al., 2002; Masson et al., 2009). Generally, the drag induced by buildings is proportional to the square of the mean wind speed perpendicular to the building surface times a sectional drag coefficient ($C_d$), which is generally set constant with height and with building packing density, assuming values from 0.1 (Uno et al., 1989) to 1 (Coceal et al., 2004). However, observational studies and microscale models demonstrate that $C_d$ depends on the city configuration and the height from the ground (Ahmad Zaki et al., 2012; Chen et al., 2017a; Santiago et al., 2008). Regarding the turbulent closure, UCPs generally use 1-order K-closures based on a mixing length scale, or 1.5-order closures based on a prognostic equation for turbulent kinetic energy, but generally dependent on a semi-empirical turbulent length scale. Comparing UCPs with experimental data is usually not feasible, since the simulated flow is representative of spatial averages over mesoscale grid points. For this reason, Santiago et al. (2010) proposed to use microscale computational fluid dynamics (CFD) models, based on RANS equations, to validate and develop UCPs. More recently, Nazarian et al. (2019) proposed a similar method but based on the validation of UCPs with Large Eddy Simulations (LES). Microscale models, based on either RANS or LES, have a resolution high enough to explicitly resolve the urban structures, and therefore even the turbulent flows around buildings. Examples of such simulations can be found in Antoniou et al. (2017), Auvinen et al. (2020), Dai et al. (2018), Giometto et al. (2017), Nazarian et al. (2019), and Santiago et al. (2008). Building-resolving microscale simulations outputs are then spatially averaged, to inform and improve one-dimensional mesoscale UCPs. Adopting this method, Santiago et al. (2010) used CFD simulations over staggered arrays of cubes, validated against direct numerical simulations (DNS) and wind tunnel data of Santiago et al. (2008) to upgrade the multi-layer UCP presented in Martilli et al. (2002), based on a 1.5-order $k-\ell$ turbulence closure. Specifically, CFD outputs have been used to evaluate the dependence of the mixing length scale of dissipation rate $l_\varepsilon$ and of the drag coefficient $C_d$ on packing density and height from the ground. Subsequently, Nazarian et al. (2019) further improved this UCP, employing LES to estimate the dependence of the displacement height and

of the turbulent length scale of $l_k$ on building packing density, through the tuning of related coefficients.

However models employing a $k-\ell$-based turbulence closure require an empirical or semi-empirical computation of the mixing length scales, which is often adapted for particular case studies. Moreover, even in the case of flat and heterogeneous surfaces, the estimation of the length scale relies on empirical data and physical approximations.

In this paper, we propose a multi-layer urban canopy parameterization, built on the same model set-up of Santiago et al. (2010) and Nazarian et al. (2019), which does not depend on a $k-\ell$ turbulence closure, but instead, the turbulent transport is modelled with the $k-\varepsilon$ turbulence closure. $k-\varepsilon$-based turbulence closures differ from $k-\ell$ closures by the additional prognostic equation of the dissipation rate of turbulent kinetic energy $\varepsilon$. This turbulent closure, adopted for atmospheric flows by Launder et al. (1974), has been successfully employed in the following years for various PBL schemes (Duynkerke, 1988; Langland et al., 1996; van der Laan et al., 2017; Zeng et al., 2020b; Zhang et al., 2020). Beljaars et al. (1987) compared $k-\ell$ and $k-\varepsilon$ based schemes and found that the $k-\varepsilon$ better retains memory effects in velocity scales when surface conditions change. This kind of closure has been already been employed for multi-layer vegetation canopy models (Katul et al., 2004; Sanz, 2003; Tolladay et al., 2021; Wilson et al., 1998), but never before in the case of urban canopies. In this work, we propose two different UCPs, differing on the additional sources/sinks due to buildings in the prognostic equations of turbulent kinetic energy and dissipation rate. The same spatially-averaged CFD simulations of Santiago et al. (2010) are used as guidance to set the values of an additional drag coefficient for the prognostic equation of the dissipation rate and to validate the $k-\varepsilon$-based urban canopy parameterizations.

The paper is organized as follows: Section 4.2 describes the dynamical part of the urban canopy parameterization, along with the turbulence closure tested in this work. The set-up of one-dimensional (UCP) mesoscale and three-dimensional microscale (CFD) simulations is described in Section 4.3. Section 4.4 presents the novel additional terms in the prognostic equations to account for the drag induced by buildings, while results for configurations with different packing densities are shown in Section 4.5. Finally, conclusions are given in Section 4.6.

## 4.2 Model description

The momentum equation solved by a mesoscale model over urban areas involves two averaging processes, in time (to filter out turbulent motions) and in space over the grid cell (to filter out the structures whose characteristic length scales are smaller than the grid resolution). Assuming both averages, and assuming 1) horizontal homogeneity and 2) no mean vertical motion (for the continuity equation, assuming a one-dimensional scheme), the equation of the horizontal wind speed $u$ reads:

$$\frac{\partial \rho \langle \overline{u} \rangle}{\partial t} = -\frac{\partial \rho \langle \overline{u'w'} \rangle}{\partial z} - \rho D_u \tag{4.1}$$

where the overbars refer to the time mean, angle brackets to the space average, $u', w'$ are the turbulent components (assuming that a variable $c$ can be decomposed as $c = \overline{c} + c'$, i.e. into a mean part and a turbulent part) and $\rho$ the air density. The first term on the r.h.s. is the contribution of the turbulent flux of momentum, and the second ($D_u$) the drag induced by buildings, which will be explained in section 4.4. In this work, we neglect the contribution of the departure of the mean wind component from its spatial average (Eq. 1 in Santiago et al. (2010)). This will result in a limitation for the present model. The spatially-averaged turbulent momentum flux is parameterized through a K-theory:

$$\langle \overline{u'w'} \rangle = -K_m \frac{\partial \langle \overline{u} \rangle}{\partial z} \tag{4.2}$$

where $K_m$ is the eddy viscosity. In Santiago et al. (2010), $K_m$ is calculated using a $k-\ell$ closure (as in Martilli et al. (2002), based on Bougeault et al. (1989)):

$$K_m = C_k \ell_k \langle \overline{k} \rangle^{1/2} \tag{4.3}$$

where $C_k$ is a model constant, $\ell_k$ is a length scale and $\langle \overline{k} \rangle$ the spatially- and temporally-averaged turbulent kinetic energy (TKE). A detailed description of the closure constants and length scales for this parameterization is shown in Sec. 4.4. For the $k-\varepsilon$, since we aim to avoid the definition of an ad-hoc length scale, the diffusion coefficient is computed as:

$$K_m = C_\mu \frac{\langle \overline{k} \rangle^2}{\langle \overline{\varepsilon} \rangle} \tag{4.4}$$

where $C_\mu$ is a model constant, set to 0.09, $k$ and $\varepsilon$ is the TKE dissipation rate. The spatially-averaged turbulent kinetic energy is calculated through its prognostic equation:

$$\frac{\partial \rho \langle \overline{k} \rangle}{\partial t} = -\frac{\partial \rho \langle \overline{k'w'} \rangle}{\partial z} + \rho K_m \left[ \left( \frac{\partial \langle \overline{u} \rangle}{\partial z} \right)^2 + \left( \frac{\partial \langle \overline{v} \rangle}{\partial z} \right)^2 \right] - \rho K_m \frac{g}{\theta_0} \frac{\partial \langle \overline{\theta} \rangle}{\partial z} - \rho \langle \overline{\varepsilon} \rangle + \rho D_k \tag{4.5}$$

where the first term on the r.h.s. is the vertical diffusion of $TKE$, the second the production by shear, the third the production/destruction by buoyancy, the fourth the $TKE$ dissipation and $D_k$ is the source of $\langle \overline{k} \rangle$ generated by the interaction between the buildings and the mean flow. In this particular case, where we assume neutral stratification, the buoyant production term is zero. In this equation, the $\varepsilon$ term needs to be parameterized: assuming a $k-\ell$ closure, Santiago et al. (2010) suppose a diagnostic equation:

$$\langle \overline{\varepsilon} \rangle = C_\varepsilon \frac{\langle \overline{k} \rangle^{3/2}}{l_\varepsilon} \tag{4.6}$$

A length scale is required to parameterize $\varepsilon$. In order to avoid to define a length scale as in Eq. 4.6, $\varepsilon$ is calculated through its prognostic equation, in a way similar to Katul et al. (2004):

$$\frac{\partial \rho \langle \overline{\varepsilon} \rangle}{\partial t} = -\frac{\partial \rho \langle \overline{\varepsilon' w'} \rangle}{\partial z} + \rho K_m \left( c_1 \left[ \left( \frac{\partial \langle \overline{u} \rangle}{\partial z} \right)^2 + \left( \frac{\partial \langle \overline{v} \rangle}{\partial z} \right)^2 \right] - c_3 \frac{g}{\theta_0} \frac{\partial \langle \overline{\theta} \rangle}{\partial z} \right) \frac{\langle \overline{\varepsilon} \rangle}{\langle \overline{k} \rangle} - c_2 \frac{\langle \overline{\varepsilon} \rangle^2}{\langle \overline{k} \rangle} + \rho D_\varepsilon \quad (4.7)$$

where the first term on the r.h.s. is the vertical diffusion, the second term is the production/destruction of dissipation rate by shear (first part) and buoyancy (second part), the third is the dissipation and the fourth ($D_\varepsilon$) is the source of $\langle \overline{\varepsilon} \rangle$ generated by the interaction between the buildings and the mean flow. $c_1$, $c_2$ and $c_3$ are model constants, usually set to 1.44, 1.92 and 1.44 (Launder et al. (1983)).

## 4.3 Methodology and Simulation set-up

CFD runs, performed with a standard $K-\varepsilon$ RANS model, are identical to the ones of Santiago et al. (2010). Different packing densities of staggered arrays of cubes, with incident wind along the $x$ direction are tested, at a three-dimensional resolution of one meter. Urban geometry is characterized by the plan area ratio ($\lambda_p$) and the front area ratio ($\lambda_f$):

$$\lambda_p = \frac{A_p}{A_t} = \frac{LW}{(W+S_y)(L+S_x)} \quad (4.8)$$

and,

$$\lambda_f = \frac{A_f}{A_t} = \frac{hW}{(W+S_y)(L+S_x)} \quad (4.9)$$

where $h$ is the building height, $W$ and $L$ the building horizontal dimensions, and $S_x$ and $S_y$ are the distances between the obstacles, as shown in Fig. 4.1. In this study, the buildings are cubes with $h = W = L = 16$ m, therefore, for each urban configuration, $\lambda_p = \lambda_f$. In order to cover a large spectrum of possible urban geometries, as suggested by Grimmond et al. (1999), six different packing densities are tested, with $\lambda_p = 0.0625, 0.11, 0.16, 0.33, 0.44$, that correspond, assuming to keep constant the dimensions of the buildings, to set $S_x = S_y = 48, 32, 24, 16, 12, 8$

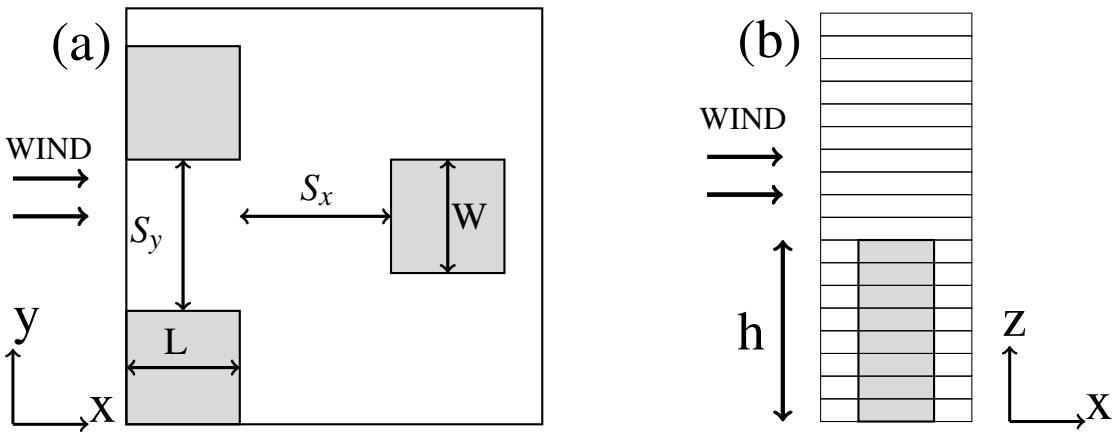


**Figure 4.1:** Design of the CFD simulations: (a) plan view of the staggered array, (b) the vertical section for a single building.

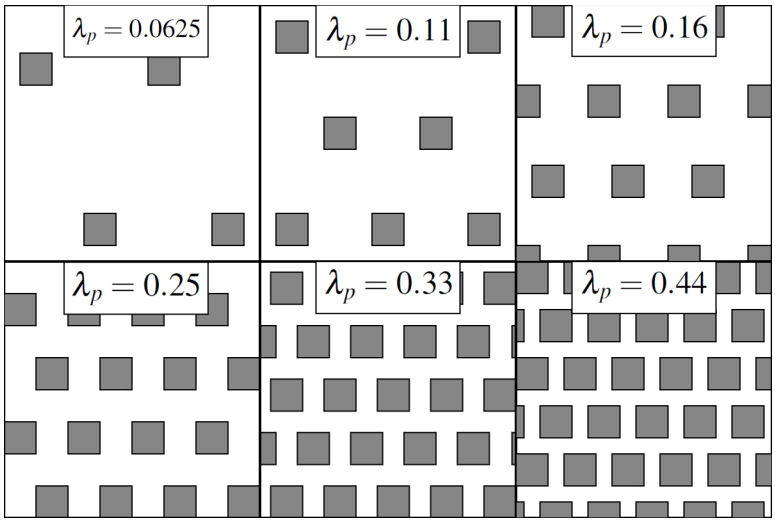


**Figure 4.2:** Plan view of the various packing densities tested in this study.

m, respectively (see Fig. 4.2 for a visual representation of the various packing densities). The extension of the domain is $16h \times 12h \times 8h$ in the $z$, $x$ and $y$ directions respectively. Symmetric boundary conditions are set in the $y$ direction and periodic boundary conditions in the direction of the wind ($x$), to simulate an infinite array of buildings. The flow is originated by a horizontal pressure gradient $\tau = \rho u_\tau^2/4h$, where $u_\tau = 1\ \mathrm{m\,s^{-1}}$. At the domain top, to obtain a parallel flow with null vertical motion, symmetric conditions are set, to obtain zero vertical derivatives for all the variables. In the CFD simulations, performed using the model FLUENT, buildings are resolved by 16 cells in each direction, and they are based on the steady state RANS equations and the standard $k-\varepsilon$ turbulence closure. For a detailed description of the CFD simulations set-up, see Santiago et al. (2008). Simulations output for the case of $\lambda_p = 0.25$ were validated against DNS simulations (Coceal et al., 2006) and experimental results (Cheng et al., 2007). The urban canopy parameterization is run as a one-dimensional column, with the same vertical computational domain of the CFD simulations (i.e. 64 vertical layers with a resolution of one meter). For the $k-l$ closure, the steady state equations are, for wind speed and $TKE$ respectively (neglecting the temporal derivative, that once the steady state is reached, it is zero) are:

$$0 = \frac{\partial}{\partial z}\left(\rho K_m \frac{\partial \langle \overline{u} \rangle}{\partial z}\right) - \rho D_u \tau \tag{4.10}$$

$$0 = \frac{\partial}{\partial z}\left(\rho K_m \frac{\partial \langle \overline{k} \rangle}{\partial z}\right) + \rho K_m \left(\frac{\partial \langle \overline{u} \rangle}{\partial z}\right)^2 - \rho \langle \overline{\varepsilon} \rangle + \rho D_k \tag{4.11}$$

where $K_m$ is computed using Eq. 4.3, and $\varepsilon$ using Eq. 4.6.

For the $k-\varepsilon$ closure instead, $K_m$ is computed through Eq. 4.4, while $\varepsilon$ is calculated with its prognostic equation:

$$0 = \frac{\partial}{\partial z}\left(\rho \frac{K_m}{Pr} \frac{\partial \langle \overline{\varepsilon} \rangle}{\partial z}\right) + \rho c_1 \langle \overline{k} \rangle \left(\frac{\partial \langle \overline{u} \rangle}{\partial z}\right)^2 - \rho c_2 \frac{\langle \overline{\varepsilon} \rangle^2}{\langle \overline{k} \rangle} + \rho D_\varepsilon \tag{4.12}$$

A description of the calculation of $D_u$, $D_k$ and $D_\varepsilon$ is given in section 4.4.

For the UCP, it is assumed that all horizontal gradients are null, except for a pressure gradient ($\tau$) imposed to force a horizontal and parallel flow in the $x$ direction. The aim is to use a single-column model to simulate the whole array of cubes of the CFD domain. To compare the building-resolving CFD with the "mesoscale" simulations adopting the urban canopy parameterization, the CFD outputs after the steady-state is reached are horizontally averaged over each vertical level. Therefore, if $C$ is a variable of the flow, its spatial average is computed as:

$$\langle C \rangle = \frac{1}{V_{air}} \iint C(x,y,z,t)\, dx\, dy\, dz \tag{4.13}$$

where $V_{air}$ is the air volume of each vertical level, excluding the volume occupied by buildings.

## 4.4 Drag induced by buildings

UCPs treat urban areas as a porous material, modelled by means of a drag force. This drag force appears in the equations since the buildings cannot be explicitly resolved because the resolution of mesoscale models is usually much larger than the building dimension. The common model for $D_u$, whose physical meaning is an extra negative horizontal gradient of pressure induced by the buildings, makes the sink of momentum due to the canopy obstacles dependent on the wind speed itself. At a certain height $z$, the drag term for wind speed reads:

$$D_u = \frac{1}{\rho} \left\langle \frac{\partial \overline{p}}{\partial x} \right\rangle \Bigg|_z = -S(z) C_d \langle \overline{u(z)} \rangle \left| \langle \overline{u(z)} \rangle \right| \tag{4.14}$$

where $S(z)$ is the upwind vertical surface building density, $C_d$ is the sectional drag coefficient (to be modelled), and $\langle \overline{u(z)} \rangle$ is the spatially-averaged mean wind speed at level $z$.
The drag term for turbulent kinetic energy is parameterized, in analogy with the momentum equation, as:

$$D_k = S(z) C_d \left| \langle \overline{u(z)} \rangle \right|^3 \tag{4.15}$$

A turbulence closure with no prognostic equations for the dissipation rate ($k-\ell$ hereafter), with the definition of a length scale for the closure of dissipation rate and eddy diffusivity, does not need any additional term, and for this reason, it has been widely used in literature, since it does not need additional prognostic equations, but only model constants tuning, depending on the system considered.
On the other hand, one of the primary reasons that discouraged the development of $k-\varepsilon$ models for canopy sub-layer flows is the difficulty in modelling the effects of the canopy (Katul et al., 2004), i.e. to parameterize the terms $D_u$, $D_k$, and $D_\varepsilon$. The primary weakness of a $k-\varepsilon$ approach is the calculation of $D_\varepsilon$ (Wilson et al., 1998).
In the literature, no examples are found usinga $k-\varepsilon$ closure in UCPs. For vegetated canopies however, different approaches can be found. The simplest one is the closure adopted by Tolladay et al. (2021), where the dissipation rate is increased by a factor that depends linearly on the wind speed and on $\varepsilon$ itself:

$$D_\varepsilon = S(z) C_{d\varepsilon} |\langle \overline{u} \rangle| \langle \overline{\varepsilon} \rangle \tag{4.16}$$

In this case, the drag coefficient for the dissipation rate $C_{d\varepsilon}$ has to be derived along with the coefficient for the TKE. This closure will be called $k-\varepsilon-1T$ hereafter, since it depends on a single additional term, with respect to Santiago et al. (2010).
Going towards more complex models, through the analogy with parameterizations for vegetated canopies, Sanz (2003) and Katul et al. (2004) suggested the following formulations for $D_k$ and $D_\varepsilon$, respectively:

$$D_k = S(z)C_d\left(\alpha_1|\langle\overline{u}\rangle|^3 - \alpha_2|\langle\overline{u}\rangle|\langle\overline{\varepsilon}\rangle\right) \tag{4.17}$$

$$D_\varepsilon = S(z)C_d\left(\beta_1\frac{\langle\overline{\varepsilon}\rangle}{\langle\overline{k}\rangle}|\langle\overline{u}\rangle|^3 - \beta_2|\langle\overline{u}\rangle|\langle\overline{\varepsilon}\rangle\right) \tag{4.18}$$

where $C_d$ is the same drag coefficient of Eq. 4.14 and $\alpha_1$, $\alpha_2$, $\beta_1$ and $\beta_2$ are closure constants to be determined. The first terms on the r.h.s are based on the standard dimensional analysis of the $k-\varepsilon$ approach. The second term comes from wind-tunnel studies (Liu et al., 1996), and it was introduced to fit the experimental data. Its physical meaning is that obstacles lead to a "short-circuiting" of Kolmogorov's cascade. This closure is called $k-\varepsilon-3T$ hereafter since three additional terms have been added (and modeled) with respect to Santiago et al. (2010).
Katul et al. (2004) showed that for vegetated canopies $\alpha_1 \sim \beta_1 \sim 1$, so we decided to keep these constants equal to 1 and to vary the two remaining coefficients, in order to reduce the degrees of freedom. On the other hand, the comparison between this column-model and CFD output shows that the best results are given setting $\alpha_2 = 8$ and $\beta_2 = 5.5$.
In the next subsection (4.3, we will present the models developed to parameterize $C_d$ (appearing in Eq. 4.14, 4.15, 4.17 and 4.18) and $C_{d\varepsilon}$, used to calculate the drag term for $\varepsilon$ in Eq. 4.16.

### 4.4.1 The drag coefficient

The drag coefficients $C_d$ and $C_{d\varepsilon}$ need to be parameterized for various urban configurations. Usually, $C_d$ is set constant with packing density and with height, with values that range from 0.1 to 1 (Coceal et al., 2004). However, experiments show that it depends on packing density, on the building horizontal distribution (staggered or aligned) and it has a strong dependency on height (Santiago et al., 2008). Suitable information about the vertical profiles of $C_d$ and $C_{d\varepsilon}$ is difficult to obtain experimentally, because it is difficult to quantify the pressure deficit for an obstacle, and the drag coefficient close to the ground is usually very large because of small wind speeds, and not integrable within one-dimensional models. Accordingly, Santiago et al. (2010) calculated an equivalent drag coefficient, constant with height, that appears in the drag force for $TKE$ and $u$. This calculation involves the pressure differences between the two sides of a building obtained through a building-resolving RANS-CFD simulation, spatially-averaged over the domain of simulation:

$$C_{deq} = \frac{\frac{-1}{\rho h}\int_0^h \Delta\langle\overline{p(z)}\rangle dz}{\frac{-1}{h}\int_0^h \langle\overline{u(z)}\rangle\left|\langle\overline{u(z)}\rangle\right| dz} \tag{4.19}$$

The drag coefficient computed with this method, hereafter called $C_{deq}$, depends on the configuration (staggered or aligned buildings) and on the packing density. By fitting the results of the

CFD simulations performed with different packing densities,Santiago et al. (2010) found the following relation between $C_{deq}$ and $\lambda_p$ for staggered building arrays:

$$C_{deq}(\lambda_p) = \begin{cases} 3.31\,\lambda_p^{0.47} & \text{if } \lambda_p \leq 0.29 \\ 1.85 & \text{if } \lambda_p > 0.29 \end{cases} \tag{4.20}$$

The variation of $C_d$ with packing density is shown in panel (a) in Fig. 4.3. As expected, the

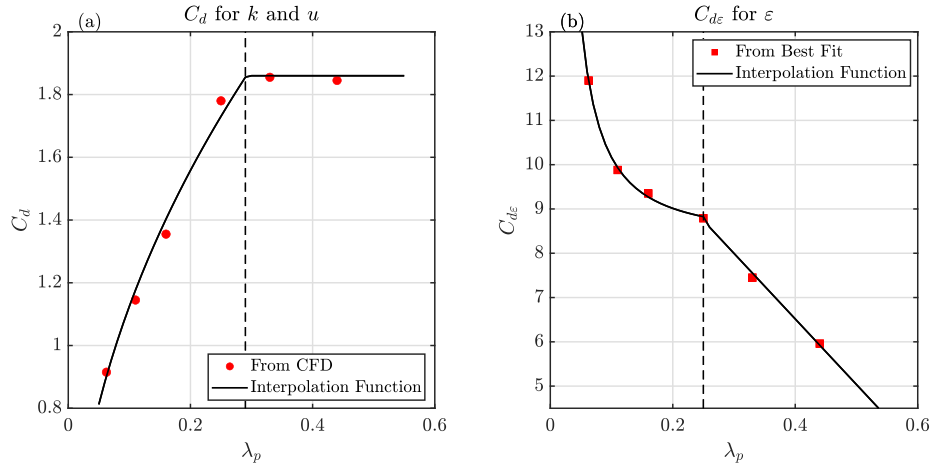


**Figure 4.3:** Variation of drag coefficients with packing density, obtained with CFD simulations through Eq. 4.20 for $C_d$ and through the best fit for $C_{d\varepsilon}$.

drag coefficient increases with increasing packing density. But once the threshold of $\lambda_p = 0.29$ is reached, the flow interprets the top of the building array as a displaced surface, and the flow in the canopy layer is low and negligible with respect to the flow above the canopy layer.
The $k-\ell$ closure also requires a model for the length scales $l_k$ and $l_\varepsilon$. The following relation between these two length scales can be obtained using Eqs. 4.3, 4.4 and 4.6:

$$C_k \ell_k = C_\mu \frac{\ell_\varepsilon}{C_\varepsilon} \tag{4.21}$$

Therefore, from the CFD outputs, using Eq. 4.6 Santiago et al. (2010) calculated the ratio $\ell_\varepsilon/C_\varepsilon$, assuming this value 1) to be constant within the canopy layer ($z/h < 1$), 2) to be linearly growing in a zone of transition in the area just above the canopy layer ($1 < z/h < 1.5$) and 3) to increase linearly well above the canopy ($z/h > 1.5$):

$$\frac{\ell_\varepsilon}{C_\varepsilon} = \begin{cases} 2.24(h-d) & \text{if } z/h \leq 1 \\ 2.24(z-d) & \text{if } 1 < z/h \leq 1.5 \\ 1.12(z-d_2) & \text{if } z/h > 1.5 \end{cases} \tag{4.22}$$

where the coefficients are calculated using the urban configuration with $\lambda_p = 0.25$, $d_2$ is computed in order to make $\ell_\varepsilon/C_\varepsilon$ continuous at $z/h = 1.5$ and $d/h = \lambda_p^{0.13}$, obtained fitting the CFD data in the different configurations.

The advantage of using a $k-\varepsilon$ turbulence scheme for this particular case is that a length

scale is not needed, therefore the calculation of the different length scales and of the displacement height $d$ is not required. $C_{d\varepsilon}$ needs to be calculated for the $k-\varepsilon-1T$ closure, while the $k-\varepsilon-3T$ scheme adopts the same drag coefficient of the $k-\ell$ closure. However, despite we tried to obtain $C_{d\varepsilon}$ inverting Eqs. 4.12 and 4.16 and fitting the result, we could not find reasonable values, since within the canopy the flow variables tend to reach zero (for example $u$) or to large value (like $\varepsilon$). For this reason, for each packing density a large number of simulations are performed varying $C_{d\varepsilon}$, and taking the value which minimizes the mean of the Root Mean Square Error of $u$, $k$ and $\varepsilon$ along the vertical domain, adopting the CFD output as reference. The dependence of $C_{d\varepsilon}$ on the packing density (shown in Fig. 4.3), follows two different functions: a parabola up to $\lambda_p = 0.25$, and a straight line for higher packing densities. Its dependence on $\lambda_p$ reads:

$$C_{d\varepsilon}(\lambda_p) = \begin{cases} a_1 \lambda_p^{-b_1} + b_2 & \text{if } \lambda_p \leq 0.25 \\ -a_2 \lambda_p + b_3 & \text{if } \lambda_p > 0.25 \end{cases} \tag{4.23}$$

with $a_1 = 0.07$, $b_1 = -1.4$, $b_2 = 8.3$, $a_2 = 14.8$ and $b_3 = 12.4$. Note that while $C_d$ increases with packing density, $C_{d\varepsilon}$ decreases with increasing $\lambda_p$. The reason is that large packing densities tend to decrease the turbulence generated within the canopy layer, and a decrease in turbulence intensity is reflected in a decrease of the dissipation rate $\varepsilon$. As we will show in the next section (4.5), for larger packing densities the flow variables are almost null within the canopy layer, and the horizontal flow starts to develop over the roof level.
The limitation of the model using the $C_{d\varepsilon}$ estimated with the CFD output lies in the function for the drag coefficient for $\lambda_p < 0.25$. With $\lambda_p$ approaching zero, $C_{d\varepsilon}$ tends to increase rapidly, and so does proportionally the dissipation rate. Therefore, additional CFD simulations should be performed to estimate the drag coefficient for $\lambda_p < 0.0625$, where this model is not able to reproduce correctly the flow in the urban canopy layer.

## 4.5 Results: Validation of One-Dimensional UCP with Spatially-Averaged CFD simulations

This section shows the comparison between the the three 1-D column models and the CFD simulations. The 1-D column models (summarized in Table 4.1) evaluated here are:

1) the $k-\ell$ turbulence closure, where $D_u$ and $D_k$ are calculated through Eq. 4.14 and 4.15, respectively. The drag coefficient $C_d$ is estimated using the CFD simulations, and it is given by Eq. 4.20. Moreover, the length scales are calculated with Eq. 4.22. For further details, refer to Santiago et al. (2010);

2) the $k-\varepsilon-1T$ turbulence closure. Here $D_u$ and $D_k$ are the same as in the $k-\ell$ closure, but, in addition, the dissipation rate $\varepsilon$ is computed prognostically with Eq. 4.12. The drag force induced by buildings ($D_\varepsilon$) is calculated through Eq. 4.16, and the drag coefficient specific for $\varepsilon$ is calculated with Eq. 4.23. This estimation is deduced through a best-fit analysis between the $k-\varepsilon$ and the CFD outputs, for all the packing densities.

3) the $k-\varepsilon-3T$ turbulence closure. $D_u$ is the same as in the $k-\ell$ closure, but $D_k$ is computed through equation 4.17, while $D_\varepsilon$ through Eq. 4.18. The advantage with respect

| | $k$ Equation | $\varepsilon$ Equation | $D_k$ | $D_\varepsilon$ | Model Constants |
|---|---|---|---|---|---|
| $k-\ell$ | Eq. 4.5 | Eq. 4.6 | $S(z)C_d\left\|\langle\overline{u(z)}\rangle\right\|^3$ | - | $C_d$ (Eq. 4.20)<br>$\ell_\varepsilon/C_\varepsilon$ (Eq. 4.22) |
| $k-\varepsilon-T1$ | Eq. 4.5 | Eq. 4.7 | $S(z)C_d\left\|\langle\overline{u(z)}\rangle\right\|^3$ | $S(z)C_{d\varepsilon}\|\langle\overline{u}\rangle\|\langle\overline{\varepsilon}\rangle$ | $C_d$ (Eq. 4.20)<br>$C_{d\varepsilon}$ (Eq. 4.23) |
| $k-\varepsilon-T3$ | Eq. 4.5 | Eq. 4.7 | Eq. 4.17 | Eq. 4.18 | $C_d$ (Eq. 4.20)<br>$\alpha_2=8$, $\beta_2=5.5$ |

**Table 4.1:** Overview of the different terms employed for the three UCPs tested against CFD output.

to the previous two models is that this scheme does not require a parameterization (i.e. a dependence between model constants and packing density) neither for a length scale nor for the drag coefficient for the dissipation rate.

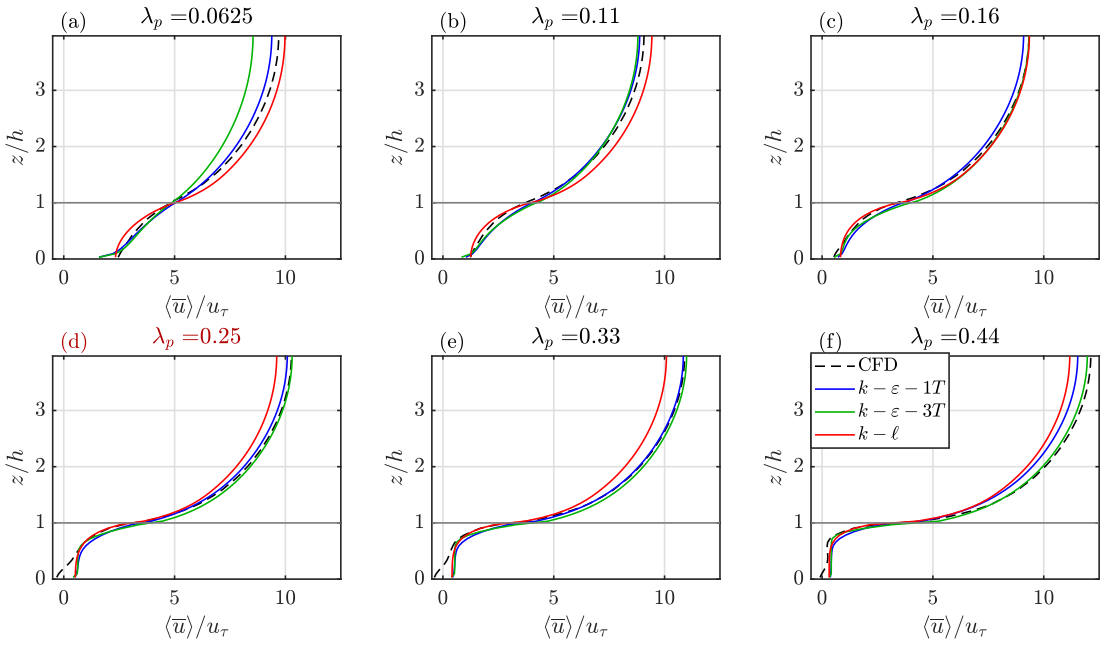


**Figure 4.4:** Vertical profiles of normalized mean wind speed for all the packing densities.

To quantify the differences between the UCPs and the CFD simulations, taken as reference, for each variable of the flow and for each packing density, the Root-Mean-Square-Error (RMSE) has been computed. It reads:

$$RMSE=\sqrt{\frac{\sum_{n=1,N}\left(\langle\overline{\Psi_{CFD}}\rangle-\langle\overline{\Psi_{UCP}}\rangle\right)^2}{N}} \tag{4.24}$$

where $\Psi=(u,k,\varepsilon,K_m,u'w')$, and $n=1,N$ are the vertical levels. Vertical profiles for the spatially-averaged CFD (black dashed line), $k-\ell$ (red line), $k-\varepsilon-1T$ (blue line) and $k-\varepsilon-3T$ (green line) are shown for each $\lambda_p$ and for the variables of the flow $\langle\overline{u}\rangle$, $\langle\overline{k}\rangle$, $\langle\overline{\varepsilon}\rangle$, $K_m$, $\langle\overline{u'w'}\rangle$ in Fig. 4.4, 4.5, 4.6, 4.7 and 4.8, respectively. All the variables, apart for $\langle\overline{\varepsilon}\rangle$, are normalized by means of $u_\tau$ and $h$. The RMSEs have been computed separately for the vertical points within the urban canopy (Fig. 4.9), above the urban canopy (Fig. 4.10), and over all the column of air (Fig. 4.11). We will discuss first the results for the simulations with $\lambda_p=0.25$, displayed in

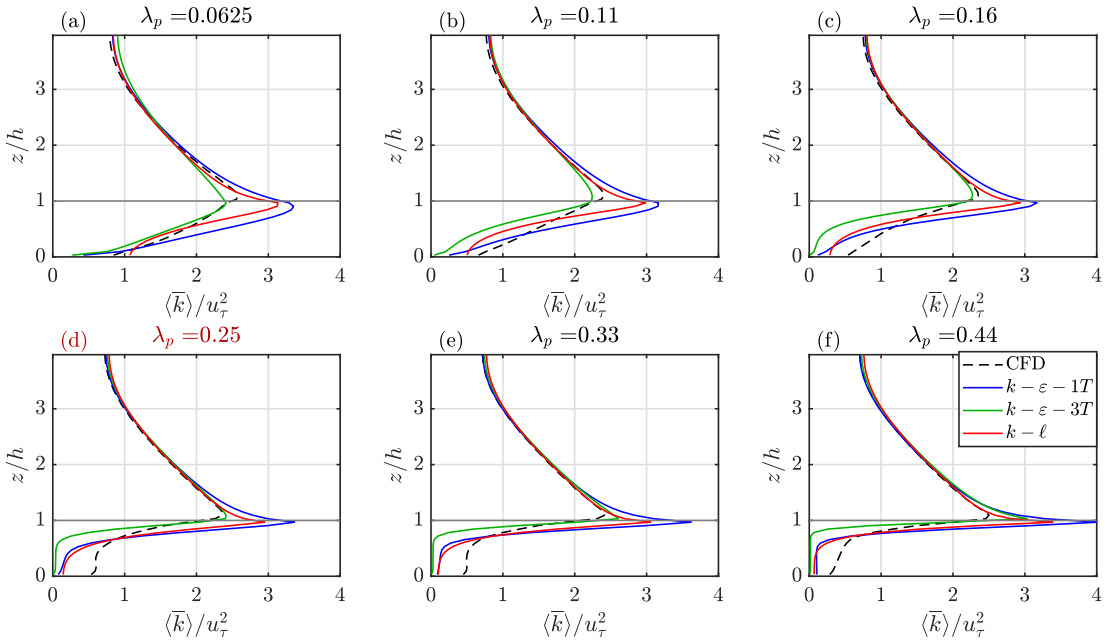


**Figure 4.5:** Vertical profiles of normalized mean $TKE$ for all the packing densities.

panel (d) in the various figures, which is the case that was previously validated against experimental data and DNS simulations (Cheng et al., 2007; Coceal et al., 2006).

The vertical profile of the spatially-averaged wind speed (Fig. 4.4) resembles the typical profile of a neutral boundary layer, with the presence of obstacles: up to $z \sim h/2$ the wind is almost constant for all UCP simulations, while the CFD simulation displays even negative wind speed because it is able to resolve the vortexes developing within urban canyons. At $z \sim h$ there is the largest wind shear, because the horizontal pressure gradient forces a wind of $\sim 10$ m s$^{-1}$ above the canopy, which is strongly reduced below roof level due to the presence of the buildings. Indeed, over the canopy layer, the profile follows the log law. As expected, UCP simulations cannot capture the negative wind speed close to the surface, since in 1-D simulations buildings are not explicitly resolved and then re-circulation cells cannot be reproduced. However, from $z \sim h/2$ all UCPs can reproduce the wind speed shown by the CFD simulation, in particular, $k-\ell$ is in good agreement up to the first levels above the canopy, but from $z \sim 1.5h$ it underestimates the wind speed. On the other hand, $k-\varepsilon-3T$ works better than $k-\ell$, but it slightly overestimates $\langle\overline{u}\rangle$ right above the buildings top, while $k-\varepsilon-1T$ is the UCP which shows the best agreement.

Since the largest shear is close to the building top, the $TKE$ vertical profile presents its largest value around $h$, as shown by Fig. 4.5. Within the canopy layer, $TKE$ is low and almost constant with height, then it rapidly grows and finally decreases with increasing height. All UCPs underestimate the $TKE$ within the canopy layer since they underestimate the wind shear. The underestimation grows with increasing the packing density. On the other hand, they can reproduce the peak at $z \sim h$. Specifically, $k-\ell$ and $k-\varepsilon-1T$ overestimate the intensity of the peak and underestimate its height. On the other hand, $k-\varepsilon-3T$ is the best in reproducing the $TKE$ peak, despite the higher underestimation within the canopy layer. Above the canopy, all simulations can represent the decrease of $TKE$.

Dissipation rate vertical profiles of Fig. 4.6 display a shape similar to the $TKE$, with the high-

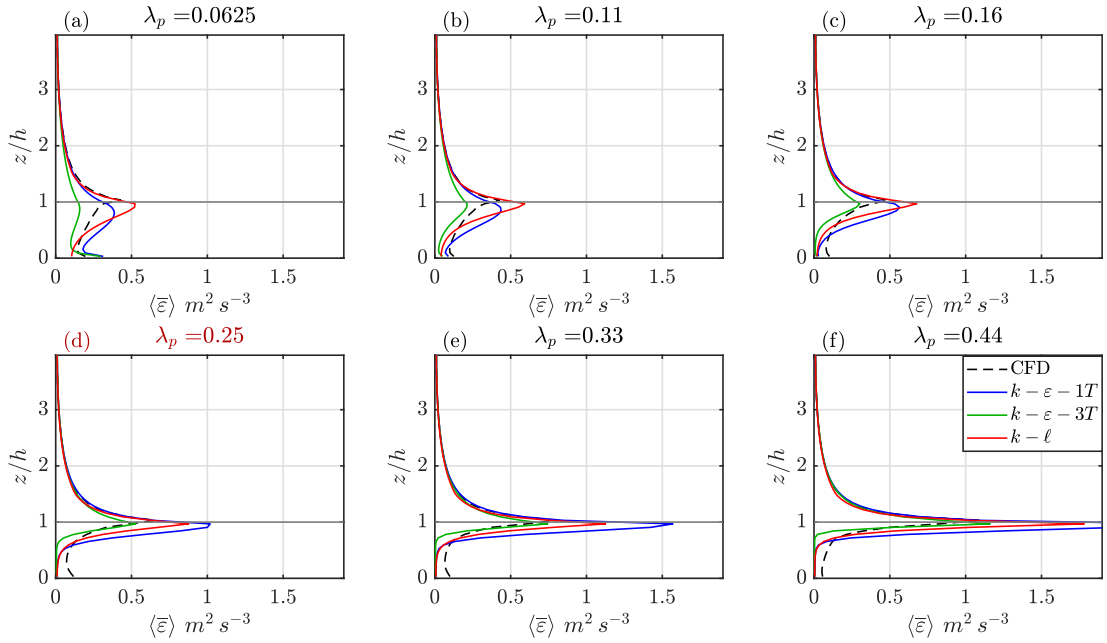


**Figure 4.6:** Vertical profiles of dissipation rate for all the packing densities.

est value at $z \sim h$. Again, $k-\ell$ and $k-\varepsilon-1T$ overestimate the peak intensity and underestimate $\langle\overline{\varepsilon}\rangle$ within the canopy, while $k-\varepsilon-3T$ better agrees with the CFD simulation, despite a slight underestimation of the peak. Through Eqs. 4.3 and 4.4 for $k-\ell$ an $k-\varepsilon$, respectively, one can

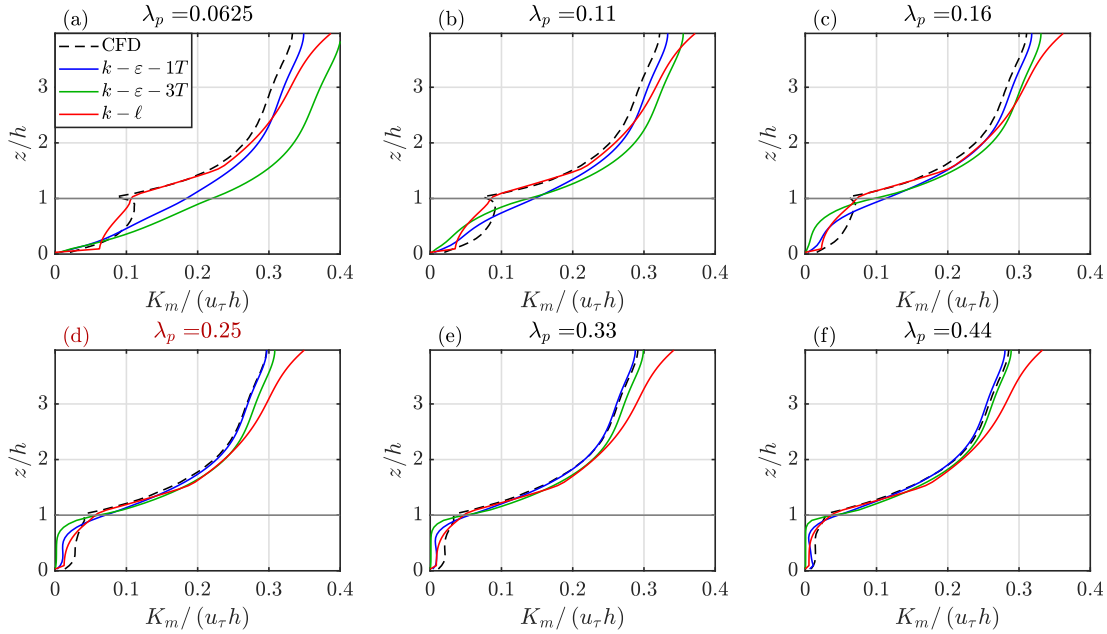


**Figure 4.7:** Vertical profiles of normalized mean eddy diffusivity for all the packing densities.

estimate the eddy diffusivity, which is shown in Fig. 4.7. Because of the underestimation of the $TKE$, all the UCPs underestimate $K_m$ within the canopy layer. Around $z \sim h$, instead, they all start to agree with the CFD simulation, with a better agreement for $k-\ell$ and $k-\varepsilon-3T$, which better capture the height and the slope of the maximum increase of the eddy diffusivity. From $z \sim 2h$, $k-\ell$ eddy diffusivity starts to diverge, with an overestimation of $K_m$, while the

two $k-\varepsilon$ are in better agreement. This is an expected result, since at higher levels the flow becomes more spatially homogeneous, and the two $k-\varepsilon$ and the CFD simulation adopt the same turbulence closure, that in absence of obstacles becomes identical.

On the other hand, $k-\ell$ is the best in reproducing the profiles of the spatially-averaged vertical

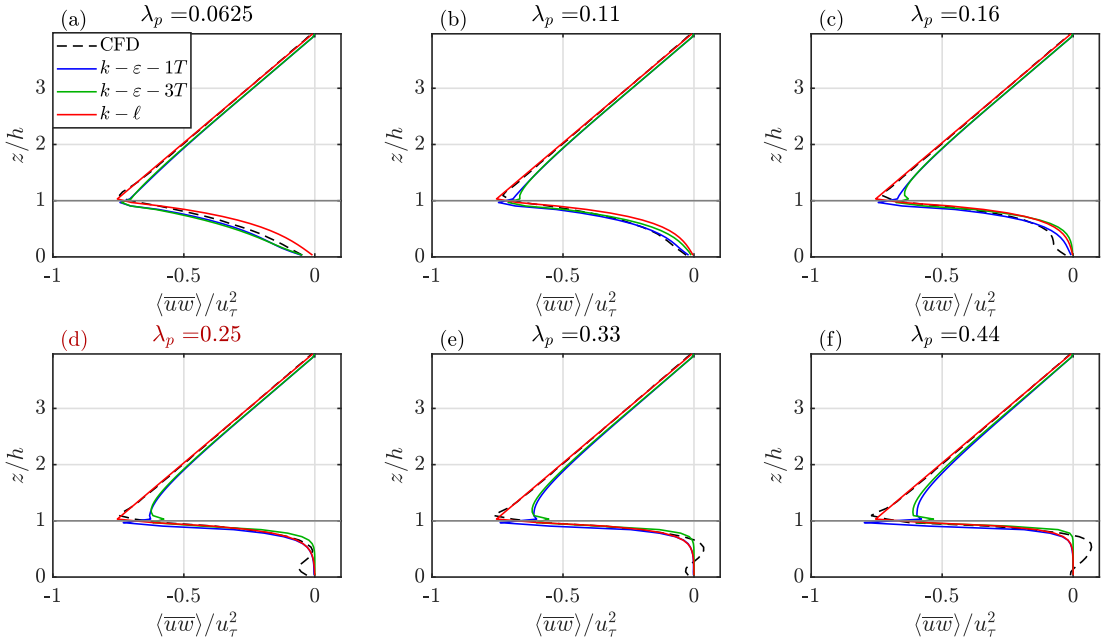


**Figure 4.8:** Vertical profiles of normalized mean vertical momentum flux for all the packing densities.

momentum flux (Fig 4.8): again, within the canopy, the profile is constant (and almost null) for all UCPs, while the CFD simulation shows small oscillations because of the recirculation cells. The negative peak takes place at $z \sim h$. It is not well captured by $k-\varepsilon-1T$, while $k-\varepsilon-3T$ is in good agreement in terms of the peak intensity. However, right above the canopy, while $k-\ell$ truly follows the linear decrease (in absolute value) of $\langle\overline{u'w'}\rangle$, the two $k-\varepsilon$ display a rapid decrease of the momentum flux, which is in good agreement only for $z > 2h$.

Analyzing the RMSEs within the canopy (Fig. 4.9), for $\lambda_p = 0.25$ (fourth columns), all UCPs perform similarly in terms of wind speed, with slightly better results for $k-\ell$. The latter shows a better agreement with respect to the CFD simulation even for $TKE$, $K_m$ and $\langle\overline{u'w'}\rangle$. On the other hand, $k-\varepsilon-3T$ largely improves the vertical profiles of the dissipation rate (panel (c)), and it performs similarly to $k-\ell$ for wind speed and $\langle\overline{u'w'}\rangle$. Hence, in general $k-\ell$ performs better than the two $k-\varepsilon$ within the canopy layer, apart for $\langle\overline{\varepsilon}\rangle$.

On the other hand, if we analyze the RMSE for the vertical levels above the canopy layer ($h < z < 4h$) it is clear that $k-\varepsilon-3T$ better performs with respect to the other two: the wind speed is reproduced similarly to $k-\varepsilon-1T$, and errors are half with respect to $k-\ell$, while the reproduction of the dissipation rate and $TKE$ is largely improved. However, $k-\ell$ remains the best in reproducing the vertical momentum flux, because of the error committed by the two $k-\varepsilon$ at the levels right above the buildings top.

In general, the errors above the canopy are half with respect to those within the canopy, since the mean flow is disturbed by the presence of the buildings, and the UCP simulations cannot

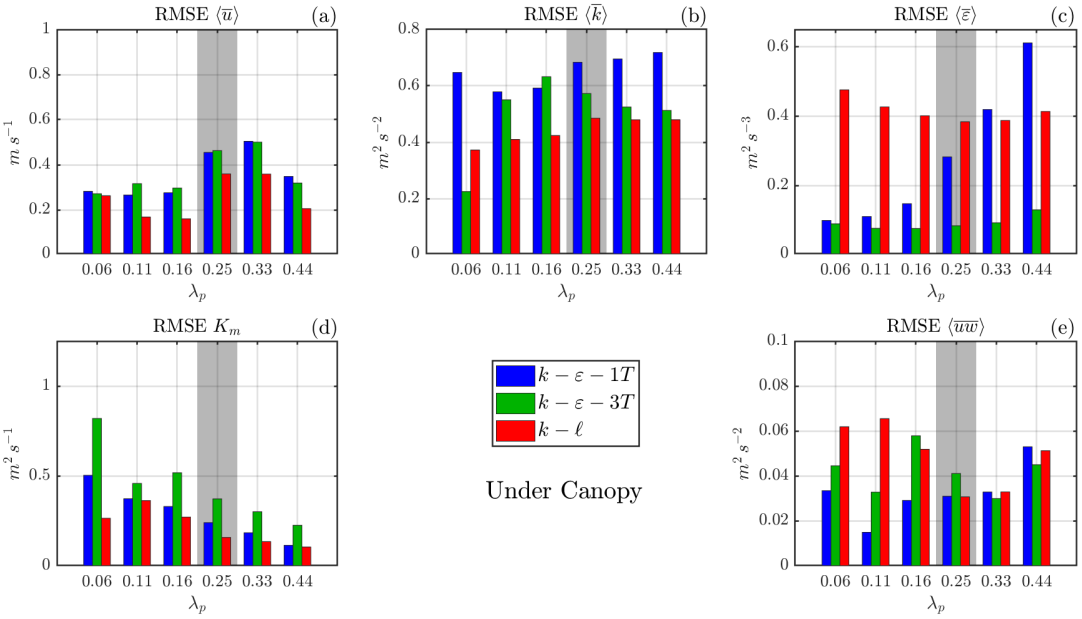


**Figure 4.9:** RMSEs computed for the vertical points within the urban canopy layer (0-$h$), for all the variables and packing densities.

resolve the obstacles. Figure 4.11 displays the errors for all the air column ($0 < z < 4h$). For $\lambda_p = 0.25$, the two $k-\varepsilon$ better perform than $k-\ell$ in terms of wind speed, dissipation rate and eddy diffusivity. However, they cannot improve the reproduction of $TKE$ and vertical momentum flux. Comparing the two $k-\varepsilon$, $k-\varepsilon-3T$ performs slightly better than $k-\varepsilon-1T$ in terms of $TKE$ and $\langle\overline{u'w'}\rangle$, while it reproduces much better the dissipation rate.

Now, we will discuss the results of the different simulations considering all the packing den-

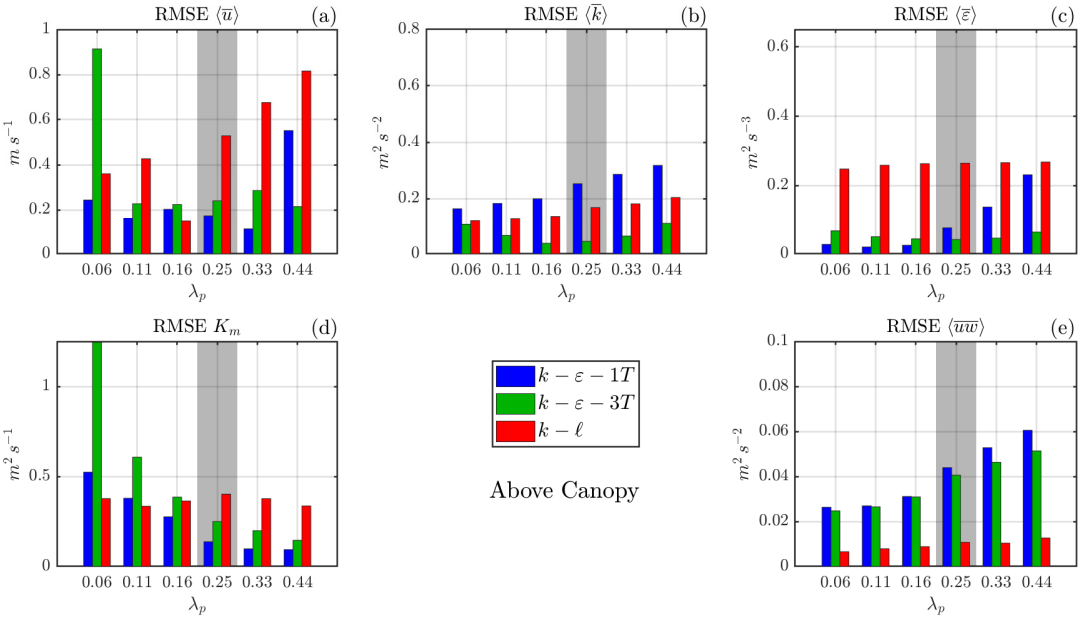


**Figure 4.10:** RMSEs computed for the vertical points above the urban canopy layer ($h$-4$h$), for all the variables and packing densities.

sity spectrum ($\lambda_p = 0.0625 - 0.44$). In terms of wind speed (Fig. 4.4), the largest discrepancy between UCPs and the CFD simulations is displayed by the configuration with $\lambda_p = 0.0625$: here, while $k-\ell$ underestimates the wind speed within the canopy and overestimates it above the canopy, the two $k-\varepsilon$ better reproduce the wind speed within the canopy (apart for a large underestimation in the layer closer to the ground), while they underestimate the wind speed above the canopy. In particular, $k-\varepsilon-3T$ is the one that shows the largest difference with the CFD simulations at the highest levels. With increasing $\lambda_p$, all UCP simulations well perform in the layers between $h/2 < z < h$, while they cannot capture the re-circulation cell at $z < h/2$. The maximum wind speed increases with increasing packing density, since packed buildings produce less turbulence through the drag, and less energy is therefore dissipated at higher levels. Above the canopy layer, the largest discrepancies take place for $k-\ell$, which overestimates the maximum wind speed for low packing densities, and underestimates it for higher $\lambda_p$, while the two $k-\varepsilon$ better capture the wind maximum, with a better agreement shown by $k-\varepsilon-1T$ at low $\lambda_p$ and by $k-\varepsilon-3T$ at high $\lambda_p$. Wind speed RMSEs (panel (a) in Fig. 4.9, 4.10 and 4.11) are similar for all UCPs within the canopy layer, with a slightly better performance by $k-\ell$. However, above the canopy layer, $k-\ell$ departs from CFD simulations with increasing $\lambda_p$. On the other hand, the error displayed by the two $k-\varepsilon$ remains low and constant for the central range of $\lambda_p$, with higher discrepancies at the two extremes.

Fig. 4.5 shows the vertical profiles of $TKE$. Within the canopy, UCPs perform better for low packing densities than for high packing densities, where $TKE$ decreases too fast with respect to CFD simulations. At $z \sim h$, the turbulent kinetic energy presents a peak, almost constant with varying $\lambda_p$. While $k-\ell$ and $k-\varepsilon-1T$ generally overestimate the peak for all packing densities, $k-\varepsilon-3T$ is in better agreement with CFD simulations, despite a slight underestimation for low $\lambda_p$. Finally, above the canopy layer, all UCPs reproduce well the vertical profile of $TKE$ for all the packing densities. Errors within the canopy are lower for $k-\ell$, followed by $k-\varepsilon-3T$ (panel (b) in Fig. 4.9) and almost constant with $\lambda_p$ for all UCPs. Over the canopy, instead, $k-\varepsilon-3T$ displays RMSEs less than half with respect to $k-\ell$. The latter performs better than $k-\varepsilon-1T$, which shows RMSEs increasing with packing density.

While the $TKE$ peak remains approximately constant with increasing $\lambda_p$, the dissipation rate peak largely increases with the packing density (Fig. 4.6). The behavior is similar to the $TKE$: within the canopy, at low packing densities, UCPs agree better with CFD data than at high packing densities. In general, for $z < h$, $k-\ell$ overestimates the dissipation rate, while $k-\varepsilon-1T$ diverges with increasing $\lambda_p$. The best results are displayed by $k-\varepsilon-3T$, which, despite an underestimation for low packing densities, can capture the increase of $\varepsilon$ approaching $z = h$, and well reproduces the peak, where the other two parameterizations tend to overestimate the maximum, especially for high packing densities. In fact, $k-\varepsilon-3T$ displays much lower errors than $k-\ell$ for all packing densities, and than $k-\varepsilon-1T$ with increasing $\lambda_p$, both within the canopy (panel (c) in Fig. 4.9) and over the canopy (panel (c) in Fig. 4.10).

Eddy diffusivity vertical profiles (Fig. 4.7) follow an almost linear increase ($K_m \propto u_\star z$ for the Monin-Obukhov similarity theory) above $z \sim 2h$. Below this level, $K_m$ increases slowly up to $z \sim h$, and then more rapidly up to $z \sim 2h$. The major difference between different $\lambda_p$ takes place within the canopy layer, where $K_m$ decreases with increasing packing density. The largest

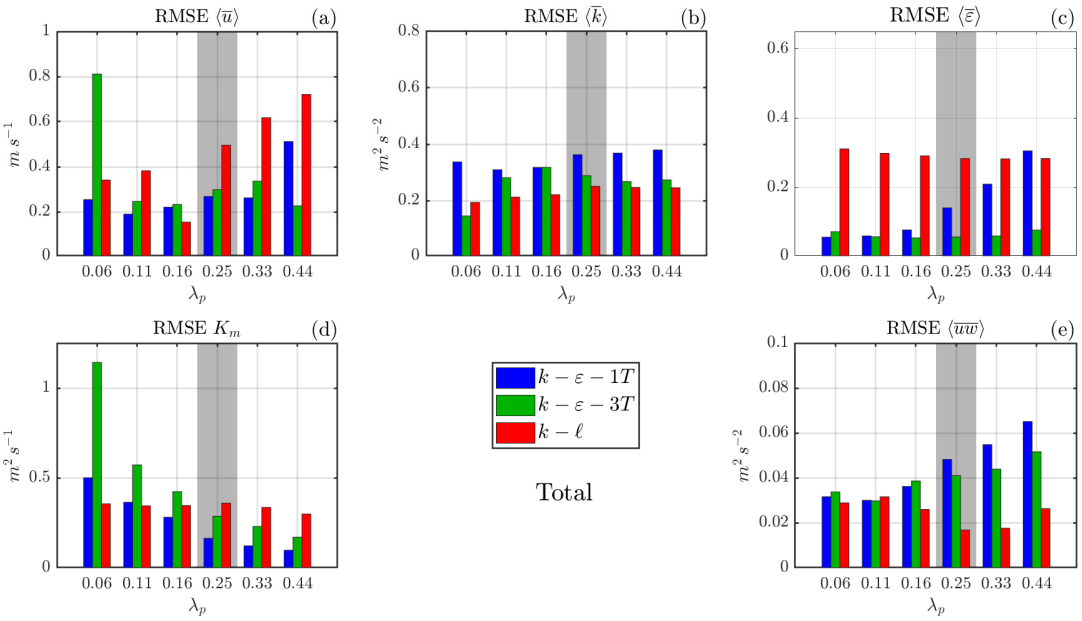


**Figure 4.11:** RMSEs computed for the vertical points for all the column of air (0-4$h$), for all the variables and packing densities.

discrepancies between CFD and UCP simulations occur for low packing densities, where all UCPs tend to overestimate the eddy diffusivity, especially for $0 < z < 2h$. The best performance is shown by $k-\ell$, while $k-\varepsilon-1T$ and $k-\varepsilon-3T$ overestimate $K_m$ along all the vertical layers, with the latter that shows the worst agreement. Increasing the packing density, all UCPs tend to well reproduce $K_m$ up to $z \sim 2h$. Above this height, $k-\ell$ overestimates the eddy diffusivity. This overestimation explains the underestimation of the wind speed above the canopy layer shown in Fig. 4.4d-e-f: the higher the eddy diffusivity, the lower the wind speed becomes since the vertical diffusion is enhanced. Within the canopy layer, RMSEs decrease with increasing $\lambda_p$ (Fig. 4.9), with higher errors for $k-\varepsilon-3T$, due to its underestimation of $K_m$. On the other hand, above the canopy top (Fig. 4.10), while $k-\ell$ shows almost constant errors with $\lambda_p$, the errors of the two $k-\varepsilon$ are higher than those of $k-\ell$ for low packing density, but they diminish increasing the packing density.

Figure 4.8 shows the vertical profiles of the turbulent momentum flux. Within the canopy layer, $\langle\overline{u'w'}\rangle$ increases in absolute value up to $z \sim h$ for all packing densities, with a slope which is quasi-linear for low packing densities, while it increases rapidly approaching the canopy layer top for high $\lambda_p$. The negative peak takes place at $z \sim h$, and it is the same for all the configurations. Above the canopy, the momentum flux linearly decreases with the same rate, and similarly for all $\lambda_p$. All UCP simulations work similarly within the canopy layer, with the best performances in terms of RMSEs by the two $k-\varepsilon$ for low packing densities. With increasing $\lambda_p$ all simulations display a similar RMSE since the momentum flux is null in the lower part of the canopy layer. At $z \sim h$ all UCPs can reproduce the negative peak which occurs in the CFD simulations. However, while for $k-\ell$ the linearity above the canopy layer is well represented, with increasing $\lambda_p$, the two $k-\varepsilon$ show a rapid decrease in the absolute value of the momentum flux, and then the linearity with height is not well represented. For this reason,

over the canopy layer, the RMSE for the two $k-\varepsilon$ closures is always higher than the error of $k-\ell$, and increases with increasing packing density (Fig 4.10). Therefore, along all the air column, the total error (Fig. 4.11) is similar between all UCPs up to $\lambda_p = 0.16$, but beyond this value errors by the two $k-\varepsilon$ start to diverge, faster for $k-\varepsilon-1T$, while RMSEs for $k-\ell$ are constant or slightly decreasing.

## 4.6 Discussion and Conclusions

In this work, we propose a one-dimensional urban canopy scheme, based on the $k-\varepsilon$ turbulence closure, suitable for reproducing the wind flow within the urban canopy layer. As reference, we consider CFD simulations with a spatial resolution high enough to resolve buildings and their interaction with the airflow. The CFD simulations from Santiago et al. (2010), performed for idealized urban configurations (staggered arrays of cubes) have been used first to derive the drag coefficients and then to evaluate the UCP schemes through a spatial average over the domain of simulation. One-dimensional $k-\varepsilon$ turbulence closures have been successfully employed for reproducing the flow within vegetated canopies (see for example Katul et al., 2004), but never for urban environments. In this work, we propose two different kinds of closure, starting from previously developed UCPs based on the $k-\ell$ turbulence scheme. The simplest one adopts an additional source term for the prognostic $\varepsilon$ equation ($k-\varepsilon-1T$), whose drag coefficient, depending on the packing density, has been derived from the CFD building-resolving simulations. The second one includes an additional term for the prognostic turbulent kinetic energy equation, and two additional terms for the prognostic $\varepsilon$ equation ($k-\varepsilon-3T$). The advantage of thhe latter is that it does not need the parameterization of the dissipation drag coefficient nor a model for the turbulent length scale (as Santiago et al., 2010 did for the $k-\ell$ closure), so it depends on the CFD just for the computation of the vertically-averaged drag coefficient due to buildings.

The results of the comparison between one-dimensional UCPs and CFD outputs demonstrate that the new closures reasonably represent the vertical profiles of the relevant variables, capturing the vertical heterogeneity of the flow induced by the buildings array. The sensitivity to packing density is well captured by all the UPCs, since vertical gradients of both mean and turbulent variables increase with increasing packing density. Comparing the various UCPs, the two $k-\varepsilon$ enhance the reproduction of wind speed with respect to $k-\ell$, especially far from the urban canopy layer. In particular, $k-\varepsilon-1T$ works better for low packing densities, while $k-\varepsilon-3T$ for densely packed buildings. Both the $k-\varepsilon$ improve the reproduction of the dissipation rate, especially within the canopy layer. Moreover, $k-\varepsilon-3T$ is the most efficient in capturing the peaks at the top of the canopy. On the other hand, $k-\ell$ remains the best performing closure in reproducing $TKE$ and vertical turbulent momentum flux.

Besides the improvement in the reproduction of the flow, the newly developed closures rely less than the $k-\ell$ on the CFD outputs for the derivation of drag coefficients, since ad-hoc mixing length scales and displacement heights are not required. In particular, $k-\varepsilon-1T$ needs two drag coefficients, while $k-\varepsilon-3T$ is even less dependent on the CFD results since it uses a single drag coefficient, which still depends on the packing density, but it is the only parameter added to the traditional $k-\varepsilon$ closure, and it is the same derived in Santiago et al. (2010).

Based on the results presented before, the formulation proposed here can be incorporated within mesoscale models, aiming to improve the representation of the interaction between cities and the atmospheric boundary layer for real case studies. Moreover, the employment of a $k-\varepsilon$-based turbulence closure is beneficial in terms of the coupling between meso- and micro-scale models, since usually microscale simulations are performed with similar closure schemes, and turbulent variables can be passed as input, resulting in a more robust coupling. Future studies will include the comparison of the current scheme with recently developed high-resolution Large Eddy Simulations for the same idealized case study (Nazarian et al., 2019), as well as the implementation within more complex state-of-the-art UCPs like BEP+BEM (Martilli et al., 2002; Salamanca et al., 2010), which includes even the thermal exchanges between the urban structures and the atmosphere.

# 5 On a New $K-\varepsilon$ Turbulence Closure for complex terrains and urban areas: an Application in the Adige Valley for the city of Trento

**Abstract**

In this study, we present novel 1.5-order PBL turbulence closures based on the $K-\varepsilon$ turbulence scheme, coupled with the BEP+BEM multi-layer urban canopy parameterization and incorporated into the Weather Research and Forecasting (WRF) model. The aim of this work is to assess the capability of a length-scale-independent turbulence closure to reproduce the Planetary Boundary Layer (PBL) dynamics for an urban area and its surroundings situated in mountainous terrain. The novel PBL closures include the standard $K-\varepsilon$ turbulence parameterization, toghether with the estimation of the Prandtl number, a correction term for the dissipation rate ($\varepsilon$) prognostic equation, a counter-gradient term for accounting of the large eddies transport, and the prognostic calculation of the potential temperature variance. The performance of the novel PBL schemes is compared with the state-of-the-art turbulence closures by Bougeault and Lacarrere (BouLac) and Mellor-Yamada-Janjic (MYJ) for four clear-sky summer days of August 2016 for the city of Trento (Italy), situated in the Alpine Adige Valley, and validated against measurements from surface weather stations. Results show that the modified versions of the $K-\varepsilon$ turbulence closure generally perform better than BouLac, MYJ, and the standard version of the $K-\varepsilon$ turbulence scheme. Specifically, improvements are detected in the reproduction of the maximum and minimum temperature, both for urban and rural areas, at weather stations situated on the valley floor. Further enhancements are found in the reproduction of the thermally-driven up-valley winds, in particular for the maximum wind intensity. These novel PBL turbulence closures can represent a further improvement in reproducing PBL processes for complex terrain and urban areas.

## 5.1 Introduction

The dynamics of the Planetary Boundary Layer (PBL) over complex terrain encompasses a broad range of phenomena, including all the scales of the atmospheric motion (Serafin et al.,

2018). For this reason, modelling PBL processes and the related turbulent dispersion in mountainous areas is a very challenging task. The task becomes even more difficult, if heterogeneous land cover is present in mountainous regions, such as in the case of urban areas. In fact, PBL processes over complex terrain present strong gradients and inhomogeneities, leading to higher inaccuracies in their representation with Numerical Weather Prediction (NWP) models at the mesoscale (Arnold et al., 2012; Baklanov et al., 2011). Moreover, different PBL schemes adopt different assumptions regarding the vertical mixing and the transport of mass and energy, leading to differences in the reproduction of PBL processes (Avolio et al., 2017; Hu et al., 2010). The simplest PBL models adopt first-order closures, that usually produce insufficient vertical transport (Moeng et al., 1989), and their lack of prognostic equations for turbulence variables and non-locality (Hong et al., 2006b) neglect the “memory effect" and the turbulent transport of higher-order moments, which can be non-negligible in inhomogeneous terrain. On the other side, approaches including prognostic equations of third order (or higher) moments, such as Colonna et al. (2009) and Zilitinkevich et al. (1999) would be beneficial, but they are often computationally too demanding or numerically unstable in complex terrain. A reasonable compromise is to employ 1.5-order PBL schemes, i.e. solving a prognostic equation for turbulent kinetic energy (TKE, Bougeault et al., 1989, Janjic, 2002). These PBL schemes are all based on diagnostic equations for the mixing length scales, employed to model the dissipation rate ($\varepsilon$) and the eddy viscosity/diffusivity ($\nu_M/\nu_H$). These kinds of turbulence closures have been widely used within the Weather Research and Forecasting (WRF) model (Skamarock et al., 2019) to simulate atmospheric flows in complex terrain (Liu et al., 2020; Tomasi et al., 2019; Tomasi et al., 2017) and in urban areas situated in mountainous regions (Giovannini et al., 2014; Pappaccogli et al., 2018; Salamanca et al., 2012a), through the coupling with the BEP+BEM (Martilli et al., 2002; Salamanca et al., 2010) multi-layer urban canopy parameterization.

However, these aforementioned 1.5-order PBL schemes usually require an ad-hoc definition of the mixing length scales, and the parameterization adopted to define them strongly influences the model performance (Ferrero et al., 2021). Moreover, these kinds of PBL schemes do not account for the “memory effects" and the turbulent transport of the length scale (and consequently of the dissipation rate), that becomes relevant over inhomogeneous surfaces and terrain (Beljaars et al., 1987).

In this work, we test the capability of a $K-\varepsilon$ turbulence closure at mesoscale resolution, opportunely modified as in Chapter 3 and coupled with the BEP+BEM multi-layer urban canopy parameterization as in Chapter 4, to reproduce PBL processes for the city of Trento (Italy), situated in the Alpine Adige Valley, adopting the WRF model. The objective is particularly challenging, due to the highly complex terrain surrounding the urban area of Trento, which is a relatively small city located in a narrow valley. Daily-periodic valley winds take place along the Adige Valley, especially on sunny days, induced by pressure gradients following the temperature contrasts between the valley and the adjacent plain (Serafin et al., 2011; Zardi et al., 2013), analyzed in detail in Giovannini et al. (2017). Recent investigations highlighted the importance of using high-resolution input datasets for correctly defining both urban morphology (Hammerberg et al., 2018; Pappaccogli et al., 2021; Zonato et al., 2020) and orography (Giovannini et al., 2014; Jee et al., 2016), especially in such heterogeneous terrain. Accordingly,

for the present study, we carefully obtained high-resolution datasets, at a suitable resolution, to improve the representation of urban areas and of the orography. The present paper is organized as follows: the theory of the newly-introduced PBL schemes is shown in Section 5.2 (the model is the same presented in Chap. 3, Section 3.2, but it is reported also here to facilitate the reader). The methodology, the simulation set-up, and the input datasets adopted are described in Section 5.3. In section 5.4, results from numerical simulations are validated against measurements from weather stations, and compared with other state-of-the-art 1.5-order PBL schemes. Finally, in Section 5.5, results are summarized and some conclusions are drawn.

## 5.2 The model

The model presented here derives from the Reynolds-averaged Navier-Stokes (RANS) equations, in which each variable of the mean flow is decomposed into its mean part (upper case letters), representing an ensemble average, and a fluctuating part (lower case letters). It is customary for the ABL over flat horizontal uniform terrain to neglect the advection terms (i.e. the material derivative coincides with the local time derivative). Then the mean flow equations are:
Zonal wind speed:

$$\frac{\partial U}{\partial t} = -\frac{\partial \overline{wu}}{\partial z} + f(V - V_g) \tag{5.1a}$$

Meridional wind speed:

$$\frac{\partial V}{\partial t} = -\frac{\partial \overline{wv}}{\partial z} - f(U - U_g) \tag{5.1b}$$

Potential temperature:

$$\frac{\partial \Theta}{\partial t} = -\frac{\partial \overline{w\theta}}{\partial z} \tag{5.1c}$$

where $f = 2\Omega \sin\phi$ is the Coriolis parameter and $\vec{U}_g = (U_g, V_g)$ is the geostrophic wind. The quantities $\overline{wc}$, where $c = (u, v, \theta)$ represent turbulent vertical fluxes. Assuming horizontally homogeneous conditions, it is possible to neglect horizontal derivatives. The aim of this work is to find a closure for the turbulent fluxes, in terms of mean quantities, that does not depend on a diagnostic length scale, which does not consider the time evolution and the vertical transport, but instead on local properties of the atmospheric state, e.g. adopting a prognostic equation for the dissipation rate, skipping the step of defining a diagnostic length scale.

### 5.2.1 The $K - \varepsilon$ Turbulence Closure

As for most turbulence models, we assume that the turbulent fluxes are proportional to the eddy viscosity/diffusivity times the mean gradients:

$$\overline{uw} = -\nu_M \frac{\partial U}{\partial z} \tag{5.2a}$$

$$\overline{vw} = -\nu_M \frac{\partial V}{\partial z} \tag{5.2b}$$

$$\overline{w\theta} = -\nu_H \frac{\partial \Theta}{\partial z} \tag{5.2c}$$

where $\nu_M$ is the eddy viscosity and $\nu_H$ the eddy diffusivity, in analogy with molecular diffusion. In order to close Eq. 5.1, the eddy coefficients need to be parameterized. A simple scaling analysis suggests:

$$\nu_M, \nu_H \sim \ell_K \cdot \sqrt{K} \tag{5.3}$$

where $\ell_K$ is a mixing length scale, and $K = \left(\overline{u^2} + \overline{v^2} + \overline{w^2}\right)/2$ is the turbulent kinetic energy (TKE) per unit of mass. The prognostic equation for $K$ allows to take into account the history and the transport effects, and it is given by:

$$\frac{\partial K}{\partial t} = -\frac{\partial \overline{kw}}{\partial z} - \overline{uw}\frac{\partial U}{\partial z} - \overline{vw}\frac{\partial V}{\partial z} + \frac{g}{\Theta_0}\overline{\theta w} - \varepsilon \tag{5.4}$$

where the terms on the right hand side represent, respectively, the turbulent transport, the shear production in both wind directions, the buoyancy production/destruction and the dissipation rate. To close Eq. 5.4, the dissipation rate $\varepsilon$ is usually set dependent to $K$ and a length scale, in a way similar to Eq. 5.3:

$$\varepsilon \sim \frac{K^{3/2}}{\ell_\varepsilon} \tag{5.5}$$

Substituting Eq. 5.5 into Eq. 5.3, assuming that the two length scales differ by a multiplicative constant factor, one obtains:

$$\nu_M = c_\mu \frac{K^2}{\varepsilon} \tag{5.6a}$$

$$\nu_H = \frac{c_\mu}{Pr}\frac{K^2}{\varepsilon} \tag{5.6b}$$

where $c_\mu$ is a constant, usually set equal to 0.09 (Launder et al., 1983), and $Pr$ is the turbulent Prandtl number. The dissipation rate $\varepsilon$ is calculated through its prognostic equation:

$$\frac{\partial \varepsilon}{\partial t} = -\frac{1}{\sigma_\varepsilon}\frac{\partial \overline{\varepsilon w}}{\partial z} - \left(c_1\left(\overline{uw}\frac{\partial U}{\partial z} + \overline{vw}\frac{\partial V}{\partial z}\right) - c_3\frac{g}{\Theta_0}\overline{\theta w}\right)\frac{\varepsilon}{K} - c_2\frac{\varepsilon^2}{K} \tag{5.7}$$

where $c_1$, $c_2$, $c_3$ and $\sigma_\varepsilon$ are set equal to 1.44, 1.92, 1.44 and 1.3, respectively (Launder et al., 1974). The terms on the right hand side represent, respectively, the turbulent transport, the shear and buoyancy production/destruction and the viscous dissipation. The Prandtl number is computed as in Hong et al. (2006b), depending on the height above the ground, on PBL height and on the state of the surface layer:

$$Pr = 1 + (Pr_0 - 1)\exp\left(\frac{-3\,(z-0.1h)^2}{h^2}\right) \tag{5.8}$$

where $Pr_0 = \phi_h/\phi_m + 0.68 v_k$, calculated using the similarity functions $\phi_i$ evaluated at the top of the surface layer, assumed 10% of the boundary layer height and $v_k = 0.4$ is the von Kármán constant. The PBL height is calculated, similarly to Nakanishi (2001), as the level at which the potential temperature first exceeds the minimum potential temperature within the boundary layer by 1.5 K. The similarity functions are defined as:

$$\phi_m = \begin{cases} 1 + 4.7\frac{z}{L} & \text{if } \frac{z}{L} \geq 0 \\ \left(1 - 16\frac{z}{L}\right)^{-1/4} & \text{if } \frac{z}{L} < 0 \end{cases} \tag{5.9a}$$

$$\phi_h = \begin{cases} 1+4.7\frac{z}{L} & \text{if } \frac{z}{L} \geq 0 \\ \left(1-16\frac{z}{L}\right)^{-1/2} & \text{if } \frac{z}{L} < 0 \end{cases} \tag{5.9b}$$

where $L$ is the Obukhov length (Monin et al., 1954).

### 5.2.2 The correction term for the $\varepsilon$ equation

The standard $K-\varepsilon$ model does not work well for flows with large mean shear, spreading of jets, or rotating turbulence (Shih et al., 1995). In fact, several terms in the exact dissipation rate equation are unknown. For this reason, the dissipation equation (Eq. 5.7) was created with a similar structure as the TKE equation, by assuming that the source and sink terms of the dissipation rate are proportional to the source and sink terms of TKE times the large eddy turnover timescale $K/\varepsilon$. To improve the standard model for the stable atmosphere, Zeng et al. (2020b) introduced an additional source term $A_\varepsilon$ in the buoyancy term of the dissipation equation, to represent the dependence of energy drain on the eddy scale:

$$A_\varepsilon = c_4 \min\left(1, \sqrt{\frac{Ri}{c_5}}\right) N\varepsilon, \tag{5.10}$$

where $Ri$ is the gradient Richardson number $Ri = \frac{g}{\Theta_0}\frac{\partial\Theta/\partial z}{(\partial U/\partial z)^2+(\partial V/\partial z)^2}$, $N$ is the Brunt-Väisälä frequency $N = \left(\frac{g}{\Theta_0}\frac{\partial\Theta}{\partial z}\right)^{1/2}$, while $c_4$ and $c_5$ are chosen to be consistent with the Monin-Obukhov similarity theory (MOST), and set equal to 0.44 and 0.8, respectively. This additional term acts only in case of stable atmosphere (i.e. when the Richardson number is greater than zero, then in the CBL it is non-zero only in the capping inversion layer).

### 5.2.3 The Counter-Gradient Heat Flux

Deardorff (1966) highlighted the need of considering a non-local term into the vertical heat flux parameterization, in order to take into account large eddies and surface-driven motions in unstable conditions. It allows a vertical transport of heat upward without a superadiabatic lapse rate. The counter-gradient enters in the vertical heat flux. It now reads:

$$\overline{w\theta} = -\nu_H\left(\frac{\partial\Theta}{\partial z} - \gamma\right) \tag{5.11}$$

and $\gamma$ is parameterized following Troen et al. (1986):

$$\gamma = C\frac{\overline{w\theta}_0}{w_\star h} \tag{5.12}$$

where $C = 10$, $\overline{w\theta}_s$ is the surface heat flux, and $w_\star = \left(g/\Theta_0\overline{w\theta}_s h\right)^{1/3}$ is the convective velocity scale. The above mentioned counter-gradient is largely adopted in state-of-the-art PBL parameterizations, demonstrating its ability in reducing instabilities and in better describing the vertical temperature profile (Ching et al., 2014).

### 5.2.4 The temperature variance equation

The counter-gradient term does not act in stably stratified regimes, when turbulence production has actually been observed (Mauritsen et al., 2007) and parameterized (Zilitinkevich et al., 2013; Zilitinkevich et al., 2007). So, its efficiency is limited to unstable regimes only; therefore for stable regimes an additional term should be considered. Standard models usually assume a critical Richardson number ($\sim 0.25$) above which turbulence is completely damped. In order to consider even turbulence in stably stratified regimes, similarly to Lazeroms et al. (2016) and Želi et al. (2019), besides the prognostic equations for $K$ ( Eq. 5.4) and $\varepsilon$ (Eq. 5.7), we added a prognostic equation for the half of the temperature variance ($K_\theta = \frac{1}{2}\overline{\theta^2}$), that reads:

$$\frac{\partial K_\theta}{\partial t} = -\frac{\partial \overline{wK_\theta}}{\partial z} - \overline{w\theta}\frac{\partial \Theta}{\partial z} - \varepsilon_\theta \tag{5.13}$$

where the terms on the right hand side represent the turbulent transport, the production/destruction by buoyancy and the dissipation, respectively. The dissipation term is parameterized as:

$$\varepsilon_\theta = \frac{K_\theta}{\tau R} \tag{5.14}$$

where $\tau = \frac{K}{\varepsilon}$ is the turbulence time scale and

$$R = \frac{2}{3\left(1+\frac{\overline{w\theta}^2}{KK_\theta}\right)} \tag{5.15}$$

as described in Craft et al. (1996).

$K_\theta$ is proportional to the turbulent potential energy (TPE), that is defined as:

$$TPE = \frac{g}{\Theta_0}\frac{K_\theta}{\frac{\partial \Theta}{\partial z}} \tag{5.16}$$

The main idea of adopting a prognostic equation for $K_\theta$ (or TPE) is the conversion between TKE and TPE depending on the vertical stratification. $K_\theta$ acts both in stable and in unstable boundary layers, as a counter-gradient in analogy to the $\gamma$ term introduced above. In particular, it enters in the computation of the vertical heat flux, which now is calculated as (Lazeroms et al., 2016):

$$\overline{w\theta} = -\nu_H \frac{\partial \Theta}{\partial z} + \Phi_{cg} \tag{5.17}$$

where:

$$\Phi_{cg} = c_\mu \frac{g}{\Theta_0}\frac{KK_\theta}{\varepsilon} \tag{5.18}$$

Its effect is larger in areas with large temperature fluctuations (i.e. large $K_\theta$), thus in the surface layer and in the inversion layer, where temperature gradients are stronger than in the other regions. $\Phi_{cg}$ replaces the counter-gradient term of Eq. 5.12. While $\gamma$ is null for stable regimes, $\Phi_{cg} > 0$.

### 5.2.5 Building-Induced Drag and Heat Flux

In order to account for the effect of buildings on mean flow and turbulence, additional terms need to be parameterized. The additional term for wind speed reads:

$$D_u = -S(z)C_{deq}U(z)|U(z)| \tag{5.19}$$

where $S(z)$ is the upwind vertical surface building density, and $C_d$ the sectional drag. The additional term that has to be added in the TKE equation to take into account the effect of buildings drag reads:

$$D_K = S(z)C_{deq}\left|U(z)\right|^3 \tag{5.20}$$

and finally, the term for $\varepsilon$:

$$D_\varepsilon = S(z)C_{d\varepsilon}|U|\varepsilon \tag{5.21}$$

where $C_{deq}$ is calculated as in Santiago et al. (2010):

$$C_{deq}(\lambda_p) = \begin{cases} 3.31\,\lambda_p^{0.47} & \text{if } \lambda_p \leq 0.29 \\ 1.85 & \text{if } \lambda_p > 0.29 \end{cases} \tag{5.22}$$

$\lambda_p$ is the plan area ratio, taken as input by the model:

$$\lambda_p = \frac{A_p}{A_t} = \frac{LW}{(W+S_y)(L+S_x)} \tag{5.23}$$

The drag coefficient for $\varepsilon$, computed by means of a best fit with CFD data, reads:

$$C_{d\varepsilon}(\lambda_p) = \begin{cases} a_1\lambda_p^{-b_1} + b_2 & \text{if } \lambda_p \leq 0.25 \\ -a_2\lambda_p + b_3 & \text{if } \lambda_p > 0.25 \end{cases} \tag{5.24}$$

with $a_1 = 0.07$, $b_1 = -1.4$, $b_2 = 8.3$, $a_2 = 14.8$ and $b_3 = 12.4$. Note that, while $C_{deq}$ increases with packing density, $C_{d\varepsilon}$ decreases with increasing $\lambda_p$. The reason is that large packing densities tend to decrease the turbulence generated within the canopy layer, and a decrease in turbulence intensity is reflected in a decrease in the dissipation rate $\varepsilon$.
For the prognostic equations of $\Theta$, $K$ and $\varepsilon$, an additional source (or sink) of sensible heat flux is added following Martilli et al. (2002). The turbulent heat flux on horizontal surfaces (roofs or ground), is computed as:

$$F_\theta^H(z) = -\rho\frac{v_k^2}{\ln\frac{\Delta z/2}{z_0}^2}|U(z)|\Delta\Theta(z)f_h\left(\frac{\Delta z/2}{z_0}, Ri_B\right)S(z) \tag{5.25}$$

where $v_k$ is the von Kármán constant, $\Delta z$ the vertical level depth of the urban grid, $z_0$ the roughness length, $U(z)^{HOR}$ the horizontal wind speed, $\Delta\Theta$ the difference between the surface temperature of the roof or canyon floor and the air temperature and $f_h$ a function dependent on atmospheric stability (see Louis, 1979 and Martilli et al., 2002 for further details regarding the parameterization).

### 5.2.6 Boundary and Initial conditions

As initial conditions for the simulations, we set the values $K_0 = 10^{-4}$ m$^2$s$^{-2}$, $\varepsilon_0 = 10^{-7}$ m$^2$s$^{-3}$ and $K_{\theta 0} = 10^{-7}$ K$^2$ for all the air column. As boundary conditions, we set $k_{TOP} = \varepsilon_{TOP} = K_{\theta TOP} = 0$ at the top of the domain. On the other hand, at the surface we use a mix of Neumann and Dirichlet boundary conditions. For $U$, $V$ and $\Theta$ we assume Neumann boundary conditions:

$$\frac{\partial U_1}{\partial t} = -\frac{u_\star^2}{\Delta z_1 |U_{TOT}|} U_1 \tag{5.26a}$$

$$\frac{\partial V_1}{\partial t} = -\frac{u_\star^2}{\Delta z_1 |U_{TOT}|} V_1 \tag{5.26b}$$

$$\frac{\partial \Theta_1}{\partial t} = \frac{\overline{w\theta}_s}{\Delta z_1} \tag{5.26c}$$

where the subscript "1" refers to the variable calculated at the center of the first grid cell close to the surface, $u_\star$ is the friction velocity, $\Delta z_1$ is the height of the first level and $\overline{w\theta}_s$ is the turbulent heat flux at the the surface. For $K$ and $\varepsilon$, we assume Dirichlet boundary conditions, adopting the Monin–Obukhov similarity theory (Hartogensis et al., 2005; van der Laan et al., 2017):

$$k_1 = \frac{u_\star^2}{\sqrt{c_\mu}} \sqrt{\frac{\phi_\varepsilon}{\phi_m}} \tag{5.27a}$$

$$\varepsilon_1 = \frac{u_\star^3}{\nu_k \frac{\Delta z_1}{2}} \phi_\varepsilon \tag{5.27b}$$

where:

$$\phi_\varepsilon = \begin{cases} \left(1 + 2.5 \left(\frac{z}{L}\right)^{0.6}\right)^{3/2} & \text{if } \frac{z}{L} \geq 0 \\ 1 - \frac{z}{L} & \text{if } \frac{z}{L} < 0 \end{cases} \tag{5.28}$$

and $\Phi_m$ is calculated from Eq. 5.9a.
For $K_\theta$, we assume again Neumann boundary conditions, employing in Eq. 5.13 the boundary conditions in Eq. 5.26c, 5.27a and 5.27b.

## 5.3 Setup and case study

### 5.3.1 Simulation set-up

Simulations are performed with WRF version 4.1.2 (Skamarock et al., 2019). The focus is on four sunny summer days, for the period 24-27 August 2016, when daily-periodic local circulation systems were well-developed, as previously evaluated analyzing data from different surface weather stations located in the Adige Valley. Start time is set at 1800 UTC (LST=UTC+1h) 23 August 2016, with the first 18 h considered as spin-up period influenced by the initialization and not accounted for the following analysis. The horizontal domain consists of four two-way nested domains with $100 \times 100$, $100 \times 100$, $100 \times 100$ and $85 \times 106$ grid cells centered over the city of Trento, with resolution of 9, 3, 1 and 0.333 km respectively (Fig. 5.1). As to the vertical

resolution, 44 terrain-following levels with higher resolution near the ground, with 5 of them in the first 90 m above ground level, are adopted. Finer vertical resolutions are usually adopted for urban simulations (Zonato et al., 2020), but numerical instability, typical of numerical simulations over complex terrain (Giovannini et al., 2014), did not allowe refining the vertical grid. 6-hourly NCEP Final Operational Global Analysis data with a resolution of $0.25° \times 0.25°$ are used as initial and boundary conditions (National Centers for Environmental Prediction, National Weather Service, NOAA, 2015). Simulations output is written every 15 min, taking an

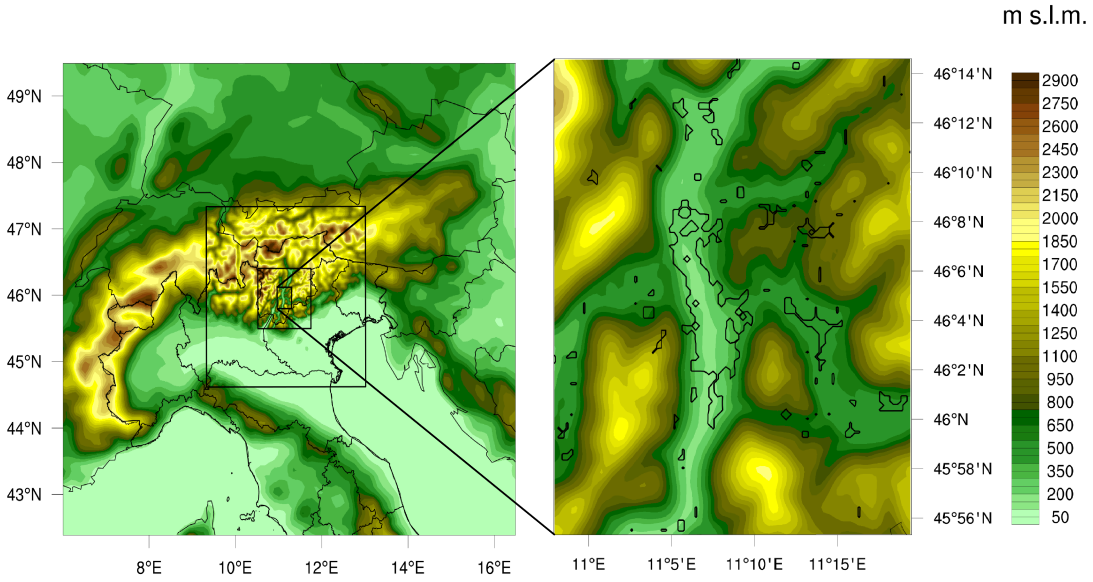


**Figure 5.1:** The four nested domains used for the numerical simulations. The zoomed-in area represents the inner domain, and the black contours the urban areas.

average over the previous time-steps. The here-presented WRF-urban simulations are run using the BEP-BEM urban schemes (Martilli et al., 2002; Salamanca et al., 2010), coupled with the NoahMP land surface model (Niu et al., 2011). For BEM, air conditioning systems are turned on for 24 h, with a target indoor temperature of 298 K, with a comfort range of 0.5 K. Windows are supposed to cover 20% of each facade of the buildings. The microphysics is modeled using the WSM 6-class scheme (Hong et al., 2006a), while the Kain-Fritsch (Kain et al., 1993) cumulus scheme is used for the outer domain, and turned off in the two innermost domains. As to the radiation parameterizations, the Rapid Radiative Transfer Model (RRTM, Mlawer et al., 1997) is used for the long-wave radiation, and the Dudhia (1989) scheme for the short-wave radiation, including the effects of slope inclination and topographic shading. Finally, for the horizontal diffusion, we use the Smagorinsky first-order closure scheme (Smagorinsky, 1963). Regarding the PBL schemes, they will be discussed in the next subsection.

### 5.3.2 PBL schemes

The aim of this work is to evaluate the capability of the new $K-\varepsilon$ turbulence schemes to reproduce the atmospheric dynamics in complex and urban terrain. For this reason, different variants of the $K-\varepsilon$ closure are tested and compared with state-of-the-art PBL schemes, already present in WRF and coupled with the BEP+BEM urban canopy parameterization. The

PBL schemes adopted here are the BouLac 1.5-order scheme (Bougeault et al., 1989) and the Mellor-Yamada-Janjic (MYJ, Janjic, 2002) 1.5-order scheme (level 2.5), based on the turbulence closure model of Mellor et al. (1982). These PBL schemes have been successfully used for urban mesoscale simulations in various cities, as shown in the introduction. The buoyancy source/sink in BouLac and MYJ is computed in the same way as in the $K-\varepsilon$ closures (Eq. 5.25), while the drag induced by buildings appears in the prognostic equation for horizontal wind speed (Eq. 5.19) and in the prognostic equation for the turbulent kinetic energy (Eq. 5.20). Finally, the drag coefficient for the additional terms in TKE and wind speed equations is computed with Eq. 5.22, while the one appearing in the equation for dissipation rate is computed with Eq. 5.24. MYJ and BouLac, not employing the diagnostic equation for dissipation rate, assume the drag induced by building to be considered only in the prognostic equations for TKE and wind speed, with the drag coefficient calculated with Eq. 5.22.
In order to evaluate the impact of the different additional terms introduced in the standard $K-\varepsilon$ model, a set of different simulations has been performed: 1) the standard $K-\varepsilon$ where the Prandtl number is equal to one, the correction terms $A_\varepsilon$ in Eq. 5.10 is null and the counter-gradient term in the turbulent heat flux is not considered, 2) the $K-\varepsilon-\gamma$, where the Prandtl number is calculated through Eq. 5.8, $A_\varepsilon$ is considered and the counter-gradient term is calculated with the diagnostic Eq. 5.12, 3) the $K-\varepsilon-\theta^2$, which differs from the previous one in the computation of the counter-gradient term, that is evaluated with Eq. 5.18, where $K_\theta$ is calculated with the prognostic equation for potential temperature (Eq. 5.13).

### 5.3.3 Input datasets

A key requisite for realistic high-resolution simulations in urban areas and complex terrain is to include high-resolution datasets, in particular for correctly representing the orography. WRF includes a default orography, with a spatial resolution of 30" ($\sim$ 1 km), that is too coarse for correctly representing the heterogeneity of orography in a so complex terrain at sub-kilometer scales. In the present work, we substitute the default orography dataset with a dataset with a resolution of 1" ($\sim$ 30 m) obtained from the Viewfinder Panoramas website (http://www.viewfinderpanoramas.org), smoothed firstly with the 1-2-1 filter already implemented in WRF, and secondly with an ad hoc filter only for slopes greater than 40°, since numerical instability occurs over sharp edges and steep slopes in the inner domain.
We substitute also the default WRF land use dataset, i.e. the MODIS-based dataset with the IGBP Land Cover Type Classification, which presents a resolution of 30", too coarse as well for our purpose. The dataset used here is the Corine Land Cover (CLC) updated at 2012, provided by the European Environment Agency (http://www.eea.europa.eu). The original spatial resolution is 100 m, and the 44 land use classes have been reclassified into the 20 MODIS (+11 urban classes categorized with the WUDAPT method) classes to fit the WRF look-up tables, and the most present value for each WRF cell has been chosen to represent the land use.
According to the reclassification, the valley floor of the Adige valley is classified as "cropland", which defines all types of cultivation. However, this definition is not appropriate, since the most diffuse cultivation consists of apple orchards. For this reason, following Tomasi et al. (2017), a new land-use class is introduced, modifying the standard look-up tables VEGPARM.TBL and

| | Deciduous broadleaf forest | Apple orchard |
|---|---|---|
| Canopy top height | 20 | 3 |
| Canopy bottom height | 11.5 | 1 |
| Min roughness length | 0.5 | 0.3 |
| Max roughness length | 0.5 | 0.3 |
| Tree density | 0.1 | 0.25 |

**Table 5.1:** Modified parameters in the "deciduous broadleaf forest" class in order to create a new ad hoc "apple orchard" land-use class

**Table 5.2:** Thermal and physical parameters for LCZs.

| LCZ | Heat Capacity (MJ $m^{-3}$ $K^{-1}$ ) | | | Thermal Conductivity ($Wm^{-1}$ $K^{-1}$) | | |
|---|---|---|---|---|---|---|
| | Roof | Walls | Road | Roof | Walls | Road |
| 2,5,6 | 1.77 | 1.37 | 1.94 | 0.84 | 0.83 | 0.75 |
| 8 | 2.11 | 2.11 | 1.94 | 1.51 | 1.51 | 0.75 |
| 11 | 1.94 | 1.94 | 1.94 | 0.75 | 0.75 | 0.75 |
| All LCZs | Roof | Walls | Road | - | - | - |
| Albedo | 0.20 | 0.20 | 0.10 | Target Temp. for ACs | | 25 °C |
| Emissivity | 0.90 | 0.90 | 0.95 | Perc. of windows | | 20% |

MPTABLE.TBL, necessary for the NoahMP land use scheme. Specifically, the class "cropland" is substituted by the class labeled by IGBP as "deciduous broadleaf forest", modifying some parameters as described in Tab 5.1.

To correctly define urban morphology, a suitable and precise dataset is needed, especially at sub-kilometer resolutions. For the BEP scheme, similarly to Zonato et al. (2020), Salamanca et al. (2011) and Giovannini et al. (2014), the urban canopy parameters used as input are the building plan area fraction $\lambda_p = A_p/A_{tot}$ (where $A_p$ is the plan area of buildings and $A_{tot}$ the total area of the WRF cell), the building wall surface area to plan area $\lambda_f = A_w/A_{tot}$ (where $A_w$ is the wall surface area), the average height of buildings $h_m$, the distribution of building heights $h_i$ every 5 m, and the urban fraction $\lambda_u$. In this case study, the urban canopy parameters are the same as in Giovannini et al. (2014), which were obtained from high-resolution lidar data of the Autonomous Province of Trento (horizontal accuracy of 1 m and vertical accuracy of 0.15 m). Figure 5.2 shows the map of the aforementioned UCPs at a resolution of 333 m.

For the urban land use, in order to assign the proper thermal parameters to each urban class, we employed the WUDAPT method (Ching et al., 2018), following the "WUDAPT categorical" technique presented in Zonato et al. (2020). The WUDAPT classification is used only for the cells where the urban fraction is greater than zero and is shown in Fig. 5.3. The building thermal properties adopted (Tab. 5.2) are representative of solid brick for LCZ 2, LCZ 5 and LCZ 6, and concrete for LCZ 8 (industrial and commercial areas), according to the typical materials of these LCZs. For all the classes, the physical properties of the asphalt have been set for the ground.

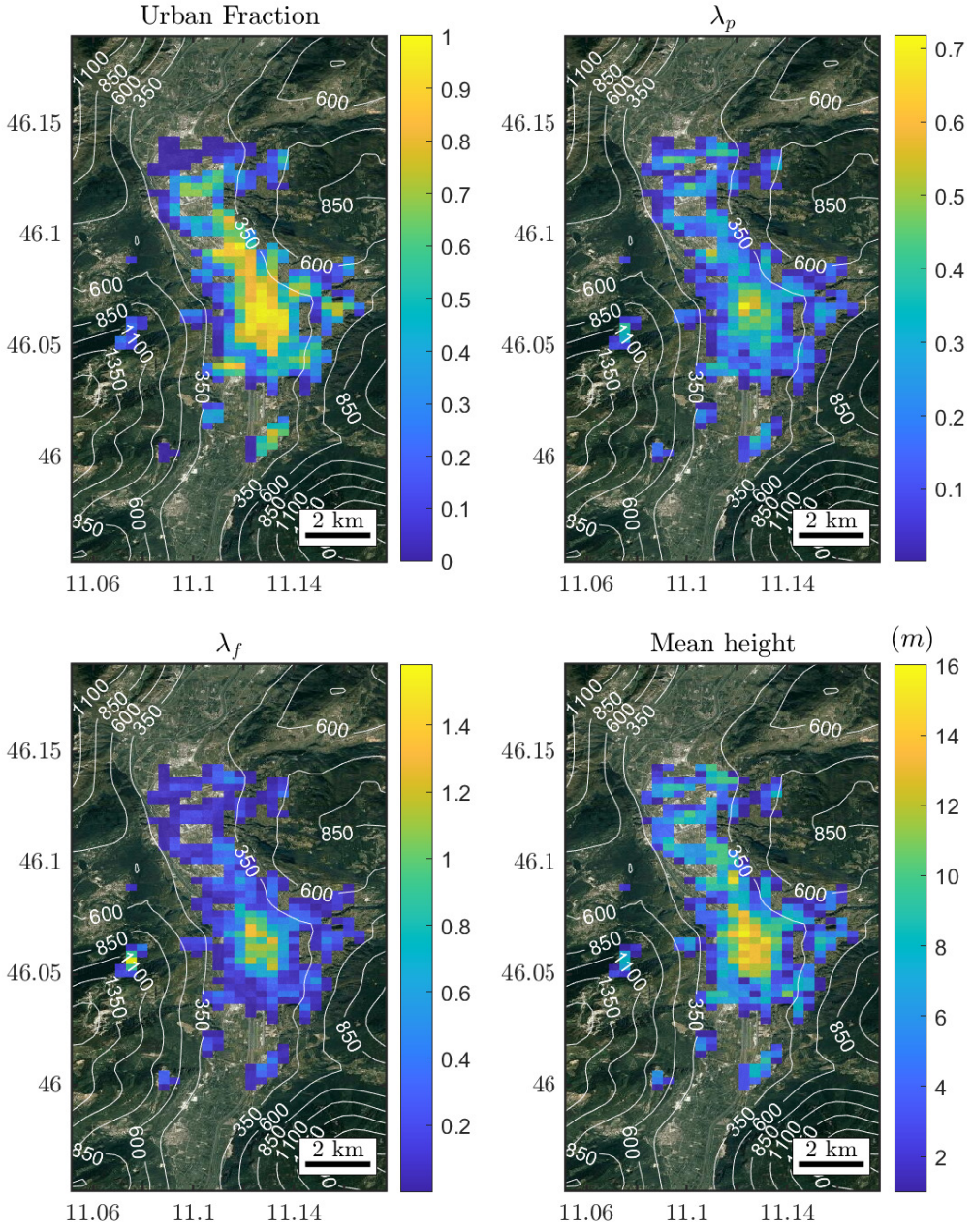


**Figure 5.2:** Urban morphology parameters used in input for the BEP+BEM scheme for the city of Trento, overlaid over satellite images. The top-left panel shows the urban fraction $\lambda_u$, the top-right panel the building plan area fraction $\lambda_p$, the bottom-left panel the building wall surface area to plan area ratio $\lambda_f$, and the bottom-right panel the average building height $h_m$. Height contours are in m above sea level (ASL).

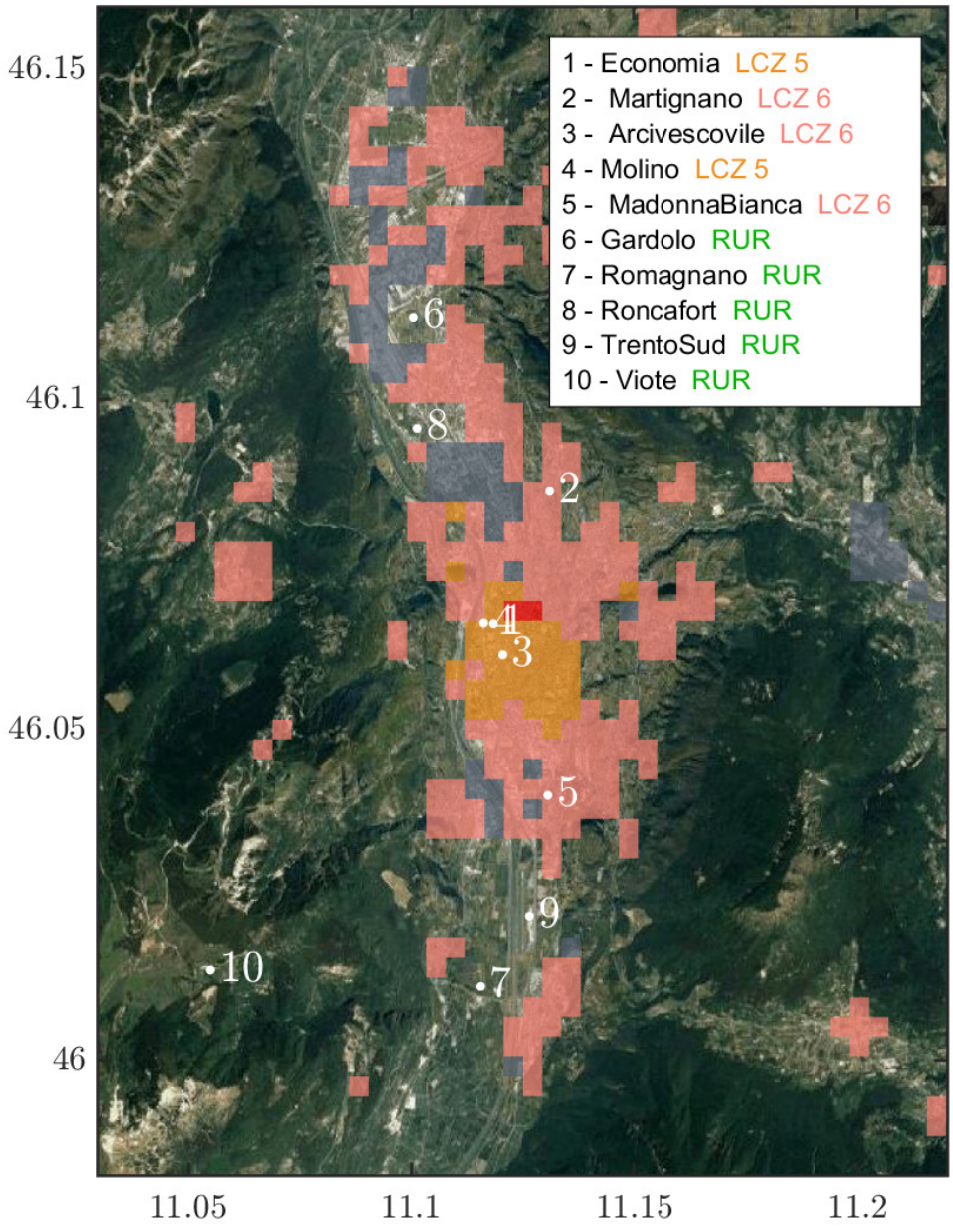


**Figure 5.3:** WUDAPT urban classes for the city of Trento, at 333 m resolution, overlaid over satellite images, and position of the weather stations (5 urban and 5 rural).

## 5.4 Results and comparison with weather stations data

In this section, the results of the five simulations, differing in the PBL scheme (BouLac, MYJ, $K-\varepsilon$, $K-\varepsilon-\gamma$ and $K-\varepsilon-\theta^2$) are validated against measurements and compared each other through a statistical analysis on temperature, wind, and turbulent variables time-series. In this work, we consider 10 surface weather stations, 5 situated in rural areas and 5 within the city (Fig. 5.3). All variables have been averaged over a time window of 15 minutes and compared with simulation output averaged over the same time span.
Observations are compared with the simulated 2-m air temperature and 10-m wind speed at all the weather stations apart for Molino, situated on the top of a tower at 33 m above ground level, where observations are compared with model results from the third vertical level.
To quantify the model performance and to compare the different simulations, the mean bias (MB) and the root-mean-square error (RMSE) between each simulation and the observations have been calculated for each weather station. These statistical indexes are defined as follows:

$$MB = \frac{1}{n}\sum_{i=1}^{n}(y_i - f_i) \tag{5.29}$$

$$RMSE = \sqrt{\frac{1}{n}\sum_{i=1}^{n}(y_i - f_i)^2} \tag{5.30}$$

where $n$ is the total number of the output time-step of the simulation, $f_i$ the modeled temperature or wind speed and $y_i$ the observation.

### 5.4.1 Air temperature timeseries

Figure 5.4 shows the time-series of air temperature recorded by the rural weather stations for the four days considered in this study. Four stations are situated in the Adige Valley, in the neighborhood of the city of Trento. All the simulations display a similar behaviour at these weather stations in all the four days, with minimum temperatures of $\sim$ 15 °C and maximum temperatures of $\sim$30 °C. Viote weather station, instead, situated at $\sim$1500 m ASL, recorded temperatures varying between $\sim$10 and $\sim$20 °C. The diurnal variation of temperature is well captured by all the PBL schemes, especially for the valley stations. However, as shown by Giovannini et al. (2014), mesoscale simulations usually overestimate minimum temperatures during nighttime on the valley floor. The same behavior is shown by MYJ, Boulac, and $K-\varepsilon$, where minimum temperatures, especially for the 25$^{\text{th}}$ and the 27$^{\text{th}}$ of August, are overestimated by $\sim$2 °C. On the other hand, $K-\varepsilon-\gamma$ and $K-\varepsilon-\theta^2$ (implementing a diagnostic equation for the Prandtl number and the additional term in Eq. 5.10 for stable regimes), better capture the minimum temperature for the stations located in the valley. The $K-\varepsilon$ based PBL schemes work better even in reproducing the maximum temperature: while the diurnal increase (and subsequent decrease) of temperature is similar for all PBL schemes, with a maximum temperature in the early afternoon, MYJ and Boulac usually underestimate the maximum temperature by $\sim$2 °C, while the simulations implementing the $K-\varepsilon$ closures are in better agreement. In particular, the standard $K-\varepsilon$ generally overestimates the maxima (especially for Gardolo, Roncafort,

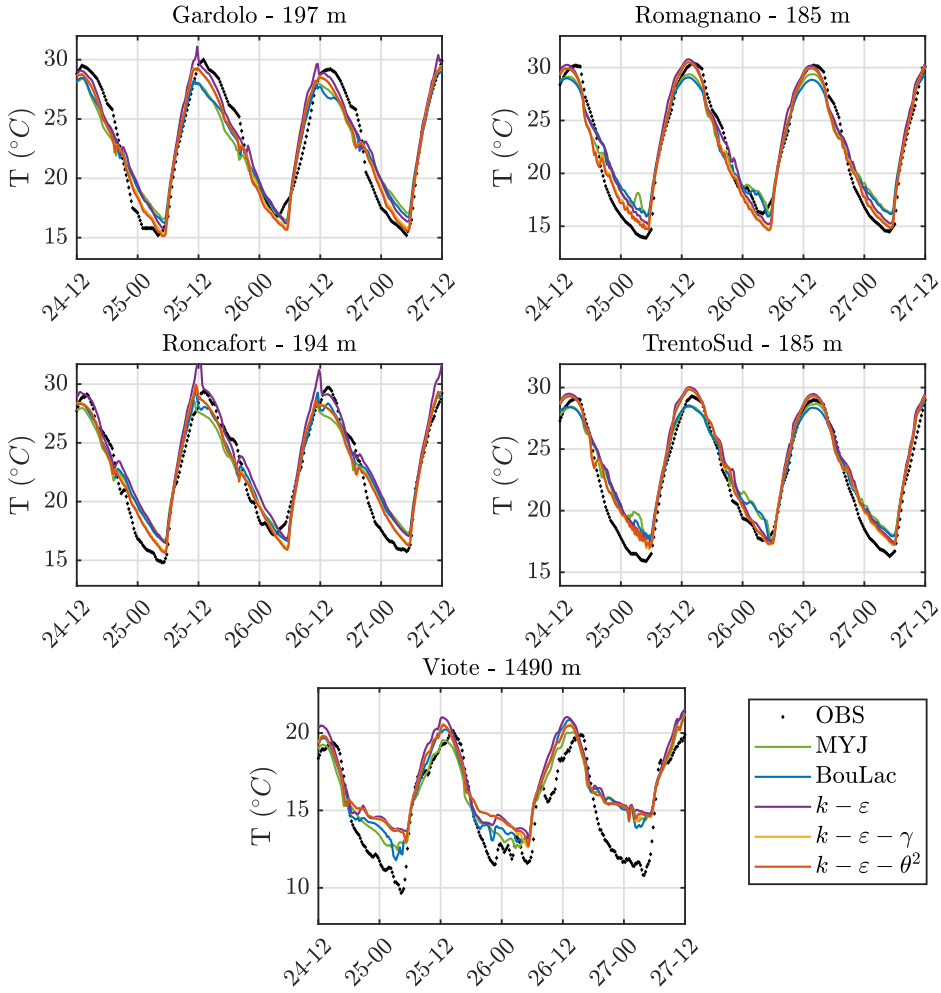


**Figure 5.4:** Timeseries of air temperature recorded by weather stations (black dots) and simulated with different PBL schemes (coloured lines) for rural locations. Station name is reported with the height of the station above sea level.

and Viote weather stations). The improvement shown by $K-\varepsilon-\gamma$ and $K-\varepsilon-\theta^2$ in the simulation of the maximum temperature is probably linked to the calculation of the Prandt number: in unstable regimes, $Pr$ is usually lower than one, resulting in an increased vertical temperature diffusivity. In this way, the transport of heat along the vertical is enhanced, so the first levels of the PBL result cooler than those with $Pr = 1$. The only location where the simulations with the $K-\varepsilon$ closures perform similar or slightly worse than the other two is at Viote; while $K-\varepsilon-\gamma$ and $K-\varepsilon-\theta^2$ display a slight increase in the maxima, for the minima and especially for the first and the second night, Boulac and MYJ are closer to measurements. However, despite a good agreement during daytime, during nighttime errors shown by all PBL schemes are large, with overestimations up to $\sim$4 °C during the third night. The effect of the Prandtl number is more evident from the comparison with urban weather stations data (Fig. 5.5): $K-\varepsilon$ in general overestimates the maximum temperature, in particular for the stations named Economia, Martignano, and Arcivescovile. Moreover, while for Economia, Martignano, and MadonnaBianca all the PBL schemes apart $K-\varepsilon$ display a similar maximum temperature, for Arcivescovile

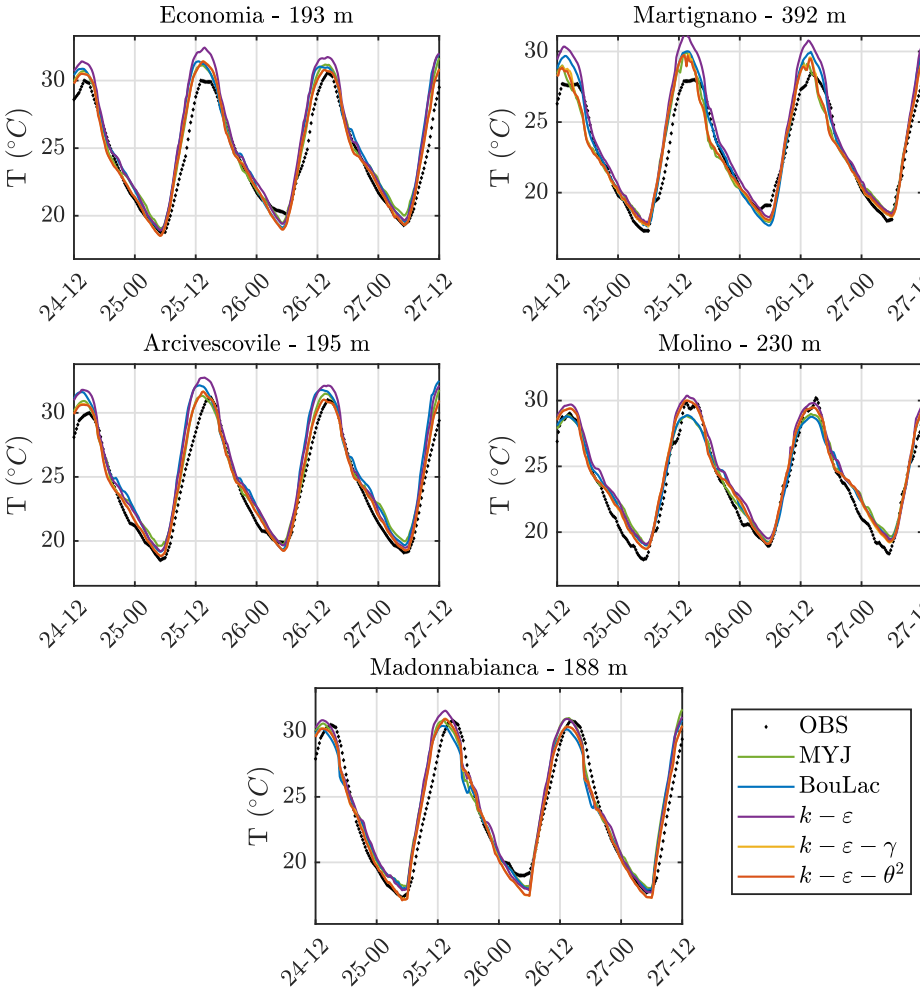


**Figure 5.5:** Timeseries of air temperature recorded by weather stations (black dots) and simulated with different PBL schemes (coloured lines) for urban locations. Station name is reported with the height of the station above sea level.

and Molino $K-\varepsilon-\gamma$ and $K-\varepsilon-\theta^2$ behave better, where Boulac and MYJ overestimate (for Arcivescovile) and underestimate (for Molino) the maxima by $\sim$2 °C. Regarding the minimum temperatures, urban stations show temperatures $\sim$5 °C higher than rural stations, because of the Urban Heat Island effect. Contrary to the case of rural locations, in the urban areas all the PBL schemes perform similarly in terms of minimum temperatures, with no particular differences between them. Figures 5.6 and 5.7 display the RMSE and the MB of temperature for all the period of simulation for all the weather stations of this case study, respectively. In general, all the PBL schemes behave well, since RMSEs are always lower than 1.5 °C for rural areas and of $\sim$ 1 °C for urban stations. $K-\varepsilon$ is the worst in representing the time-series of temperature, since it presents the largest RMSE, because of the overestimation of maxima (MBs are always positive and higher than the other PBL schemes). It is followed by MYJ and BouLac, which again tend on average to overestimate temperature. Comparing the latter two PBL schemes, MYJ performs better than BouLac for urban areas, while in rural locations Boulac is slightly better than MYJ. The best results are obtained by $K-\varepsilon-\gamma$ and $K-\varepsilon-\theta^2$: for urban areas,

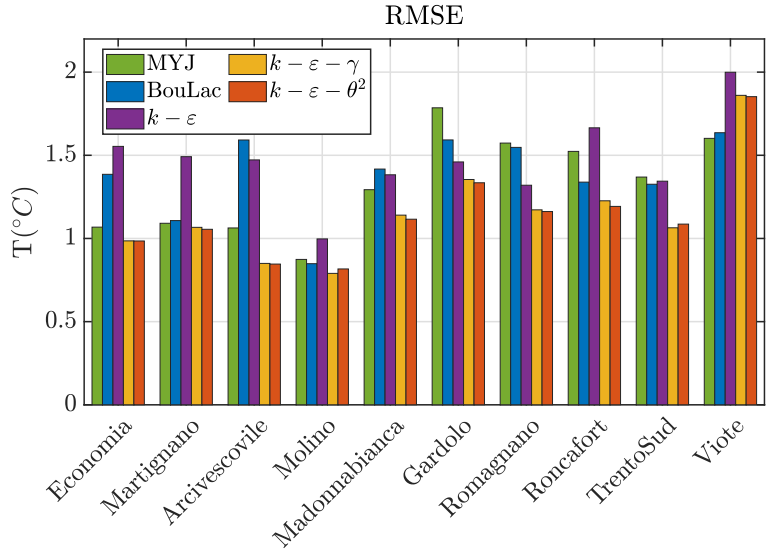


**Figure 5.6:** Root Mean Square Error of air temperature for all the period of simulation and for each weather station, calculated comparing each simulation with observational data.

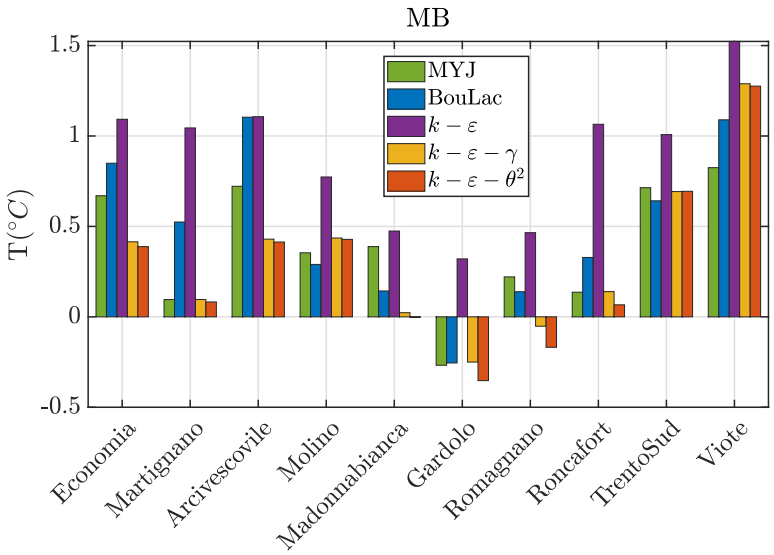


**Figure 5.7:** Mean Bias of air temperature for all the period of simulation and for each weather station, calculated comparing each simulation with observational data.

errors are slightly lower than the other PBL schemes, with a related decrease of the MB, especially for Economia and Arcivescovile, while the improvement by the latter two PBL schemes is more marked for rural stations, in particular for Romagnano and Gardolo.

As said before, the largest improvements by $K-\varepsilon-\gamma$ and $K-\varepsilon-\theta^2$ take place in reproducing maximum and minimum temperatures. Figures 5.8 and 5.9 show the RMSE and the MB of the maximum temperature, respectively, for all the weather stations. The largest improvements take place at Economia for urban areas, and at Romagnano and TrentoSud for rural areas. Improvements in reproducing the temperature maxima are reflected in a large decrease of the MB, which is almost null for $K-\varepsilon-\gamma$ and $K-\varepsilon-\theta^2$ at the weather stations where the largest improvements take place. In particular, MYJ and Boulac overestimate for urban areas, and underestimate for rural areas the maximum temperature. $K-\varepsilon-\gamma$ and $K-\varepsilon-\theta^2$ follow

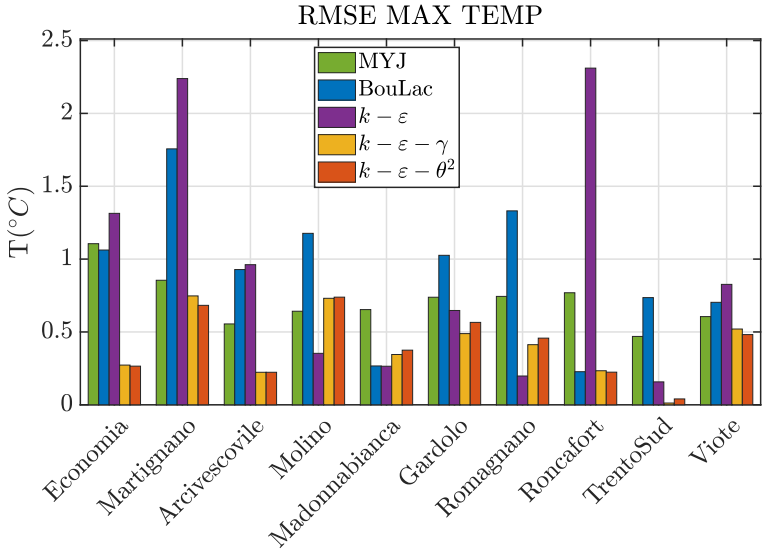


**Figure 5.8:** Root Mean Square Error of air temperature maxima for each day of simulation and for each weather station, calculated comparing each simulation with observational data.

the same trend, but with much lower discrepancies.

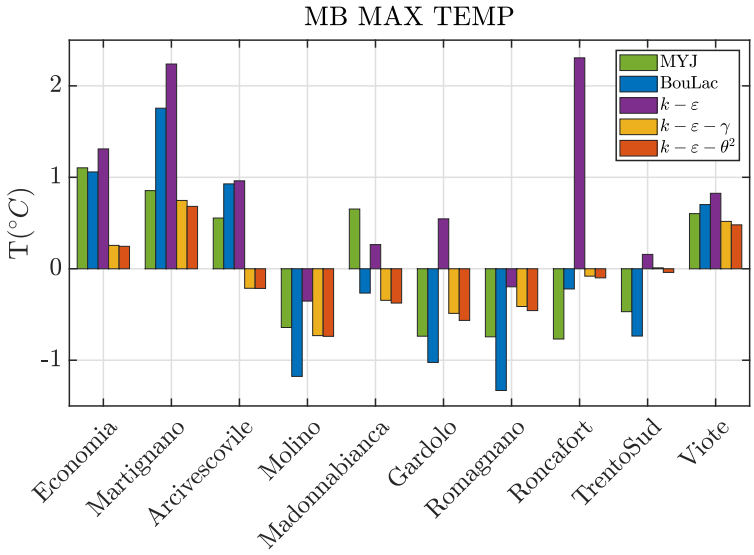


**Figure 5.9:** Mean Bias of air temperature maxima for each day of simulation and for each weather station, calculated comparing each simulation with observational data.

The statistical indexes for minimum temperatures (Fig 5.10 and 5.11) highlight again the improvements by $K-\varepsilon-\gamma$ and $K-\varepsilon-\theta^2$, especially for rural areas. The standard $K-\varepsilon$, without the computation of the Prandtl number, the additional term in the dissipation rate equation and the counter-gradient term, shows much higher discrepancies in terms of minimum temperatures, with errors up to 2 °C at Romagnano and Roncafort weather stations, with even higher errors displayed by MYJ and Boulac. On the other hand, despite all the simulations generally overestimate the minima, $K-\varepsilon-\gamma$ and $K-\varepsilon-\theta^2$ largely reduce the RMSE (and consequently the MB). RMSE for these cases is always lower than 1 °C for all the stations situated on the valley floor and for Gardolo, Romagnano, and TrentoSud the improvement is

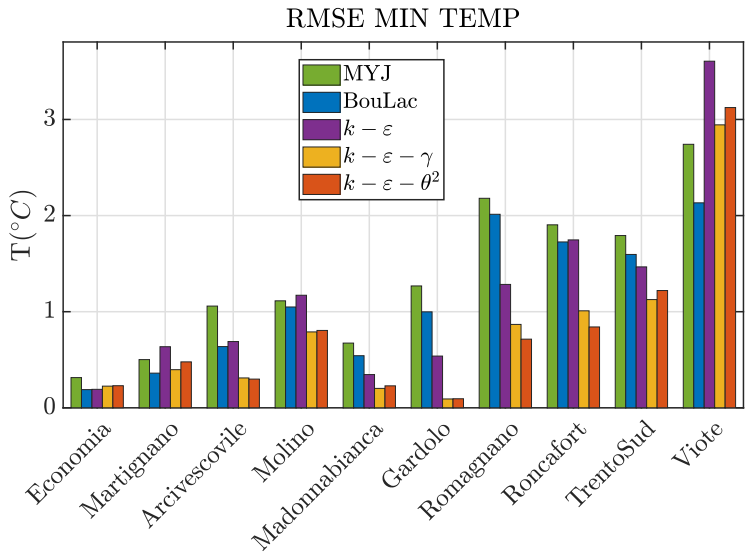


**Figure 5.10:** Root Mean Square Error of air temperature minima for each day of simulation and for each weather station, calculated comparing each simulation with observational data.

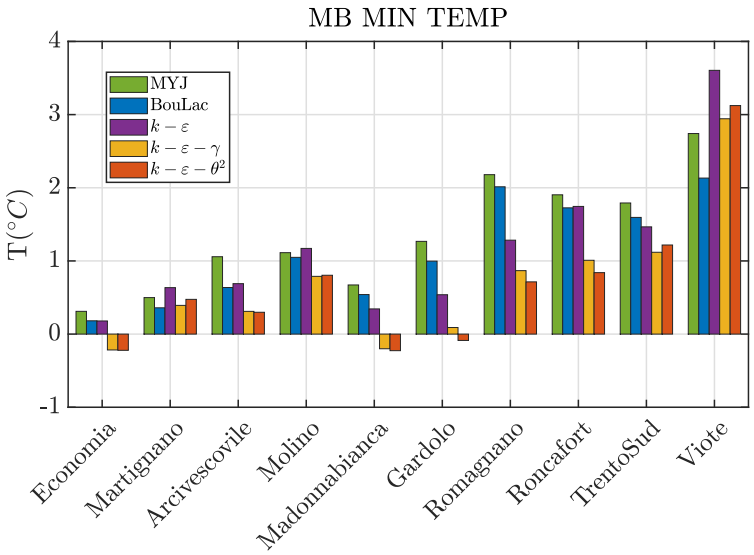


**Figure 5.11:** Mean Bias of air temperature minima each day of simulation and for each weather station, calculated comparing each simulation with observational data.

even higher than 1 °C with respect to the other PBL schemes.
In general, no particular differences are found between $K-\varepsilon-\gamma$ and $K-\varepsilon-\theta^2$; that means that, for real case simulations, the way the counter-gradient term is parameterized does not influence the PBL scheme performance in terms of maximum and minimum temperature, at least for this particular real case study. Moreover, for this particular case, the calculation of the temperature variance does not noticeably affect temperature during night hours.

### 5.4.2 Wind speed timeseries

Figure 5.12 shows the observed wind vectors for TrentoSud, Roncafort, and Viote. The first two stations, situated on the valley floor, show the typical characteristics of a thermally-driven

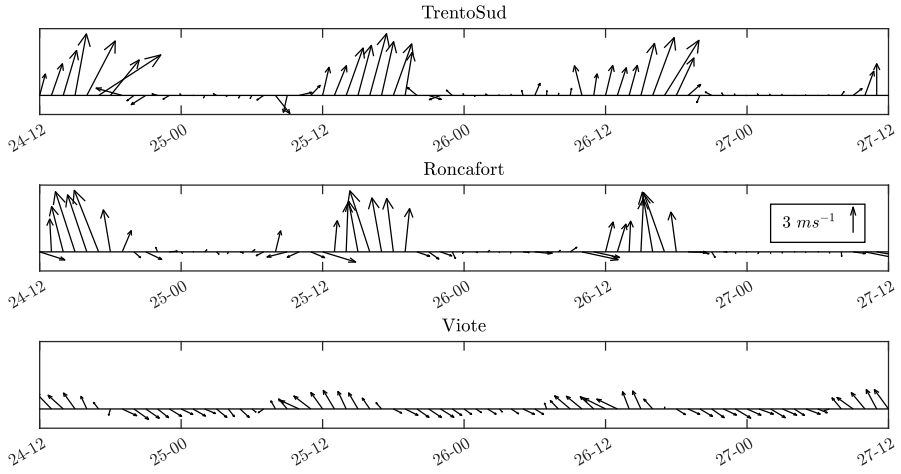


**Figure 5.12:** Horizontal wind vectors as observed at TrentoSud (top), Roncafort (center) and Viote (bottom).

along-valley circulation in the absence of strong synoptic forcing, with light or null down-valley wind during the night, and stronger up-valley wind ($\sim$ 7 m s$^{-1}$) during the day, as shown in Giovannini et al. (2017). The Viote station, situated at a mountain pass, at the end of a narrow valley oriented in the SE-NW direction, captures a down-slope wind during the night, and a more intense up-valley wind during the day.

Figures 5.13, 5.14 and 5.15 show the time-series of the simulated and observed wind speed, along with the RMSE and MB for the different PBL schemes. TrentoSud and Roncafort, sit-

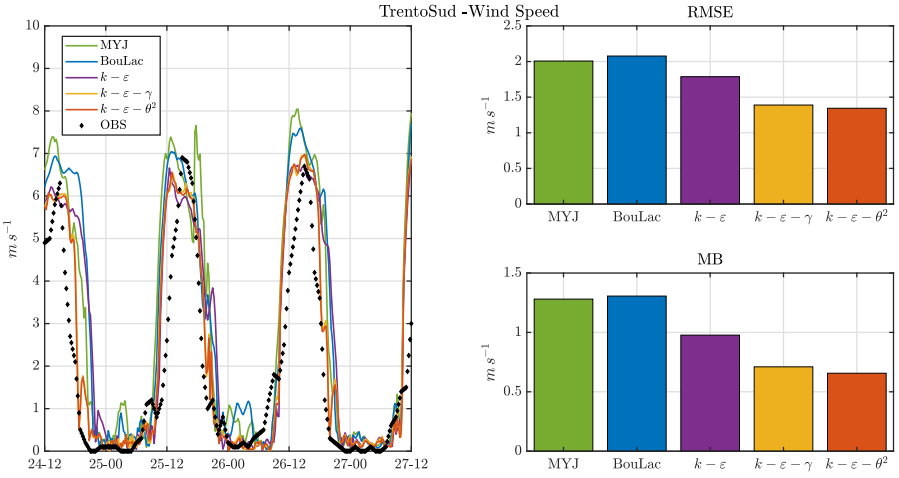


**Figure 5.13:** Timeseries of wind speed (left) recorded by the TrentoSud weather station (black dots) and simulated with different PBL schemes (coloured lines). Top-right and bottom-right panels report the RMSE and the MB respectively, for the different PBL schemes.

uated at the southern and northern end of the city, respectively, show a similar pattern, with low or null wind speed during nighttime, and a diurnal peak at around 1600 LST of $\sim$7 m s$^{-1}$. All PBL schemes can capture the daily cycle of the valley wind. In particular, while for

Roncafort the timing of the wind transition (from strong up-valley to weak down-valley approaching nighttime and from weak down-valley to strong up-valley approaching daytime) is well captured by all the PBL schemes, for TrentoSud MYJ, Boulac and $K-\varepsilon$ show a delay of $\sim$ 2 hours. On the other hand, the timing of the transition from up- to down-valey is well captured by $K-\varepsilon-\gamma$ and $K-\varepsilon-\theta^2$, but the transition from down- to up-valley is still anticipated. Moreover, at Roncafort, MYJ and Boulac show some peaks in the wind speed of $\sim$ 1 m

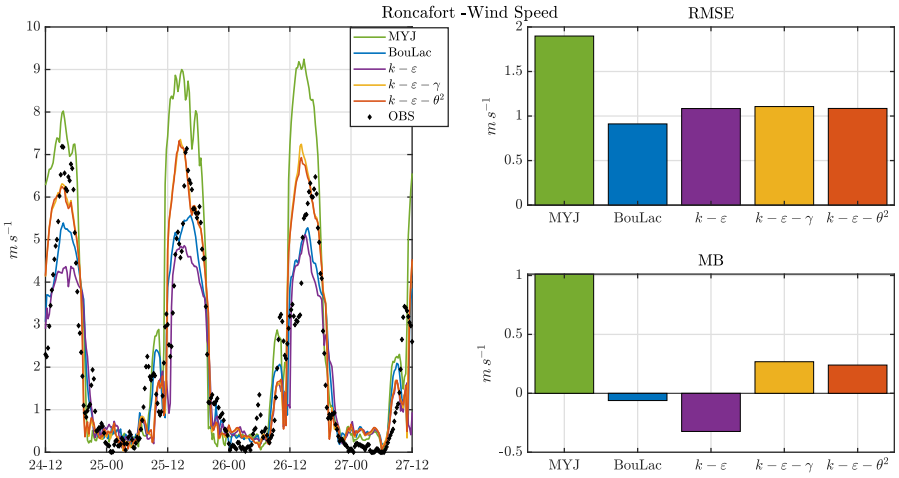


**Figure 5.14:** Timeseries of wind speed (left) recorded by the Roncafort weather station (black dots) and simulated with different PBL schemes (coloured lines). Top-right and bottom-right panels report the RMSE and the MB respectively, for the different PBL schemes.

s$^{-1}$ during the first and the second night, that have not been observed by the weather stations. Regarding the maximum wind speed during daytime, despite peaks are comparable between TrentoSud and Roncafort, the different PBL schemes behave differently in the two locations. For TrentoSud, while MYJ and BouLac overestimate the peaks by $\sim$ 1 m s$^{-1}$ on the first and the second day, the three $K-\varepsilon$ based PBL schemes agree better with observational data.

On the other hand, at Roncafort, MYJ overestimates, while Boulac and $K-\varepsilon$ underestimate the maximum wind speed by $\sim$ 2 m s$^{-1}$. $K-\varepsilon-\gamma$ and $K-\varepsilon-\theta^2$ instead capture well the maximum wind speed, despite slight underestimations during the first day. In terms of RMSE and MB, at TrentoSud all simulations overestimate on average the wind speed. In particular, $K-\varepsilon-\gamma$ and $K-\varepsilon-\theta^2$ halve the MB with respect to MYJ and BouLac. The RMSEs of $K-\varepsilon-\gamma$ and $K-\varepsilon-\theta^2$ are lower than 1.5 m s$^{-1}$, while the ones of MYJ and BouLac reach 2 m s$^{-1}$. At Roncafort, the best performance in terms of MB and RMSE is shown by BouLac and the three $K-\varepsilon$, which largely outperform MYJ.

Regarding Viote, the wind pattern is different from the previous two stations. Observed up-valley wind speed peaks during daytime are of $\sim$ 2.5 m s$^{-1}$, and after the evening transition, when the wind speed rapidly decreases, a non-negligible down-valley wind of $\sim$ 1.5 m s$^{-1}$ is detected. In general, all simulations apart for BouLac overestimate the diurnal peak by $\sim$ 0.5 m s$^{-1}$. However, while MYJ, $K-\varepsilon-\gamma$ and $K-\varepsilon-\theta^2$ can capture the rapid decrease of wind speed at the evening transition, BouLac and $K-\varepsilon$ show a large delay, especially for the first and the second day. The latter three PBL schemes are even able to truly reproduce the intensity and the timing of the nocturnal down-valley wind for the first and the second day. On the other

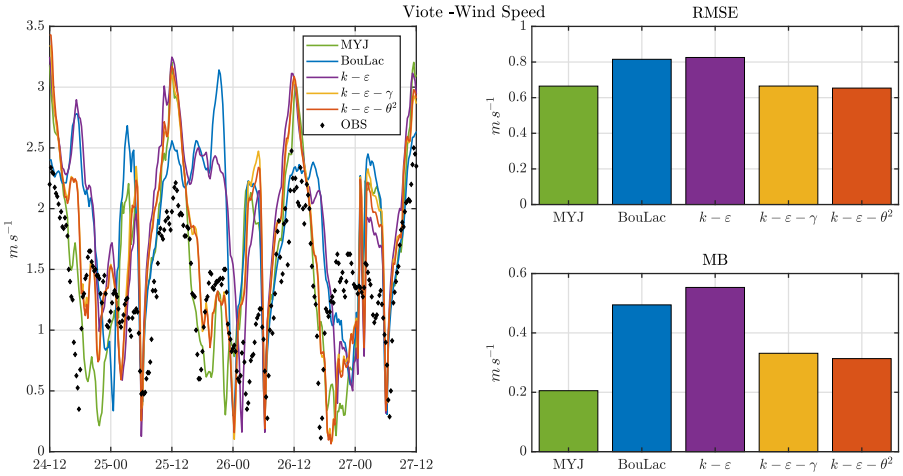


**Figure 5.15:** Timeseries of wind speed (left) recorded by the Viote weather station (black dots) and simulated with different PBL schemes (coloured lines). Top-right and bottom-right panels report the RMSE and the MB respectively, for the different PBL schemes.

hand, all PBL schemes show a peak during the second part of the night, that has actually not been observed. Statistical errors for Viote are similar for all the PBL schemes, because of the presence of not measured peaks during the second part of the night. The best performance is shown by MYJ, $K-\varepsilon-\gamma$ and $K-\varepsilon-\theta^2$, especially in terms of MB, that is largely lower than the closures that cannot correctly capture the evening wind transition.

## 5.5 Summary and Conclusions

In this study, we have tested the performance of novel PBL schemes based on the 1.5-order $K-\varepsilon$ turbulence closure, coupled with the multi-layer urban parameterization scheme BEP+BEM and implemented in the WRF model, with the aim of reproducing the boundary layer dynamics for the urban area of Trento and its surrounding areas, in the absence of strong synoptic forcing, during four sunny summer days with well-developed valley winds. Three different kinds of the $K-\varepsilon$ turbulence closure have been tested: the standard $K-\varepsilon$ of Launder et al. (1974), the $K-\varepsilon-\gamma$, where the computation of the Prandtl number as in Hong et al. (2006b), an additional term in the prognostic equation of $\varepsilon$ as in Zeng et al. (2020b), and a counter-gradient term in the prognostic equation of potential temperature as in Ching et al. (2014) have been added, and the $K-\varepsilon-\theta^2$, where the counter-gradient term has been computed through a prognostic equation for the potential temperature variance as in Lazeroms et al. (2016). The novel PBL schemes were compared with other two 1.5-order state-of-the-art closures: BouLac (Bougeault et al., 1989) and MYJ (Janjic, 2002), which have been already coupled with the BEP+BEM urban canopy scheme. High resolution input datasets were adopted to better represent the complex orography, the urban heterogeneity, and the land-use, as they are more suitable for the 333 m horizontal resolution of the present numerical simulations than the standard datasets present in the WRF model. Model results were compared against measurements from surface weather stations, highlighting that the simulations performed with the standard $K-\varepsilon$ closure generally do not improve the model performance with respect to MYJ and BouLac, since temperature

range and wind transitions show discrepancies with respect to observations. It is well known that in Alpine valleys maximum and minimum temperatures and wind speed intensities are difficult to capture by mesoscale NWP models (Chen et al., 2017b; Giovannini et al., 2014). However, adding the computation of the Prandtl number, opportunely correcting the prognostic dissipation rate equation, and including a counter-gradient term in the prognostic equation of potential temperature, the new closures perform better than state-of-the-art turbulence closures coupled with the multi-layer urban canopy parameterization. Specifically, benefits have been found in the reproduction of minimum and maximum temperature, along with improvements in the simulation of the maximum intensity of the up-valley wind and of the timing of its transition to down-valley wind. The largest enhancements take place for rural stations situated on the valley floor, where usually conventional PBL schemes cannot capture the minimum temperature under stable stratification.

The additional advantage of a $K-\varepsilon$-based turbulence closure is the absence of a parameterization of a length scale, included in most 1.5-order PBL schemes. Turbulent length scales are calculated through diagnostic equations, usually appealing to empiric constant valid for particular cases, in general for flat terrain with spatially homogeneous surface fluxes. In mountainous and urban terrain, where heterogeneity leads to more complex and unsteady PBL structures, a prognostic equation for the dissipation rate (or equivalently for the length scale) has the advantage, with respect to conventional $K-\ell$-based PBL closures, to take into account history and transport effects, which get more dominant as the complexity of the PBL increases.

Future works will focus on the application of these newly developed $K-\varepsilon$-based PBL schemes for other case studies, in order to assess their performance for various atmospheric features. Moreover, we are planning to carry out additional comparisons with observed vertical profiles of temperature and wind speed in the valley atmosphere, in order to evaluate their efficiency in stable regimes, where state-of-the-art PBL schemes usually cannot reproduce the vertical stratification (Zilitinkevich et al., 2007).

# Bibliography

Ahmad Zaki, S., Hagishima, A., & Tanimoto, J. (2012). Experimental study of wind-induced ventilation in urban building of cube arrays with various layouts. *Journal of Wind Engineering and Industrial Aerodynamics*, *103*, 31–40. https://doi.org/10.1016/j.jweia.2012.02.008

Angevine, W. M., Jiang, H., & Mauritsen, T. (2010). Performance of an eddy diffusivity-mass flux scheme for shallow cumulus boundary layers. *Monthly Weather Review*, *138*(7), 2895–2912. https://doi.org/10.1175/2010MWR3142.1

Antoniou, N., Montazeri, H., Wigo, H., Neophytou, M. K., Blocken, B., & Sandberg, M. (2017). CFD and wind-tunnel analysis of outdoor ventilation in a real compact heterogeneous urban area: Evaluation using "air delay". *Building and Environment*, *126*(June), 355–372. https://doi.org/10.1016/j.buildenv.2017.10.013

Arnold, D., Morton, D., Schicker, I., Seibert, P., Rotach, M. W., Horvath, K., Dudhia, J., Satomura, T., Müller, M., Zängl, G., Takemi, T., Serafin, S., Schmidli, J., & Schneider, S. (2012). High Resolution Modelling in Complex Terrain . Report on the HiRCoT 2012 Workshop, Vienna, 21-23 February 2012. *BOKU-Met Report*, *21*(February), 42pp. https://meteo.boku.ac.at/report/BOKU-Met_Report_21_online.pdf

Auvinen, M., Boi, S., Hellsten, A., Tanhuanpää, T., & Järvi, L. (2020). Study of Realistic Urban Boundary Layer Turbulence with High-Resolution Large-Eddy Simulation. *Atmosphere*, *11*(2), 201. https://doi.org/10.3390/atmos11020201

Avolio, E., Federico, S., Miglietta, M., Lo Feudo, T., Calidonna, C., & Sempreviva, A. (2017). Sensitivity analysis of WRF model PBL schemes in simulating boundary-layer variables in southern Italy: An experimental campaign. *Atmospheric Research*, *192*(April), 58–71. https://doi.org/10.1016/j.atmosres.2017.04.003

Baklanov, A. A., Grisogono, B., Bornstein, R., Mahrt, L., Zilitinkevich, S. S., Taylor, P., Larsen, S. E., Rotach, M. W., & Fernando, H. J. S. (2011). The Nature, Theory, and Modeling of Atmospheric Planetary Boundary Layers. *Bulletin of the American Meteorological Society*, *92*(2), 123–128. https://doi.org/10.1175/2010BAMS2797.1

Beare, R. J., Macvean, M. K., Holtslag, A. A., Cuxart, J., Esau, I., Golaz, J. C., Jimenez, M. A., Khairoutdinov, M., Kosovic, B., Lewellen, D., Lund, T. S., Lundquist, J. K., McCabe, A., Moene, A. F., Noh, Y., Raasch, S., & Sullivan, P. (2006). An intercomparison of large-eddy simulations of the stable boundary layer. *Boundary-Layer Meteorology*, *118*(2), 247–272. https://doi.org/10.1007/s10546-004-2820-6

Beljaars, A. C. M., Walmsley, J. L., & Taylor, P. A. (1987). A mixed spectral finite-difference model for neutrally stratified boundary-layer flow over roughness changes and topography. *Boundary-Layer Meteorology*, *38*(3), 273–303. https://doi.org/10.1007/BF00122448

Bougeault, P., & Lacarrere, P. (1989). Parameterization of Orography-Induced Turbulence in a Mesobeta–Scale Model. *Monthly Weather Review*, *117*(8), 1872–1890. https://doi.org/10.1175/1520-0493(1989)117<1872:POOITI>2.0.CO;2

Breiman, L. (2001). Random Forests. *Mach. Learn.*, *45*(1), 5–32. https://doi.org/10.1088/1751-8113/44/8/085201

Britter, R. E., & Hanna, S. R. (2003). Flow and Dispersion in Urban Areas. *Annual Review of Fluid Mechanics*, *35*(1), 469–496. https://doi.org/10.1146/annurev.fluid.35.101101.161147

Broadbent, A. M., Krayenhoff, E. S., Georgescu, M., & Sailor, D. J. (2019). The Observed Effects of Utility-Scale Photovoltaics on Near-Surface Air Temperature and Energy Balance. *Journal of Applied Meteorology and Climatology*, *58*(5), 989–1006. https://doi.org/10.1175/JAMC-D-18-0271.1

Brousse, O., Martilli, A., Foley, M., Mills, G., & Bechtel, B. (2016). WUDAPT, an efficient land use producing data tool for mesoscale models? Integration of urban LCZ in WRF over Madrid. *Urban Climate*, *17*, 116–134. https://doi.org/10.1016/j.uclim.2016.04.001

Chapman, S., Watson, J. E. M., Salazar, A., Thatcher, M., & McAlpine, C. A. (2017). The impact of urbanization and climate change on urban temperatures: a systematic review. *Landscape Ecology*, *32*(10), 1921–1935. https://doi.org/10.1007/s10980-017-0561-4

Chen, F., Kusaka, H., Bornstein, R., Ching, J., Grimmond, C. S. B., Grossman-Clarke, S., Loridan, T., Manning, K. W., Martilli, A., Miao, S., Sailor, D., Salamanca, F. P., Taha, H., Tewari, M., Wang, X., Wyszogrodzki, A. A., & Zhang, C. (2011). The integrated WRF/urban modelling system: development, evaluation, and applications to urban environmental problems. *Int. J. Climatol.*, *31*(2), 273–288. https://doi.org/10.1002/joc.2158

Chen, L., Hang, J., Sandberg, M., Claesson, L., Di Sabatino, S., & Wigo, H. (2017a). The impacts of building height variations and building packing densities on flow adjustment and city breathability in idealized urban models. *Building and Environment*, *118*, 344–361. https://doi.org/10.1016/j.buildenv.2017.03.042

Chen, L., Hang, J., Sandberg, M., Claesson, L., Di Sabatino, S., & Wigo, H. (2017b). The impacts of building height variations and building packing densities on flow adjustment and city breathability in idealized urban models. *Building and Environment*, *118*(1-2), 344–361. https://doi.org/10.1016/j.buildenv.2017.03.042

Cheng, H., Hayden, P., Robins, A., & Castro, I. (2007). Flow over cube arrays of different packing densities. *Journal of Wind Engineering and Industrial Aerodynamics*, *95*(8), 715–740. https://doi.org/10.1016/j.jweia.2007.01.004

Ching, J., Mills, G., Bechtel, B., See, L., Feddema, J., Wang, X., Ren, C., Brousse, O., Martilli, A., Neophytou, M., Mouzourides, P., Stewart, I., Hanna, A., Ng, E., Foley, M., Alexander, P., Aliaga, D., Niyogi, D., Shreevastava, A., … Theeuwes, N. (2018). WUDAPT: An Urban Weather, Climate, and Environmental Modeling Infrastructure for the Anthropocene. *Bulletin of the American Meteorological Society*, *99*(9), 1907–1924. https://doi.org/10.1175/BAMS-D-16-0236.1

Ching, J., Rotunno, R., LeMone, M., Martilli, A., Kosovic, B., Jimenez, P. A., & Dudhia, J. (2014). Convectively Induced Secondary Circulations in Fine-Grid Mesoscale Numerical Weather Prediction Models. *Monthly Weather Review*, *142*(9), 3284–3302. https://doi.org/10.1175/MWR-D-13-00318.1

Chrobok, G., Raasch, S., & Etling, D. (1992). A comparison of local and non-local turbulence closure methods for the case of a cold air outbreak. *Boundary-Layer Meteorology*, *58*(1-2), 69–90. https://doi.org/10.1007/BF00120752

Coceal, O., & Belcher, S. E. (2004). A canopy model of mean winds through urban areas. *Quarterly Journal of the Royal Meteorological Society*, *130*(599 PART B), 1349–1372. https://doi.org/10.1256/qj.03.40

Coceal, O., Thomas, T. G., Castro, I. P., & Belcher, S. E. (2006). Mean Flow and Turbulence Statistics Over Groups of Urban-like Cubical Obstacles. *Boundary-Layer Meteorology*, *121*(3), 491–519. https://doi.org/10.1007/s10546-006-9076-2

Cohen, A. E., Cavallo, S. M., Coniglio, M. C., & Brooks, H. E. (2015). A review of planetary boundary layer parameterization schemes and their sensitivity in simulating southeastern U.S. cold season severe weather environments. *Weather and Forecasting*, *30*(3), 591–612. https://doi.org/10.1175/WAF-D-14-00105.1

Colonna, N. M., Ferrero, E., & Rizza, U. (2009). Nonlocal boundary layer: The pure buoyancy-driven and the buoyancy-shear-driven cases. *Journal of Geophysical Research*, *114*(D5), D05102. https://doi.org/10.1029/2008JD010682

Craft, T., Ince, N., & Launder, B. (1996). Recent developments in second-moment closure for buoyancy-affected flows. *Dynamics of Atmospheres and Oceans*, *23*(1-4), 99–114. https://doi.org/10.1016/0377-0265(95)00424-6

Cuxart, J., Holtslag, A. A., Beare, R. J., Bazile, E., Beljaars, A., Cheng, A., Conangla, L., Ek, M., Freedman, F., Hamdi, R., Kerstein, A., Kitagawa, H., Lenderink, G., Lewellen, D., Mailhot, J., Mauritsen, T., Perov, V., Schayes, G., Steeneveld, G. J., ... Xu, K. M. (2006). Single-column model intercomparison for a stably stratified atmospheric boundary layer. *Boundary-Layer Meteorology*, *118*(2), 273–303. https://doi.org/10.1007/s10546-005-3780-1

Dai, Y., Mak, C. M., Ai, Z., & Hang, J. (2018). Evaluation of computational and physical parameters influencing CFD simulations of pollutant dispersion in building arrays. *Building and Environment*, *137*(January), 90–107. https://doi.org/10.1016/j.buildenv.2018.04.005

de Munck, C., Lemonsu, A., Masson, V., Le Bras, J., & Bonhomme, M. (2018). Evaluating the impacts of greening scenarios on thermal comfort and energy and water consumptions for adapting Paris city to climate change. *Urban Climate*. https://doi.org/10.1016/j.uclim.2017.01.003

de Munck, C. S., Lemonsu, A., Bouzouidja, R., Masson, V., & Claverie, R. (2013). The GREENROOF module (v7.3) for modelling green roof hydrological and energetic performances within TEB. *Geoscientific Model Development*, *6*(6), 1941–1960. https://doi.org/10.5194/gmd-6-1941-2013

De Munck, C., Pigeon, G., Masson, V., Meunier, F., Bousquet, P., Tréméac, B., Merchat, M., Poeuf, P., & Marchadier, C. (2013). How much can air conditioning increase air temperatures for a city like Paris, France? *Int. J. Climatol.*, *33*(1), 210–227. https://doi.org/10.1002/joc.3415

Deardorff, J. W. (1966). The Counter-Gradient Heat Flux in the Lower Atmosphere and in the Laboratory. *Journal of the Atmospheric Sciences*, *23*(5), 503–506. https://doi.org/10.1175/1520-0469(1966)023<0503:TCGHFI>2.0.CO;2

Deardorff, J. W. (1980). Stratocumulus-capped mixed layers derived from a three-dimensional model. *Boundary-Layer Meteorology*, *18*(4), 495–527. https://doi.org/10.1007/BF00119502

Detering, H. W., & Etling, D. (1985). Application of the E-$\varepsilon$ turbulence model to the atmospheric boundary layer. *Boundary-Layer Meteorology*, *33*(2), 113–133. https://doi.org/10.1007/BF00123386

di Sabatino, S., Leo, L. S., Cataldo, R., Ratti, C., & Britter, R. E. (2010). Construction of digital elevation models for a southern European city and a comparative morphological analysis with respect to Northern European and North American cities. *Journal of Applied Meteorology and Climatology*, *49*(7), 1377–1396. https://doi.org/10.1175/2010JAMC2117.1

Di Sabatino, S., Solazzo, E., Paradisi, P., & Britter, R. (2008). A Simple Model for Spatially-averaged Wind Profiles Within and Above an Urban Canopy. *Boundary-Layer Meteorology*, *127*(1), 131–151. https://doi.org/10.1007/s10546-007-9250-1

Dimitrova, R., Silver, Z., Zsedrovits, T., Hocut, C. M., Leo, L. S., Di Sabatino, S., & Fernando, H. J. S. (2016). Assessment of Planetary Boundary-Layer Schemes in the Weather Research and Forecasting Mesoscale Model Using MATERHORN Field Data. *Boundary-Layer Meteorology*, *159*(3), 589–609. https://doi.org/10.1007/s10546-015-0095-8

Dominguez, A., Klessl, J., & Luvall, J. (2011). Effects of Solar Photovoltaic Panels on Roof Heat Transfer. *Solar Energy 85:2244–2255*, 1–21.

Dudhia, J. (1989). Numerical Study of Convection Observed during the Winter Monsoon Experiment Using a Mesoscale Two-Dimensional Model. *J. Atmos. Sci.*, *46*(20), 3077–3107. https://doi.org/10.1175/1520-0469(1989)046<3077:NSOCOD>2.0.CO;2

Duynkerke, P. G. (1988). Application of the E - $\varepsilon$ turbulence closure model to the neutral and stable atmospheric boundary layer. https://doi.org/10.1175/1520-0469(1988)045<0865:AOTTCM>2.0.CO;2

Eurostat. (2018). *Living conditions in Europe, 2018 edition*. https://doi.org/10.2785/39876

Ferrero, E., & Canonico, M. (2021). Analysis of the Influence of the Length Scales in a Boundary-Layer Model. *Boundary-Layer Meteorology*, *179*(3), 385–401. https://doi.org/10.1007/s10546-020-00602-0

Giometto, M., Christen, A., Egli, P., Schmid, M., Tooke, R., Coops, N., & Parlange, M. (2017). Effects of trees on mean wind, turbulence and momentum exchange within and above a real urban environment. *Advances in Water Resources*, *106*(June), 154–168. https://doi.org/10.1016/j.advwatres.2017.06.018

Giovannini, L., Laiti, L., Serafin, S., & Zardi, D. (2017). The thermally driven diurnal wind system of the Adige Valley in the Italian Alps. *Quarterly Journal of the Royal Meteorological Society*, *143*(707), 2389–2402. https://doi.org/10.1002/qj.3092

Giovannini, L., Zardi, D., & de Franceschi, M. (2011). Analysis of the urban thermal fingerprint of the city of trento in the alps. *Journal of Applied Meteorology and Climatology*, *50*(5), 1145–1162. https://doi.org/10.1175/2010JAMC2613.1

Giovannini, L., Zardi, D., & de Franceschi, M. (2013). Characterization of the Thermal Structure inside an Urban Canyon: Field Measurements and Validation of a Simple Model. *Journal of Applied Meteorology and Climatology*, *52*(1), 64–81. https://doi.org/10.1175/JAMC-D-12-06.1

Giovannini, L., Zardi, D., de Franceschi, M., & Chen, F. (2014). Numerical simulations of boundary-layer processes and urban-induced alterations in an Alpine valley. *International Journal of Climatology*, *34*(4), 1111–1131. https://doi.org/10.1002/joc.3750

Glotfelty, T., Tewari, M., Sampson, K., Duda, M., Chen, F., & Ching, J. (2013). *NUDAPT 44 Documentation Introduction* (tech. rep.). https://ral.ucar.edu/sites/default/files/public/product-tool/NUDAPT_44_Documentation.pdf

Grell, G. A., & Dévényi, D. (2002). A generalized approach to parameterizing convection combining ensemble and data assimilation techniques. *Geophys. Res. Lett.*, *29*(14), 38–1–38–4. https://doi.org/10.1029/2002GL015311

Grimm, N. B., Faeth, S. H., Golubiewski, N. E., Redman, C. L., Wu, J., Bai, X., & Briggs, J. M. (2008). Global Change and the Ecology of Cities. *Science (80-. ).*, *319*(5864), 756–760. https://doi.org/10.1126/science.1150195

Grimmond, C. S. B., & Oke, T. R. (1999). Aerodynamic Properties of Urban Areas Derived from Analysis of Surface Form. *Journal of Applied Meteorology*, *38*(9), 1262–1292. https://doi.org/10.1175/1520-0450(1999)038<1262:APOUAD>2.0.CO;2

Gutierrez, E. (2015). *Quantification of environmental impacts of heat fluxes from built environments* (Doctoral dissertation). The City University of New York.

Gutiérrez, E., González, J. E., Martilli, A., & Bornstein, R. (2015). On the Anthropogenic Heat Fluxes Using an Air Conditioning Evaporative Cooling Parameterization for Mesoscale Urban Canopy Models. *J. Sol. Energy Eng.*, *137*(5), 051005. https://doi.org/10.1115/1.4030854

Hammerberg, K., Brousse, O., Martilli, A., & Mahdavi, A. (2018). Implications of employing detailed urban canopy parameters for mesoscale climate modelling: a comparison between WUDAPT and GIS databases over Vienna, Austria. *Int. J. Climatol.*, *38*(February), e1241–e1257. https://doi.org/https://doi.org/10.1023/A:1010933404324

Han, J., Witek, M. L., Teixeira, J., Sun, R., Pan, H.-L., Fletcher, J. K., & Bretherton, C. S. (2016). Implementation in the NCEP GFS of a Hybrid Eddy-Diffusivity Mass-Flux (EDMF) Boundary Layer Parameterization with Dissipative Heating and Modified Stable Boundary Layer Mixing. *Weather and Forecasting*, *31*(1), 341–352. https://doi.org/10.1175/WAF-D-15-0053.1

Hartogensis, O. K., & Bruin, H. A. R. D. (2005). Monin–Obukhov Similarity Functions of the Structure Parameter of Temperature and Turbulent Kinetic Energy Dissipation Rate

in the Stable Boundary Layer. *Boundary-Layer Meteorology*, *116*(2), 253–276. https://doi.org/10.1007/s10546-004-2817-1

Hong, S.-Y., & Lim, J. (2006a). The wrf single-moment 6-class microphysics scheme (wsm6). *Asia-pacific Journal of Atmospheric Sciences*, *42*, 129–151.

Hong, S.-Y., Noh, Y., & Dudhia, J. (2006b). A New Vertical Diffusion Package with an Explicit Treatment of Entrainment Processes. *Monthly Weather Review*, *134*(9), 2318–2341. https://doi.org/10.1175/MWR3199.1

Hu, X. M., Nielsen-Gammon, J. W., & Zhang, F. (2010). Evaluation of three planetary boundary layer schemes in the WRF model. *Journal of Applied Meteorology and Climatology*, *49*(9), 1831–1844. https://doi.org/10.1175/2010JAMC2432.1

Jacquemin, B., & Noilhan, J. (1990). Sensitivity study and validation of a land surface parameterization using the HAPEX-MOBILHY data set. *Boundary-Layer Meteorology*, *52*(1-2), 93–134. https://doi.org/10.1007/BF00123180

Janjic, Z. (2002). Nonsingular Implementation of the Mellor-Yamada Level 2.5 Scheme in the NCEP Meso model. *NCEP Office Note*, *437*, 61. http://www.emc.ncep.noaa.gov/officenotes/newernotes/on437.pdf

Jee, J.-B., & Kim, S. (2016). Sensitivity Study on High-Resolution Numerical Modeling of Static Topographic Data. *Atmosphere*, *7*(7), 86. https://doi.org/10.3390/atmos7070086

Jones, A. D., & Underwood, C. P. (2002). A thermal model for photovoltaic systems. *Fuel and Energy Abstracts*, *43*(3), 199. https://doi.org/10.1016/S0140-6701(02)85831-3

Kain, J. S., & Fritsch, J. M. Convective Parameterization for Mesoscale Models: The Kain-Fritsch Scheme. In: *The representation of cumulus convection in numerical models*. Vol. 43. *1*. Boston, MA: American Meteorological Society, 1993, pp. 165–170. https://doi.org/10.1007/978-1-935704-13-3_16.

Kanda, M., Kawai, T., Kanega, M., Moriwaki, R., Narita, K., & Hagishima, A. (2005). A Simple Energy Balance Model for Regular Building Arrays. *Boundary-Layer Meteorology*, *116*(3), 423–443. https://doi.org/10.1007/s10546-004-7956-x

Katul, G. G., Mahrt, L., Poggi, D., & Sanz, C. (2004). ONE- and TWO-Equation Models for Canopy Turbulence. *Boundary-Layer Meteorology*, *113*(1), 81–109. https://doi.org/10.1023/B:BOUN.0000037333.48760.e5

Kolokotroni, M., Gowreesunker, B., & Giridharan, R. (2013). Cool roof technology in London: An experimental and modelling study. *Energy and Buildings*, *67*, 658–667. https://doi.org/10.1016/j.enbuild.2011.07.011

Kosović, B., & Curry, J. A. (2000). A large eddy simulation study of a quasi-steady, stably stratified atmospheric boundary layer. *Journal of the Atmospheric Sciences*, *57*(8), 1052–1068. https://doi.org/10.1175/1520-0469(2000)057<1052:ALESSO>2.0.CO;2

Kusaka, H., Kondo, H., Kikegawa, Y., & Kimura, F. (2001). A Simple Single-Layer Urban Canopy Model For Atmospheric Models: Comparison With Multi-Layer And Slab Models. *Boundary-Layer Meteorol.*, *101*(3), 329–358. https://doi.org/10.1023/A:1019207923078

Lai, D., Liu, W., Gan, T., Liu, K., & Chen, Q. (2019). A review of mitigating strategies to improve the thermal environment and thermal comfort in urban outdoor spaces. *Science of The Total Environment*, *661*, 337–353. https://doi.org/10.1016/j.scitotenv.2019.01.062

Langland, R. H., & Liou, C.-S. (1996). Implementation of an E – Parameterization of Vertical Subgrid-Scale Mixing in a Regional Model. *Monthly Weather Review*, *124*(5), 905–918. https://doi.org/10.1175/1520-0493(1996)124<0905:IOAPOV>2.0.CO;2

Launder, B., & Spalding, D. (1974). The numerical computation of turbulent flows. *Computer Methods in Applied Mechanics and Engineering*, *3*(2), 269–289. https://doi.org/10.1016/0045-7825(74)90029-2

Launder, B., & Spalding, D. The numerical computation of turbuulent flows. In: *Numerical prediction of flow, heat transfer, turbulence and combustion*. Elsevier, 1983, pp. 96–116. https://doi.org/10.1016/B978-0-08-030937-8.50016-7.

Lazeroms, W. M. J., Svensson, G., Bazile, E., Brethouwer, G., Wallin, S., & Johansson, A. V. (2016). Study of Transitions in the Atmospheric Boundary Layer Using Explicit Algebraic Turbulence Models. *Boundary-Layer Meteorology*, *161*(1), 19–47. https://doi.org/10.1007/s10546-016-0194-1

Lazeroms, W., Brethouwer, G., Wallin, S., & Johansson, A. (2015). Efficient treatment of the nonlinear features in algebraic Reynolds-stress and heat-flux models for stratified and convective flows. *International Journal of Heat and Fluid Flow*, *53*, 15–28. https://doi.org/10.1016/j.ijheatfluidflow.2015.01.005

Lee, W. (2011). Tridiagonal matrices: Thomas algorithm. *MS6021, Scientific Computation, University of Limerick*.

Lehner, M., & Rotach, M. (2018). Current Challenges in Understanding and Predicting Transport and Exchange in the Atmosphere over Mountainous Terrain. *Atmosphere*, *9*(7), 276. https://doi.org/10.3390/atmos9070276

Lew, A. J., Buscaglia, G. C., & Carrica, P. M. (2001). A Note on the Numerical Treatment of the k-$\varepsilon$ Turbulence Model. *International Journal of Computational Fluid Dynamics*, *14*(3), 201–209. https://doi.org/10.1080/10618560108940724

Li, D., & Bou-Zeid, E. (2013). Synergistic Interactions between Urban Heat Islands and Heat Waves: The Impact in Cities Is Larger than the Sum of Its Parts*. *Journal of Applied Meteorology and Climatology*, *52*(9), 2051–2064. https://doi.org/10.1175/JAMC-D-13-02.1

Li, D., Bou-Zeid, E., & Oppenheimer, M. (2014). The effectiveness of cool and green roofs as urban heat island mitigation strategies. *Environmental Research Letters*, *9*(5), 055002. https://doi.org/10.1088/1748-9326/9/5/055002

Li, H., Wolter, M., Wang, X., & Sodoudi, S. (2018). Impact of land cover data on the simulation of urban heat island for Berlin using WRF coupled with bulk approach of Noah-LSM. *Theor. Appl. Climatol.*, *134*(1-2), 67–81. https://doi.org/10.1007/s00704-017-2253-z

Liu, J., Chen, J. M., Black, T. A., & Novak, M. D. (1996). E - $\varepsilon$ modelling of turbulent air flow downwind of a model forest edge. *Boundary-Layer Meteorology*, *77*(1), 21–44. https://doi.org/10.1007/BF00121857

Liu, Y., Liu, Y., Muñoz-Esparza, D., Hu, F., Yan, C., & Miao, S. (2020). Simulation of Flow Fields in Complex Terrain with WRF-LES: Sensitivity Assessment of Different PBL Treatments. *Journal of Applied Meteorology and Climatology*, *59*(9), 1481–1501. https://doi.org/10.1175/JAMC-D-19-0304.1

Louis, J. F. (1979). A parametric model of vertical eddy fluxes in the atmosphere. *Boundary-Layer Meteorology*, *17*(2), 187–202. https://doi.org/10.1007/BF00117978

Martilli, A. (2014). An idealized study of city structure, urban climate, energy consumption, and air quality. *Urban Climate*, *10*(P2), 430–446. https://doi.org/10.1016/j.uclim.2014.03.003

Martilli, A., Brousse, O., & Ching, J. (2016). *WUDAPT to WRF (W2W) : Urbanized WRF modeling using WUDAPT* (tech. rep.). https://doi.org/10.13140/RG.2.1.3405.2724

Martilli, A., Clappier, A., & Rotach, M. W. (2002). An Urban Surface Exchange Parametrization for Mesoscale Models. *Boundary-Layer Meteorology*, *104*(2), 261–304.

Masson, V., Bonhomme, M., Salagnac, J.-L., Briottet, X., & Lemonsu, A. (2014). Solar panels reduce both global warming and urban heat island. *Frontiers in Environmental Science*, *2*(June), 1–10. https://doi.org/10.3389/fenvs.2014.00014

Masson, V. (2000). A Physically-Based Scheme For The Urban Energy Budget In Atmospheric Models. *Boundary-Layer Meteorol.*, *94*(3), 357–397. https://doi.org/10.1023/A:1002463829265

Masson, V., & Seity, Y. (2009). Including Atmospheric Layers in Vegetation and Urban Offline Surface Schemes. *Journal of Applied Meteorology and Climatology*, *48*(7), 1377–1397. https://doi.org/10.1175/2009JAMC1866.1

Masson, V. (2006). Urban surface modeling and the meso-scale impact of cities. *Theor. Appl. Climatol.*, *84*(1-3), 35–45. https://doi.org/10.1007/s00704-005-0142-3

Mauritsen, T., Svensson, G., Zilitinkevich, S. S., Esau, I., Enger, L., & Grisogono, B. (2007). A Total Turbulent Energy Closure Model for Neutrally and Stably Stratified Atmospheric Boundary Layers. *Journal of the Atmospheric Sciences*, *64*(11), 4113–4126. https://doi.org/10.1175/2007JAS2294.1

Mellor, G. L., & Yamada, T. (1982). Development of a turbulence closure model for geophysical fluid problems. *Reviews of Geophysics*, *20*(4), 851. https://doi.org/10.1029/RG020i004p00851

Mlawer, E. J., Taubman, S. J., Brown, P. D., Iacono, M. J., & Clough, S. A. (1997). Radiative transfer for inhomogeneous atmospheres: RRTM, a validated correlated-k model for the longwave. *Journal of Geophysical Research Atmospheres*, *102*(14), 16663–16682. https://doi.org/10.1029/97jd00237

Moeng, C.-H., Dudhia, J., Klemp, J., & Sullivan, P. (2007). Examining Two-Way Grid Nesting for Large Eddy Simulation of the PBL Using the WRF Model. *Monthly Weather Review*, *135*(6), 2295–2311. https://doi.org/10.1175/MWR3406.1

Moeng, C.-H., & Wyngaard, J. C. (1989). Evaluation of Turbulent Transport and Dissipation Closures in Second-Order Modeling. *Journal of the Atmospheric Sciences*, *46*(14), 2311–2330. https://doi.org/10.1175/1520-0469(1989)046<2311:EOTTAD>2.0.CO;2

Monin, A. S., & Obukhov, A. M. (1954). Basic laws of turbulent mixing in the surface layer of the atmosphere. *Nauk SSSR Geophiz. Inst.*, *24*(151), 163–187.

Muñoz-Esparza, D., Sharman, R. D., & Lundquist, J. K. (2018). Turbulence Dissipation Rate in the Atmospheric Boundary Layer: Observations and WRF Mesoscale Modeling during the XPIA Field Campaign. *Monthly Weather Review*, *146*(1), 351–371. https://doi.org/10.1175/MWR-D-17-0186.1

Nakanishi, M. (2001). Improvement of the Mellor-Yamada turbulence closure model based on large-eddy simulation data. *Boundary-Layer Meteorology*, *99*(3), 349–378. https://doi.org/10.1023/A:1018915827400

Nakanishi, M., & Niino, H. (2004). An improved Mellor-Yamada Level-3 model with condensation physics: Its design and verification. *Boundary-Layer Meteorology*, *112*(1), 1–31. https://doi.org/10.1023/B:BOUN.0000020164.04146.98

National Centers for Environmental Prediction, National Weather Service, NOAA, U. D. o. C. (2015). No Title. *Research Data Archive at the National Center for Atmospheric Research, Computational and Information Systems Laboratory*. https://doi.org/https://doi.org/10.5065/D65Q4T4Z

Nazarian, N., Krayenhoff, E. S., & Martilli, A. (2019). A One-Dimensional Model of Turbulent Flow Through 'Urban' Canopies: Updates Based on Large-Eddy Simulation. *Geoscientific Model Development*, (October), 1–24. https://doi.org/10.5194/gmd-2019-230

NCEP. (2000). Research Data Archive at the National Center for Atmospheric Research, Computational and Information Systems Laboratory. https://doi.org/10.5065/D6M043C6

Nielsen-Gammon, J. W., Hu, X. M., Zhang, F., & Pleim, J. E. (2010). Evaluation of planetary boundary layer scheme sensitivities for the purpose of parameter estimation. *Monthly Weather Review*, *138*(9), 3400–3417. https://doi.org/10.1175/2010MWR3292.1

Niu, G. Y., Yang, Z. L., Mitchell, K. E., Chen, F., Ek, M. B., Barlage, M., Kumar, A., Manning, K., Niyogi, D., Rosero, E., Tewari, M., & Xia, Y. (2011). The community Noah land surface model with multiparameterization options (Noah-MP): 1. Model description and evaluation with local-scale measurements. *J. Geophys. Res. Atmos.*, *116*(12), 1–19. https://doi.org/10.1029/2010JD015139

NREL. (2020). Best Research-Cell Efficiencies Chart. Retrieved February 12, 2020, from https://www.nrel.gov/pv/cell-efficiency.html

Oke, T. R. (1987). Boundary layer climates. 2ª edition. *J. Chem. Inf. Model.*, 274–300. https://doi.org/10.1017/CBO9781107415324.004

Oke, T. R., Mills, G., Christen, A., & Voogt, J. A. (2017). *Urban Climates*. Cambridge University Press. https://doi.org/10.1017/9781139016476

Pappaccogli, G., Giovannini, L., Cappelletti, F., & Zardi, D. (2018). Challenges in the application of a WRF/Urban-TRNSYS model chain for estimating the cooling demand of buildings: A case study in Bolzano (Italy). *Science and Technology for the Built Environment*, *24*(5), 529–544. https://doi.org/10.1080/23744731.2018.1447214

Pappaccogli, G., Giovannini, L., Zardi, D., & Martilli, A. (2020). Sensitivity analysis of urban microclimatic conditions and building energy consumption on urban parameters by means of idealized numerical simulations. *Urban Climate*, *34*(April), 100677. https://doi.org/10.1016/j.uclim.2020.100677

Pappaccogli, G., Giovannini, L., Zardi, D., & Martilli, A. (2021). Assessing the Ability of WRF-BEP + BEM in Reproducing the Wintertime Building Energy Consumption of an Italian Alpine City. *Journal of Geophysical Research: Atmospheres*, *126*(8). https://doi.org/10.1029/2020JD033652

Park, S. H., Klemp, J. B., & Kim, J. H. (2019). Hybrid mass coordinate in WRF-ARW and its impact on upper-level turbulence forecasting. *Monthly Weather Review*, *147*(3), 971–985. https://doi.org/10.1175/MWR-D-18-0334.1

Rampanelli, G., Zardi, D., & Rotunno, R. (2004). Mechanisms of Up-Valley Winds. *Journal of the Atmospheric Sciences*, *61*(24), 3097–3111. https://doi.org/10.1175/JAS-3354.1

Rotach, M. W., Gohm, A., Lang, M. N., Leukauf, D., Stiperski, I., & Wagner, J. S. (2015). On the vertical exchange of heat, mass, and momentum over complex, mountainous terrain. *Frontiers in Earth Sciences*, *3*(December), 1–14. https://doi.org/10.3389/feart.2015.00076

Roth, M. (2000). Review of atmospheric turbulence over cities. *Quarterly Journal of the Royal Meteorological Society*, *126*(564), 941–990. https://doi.org/10.1256/smsqj.56408

Salamanca, F., Georgescu, M., Mahalov, A., Moustaoui, M., & Martilli, A. (2016). Citywide Impacts of Cool Roof and Rooftop Solar Photovoltaic Deployment on Near-Surface Air Temperature and Cooling Energy Demand. *Boundary-Layer Meteorology*, *161*(1), 203–221. https://doi.org/10.1007/s10546-016-0160-y

Salamanca, F., Krpo, A., Martilli, A., & Clappier, A. (2010). A new building energy model coupled with an urban canopy parameterization for urban climate simulations—part I. formulation, verification, and sensitivity analysis of the model. *Theoretical and Applied Climatology*, *99*(3-4), 331–344. https://doi.org/10.1007/s00704-009-0142-9

Salamanca, F., Martilli, A., Tewari, M., & Chen, F. (2011). A study of the urban boundary layer using different urban parameterizations and high-resolution urban canopy parameters with WRF. *J. Appl. Meteorol. Climatol.*, *50*(5), 1107–1128. https://doi.org/10.1175/2010JAMC2538.1

Salamanca, F., Martilli, A., & Yag??e, C. (2012a). A numerical study of the Urban Heat Island over Madrid during the DESIREX (2008) campaign with WRF and an evaluation of simple mitigation strategies. *Int. J. Climatol.*, *32*(15), 2372–2386. https://doi.org/10.1002/joc.3398

Salamanca, F., Martilli, A., & Yagüe, C. (2012b). A numerical study of the Urban Heat Island over Madrid during the DESIREX (2008) campaign with WRF and an evaluation of simple mitigation strategies. *Int. J. Climatol.*, *32*(15), 2372–2386. https://doi.org/10.1002/joc.3398

Salamanca, F., Zhang, Y., Barlage, M., Chen, F., Mahalov, A., & Miao, S. (2018). Evaluation of the WRF-Urban Modeling System Coupled to Noah and Noah-MP Land Surface Models Over a Semiarid Urban Environment. *J. Geophys. Res. Atmos.*, *123*(5), 2387–2408. https://doi.org/10.1002/2018JD028377

Santamouris, M. (2014). Cooling the cities – A review of reflective and green roof mitigation technologies to fight heat island and improve comfort in urban environments. *Solar Energy*, *103*, 682–703. https://doi.org/10.1016/j.solener.2012.07.003

Santiago, J. L., Coceal, O., Martilli, A., & Belcher, S. E. (2008). Variation of the sectional drag coefficient of a group of buildings with packing density. *Boundary-Layer Meteorology*, *128*(3), 445–457. https://doi.org/10.1007/s10546-008-9294-x

Santiago, J. L., & Martilli, A. (2010). A Dynamic Urban Canopy Parameterization for Mesoscale Models Based on Computational Fluid Dynamics Reynolds-Averaged Navier-Stokes

Microscale Simulations. *Boundary-Layer Meteorology*, *137*(3), 417–439. https://doi.org/10.1007/s10546-010-9538-4

Sanz, C. (2003). A note on $\kappa$ - $\varepsilon$ modelling of vegetation canopy air-flows. *Boundary-Layer Meteorology*, *108*(1), 191–197. https://doi.org/10.1023/A:1023066012766

Scherba, A., Sailor, D. J., Rosenstiel, T. N., & Wamser, C. C. (2011). Modeling impacts of roof reflectivity, integrated photovoltaic panels and green roof systems on sensible heat flux into the urban environment. *Building and Environment*, *46*(12), 2542–2551. https://doi.org/10.1016/j.buildenv.2011.06.012

Schmidli, J., Billings, B., Chow, F. K., de Wekker, S. F., Doyle, J., Grubišić, V., Holt, T., Jiang, Q., Lundquist, K. A., Sheridan, P., Vosper, S., Whiteman, C. D., Wyszogrodzki, A. A., & Zängl, G. (2011). Intercomparison of mesoscale model simulations of the daytime valley wind system. *Monthly Weather Review*, *139*(5), 1389–1409. https://doi.org/10.1175/2010MWR3523.1

Serafin, S., Adler, B., Cuxart, J., De Wekker, S., Gohm, A., Grisogono, B., Kalthoff, N., Kirshbaum, D., Rotach, M., Schmidli, J., Stiperski, I., Večenaj, Ž., & Zardi, D. (2018). Exchange Processes in the Atmospheric Boundary Layer Over Mountainous Terrain. *Atmosphere*, *9*(3), 102. https://doi.org/10.3390/atmos9030102

Serafin, S., & Zardi, D. (2010). Structure of the atmospheric boundary layer in the vicinity of a developing upslope flow system: A numerical model study. *Journal of the Atmospheric Sciences*, *67*(4), 1171–1185. https://doi.org/10.1175/2009JAS3231.1

Serafin, S., & Zardi, D. (2011). Daytime Development of the Boundary Layer over a Plain and in a Valley under Fair Weather Conditions: A Comparison by Means of Idealized Numerical Simulations. *Journal of the Atmospheric Sciences*, *68*(9), 2128–2141. https://doi.org/10.1175/2011JAS3610.1

Shih, T.-H., Liou, W. W., Shabbir, A., Yang, Z., & Zhu, J. (1995). A new k-$\varepsilon$ eddy viscosity model for high reynolds number turbulent flows. *Computers & Fluids*, *24*(3), 227–238. https://doi.org/10.1016/0045-7930(94)00032-T

Short, D., Dawes, R. W., & White, I. (1995). The practicability of using Richards' equation for general purpose soil-water dynamics models. *Environment International*, *21*(5), 723–730. https://doi.org/10.1016/0160-4120(95)00065-S

Skamarock, W. C., Klemp, J. B., Dudhia, J., Gill, D., Barker, D. M., Duda, M. G, Huang, X.-Y., Wang, W., & Powers, J. G. (2008). A Description of the Advanced Research WRF Version 3. *NCAR Tech. Note NCAR/TN-475+STR*. https://doi.org/10.1080/07377366.2001.10400427

Skamarock, W., Klemp, J., Dudhia, J., Gill, D., Zhiquan, L., Berner, J., Wang, W., Powers, J., Duda, M. G., Barker, D. M., & Huang, X.-Y. (2019). A Description of the Advanced Research WRF Model Version 4. *NCAR Technical Note NCAR/TN-475+STR*, 145. https://doi.org/10.5065/1dfh-6p97

Smagorinsky, J. (1963). General circulation experiments with the primitive equations. I. The basic experiment. *Monthly Weather Review*, *91*(3), 99–164. https://doi.org/10.1175/1520-0493(1963)091<0099:GCEWTP>2.3.CO;2

Stewart, I. D., & Oke, T. R. (2012). Local climate zones for urban temperature studies. *Bulletin of the American Meteorological Society*, *93*(12), 1879–1900. https://doi.org/10.1175/BAMS-D-11-00019.1

Stewart, I. D., Oke, T. R., & Krayenhoff, E. S. (2014). Evaluation of the 'local climate zone' scheme using temperature observations and model simulations. *Int. J. Climatol.*, *34*(4), 1062–1080. https://doi.org/10.1002/joc.3746

Stull, R. B. (Ed.). (1988). *An Introduction to Boundary Layer Meteorology*. Springer Netherlands. https://doi.org/10.1007/978-94-009-3027-8

Sukoriansky, S., Galperin, B., & Perov, V. (2005). Application of a new spectral theory of stably stratified turbulence to the atmospheric boundary layer over sea ice. *Boundary-Layer Meteorology*, *117*(2), 231–257. https://doi.org/10.1007/s10546-004-6848-4

Taylor, K. E. (2001). Summarizing multiple aspects of model performance in a single diagram. *J. Geophys. Res. Atmos.*, *106*(D7), 7183–7192. https://doi.org/10.1029/2000JD900719

Tewari, M., Salamanca, F., Martilli, A., Treinish, L., & Mahalov, A. (2017). Impacts of projected urban expansion and global warming on cooling energy demand over a semiarid region. *Atmospheric Science Letters*, *18*(11), 419–426. https://doi.org/10.1002/asl.784

Tolladay, J., & Chemel, C. (2021). Numerical Modelling of Neutral Boundary-layer Flow Across a Forested Ridge. *Boundary-Layer Meteorology*. https://doi.org/10.1007/s10546-021-00628-y

Tomasi, E., Giovannini, L., Falocchi, M., Antonacci, G., Jiménez, P. A., Kosovic, B., Alessandrini, S., Zardi, D., Delle Monache, L., & Ferrero, E. (2019). Turbulence parameterizations for dispersion in sub-kilometer horizontally non-homogeneous flows. *Atmospheric Research*, *228*(April), 122–136. https://doi.org/10.1016/j.atmosres.2019.05.018

Tomasi, E., Giovannini, L., Zardi, D., & de Franceschi, M. (2017). Optimization of Noah and Noah_MP WRF Land Surface Schemes in Snow-Melting Conditions over Complex Terrain. *Monthly Weather Review*, *145*(12), 4727 –4745. https://doi.org/10.1175/MWR-D-16-0408.1

Troen, I. B., & Mahrt, L. (1986). A simple model of the atmospheric boundary layer; sensitivity to surface evaporation. *Boundary-Layer Meteorology*, *37*(1-2), 129–148. https://doi.org/10.1007/BF00122760

UNI/TS 11300–1. (2014). Energy Performance of Buildings Part 1: Evaluation of Energy Need for Space Heating and Cooling Rome.

Uno, I., Ueda, H., & Wakamatsu, S. (1989). Numerical modeling of the nocturnal urban boundary layer. *Boundary-Layer Meteorology*, *49*(1-2), 77–98. https://doi.org/10.1007/BF00116406

US Department of Energy. (2010). EnergyPlus Engineering Reference: The Reference to EnergyPlus Calculations. *US Department of Energy*, (100), 868. https://doi.org/citeulike-article-id:10579266

van der Laan, M. P., Kelly, M. C., & Sørensen, N. N. (2017). A new k-epsilon model consistent with Monin-Obukhov similarity theory. *Wind Energy*, *20*(3), 479–489. https://doi.org/10.1002/we.2017

Wagner, J. S., Gohm, A., & Rotach, M. W. (2014). The impact of horizontal model grid resolution on the boundary layer structure over an idealized valley. *Monthly Weather Review*, *142*(9), 3446–3465. https://doi.org/10.1175/MWR-D-14-00002.1

Wang, Y. (2001). An Explicit Simulation of Tropical Cyclones with a Triply Nested Movable Mesh Primitive Equation Model: TCM3. Part I: Model Description and Control Experiment. *Monthly Weather Review*, *129*(12), 1370–1394. https://doi.org/10.1175/1520-0493(2002)130<3022:AESOTC>2.0.CO;2

Wang, Y. (2002). An Explicit Simulation of Tropical Cyclones with a Triply Nested Movable Mesh Primitive Equation Model: TCM3. Part II: Model Refinements and Sensitivity to Cloud Microphysics Parameterization*. *Monthly Weather Review*, *130*(12), 3022–3036. https://doi.org/10.1175/1520-0493(2002)130<3022:AESOTC>2.0.CO;2

Willis, G. E., & Deardorff, J. W. (1974). A Laboratory Model of the Unstable Planetary Boundary Layer. *Journal of the Atmospheric Sciences*, *31*(5), 1297–1307. https://doi.org/10.1175/1520-0469(1974)031<1297:ALMOTU>2.0.CO;2

Wilson, J. D., Finnigan, J. J., & Raupach, M. R. (1998). A first-order closure for disturbed plant-canopy flows, and its application to winds in a canopy on a ridge. *Quarterly Journal of the Royal Meteorological Society*, *124*(547), 705–732. https://doi.org/10.1256/smsqj.54703

WMO. Technical Regulations. In: *Encyclopedia of food and agricultural ethics*. Vol. 1. *2*. Dordrecht: Springer Netherlands, 2019, pp. 2338–2338. ISBN: 9789263100498. https://doi.org/10.1007/978-94-024-1179-9_301503.

Yang, J., Wang, Z.-H., Chen, F., Miao, S., Tewari, M., Voogt, J. A., & Myint, S. (2015). Enhancing Hydrologic Modelling in the Coupled Weather Research and Forecasting–Urban Modelling System. *Boundary-Layer Meteorology*, *155*(1), 87–109. https://doi.org/10.1007/s10546-014-9991-6

Yang, L., Yan, H., & Lam, J. C. (2014). Thermal comfort and building energy consumption implications – A review. *Applied Energy*, *115*, 164–173. https://doi.org/10.1016/j.apenergy.2013.10.062

Zardi, D., & Whiteman, C. D. Diurnal mountain wind systems. (F. K. Chow, S. F. De Wekker, & B. J. Snyder, Eds.). In: In *Mountain weather research and forecasting: Recent progress and current challenges* (F. K. Chow, S. F. De Wekker, & B. J. Snyder, Eds.). Ed. by Chow, F. K., De Wekker, S. F., & Snyder, B. J. Springer: Dordrecht, The Netherlands, 2013, pp. 35–119. ISBN: 978-94-007-4097-6 (Print) 978-94-007-4098-3 (Online). https://www.pmf.unizg.hr/_download/repository/Zardi-Whiteman_Chptr2%5B1%5D.pdf

Želi, V., Brethouwer, G., Wallin, S., & Johansson, A. V. (2019). Consistent Boundary-Condition Treatment for Computation of the Atmospheric Boundary Layer Using the Explicit Algebraic Reynolds-Stress Model. *Boundary-Layer Meteorology*, *171*(1), 53–77. https://doi.org/10.1007/s10546-018-0415-x

Zeng, X., & Wang, Y. (2020a). A k–$\varepsilon$ Turbulence Model for the Convective Atmosphere. *Journal of the Atmospheric Sciences*, *77*(11), 3891–3906. https://doi.org/10.1175/JAS-D-20-0072.1

Zeng, X., Wang, Y., & MacCall, B. T. (2020b). A k–$\varepsilon$ Turbulence Model for the Stable Atmosphere. *Journal of the Atmospheric Sciences*, *77*(1), 167–184. https://doi.org/10.1175/JAS-D-19-0085.1

Zhang, C., Wang, Y., & Xue, M. (2020). Evaluation of an E- and three other boundary layer parameterization schemes in the WRF model over the southeast pacific and the Southern Great Plains. *Monthly Weather Review*, *148*(3), 1121–1145. https://doi.org/10.1175/MWR-D-19-0084.1

Zhang, X., Bao, J. W., Chen, B., & Grell, E. D. (2018). A three-dimensional scale-adaptive turbulent kinetic energy scheme in the WRF-ARW model. *Monthly Weather Review*, *146*(7), 2023–2045. https://doi.org/10.1175/MWR-D-17-0356.1

Zilitinkevich, S., Gryanik, V. M., Lykossov, V. N., & Mironov, D. V. (1999). Third-Order Transport and Nonlocal Turbulence Closures for Convective Boundary Layers*. *Journal of the Atmospheric Sciences*, *56*(19), 3463–3477. https://doi.org/10.1175/1520-0469(1999)056<3463:TOTANT>2.0.CO;2

Zilitinkevich, S. S., Elperin, T., Kleeorin, N., Rogachevskii, I., & Esau, I. (2013). A Hierarchy of Energy- and Flux-Budget (EFB) Turbulence Closure Models for Stably-Stratified Geophysical Flows. *Boundary-Layer Meteorology*, *146*(3), 341–373. https://doi.org/10.1007/s10546-012-9768-8

Zilitinkevich, S. S., Elperin, T., Kleeorin, N., & Rogachevskii, I. (2007). Energy- and flux-budget (EFB) turbulence closure model for stably stratified flows. Part I: Steady-state, homogeneous regimes. *Boundary-Layer Meteorology*, *125*(2), 167–191. https://doi.org/10.1007/s10546-007-9189-2

Zonato, A., Martilli, A., Di Sabatino, S., Zardi, D., & Giovannini, L. (2020). Evaluating the performance of a novel WUDAPT averaging technique to define urban morphology with mesoscale models. *Urban Climate*, *31*. https://doi.org/10.1016/j.uclim.2020.100584

Contents on this book are licensed under a Creative Common Attribution
Non Commercial - No Derivatives
4.0 International License, except for the parts already published by other publishers.

University of Trento
Doctoral School in Civil, Environmental and Mechanical Engineering
*http://web.unitn.it/en/dricam*
Via Mesiano 77, I-38123 Trento
Tel. +39 0461 282670 / 2611 - *dicamphd@unitn.it*

**Andrea Zonato**